Conceptual Design Report
for
The Measurement of the Muon Anomalous Magnetic Moment $g - 2$ and Electric Dipole Moment at J-PARC

December 12, 2011

Table of Contents

5   Muon Linac   92

6   Muon Storage Field and Injection   114

7   Detection of Decay Positrons   148

8   Readout Electronics and DAQ System   191

9   Muon Storage Magnet

List of Contributors

Msaharu Aoki[8], Pavel Bakule[20], Bernd Bassalleck[24], George Beer[26], Gerry Bunce[27],
Abhay Deshpande[19], Simon Eidelman[4], Douglas E. Fields[24], Miloslav Finger[6], Michael Finger Jr.[6],
Yuya Fujiwara[17,14], Yoshinori Fukao[10], Noriyosu Hayashizaki[16], Seiko Hirota[10,14], Hiromi Iinuma[10],
Masanori Ikegami[10], Masahiro Ikeno[10], Katsuhiko Ishida[17], Masa Iwasaki[17], Ryosuke Kadono[10],
Takuya Kakurai[12], Takuya Kamitani[10], Yukihide Kamiya[10], Sohtaro Kanda[12], Frédéric Kapusta[5],
Naritoshi Kawamura[12], Takashi Kohriki[10], Sachio Komamiya[14], Kunio Koseki[10], Yoshitaka Kuno[8],
Alfredo Luccio[12], Oleg Luchev[2], Muneyoshi Maki[12], Glen Marshall[22], Mika Masuzawa[10],
Yasuyuki Matsuda[9], Teijiro Matsuzaki[17], Tsutomu Mibe[10], Katsumi Midorikawa[2], Satoshi Mihara[10],
Yasuhiro Miyake[10], William M. Morse[3], Jiro Murata[17,13], Ryotaro Muto[10],
Kanetada Nagamine[23,10,18], Takashi Naito[10], Hisayoshi Nakayama[10], Megumi Naruki[10],
Makiko Nio[21], Hajime Nishiguchi[10], Daisuke Nomura[10], Hiroyuki Noumi[15], Tomoko Ogawa[2],
Toru Ogitsu[10], Kazuki. Ohishi[17], Katsunobu Oide[10], Masahiro Okamura[3], Art Olin[22,26],
Norihito F. Saito[2], Naohito Saito[10,14], Yasuhiro Sakemi[7], Ken-ichi Sasaki[10], Osamu Sasaki[10],
Akira Sato[12], Aurore Savoy-Navaro[5], Yannis K. Semertzidis[3], Yuri Shatunov[12],
Koichiro Shimomura[10], Boris Shwartz[4], Wilfrid da Silva[25], Patrick Strasser[10], Ryuhei Sugahara[10],
Michinaka Sugano[10], Ken-ichi Tanaka[10], Manobu Tanaka[10], Nobuhiro Terunuma[10],
Nobukazu Toge[10], Dai Tomono[17], Eiko Torikai[12], Toshiyuki Toshito[11], Akihisa Toyoda[10],
Kyo Tsukada[12], Tomohisa Uchida[10], Kazuki Ueno[17], Vlasov Vrba[1], Satoshi Wada[2],
Akira Yamamoto[10], Kaoru Yokoya[10], Koji Yokoyama[17], Makoto Yoshida[10], Mitsuhiro Yoshida[10],
Koji Yoshimura[10]

List of Institutions

[1] *Academy of Science of Czech Republic, Institute of Physics, Na Slovance 2, CZ-18221 Prague 8, Czech Republic*

[2] *Advanced Research Institute, RIKEN, 2-1 Hirosawa, Wako, Saitama, 351-0198, Japan*

[3] *Brookhaven National Laboratory, Upton, NY 11973, USA*

[4] *Budker Institute of Nuclear Physics, 630090 Novosibirsk, Russia*

[5] *Centre National de la Recherche Scientifique, 3 rue Michel-Ange - F-75794 Paris cedex 16, France*

[6] *Charles University, Faculty of Mathematics and Physics, V Holesovickach 2, CZ-18000 Prague 8, Czech Republic*

[7] *Cyclotron and Radioisotope Center, Tohoku University, Sendai, Miyagi 980-8578, Japan*

[8] *Graduate School / School of Science, Osaka University, 1-1 Machikaneyama-cho, Toyonaka, Osaka 560-0043, Japan*

[9] *Graduate School of Arts and Sciences, the University of Tokyo, 3-8-1 Komaba, Meguro-ku, Tokyo 153-8902, Japan*

[10] *KEK, High Energy Accelerator Research Organization, 1-1, Oho, Tsukuba, Ibaraki, 305-0801, Japan*

[11] *National Institute of Radiological Sciences, 4-9-1, Anagawa, Inage-ku, Chiba, 263-8555, Japan*

[12] *Need to be checked and confirmed.*

[13] Physics Department, Rikkyo University, 3-34-1Nishi-Ikebukuro, Toshima, Tokyo 171-8501, Japan

[14] Physics Department, University of Tokyo, 7-3-1 Hongo, Bunkyo-ku, Tokyo, 113-0033, Japan

[15] Research Center for Nuclear Physics, Osaka University, 10-1 Mihogaoka, Ibaraki, Osaka 567-0047, Japan

[16] Research Laboratory for Nuclear Reactors, Tokyo Institute of Technology, 2-12-1 N1-16 O-okayama, Tokyo 15208550, Japan

[17] RIKEN Nishina Center for Accelerator Based Science, 2-1 Hirosawa, Wako, Saitama, 351-0198, Japan

[18] RIKEN, 2-1 Hirosawa, Wako, Saitama, 351-0198, Japan

[19] State University of New York, Department of Physics and Astronomy, Stony Brook, NY 11794-3800,USA

[20] STFC, Rutherford Appleton Laboratory, ISIS Muon group & RIKEN-RAL Muon Facility, Building R3, UG16, Chilton,OX11 0QX,Oxfordshire,United Kingdom

[21] Theoretical Physics Laboratory, Nishina Center, RIKEN, Wako, Japan 351-0198

[22] TRIUMF, Vancouver, BC, V6T 2A3, Canada

[23] University of California, Department of Physics and Astronomy, Riverside, CA 92521-0413, USA

[24] University of New Mexico, Albuquerque, New Mexico 87131, USA

[25] University of Paris 6, LPNHE, Paris , France

[26] University of Victoria, Finnerty Rd., Victoria, Canada

[27] Retired, Boulder, Colorado USA. email: bunce@bnl.gov

Preface

This document describes the conceptual design of the proposed experiment to measure the muon anomalous magnetic moment $(g-2)$ and electric dipole moment (EDM) at J-PARC.

We have submitted the proposal to the J-PARC PAC back in December 2009. Since then, we have gone through significant R&D efforts in various area of the project. As noticed by many, the project involves a wide field of expertise, material science for muonium production target, accelerator physics for muon acceleration, injection, and storage, precision field control and its measurement, and very high rate detection system.

Thanks to a generous support by the lab, we were able to gone through many of them. While those studies are not fully complete yet, as you will find out in this document, we now have a pretty clear idea on how to construct the experiment. For example, the experience with the protptype magnet design and partial construction has been beneficial in developing concrete design for the real magnet for the g-2/EDM measurement.

In parallel, the muon facility at J-PARC is also developing, again thanks to generous support by the lab. The muon facility group are going to complete the magnets near the primary target area especially in H-line, where our experiment is planned. The facility faced a significant risk of abandoning the beam line, if they could not receive the support. Resources are secured "just in time" to complete the work near the high dose area. This represents the positive step forward to realize our experiment.

We have tried to provide an overview and a current status of the project in "Overview" chapter, which also provides a pointer to a more detailed description for interested readers. We have also produced a list of milestones to set a goal of each R&D effort. The milestones are also described in "Overview" chapter.

Physics of Muon $g-2$ and EDM will be described in Chapter 2. Surface muon production and

its transport will be describe in Chapter 3. Ultra-cold muon production, which include muonium production and its laser ionization will be described in Chapter 4. Chapter 5 describes the Muon linac with a new design including the RFQ. The concept of the muon beam injection and storage in the precision field is described in Chapter 6.

Detector system and its read out system are described in Chapter 7 and Chapter 8, respectively. The detailed design of the precision magnet and its monitoring system are depicted in Chapter 9.

Extraction of the precession frequency vector $\vec{\omega}$ is detailed in Chapter 10, followed by its ω_a and ω_η parts converted into anomaly a_μ and EDM, respectively, in Chapter 11.

Cost and schedule are discussed in Chapter 12.

In the end, we would like to express our sincere gratitude to all supporters of the experiment for their continual encouragements in various forms. We believe that a realization of the experiment in timely manner will be a best return.

Tsukuba, December 2011,

Collaboration for the Muon $g-2$/EDM Experiment at J-PARC

CHAPTER 1

Overview

Contents

In this document we present the baseline design for the muon $g − 2$/EDM experiment proposed for the J-PARC muon facility at MLF.

This conceptual design report (CDR) contains plans based on experimental and engineering studies, and plans which require experimental verification. The plans for the beamlines and storage ring magnet and field measurement are being developed at level, including involvement of a company that specializes in precision MRI magnets. The plan for the muonium production target region is based on published measurements, but requires detailed tests of the planned configuration, including a new high-power laser, to confirm our plan. For this region we have used our calculations to give expected rates and sensitivity for the CDR. The CDR includes a set of detailed milestones toward reaching an engineering plan for the experiment.

We propose to use the J-PARC muon facility at MLF, MUSE to perform a new experiment to measure the muon's anomalous magnetic moment $(g−2)$ and its electric dipole moment (EDM). The sensitivity goal is 0.1 parts per million (ppm). The experiment would store μ^+ in an MRI-type solenoid magnet and measure polarized μ^+ decays to positrons. More higher energy e^+ are emitted with the muon spin direction aligned with its motion in the storage ring. Muon spin precession as the muons orbit in the storage ring result in the number of high energy e^+ oscillating as the muon spin precess es from forward to backward from the muon direction. This precession, due to an advance of the muon spin precession compared to the muon momentum in a magnetic field, is due to the difference $g − 2$. Detectors on the inside of the muon storage orbit will track the decay e^+, and the experiment collects the number of higher energy e^+ versus time in store, as the muon spin precesses in the magnetic field. The anomaly $g − 2$ is the advance of the muon spin from its momentum vector divided by the storage magnet field strength. The $g − 2$ experiment requires precision measurements of the higher energy e^+ with time, and of the magnetic field.

The EDM measurement will be done with the same μ^+ decays as the $g−2$ measurement. As described in details in the later sections, both dipole measurements can be done at the same time. We propose to measure the precession frequency as a vector, specifically one component parallel to the magnetic field, and the other component orthogonal to both momentum vector and the magnetic field. The latter corresponds to the precession due to the muon EDM.

The J-PARC muon $g − 2$/EDM measurement will use a very different approach compared to previous muon $g − 2$ experiments. The J-PARC experiment will use an order of magnitude lower energy and an order of magnitude smaller diameter storage ring. Previous experiment used 3.1 GeV muons and a 14 m diameter storage ring, and used calorimetry to measure the decay positrons. The energy of the previous experiments was set by a cancellation in the contribution to the spin precession from strong electric field focusing at this energy. For J-PARC, it is proposed to develop a source of ultra-cold muons, which require only weak focusing to maintain the beam size in a storage ring. This releases the requirement on the muon energy, and a momentum of 300 MeV/c was chosen with a 3 T MRI-type solenoid used to store the muons. Tracking will measure the decay e^+ momentum.

Previous experiments reached a sensitivity on muon $g−2$ of 0.54 ppm, with the uncertainty dominated by statistics. The result, with the most recent and sensitive from E821 at Brookhaven National Laboratory (BNL), is not described by the Standard Model of particle physics, with a ∼3 sigma
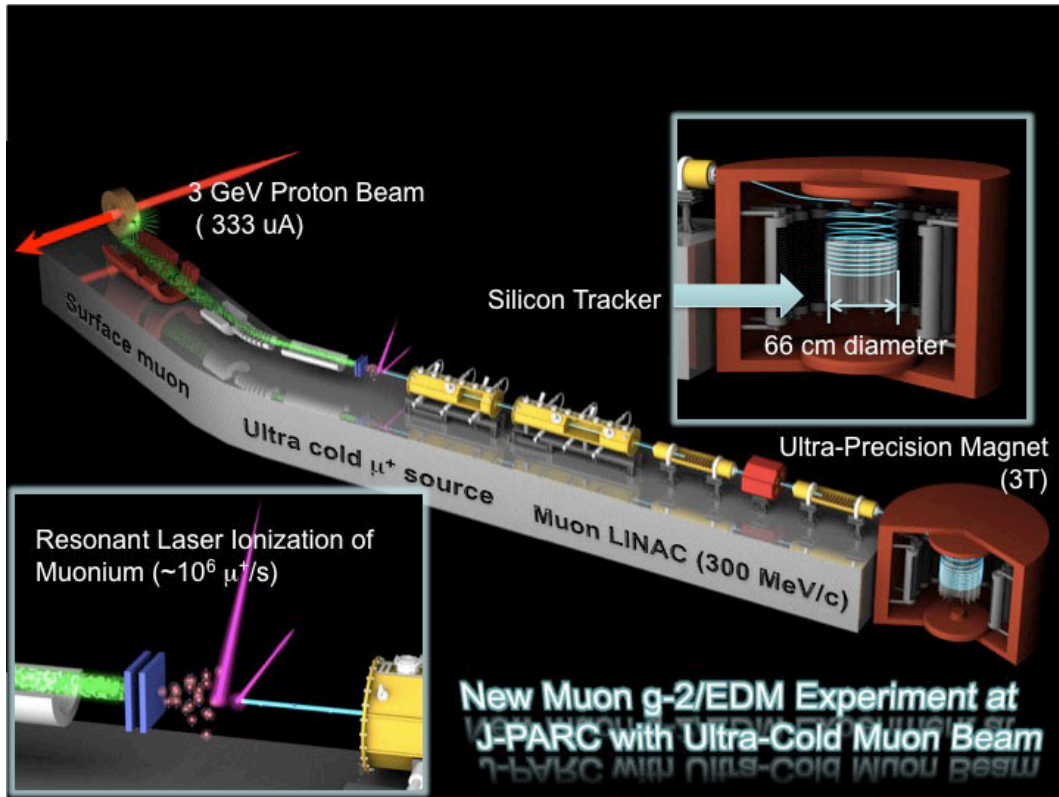
Figure 1.1: *Conceptual representation of the muon $g - 2$/EDM experiment at J-PARC MLF.*

deviation, suggesting the need for physics beyond the Standard Model. Muon $g - 2$ is a fundamental observable of elementary particle and it is valuable to improve upon its measurement and also to perform the experiment using different approaches. Any comprehensive theory of particle physics must describe muon $g - 2$. We have proposed the J-PARC experiment to make a completely independent measurement of muon $g - 2$, with completely different experimental issues and systematics. We also aim to improve the $g - 2$ uncertainty from the BNL experiment by a factor 5. We note that a $g - 2$ experiment is going forward at Fermilab using, in general, the same technique as at BNL, with 3.1 GeV muons and plans to transport the 14 m storage ring from BNL to Fermilab. They also aim to reach a sensitivity of 0.1 ppm.

We note here that the lower energy beam for the J-PARC experiment will allow us to frequently reverse the muon spins. This will be a powerful tool to cancel difficult systematics such as pile-up which can change detection efficiency versus time. This spin reversal is not available to the Fermilab experiment, and has not been used before in previous $g - 2$ experiments. We also note that the spin reversal is beneficial in reducing the systematic uncertainties in the EDM measurement.

The J-PARC experiment uses techniques that are completely new to the $g - 2$ measurement which, while providing very different systematic uncertainty issues compared with previous (and future, at Fermilab) measurements, this requires experimental tests of many new techniques. We describe in

this overview the approach, and indicate the areas that must be assessed. These tests are included in a list of detailed milestones that follow this overview. Details of each experimental step then follow the milestones.

Table 1.1 compares the proposed experiment with the previous experiment, BNL-E821, and its continuation at Fermilab. The Fermilab experiment is going to utilize the same storage ring as the E821. Statistical precision of J-PARC experiment is projected to be comparable thanks to the higher field and larger number of muon decays even with the more rapidly decaying muon due to lower energy.

Table 1.1: *Comparison of the previous experiment BNL-E821, FNAL-E989, and this experiment.*

	BNL-E821	FNAL-E989	This Experiment
Muon momentum	3.09 GeV/c		0.3 GeV/c
γ	29.3		3
Polarization	100%		$> 90\%$
Storage field	$B = 1.45$ T		$B = 3.0$ T
Focusing field	Electric Quad.		very-weak magnetic
Cyclotron period	149 ns		7.4 ns
Anomalous spin precession period	4.37 μs		2.11 μs
# of detected e^+	5.0×10^9	1.8×10^{11}	1.5×10^{12}
# of detected e^-	3.6×10^9	–	–
Statistical precision	0.46 ppm	0.1 ppm	0.1 ppm

1.1 Principle of Measurement

In the presence of the static magnetic and electric field, the muon spin will go through a precession as follows:

$$\vec{\omega} = \vec{\omega_a} + \vec{\omega_\eta} \tag{1.1}$$

$$= -\frac{e}{m}\left[a_\mu \vec{B} - \left(a_\mu - \frac{1}{\gamma^2 - 1} \right) \frac{\vec{\beta} \times \vec{E}}{c} + \frac{\eta}{2}\left(\vec{\beta} \times \vec{B} + \frac{\vec{E}}{c} \right) \right] \tag{1.2}$$

Here $\vec{\omega}$ is separated into $\vec{\omega}_a$, precession due to an anomalous magnetic moment,

$$a_\mu = \frac{g - 2}{2} \quad \text{with} \quad \vec{\mu} = g\left(\frac{e}{2m} \right) \vec{s}, \tag{1.3}$$

and, $\vec{\omega}_\eta$, the one due to EDM,

$$\vec{d} = \eta \left(\frac{e}{2mc} \right) \vec{s}. \tag{1.4}$$

In the previous $g - 2$ measurements at CERN and BNL, the energy of the muon was chosen to cancel the term of $\vec{\beta} \times \vec{E}$. This was unavoidable solution, because the muon beam was widely spread over the phase space due to its production as a tertiary beam, which required electric focusing. In addition, the EDM term, $\vec{\omega}_\eta$ was neglected basing on the electron EDM limit with a mass scaling assumption.

Instead, we have chosen to eliminate the electric field so that we have simplified the equation as

$$\vec{\omega} = -\frac{e}{m}\left[a_\mu\vec{B} + \frac{\eta}{2}\left(\vec{\beta}\times\vec{B}\right)\right].\tag{1.5}$$

Since the precession vectors $\vec{\omega}_a$ and $\vec{\omega}_\eta$ are orthogonal each other, we should be able to separate by having an appropriate detector design.

Figure 1.2 displays the projected "wiggle plot" to extract the absolute value of the precession vector $|\vec{\omega}|$. Figure 1.3 displays the possible EDM precession with the assumed value of 2×10^{-20} e·cm.
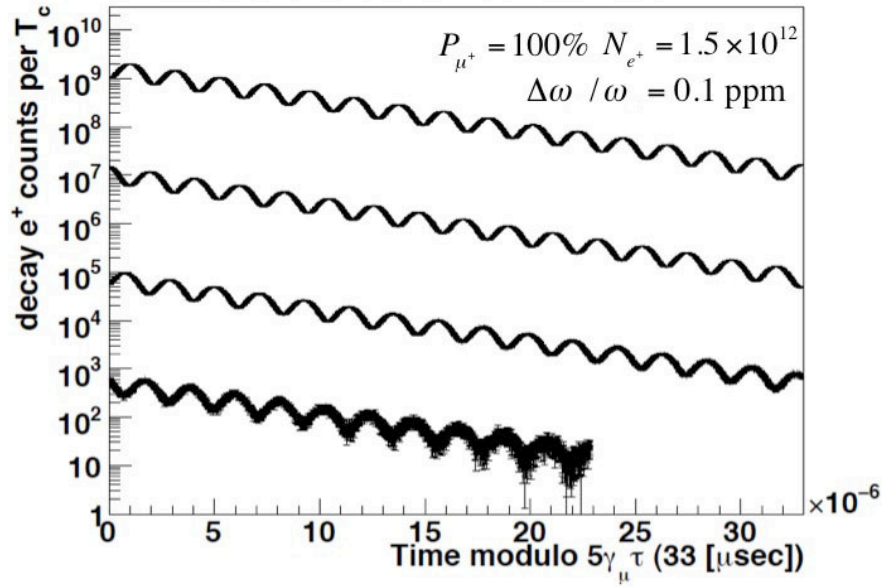

Figure 1.2: *Expected wiggle plot from the simulation studies. Here we assume 100% polarized muon and 1.5×10^{12} muon decays, which is possible in one year of running with the projected number of ultra-cold muons, $1\times10^6\mu^+/s$.*

Extraction of the precession frequency is described in Chapter 10. Both precession frequencies should be converted to the dipole moment values. We decided to follow the prescription of the previous experimental approach. We plan to perform the measurement of hyper-fine splitting of the muonium at J-PARC MLF at the same beamline. Details are described in Chapter 11.

1.2 Surface Muons and Transport Beamline

We intend to use the planned μ^+ surface muon beam from the MUSE H-line at J-PARC MLF as displayed in Fig. 1.4. with $1 \times 10^8\mu^+/s$ at 28 MeV/c in a 5% (rms) momentum bite, with 100% polarized muons. This beamline is largely designed, with the upstream capture solenoid being built,
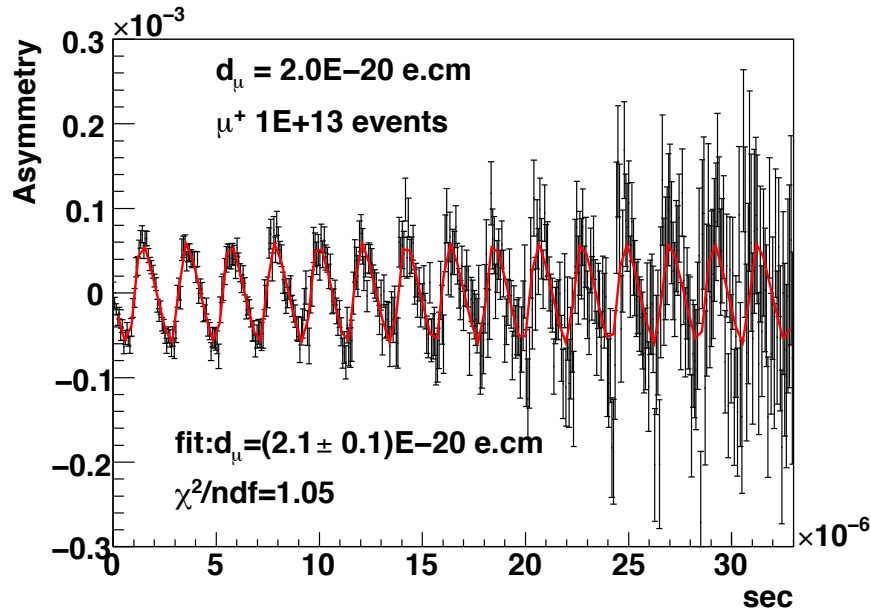
Figure 1.3: *Expected asymmetry plot from the simulation studies. Polarization and number of muons are identical to the "wiggle" plot.*

and with the design completed on the first bending magnet, both to be installed in summer 2012. This early installation date avoids high levels of radiation due to planned MUSE running for other beamlines.

A detailed design of the H-line is also being developed. The effort was originally triggered by the needs for DeeMe experiment. Now the design is optimized for the $g - 2$ experiment with the G4Beamline as depicted in Fig. 1.5.

The expected muon flux is based on measurements at CERN and at the MUSE D-line of MLF. See Chapter 3 for details. In addition, a realistic simulation studies are ongoing to further confirming the shielding strategy around the H-line.

1.3 Mu Production Target and Production of Ultra-Cold Muons

The 28 MeV/c μ^+ beam will be focused on to a muonium production target. By producing muonium (Mu), a $\mu^+ - e^-$ atom, the muon is effectively stopped, but maintains its polarization. The e^- are then stripped from the muonium atoms using a powerful new laser beams. The ultra-cold μ^+ produced this way will be fully polarized, with very little transverse momentum. We refer to these as ultra-cold muons.

A crucial issue for this experiment is to reach an efficiency of order 1% in the production of fully
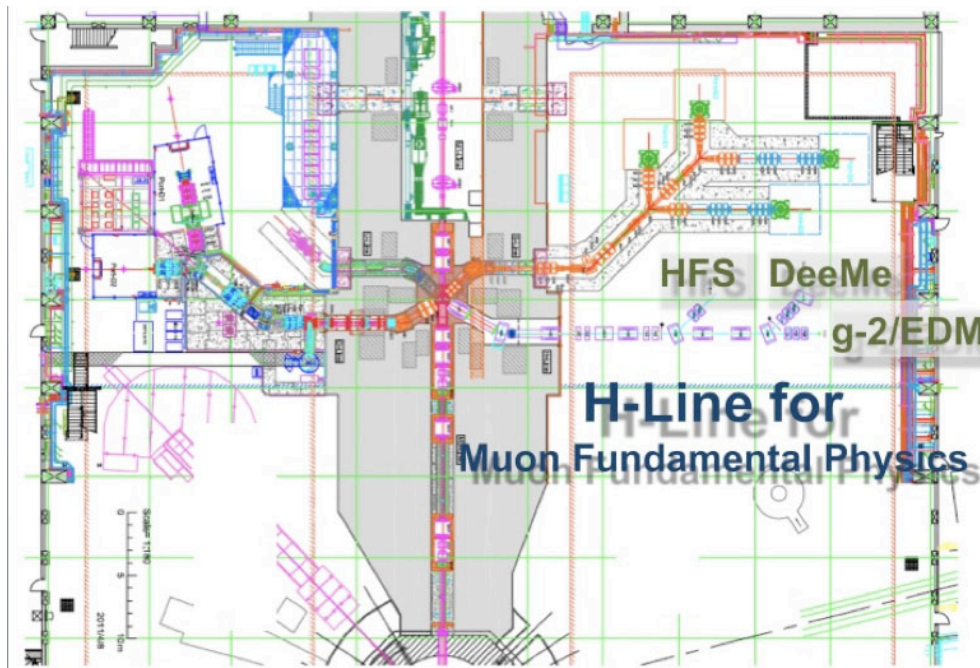
Figure 1.4: *Top view of the MUSE facility at J-PARC MLF with H-line for muon fundamental physics. The beam line can accommodate Mu HFS experiment, $\mu - e$ conversion experiment, and muon $g - 2$/EDM experiment.*

Figure 1.5: *G4Beamline model for the H-line at MUSE.*

polarized ultra-cold muons. This CDR presents a tungsten foil target in a 0.3 T longitudinal magnetic field, with the tungsten heated to 2,000 K, as the muonium production target. The magnetic field

Figure 1.6: *Conceptual representation of muonium production and ionization chamber. Adopted from the RIKEN-RAL beamline.*
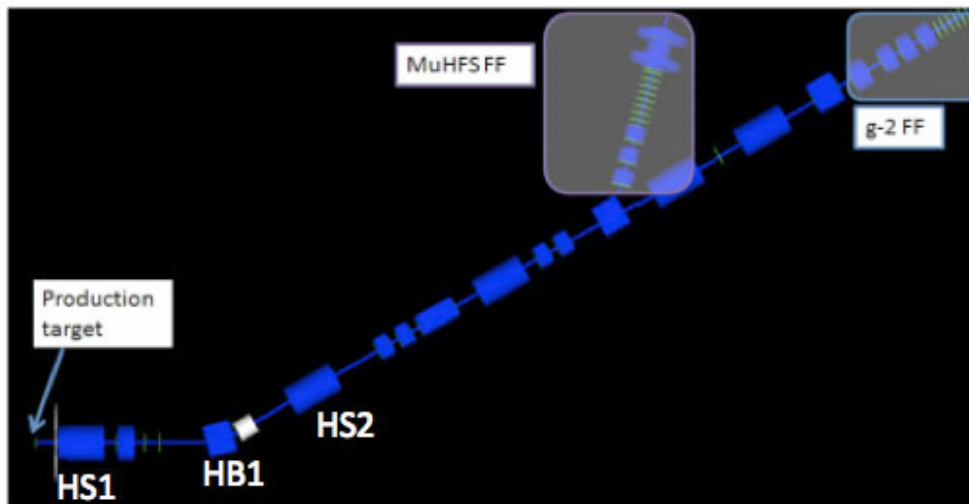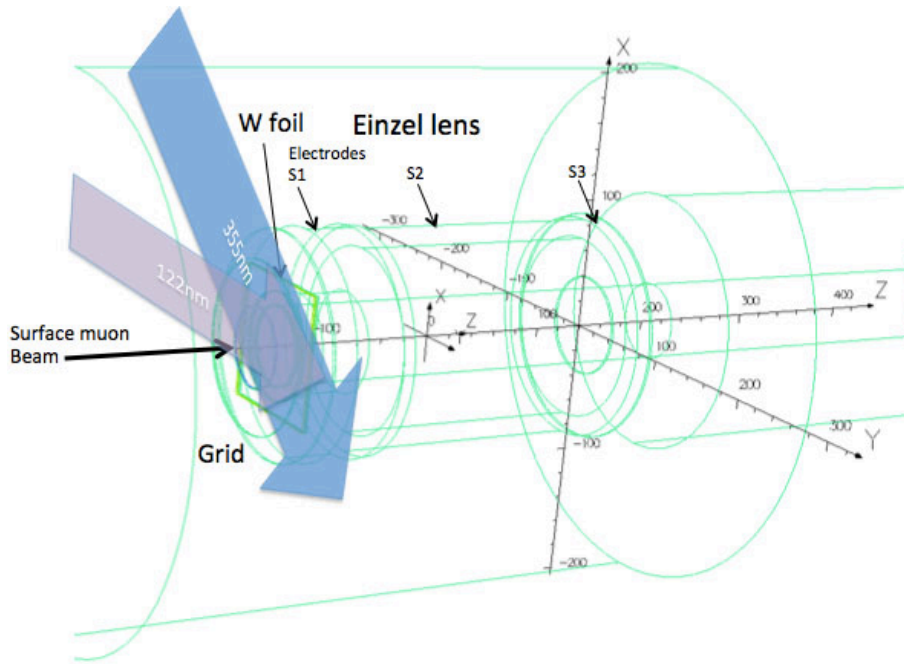
holds the muon spins, maintaining full muon polarization, during muonium formation. We ionize the muonium via 1S-2P transition by 122 nm and 355 nm laser. We use the 100 μJ 122 nm laser being completed at RIKEN to strip the electrons from the muonium atoms. The core μ^+ will be accelerated by the electric field to 5.7-keV, then injected into the first accelerator component with radio frequency, RFQ. The magnetic field should be eliminated at the time of the extraction, to avoid emittance growth.

This design is based on the our R&D at both TRIUMF and at Rutherford Appleton Laboratory (RAL). The TRIUMF experiment S1249 focused on the optimization of the muonium production target and measurement of space-time distribution of the muonium emitted into the vacuum. The ionization efficiency estimate became more accurate by using the results from the S1249 measurement.

The RIKEN muon facility at Rutherford Appleton Laboratory (RAL) has been using a heated tungsten target, and a 1 μJ 122 nm laser, with no holding magnetic field. A test is planned for this winter with a 10 μJ 122 nm laser to measure the efficiency for stripping the electrons from Mu. We have based the efficiency for Mu production used in this CDR on published results from this beamline, on measurements of muonium diffusion from an aerogel target at TRIUMF. We have used 50% efficiency for stripping in an 8 mm region, using two passes of the 100 μJ laser.

The RAL experiment aims to measure the laser power dependence of the ionized muon flux. The previous laser system has been significantly upgraded to have a better stability and monitoring capability. While significant efforts are made, the measurement is not completed yet. We expect to

obtain the results soon before spring, 2012. The results will be useful in the estimation of ionization efficiencies.

The overall efficiency for production of fully polarized ultra-cold muons is then 0.12%. Obviously we need another factor 8 to achieve the required efficiency.

Significant simulation studies are ongoing to be ready for the next round of the R&D. Key issues are:

- maximize the number of stopped muons by utilizing the full momentum bite, 28 MeV/$c\pm5\%$(rms),

- maximize the "surface region" from where the muon or muonium can be emitted into vacuum.

We will perform the test measurements at J-PARC D-line, once the beam operation is recovered at the facility.The measurements will be one of the major milestones of this experiment.

1.4 Acceleration of Ultra-Cold Muons

1.4.1 Initial Acceleration

An electric field will be used to extract the ultra-cold muons from the stripping region, along the magnetic field direction. It is important that the electric field lines be parallel to keep from increasing the p_T of the muons.
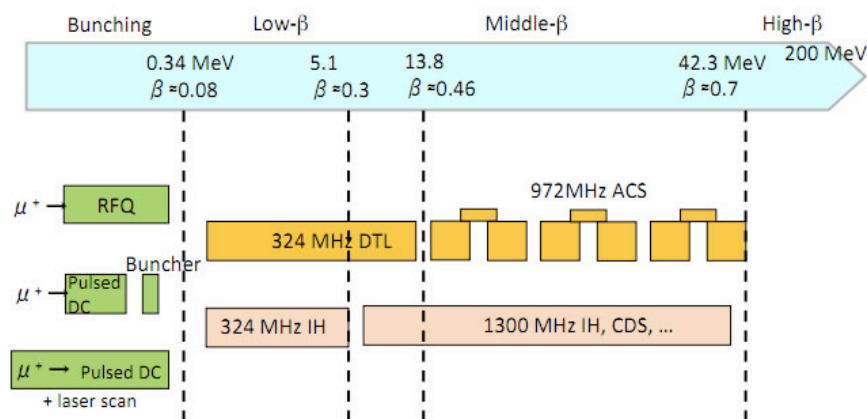

Figure 1.7: *Conceptual layout of the muon re-acceleration scheme. Current baseline is RFQ with 324 MHz IH and 1300 MHz IH.*

Muon g-2/EDM Experiment, Conceptual Design Report, Revised, December 12, 2011, 11:40 A.M.
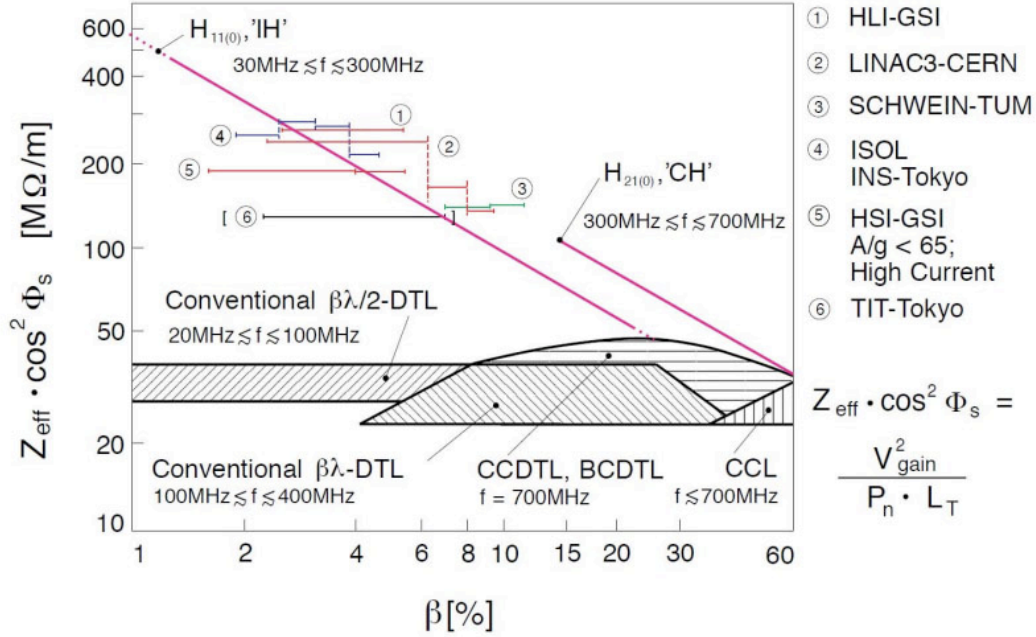
Figure 1.8: *Plot summarizes shunt impedance in various linac structure as a function of particle velocity. IH has significantly higher shunt impedance up to $\beta \sim 25\%$.*

1.4.2 Post Acceleration

The expected μ^+ beam bunch width is 3 ns after the initial acceleration by an electric field. The bunch should be further narrowed by the radio-frequency quadrupole (RFQ) to be further accelerated by an RF field to higher energies.

We will perform a test experiment of muon acceleration at U-line. We will utilize the un-used RFQ structure from J-PARC LINAC for the test. Figure 1.9 shows the existing RFQ functioning at J-PARC Linac. The field strength should be decreased according to the ratio of the muon and proton mass. Design of the power supply for the RFQ is ongoing. This test would be one of the major milestones of the experiment.

So far the existing RFQ design can be also considered as the baseline for our experiment. The design will be further refined basing on the test acceleration at U-line.

We decided to adopt an inter-digital H-mode linac (IH linac) for the post acceleration up to $\beta \sim 0.7$. An original baseline design utilizing drift-tube linac (DTL) and annular-coupling structure (ACS) can be technically solid option, however, the cost can be very high. Therefore we now take the IH linac as the primary option for the muon acceleration.

The first proto-type of the IH linac for muon acceleration will be produced as a part of the test acceleration at MUSE U-line. After the RFQ, the IH linac will accelerate the muon beam to a kinetic

Figure 1.9: *Existing RFQ at J-PARC Linac. We plan to use the second spare of the same design.*

Table 1.2: *Dimensions of the RFQ at J-PARC Linac.*

		normalize (λ =1)
wave length	0.925 m	1
mean bore radius r_0	3.7 mm	0.004
$\beta\lambda/2$ (3 MeV)	36.9 mm	0.04
vane length	3.115 m	3.37
vane: machining accuracy	15 μm	1.62×10^{-5}
vane: positioning accuracy	30 μm	3.24×10^{-5}
vane-tip curvature	0.89 r_0 - 3.293 mm	0.00356

Table 1.3: *Field parameters of the RFQ at J-PARC Linac.*

Design parameters	
RF frequency	324 MHz
Inter-vane voltage	82.9 kV
Maximum surface field	31.6 MV/m (1.77 Kilpatrik)

energy of 3 MeV.

The higher beta linac has no change in the design. The baseline design employs the disk-loaded type linac. As the muon beam achieves higher energy, the linac structure becomes more electron-like.

Muon g-2/EDM Experiment, Conceptual Design Report, Revised, December 12, 2011, 11:40 A.M.
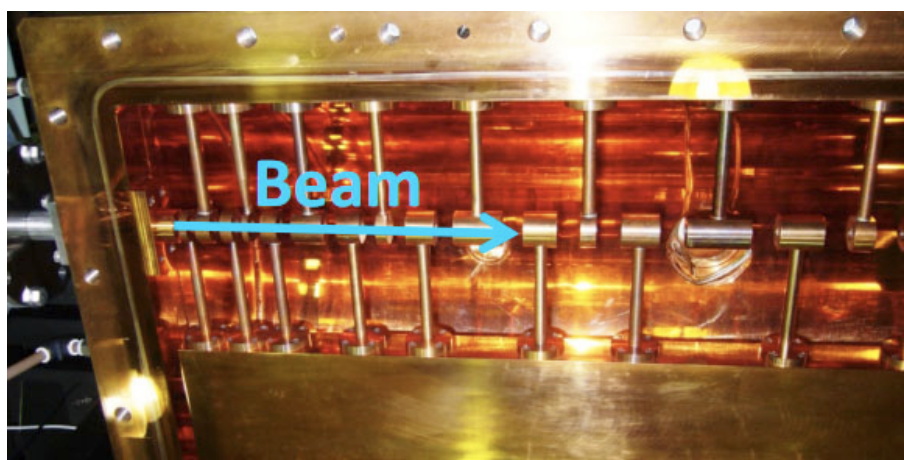
Figure 1.10: *Inner structure of the inter-digital H-mode made by the*

1.5 Injection, Storage Ring, Weak Focusing and Field Measurement

The muon beam will be injected into the storage field using the spiral injection scheme.
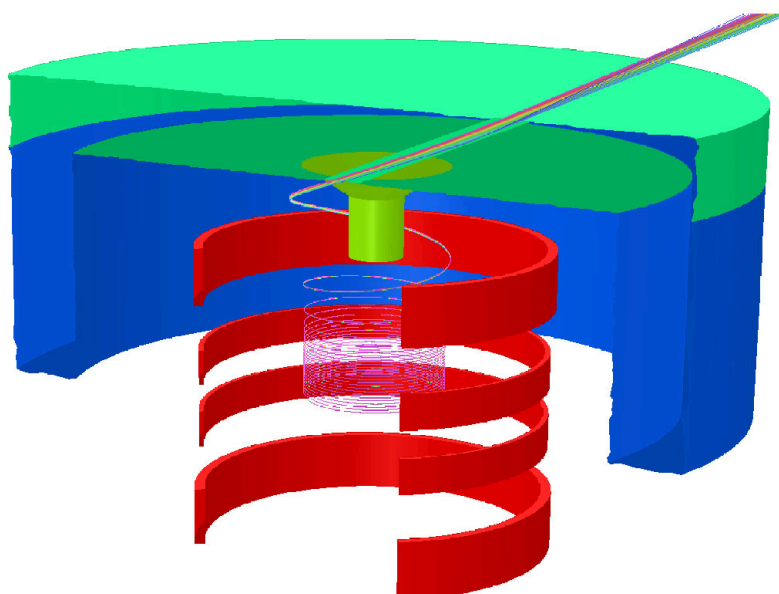

Figure 1.11: *Pictorial representation of the beam injecting. The beam will be guided into the precision field through the hole in the iron yoke, and through the radial field. Then the vertical motion of the beam will be finally stopped by a slight kick.*

Muon g-2/EDM Experiment, Conceptual Design Report, Revised, December 12, 2011, 11:40 A.M.

As displayed in Fig. 1.11, the beam will be injected with a vertical angle. The magnetic field in the injection region is carefully designed to have a radial component, which deflects the vertical momentum of the beam into horizontal. When the beam reached the storage region, a remaining vertical component will be eliminated by a slight kick by two pairs of round coils. A major change in the design from the proposal is the inclusion of a very-weak focusing field in the storage region. This decision relaxes the requirements on the beam "coldness" or the transverse dispersion, detector coverage in height, and possibly field uniformity. The storage field without the focusing field has integer tune, which would provide unstable condition for the stored beam because even a small errortic field effects would be accumulated. Therefore, we have decided to apply the very-weak focusing with the field index of

$$n = -\frac{R}{B_0}\frac{\partial B_y}{\partial r} \sim 10^{-5}. \tag{1.6}$$

The magnetic field design is almost complete at the conceptual level. The design accommodated the field requirement for the injection region with smooth radial field, highly homogeneous field in the storage region with a very weak focusing field with a field index in the order of 10^{-5}. The magnet employs four independent coils with independent current.

Table 1.4: *Specification of the storage field.*

specifications		
field strength		3 T
field uniformity	locally	≤ 1 ppm
	integral	< 0.1 ppm
uniform region	radius	33.3 ± 1.5 cm
	height	± 5.0 cm

Shimming strategy involves three steps. A field error from a static source such as coil misalignment and deformation and possible magnetic materials inside the magnet should be corrected by the pieces of irons. A field error from a dynamic source such as temperature change in the iron yoke reflected to its permeability, characteristics of the superconductor itself, and mechanical vibration, should be corrected by using both superconducting and normal conducting shimming coils.

There are progress in the quench protection, mechanical design, cryogenic design, and field monitoring system. Details are described in Chapter 9.

1.5.1   Detection of Positrons, Rates, and Uncertainties for Measurement

The precision measurement of the precession frequency requires the stable detection of the decay positrons, especially with a maximal sensitivity for muon spin orientation. We have set the energy threshold for the measurement as 200 MeV basing on the figure-of-merit analysis accounting the counting rate and analyzing power.

In addition, the detector should provide "in-plane" and "out-of-plane" precession frequencies, $\vec{\omega_a}$

and $\vec{\omega_\eta}$, respectively. Especially the latter is sensitive to the up-and-down asymmetry of the decay trajectory. Tracking would be also useful in tracing back to the muon trajectory in the storage field. It is possible to obtain the decay vertex distribution by tracing back the reconstructed track to the muon storage radius. Such a distribution would provide a good in-situ monitor of the beam trajectory.

The positron rate to be observed in the entire detector system would be as high as 30 positrons per 5 ns in the beginning of each spill, and will go down to 0.2 positrons per 5 ns after 5 times dilated life time of the muon. The detector should be highly segmented to minimize the pile-up effects in the beginning of spills.

Basing on these considerations, we have identified the baseline configuration of the detector system to be silicon tracker with 48 vanes extending from 66 mm to the 288 mm in radius, and ± 200 mm in height (in the direction of main storage field, 3T). We now have included the tungsten absorber in the inner radius to eliminate unwanted spirals of low energy positrons. Such a detector system is depicted in Fig. 1.12.

A detailed simulation study and development of track reconstruction algorithm are ongoing. Track finding is complicated especially in the beginning of the spills. However, we have found that using the $\phi - z$ and $z - t$ correlations, we can improve the track-finding efficiency significantly. Such studies are described in Chapter 7.
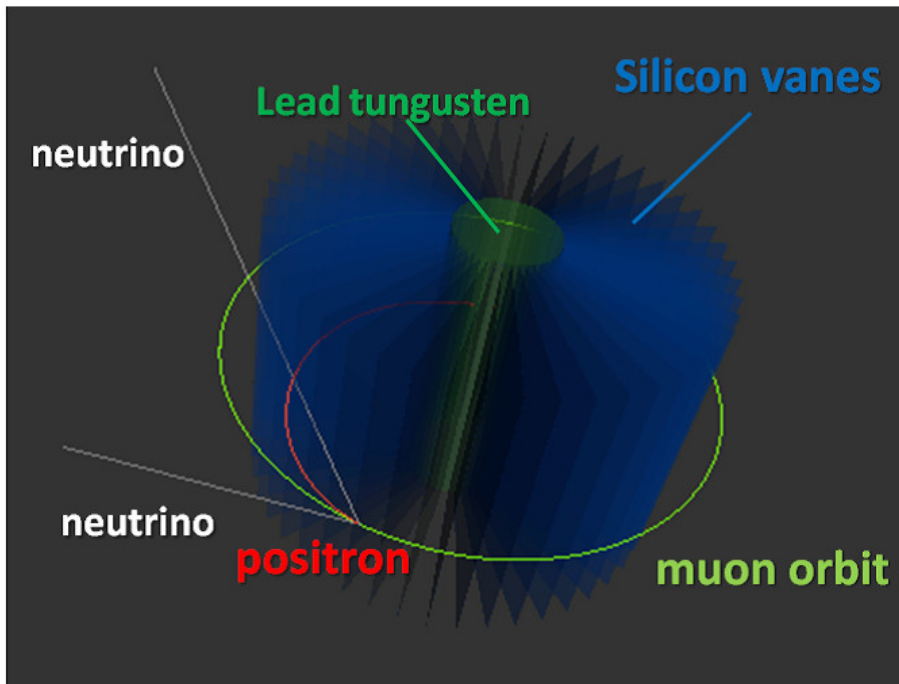

Figure 1.12: *Layout of the positron detector system.*

In parallel to such designing efforts, we are already evaluating silicon sensors especially with respect to the time response and its rate dependence. Some initial results are presented in Chapter 7.

The readout electronics are also being designed. Figure 1.13 displays the overview of the readout and data acquisition (DAQ) system. A new preamplifier-shaper-discriminator with digital buffer memory to store hits in every 5 ns time stamp is being designed at KEK. The data stored in the front end are readout in between 25 Hz beam spill via bidirectional serial links. Design of the data acquisition system are described in Chapter 8.

An accurate and stable frequency reference is necessary for the detector time stamping and also for the NMR probe. The clock distribution system utilizes a Rubidium frequency standard with remote calibration capabilities. The clock distribution system is continuously calibrated by the frequency data from GPS and the national frequency standard defined by hydrogen masers at National Metrology Institute of Japan. Anticipated stability of frequency is better than 3×10^{-11}/s. Configuration of the clock distribution system is discussed in Chapter 8.
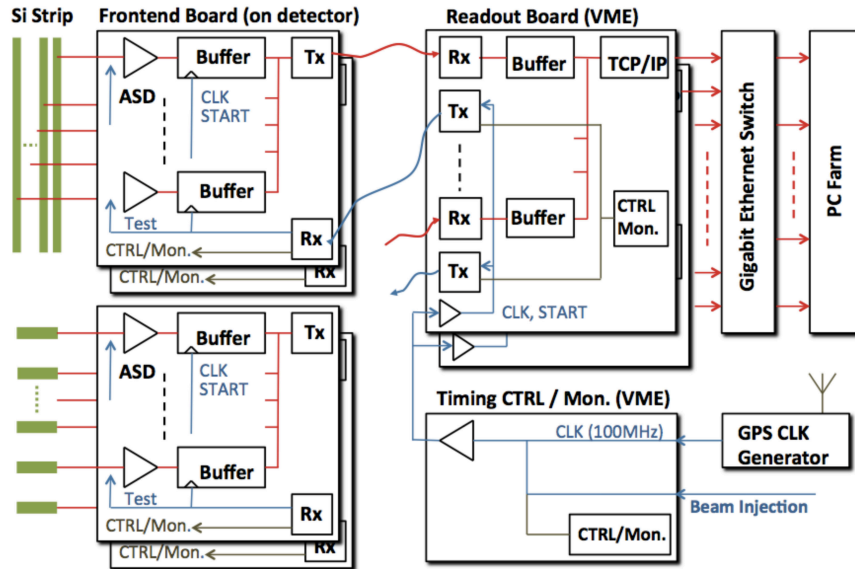

Figure 1.13: *Overview of the readout and DAQ system*

1.6   Analysis Strategies

As described in Section 1.1, we will extract the precession frequency vector $\vec{\omega}$ from the decay positron tracking. The in-plane component should be a good measure of the $g - 2$, and the out-of-plane component is the signal of the EDM.

We have started to look into the details of the frequency analysis. The χ^2 minimization procedure and blinding policies are described in Chapter 10.

Muon g-2/EDM Experiment, Conceptual Design Report, Revised, December 12, 2011, 11:40 A.M.

The extracted frequency should be converted into the $g-2$ and EDM values. Our experiment is essentially the frequency measurement, including the magnetic field, which will be measured in the form of NMR frequency. In converting the frequencies, we can utilize the ratio of muon and proton magnetic moments, determined from the measurement of the hyper-fine-splitting of Muonium (MuHFS), which is a separate experiment at H-line of MUSE at J-PARC. Some details are discussed in Chapter 11.

Obviously these efforts have just started and should be extended further with the establishment of analysis framework.

1.7 Milestones

As can be seen in the above mentioned overview of the project, the project involves several R&D issues. We have set the milestones of the project as follows.

- Demonstration of the ultra-cold muon production with the required ionization efficiency, 1%, or intensity $1\times10^6 \mu^+ s$/s,

- muon acceleration test with the baseline configuration of low-β Muon Linac, *i.e.* RFQ, and IH-Linac,

- test of spiral injection scheme,

- production of prototype magnet and development of the field monitor with the required precision, and

- demonstration of rate capability of the detector system for decay positron detection.

As described in the later chapters, significant R&D efforts are made in all areas listed above. The development of the Ultra-cold muon source are being pursued at TRIUMF and at RAL. The muon acceleration studies are being planned at the U-line at MUSE of J-PARC MLF. The necessary resources are secured to be ready for the test when the ultra-cold muon beam is available at U-line in JFY2012. A test for the spiral injection scheme is now planned with an electron beam in KEK. The prototype for the precision field magnet is already being constructed to be completed in JFY2012. A beam test for the silicon tracker prototype is planned in autumn 2012.

We will improve the conceptual design described in this document reflecting the results from these experimental verification of the basic concepts of the experiment.

1.8 Cost and Schedule

We developed a technical schedule of the experiment, assuming sufficient budget and manpower are allocated in time without significant delay. Major milestones in the schedule are that completion of the

H-line construction in JFY2013, start of muon linac operation, and installation of the kicker system in JFY2014, completion of commissioning the muon storage magnet in JFY2015, and completion of the positron detector in JFY2016. The expected date for the first beam to the detector is middle of JFY2016. The intended schedule of each subsystem is described in Chapter 12.

As for the cost, we have only high level summary as was done in the proposal. The design of the project became more detailed and we now have a much better understanding of the entire system. It should be reflected to the cost estimate to make it more precise. We expect that there would be a large cost reduction in Muon Linac by employing the IH linac structure. We should go through more detailed cost estimate for this part of the project once the acceleration test is done.

Physics of Muon $g - 2$ and EDM

Contents

2.1   Physics of Muon Dipole Moments

In this section, the physics motivation of the precision measurements of muon dipole moments are described.

2.1.1   Muon Dipole Moments

Spin is the fundamental quantum number of elementary particle in the standard model. Both magnetic and electric dipole moments are related to the particle spin as

$$\vec{\mu} = g\frac{e}{2m}\vec{s} \quad \text{and} \quad \vec{d} = \eta\left(\frac{e}{2mc}\right)\vec{s}. \tag{2.1}$$

As for the magnetic moment, the gyro-magnetic ratio g can be calculated as 2 at the leading order in Dirac equation. Higher order corrections including, quantum electrodynamics (QED), electro-weak (EW), quantum-chromodynamics (QCD), and possible new physics contribute to the difference $g - 2$. The standard model contribution to the $g - 2$ can be precisely calculated basing in the present knowledge. Any significant deviation from the standard model prediction would indicate a new physics.

On the other hand, an electric dipole moment is parity-odd and time-reversal-odd object. If the value is found to be non-zero, it would be a direct observation of the time- reversal violation. Consequently, it also means the CP-violation under the CPT theorem. All CP-violating effects discovered so far are in the quark-sector and can be explained within the Cabibbo-Kobayashi-Maskawa (CKM) theory. Therefore, if the muon EDM is measured to be finite, it is the first observation of the CP violation in the lepton sector and indicates a new physics beyond CKM theory.

2.2   Experimental Situation

The anomalous magnetic moment of the muon, a_μ has been measured with ever increasing precision for more than a half-century and served as a solid testing ground for the Standard Model of particle physics. a_μ is defined from the magnetic moment $\vec{\mu_\mu}$ and its spin vector $\vec{s}$ as

$$a_\mu = \frac{g-2}{2}, \qquad \text{where} \qquad \vec{\mu_\mu} = g\frac{e\hbar}{2m_\mu}\vec{s}. \tag{2.2}$$

The magnetic moment is parallel to the spin, since spin is the only directionality that an elementary particle can have. The value of the magnetic moment, equivalently the anomalous part a_μ can be calculated very precisely from the standard model, including electro-weak and QCD corrections. Representative diagrams for these contributions are displayed in Fig. 2.1. Therefore, a precision measurement of a_μ can test the sum of all known physics contributions directly. If any significant deviation is found, it would suggest the existence of new physics.

The most recent experiment to measure a_μ and d_μ, E821[6] at Brookhaven National Laboratory (BNL),
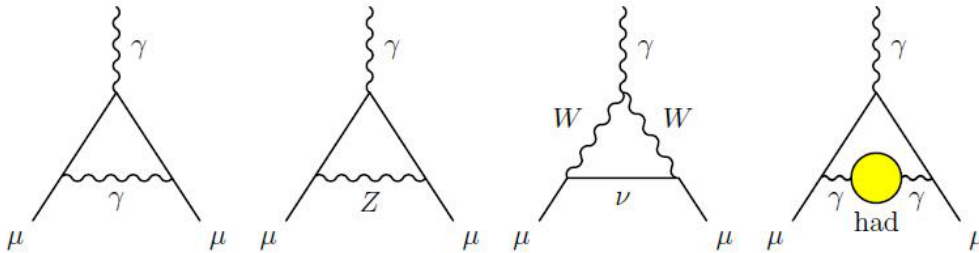
Figure 2.1: *Representative diagrams contributing to a_μ^{SM}. From the left to right: first order QED (Schwinger term), lowest order weak, lowest order hadronic contributions.*

has measured a_μ down to 0.54 ppm[2], and constrained d_μ down to $\leq 1.9 \times 10^{-19} \mathrm{e} \cdot \mathrm{cm}$. The value obtained has been compared to the most updated predictions of the Standard Model, and a_μ exhibits significant deviation of $\sim$4 sigma [2], while the d_μ limit requires improvements to be comparable to the limit from the electron with the assumption of lepton universality. Obviously further clarification is required to establish a new physics contribution for a_μ and further improvement is required for d_μ.
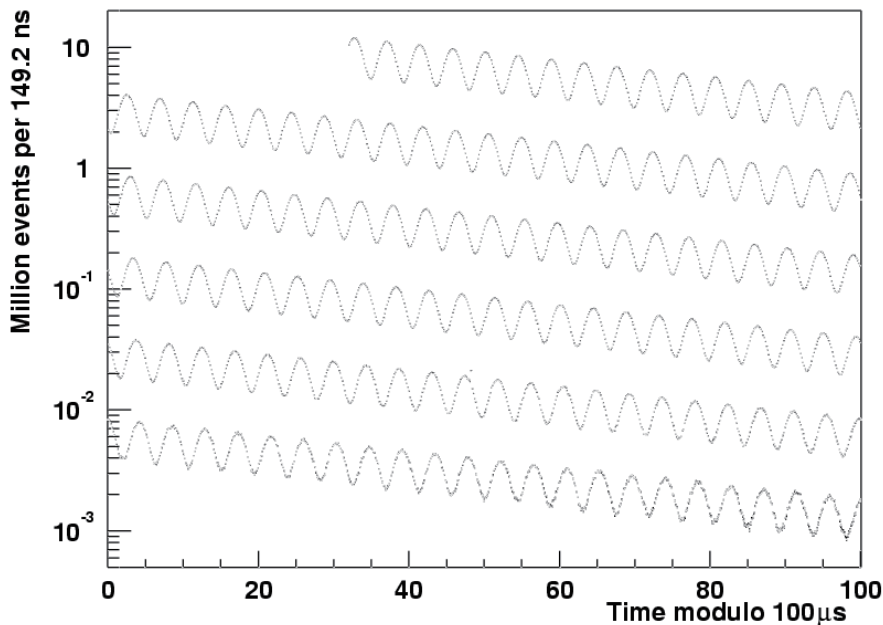

Figure 2.2: *"The wiggle plot" from the previous experiment, E821 at BNL. The figure is adopted from Ref.[6].*

---

[2]The experiment measured both positive and negative muons separately to 0.70 ppm. Quoted precision of 0.54 ppm represents the combined results assuming CPT invariance.

2.2.1   New $g − 2$ Experiments

Our experiment at J-PARC proposes to use a muon beam derived from muonium to obtain muons with very little transverse momentum. These cold muons would require only a very weak focusing field to maintain their beam size during storage. Therefore the muon momentum for the experiment is not constrained to be 3.1 GeV/c, the "magic" momentum used by the previous BNL and CERN $g − 2$ experiments, where this momentum exploits a cancellation in the coefficient for the precession of the muon spin in a (strong) electric focusing field. Our experiment proposes to use 300 MeV/c momentum muons stored in a 66 cm diameter storage region in an MRI-type solenoid, 3 T field, versus the 14 meter diameter BNL and CERN storage rings with 1.45 T field. μ^+ decays to positrons will be tracked in the solenoid using silicon detectors, versus the calorimetry used by BNL and CERN. The BNL measurement, completed in 2001, was dominated by its statistical uncertainty. In addition, a muon $g − 2$ experiment making use of the BNL storage ring magnet is going forward at Fermilab with the goal of an uncertainty of ± 0.1 ppm. We believe that an independent measurement of muon $g − 2$ by very different techniques with very different systematic uncertainties from previous experiments and also from the planned Fermilab experiment, as we propose for J-PARC with the goal of reaching ± 0.1 ppm uncertainty, would be valuable.

2.3   Theoretical Situation

After the publication from E821, there have been many theoretical activities to investigate the implication of the possible new physics to explain the deviation. For example, a possible effect on charged lepton flavor violation (cLFV) is discussed in Ref.[11]. Furthermore, implications on the electric dipole moment are also discussed in Ref.[12]. These show that studies of flavor structure in the lepton sector is important, especially in the light of leptogenesis.

Table 2.1: *Current theoretical evaluation of the muon $g − 2$ and its experimental result.*

Contribution	Results $(\times 10^{-11})$	Reference
QED	116 584 718.08 (0.14) (0.04)$_\alpha$	Kinoshita&Nio
EW	154 (2) (1)	Czarnecki
Hadronic		
LO	6 949 (42)$_{\text{exp}}$ (14)$_{\text{rad}}$ (7)$_{\text{pQCD}}$	HLMNT11
NLO	-98 (1)$_{exp}$ (0.3)$_{\text{rad}}$	HLMNT11
light-by-light	105 (26)	Prades, de Rafael, & Vainstein
SM Total	116 591 828 (49)	
Experiment	116 592 089 (63)	
Exp - Theory	261 (80)	3.3 σ discrepancy

2.3.1 The Standard Model Prediction and the hadronic term

We briefly describe the current status of the standard model prediction. Especially we discuss the hadronic term evaluation, which represents the largest uncertainty in the prediction.

One of the largest contributions to $a_\mu^{\mathrm{had,LO}}$ comes from the 2π final state (about 73%) making high-precision measurements of the corresponding cross section mandatory. CMD-2 reported their results on the pion form factor F_π from 370 to 1380 MeV [19] with a systematic error of 0.6-0.8% below 1 GeV, while SND measured F_π from 390 to 970 MeV with a systematic error of 1.3% [20]. KLOE studied F_π using the method of radiative return or ISR [21, 22] at $590 < \sqrt{s} < 970$ MeV with a sample of $3 \cdot 10^6$ events and systematic error of 0.9% [23]. The $|F_\pi|$ values from CMD-2 and SND are in good agreement. The KLOE data are basically consistent with them with a somewhat different energy dependence. The contributions to a_μ from all three experiments agree. First results on the 2π from BaBar show a slightly larger cross section [24].

Below 1.4 GeV practically all final states have been measured with consistent results by the CMD-2 and SND groups in Novosibirsk [25]. Above 1 GeV, various final states with more than two hadrons were studied by BaBar [26] using the ISR method. They measure for the first time cross sections of a few new channels and also show that some of the previous results should be reconsidered.

The results of the $a_\mu^{\mathrm{had,LO}}$ evaluation based on Ref. [2] are presented in Table VI for different energy ranges.

Table 2.2: *Updated $a_\mu^{\mathrm{had,LO}}$ according to Ref. [2].*

$\sqrt{s}$, GeV	$a_\mu^{\mathrm{had,LO}}, 10^{-10}$
$m_\pi - 1.43$	603.8 ± 3.1
$1.43 - 2.0$	34.1 ± 1.5
$2.0 - 11.1$	41.4 ± 0.9
$J/\psi, \psi'$	7.9 ± 0.2
$\Upsilon(1S - 6S)$	0.1 ± 0.0
$11.1 - \infty$	2.1 ± 0.0
Total	$689.4 \pm 3.6_{\mathrm{exp}} \pm 1.8_{\mathrm{rad}}$

It can be seen that due to a higher accuracy of e^+e^- data the uncertainty of $a_\mu^{\mathrm{had,LO}}$ is now much smaller than before [13, 18].

The most recent estimate of the next-to-leading order (NLO) hadronic term in [2] gives $a_\mu^{\mathrm{had,NLO}} = (-9.8 \pm 0.1) \cdot 10^{-10}$. The light-by-light hadronic contribution is estimated only theoretically [28]. Various predictions range between 80 and 136 (in units of $\cdot 10^{-11}$) with an uncertainty reaching $40 \cdot 10^{-11}$.

Using for the light-by-light term the result $(10.5 \pm 2.6) \cdot 10^{-10}$ [5] and adding all hadronic contributions, we obtain $a_\mu^{\mathrm{had}} = (690.1 \pm 4.8) \cdot 10^{-10}$. This result agrees with other estimations, e.g.,[33] and its accuracy benefits from the new e^+e^- data. Adding all theoretical contributions we obtain $a_\mu^{\mathrm{th}} = (11659177.3 \pm 4.8) \cdot 10^{-10}$, i.e. 4.0σ below the experimental value [2]. Similar deviation is reported by Ref. [33].

How real is the very high accuracy of the leading-order hadronic contribution obtained above? To a large extent it depends on our understanding of the radiative corrections due to initial-state radiation and vacuum polarization, and even more important effects of final state radiation. There is also a question of double counting of the hadronic final states in the leading- and higher-order hadronic terms [30], that include missing states (e.g., final states with neutral particles only).

There is still no explanation for the observed discrepancy between the predictions based on τ lepton and e^+e^- data [18]. The new high-statistics measurement of the two-pion spectral function by Belle [31] leads to about the same $a_\mu^{\mathrm{had,LO}}$ as before despite some inconsistencies between Belle and ALEPH. On the other hand, a recent comprehensive analysis of the e^+e^- data below 1 GeV and those on the 2π decay of the τ lepton performed in Ref. [32] shows that the two data sets can be reconciled if mixing between the ρ, ω, ϕ mesons is taken into account in a consistent way. A recent reevaluation of isospin-breaking effects in [33] somewhat decreases the discrepancy, see Fig. 2.3. According to it, the difference between the τ and e^+e^--based estimates is $(6.8 \pm 3.4_{\tau+IB} \pm 2.9_{ee}) \cdot 10^{-10}$ or 1.5σ only.

Finally, the authors of Ref. [34] performed a reestimation of a_μ^{had} after BaBar's $\pi\pi$ data and an increase of a_μ^{exp} by $+0.9 \cdot 10^{-10}$ due to the change of μ_μ/μ_p by CODATA. The new difference between the experimental value and the theoretical prediction becomes $(24.6 \pm 8.0) \cdot 10^{-10}$ or 3.1σ, see Fig. 2.3.

What is the future of this study? It is clear that it will be extremely difficult to improve significantly the existing accuracy of $a_\mu^{\mathrm{had,LO}}$ by measuring the cross section of e^+e^- annihilation to better than 0.3% as required by future determinations of a_μ mentioned above. One can optimistically expect substantial progress from new high-statistics ISR measurements at KLOE, BaBar and Belle together with the more precise determination of R below 4-5 GeV from CLEO-c and BES-III. Experiments will start soon at VEPP-2000, now commissioning, which is a VEPP-2M upgrade up to $\sqrt{s}$=2 GeV with $L_{\mathrm{max}} = 10^{32}$ cm^{-2}s^{-1} [35]. We can estimate that by 2012 the accuracy of $a_\mu^{\mathrm{had,LO}}$ will be improved from $4.0 \cdot 10^{-10}$ by a factor of about 2 and the total error of $3.3 \cdot 10^{-10}$ will be limited by the LBL term $(2.6 \cdot 10^{-10})$.

Let us hope that progress of theory will allow a calculation of a_μ^{had} from first principles (QCD, Lattice). One can mention here a new approach in the QCD instanton model [36] or calculations on the lattice [37].

In conclusion, it should be emphasized once again that BNL success stimulated significant progress of e^+e^- experiments and related theory. Improvement of e^+e^- data led to a substantial decrease of the $a_\mu^{\mathrm{had,LO}}$ uncertainty. For the first time the accuracy of the theoretical prediction is better than that of the experimental measurement. Future experiments as well as development of theory should clarify whether the observed difference between a_μ^{exp} and a_μ^{th} is real and what consequences for the Standard Model and for possible New Physics [38] it implies.
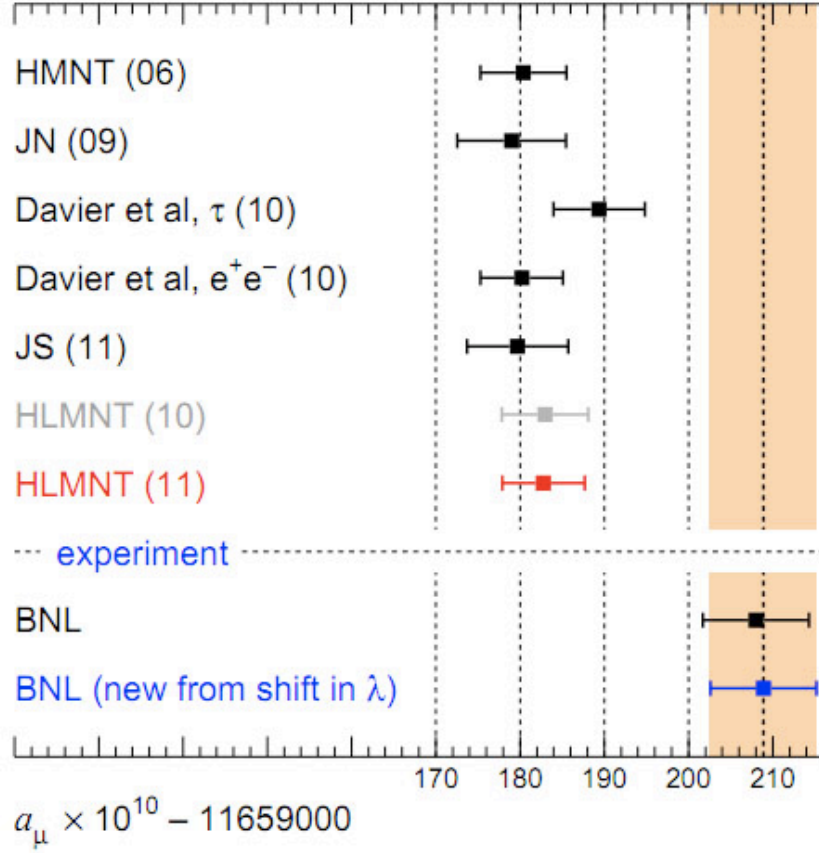
Figure 2.3: *Comparison of a_μ from theory and experiment [3].*

2.3.2 Muon $g - 2$ in the LHC Era

To end of this section, we briefly mention the importance of this experiment in the LHC and post-LHC era. One could argue that most of the new physics scenarios can be studied at LHC. Indeed, the most popular interpretation of the deviation from the Standard Model observed by the previous experiment is supersymmetry, and it can be studied very well at LHC, if the energy scale turns out to be appropriate. However, important parameters in the model such as μ and $\tan\beta$ cannot be determined very well. The muon anomalous magnetic moment a_μ is sensitive to these parameters through following expression;

$$a_\mu(\text{SUSY}) \approx (\text{sgn}\mu)\ 13 \times 10^{-10} \tan\beta (\frac{100\text{GeV}}{\tilde{\text{m}}})^2. \tag{2.3}$$

The sensitivity to $\tan\beta$ is compared to that of LHC experiments in Fig. 2.4.

However, we emphasize that it represents only one of the possible strengths of this measurement. The precision measurement of the fundamental quantities like magnetic and electric dipole moments of elementary particles has its own value.
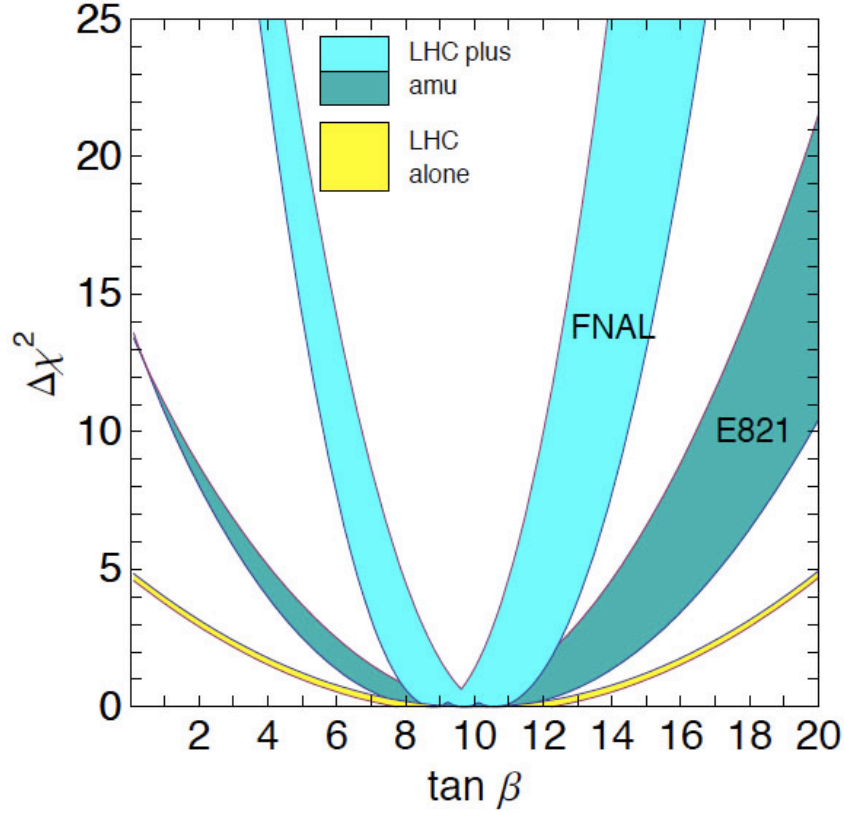
Figure 2.4: *Possible future tanβ determination from the measurement of a_μ, assuming that the MSSM reference point SPS1a is realized [7, 10]. The yellow band is from LHC alone which gives $\tan\beta^{\mathrm{LHC-fit}} = 10.0\pm4.5$ [8, 9]. The darker blue band labelled E821 assumes $\Delta a_\mu = (295\pm81)\times10^{-11}$, which comes from the present values for a_μ and the Standard-Model contribution, the lighter blue band labelled FNAL corresponds to $\Delta a_\mu = 295(34)\times10^{-11}$, which has similar sensitivity projection to the proposed experiment at J-PARC.*

References for Chapter 2

[1] T.Kinoshita and M.Nio, Phys. Rev. D73, 013003 (2006); T.Aoyama et al, Phys. Rev. Lett. 99, 110406 (2007); T.Kinoshita and M.Nio, Phys. Rev. D70, 113001 (2004); T.Kinoshita, Nucl. Phys. B144, 206 (2005) (Proc. Supp.); T.Kinoshita and M.Nio, Phys. Rev. D73, 053007 (2006); A.L. Kataev, arXiv:hep-ph/0602098; M. Passera, J. Phys. G31, 75 (2005).

[2] K. Hagiwara, R. Liao, A.D. Martin, D. Nomura, and T. Teubner, Preliminary results shown at Inernational Workshop, *Phipsi11*.

[3] K. Hagiwara, R. Liao, A.D. Martin, D. Nomura, and T. Teubner, J. Phys.**G38** (2011) 085003.

[4] A. Czarnecki, W. J. Marciano, and A. Vainshtein, Phys.Rev.**D67** (2003) 073006. Erratum-ibid.**D73** (2006) 119901.

[5] J. Prades, E. de Rafael, and A. Vainshtein, e-Print: arXiv:0901.0306 [hep-ph]

[6] G.W. Bennett *et al.* Muon G-2 Collaboration, Phys. Rev. **D73** (2006) 072003.

[7] Proposal submitted to Fermilab; *The New (g - 2) Experiment: A Proposal to Measure the Muon Anomalous Magnetic Moment to ±0.14 ppm Precision*, New $(g-2)$ Collaboration. Contact persons: D. Hertzog, and B. Roberts.

[8] R. Lafaye, T. Plehn, M. Raunch and D. Zerwas, arXiv:0709.3985 [hep-ph].

[9] M. Alexander, S. Kreiss, R. Lafaye, T. Plehn, M. Rauch, and D. Zerwas, Chapter 9 in M. M. Nojiri et al., arXiv:0802.3672 [hep-ph].

[10] Hertzog, Miller, de Rafael, Roberts and Stöckinger, hep-ph/0705.4617v1.

[11] J. Hisano and K. Tobe, Phys.Lett.**B510** (2001) 197-204.

[12] J.P. Archambault, A. Czarnecki, and M. Pospelov. Phys. Rev. **D70** (2004) 073006.

[13] S. Eidelman and F. Jegerlehner, Z. Phys. C **67** (1995) 585.

[14] S. Eidelman, Proceedings of ICHEP-06, World Scientific, Vol.1, p.547, 2006.

[15] K. Hagiwara *et al.*, Phys. Lett. B **649** (2007) 173.

[16] F. Jegerlehner, Nucl. Phys. Proc. Suppl. **181-182** (2008) 26.

[17] M. Davier *et al.*, Eur. Phys. J. C **27** (2003) 497.

[18] M. Davier *et al.*, Eur. Phys. J. C **31** (2003) 503.

[19] R.R. Akhmetshin *et al.*, Phys. Lett. B **648** (2007) 28.

[20] M.N.Achasov *et al.*, JETP **103** (2006) 380.

[21] S. Binner, H.J. Kühn, K. Melnikov, Phys. Lett. B **459** (1999) 279.

[22] M. Benayoun *et al.*, Mod. Phys. Lett. A **14** (1999) 2605.

[23] F. Ambrosino *et al.*, Phys. Lett. B **670** (2009) 285.

[24] B. Aubert *et al.*, arXiv:0908.3589.

[25] F.V. Ignatov, Nucl. Phys. Proc. Suppl. **181-182** (2008) 101.

[26] B.Aubert *et al.*, Phys. Rev. D **77** (2008) 092002.

[27] K. Hagiwara *et al.*, Phys. Rev. D **69** (2004) 093003.

[28] F. Jegerlehner and A. Nyffeler, Phys. Rept. **477** (2009) 1.

[29] J.F. Troconiz and F.J. Yndurain, Phys. Rev. D **71** (2005) 073008.

[30] Yu.M. Bystritsky *et al.*, JETP Lett. **83** (2006) 51.

[31] M. Fujikawa *et al.*, Phys. Rev. D **78**, 072006 (2008).

[32] M. Benayoun *et al.*, Eur. Phys. J. C **55** (2008) 199.

[33] M. Davier *et al.*, arXiv:0906.5443.

[34] M. Davier *et al.*, arXiv:0908.4300.

[35] S.I. Eidelman and S.I. Serednyakov, Nucl. Phys. Proc. Suppl. **131** (2004) 19.

[36] A.E. Dorokhov, Nucl. Phys. A **790** (2007) 481.

[37] T. Blum and S. Chowdhury, Nucl. Phys. Proc. Suppl. **189** (2009) 251.

[38] D. Stöckinger, Nucl. Phys. Proc. Suppl. **181-182** (2008) 32.

Surface Muon Production and Transport

3.1   Proton beam from RCS

J-PARC consists of a 400 MeV linac, 3 GeV and 50 GeV synchrotron rings, which provide an intense proton beam to pursue particle and nuclear physics, materials and life science and nuclear technology. A 1 MW proton beam is transported from the 3 GeV synchrotron ring to Materials and Life Science Facility (MLF) which consists of the muon and the spallation neutron facilities, MUSE and JSNS. As shown in Fig. 3.1 and 3.10, the proton-beam-line tunnel runs through the center of MLF building from the north to the south. The east and the west wings are experimental halls where the neutron and muon beam lines are constructed. In order to avoid the diffusion of radioactive contamination, and to make the structure of radiation shield simple, the proton-beam transport tunnel is isolated from the experimental hall. Namely, the beam transport tunnel divides the MLF building into east and west wing. While this building structure achieved its purpose, the design of the secondary beam lines is under severe geometrical constraint.
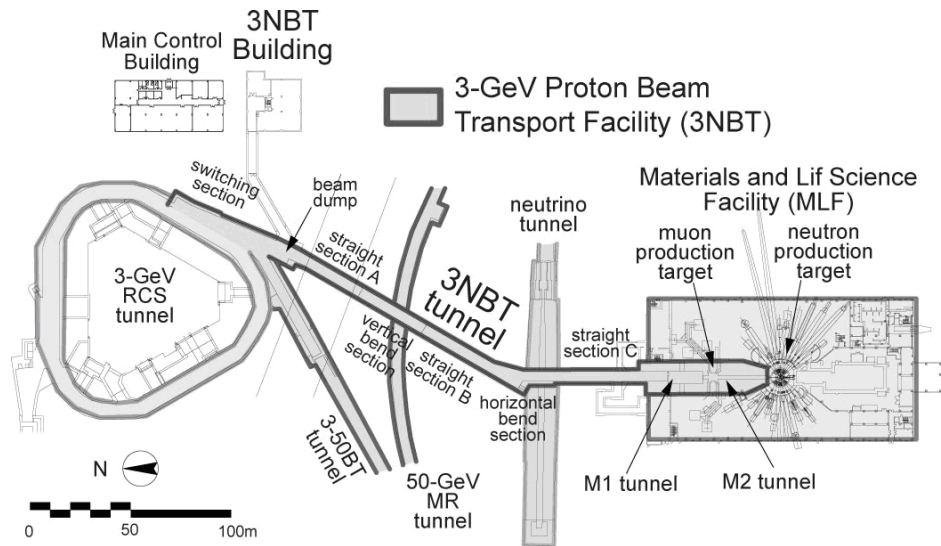

Figure 3.1: *A schematic drawing from 3 GeV rapid cycling synchrotron (RCS) to MLF.*

3.2   Muon Target and Surface Muon Production

3.2.1   Muon Production Target

The world-strongest pulsed muon beam is produced by a 1 MW proton beam injected to the target made of 20 mm thick, disc-shaped, isotropic graphite (IG-43) [1]. About 5% of proton beam is consumed at the target. The devices around the target is required to be designed, taking into account the effect of this 50 kW beam loss, *i.e.* heat deposit, radiation damage, radiation dose, maintainability and so on.

Muon g-2/EDM Experiment, Conceptual Design Report, Revised, December 12, 2011, 11:40 A.M.

The heat deposit in the target is evaluated to be 4 kW by a Monte-Carlo Code, PHITS [2], and this result is used to evaluate the temperature distribution and the thermal stress by a FEM calculation. Graphite is known to shrink by radiation damage, and the shrinkage determines the lifetime of the target. Figure 3.2 shows a picture of the muon target.

Figure 3.2: *A picture of the muon target.*

The muon target is stored in the target chamber. For shielding the radiation dose, about 2 m high iron shield is assembled above the target. The top of the radiation shield is 4 m from the floor level, and 2.4 m higher than the primary proton beam level of 1.6 m. Between the muon target and neutron target, the radiation shield is placed up to the 4 m level.

From the 4 m level to 6 m level, there is a tunnel, M2 tunnel, for maintenance, and all the pipes and the cables are connected in this tunnel. The front-end part of the secondary muon beam line is in M2 tunnel. The dose from the residual activities in M2 tunnel is enough low, around 100 μSv/h at a day after beam off, and hands-on maintenance is possible, while no one can access to the beam line level. In order to exchange the irradiated target assembly, the remote handling room is in the MLF building. A shielding vessel, "muon target transfer cask", transfers the irradiated target from the target chamber to the remote handling room. This cask is dedicated to the target assembly and the other light-weight devices below 6 t. The beam line magnets are more than 30 t typically, and it is impossible to transfer a magnet to the remote handling room. Thus, the life time of the magnet is designed to be more than 40 years. Namely, the materials are carefully selected according to the evaluated radiation dose. A typical result of the radiation dose is shown in Fig. 3.3.
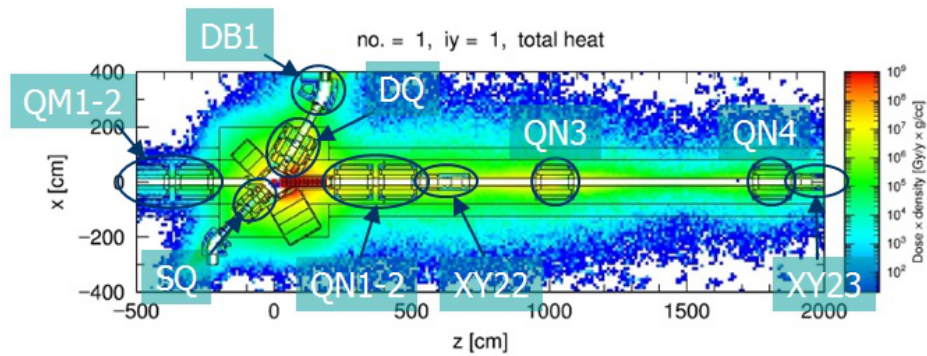
Figure 3.3: *A typical result of the radiation dose in M2 tunnel.*

Figure 3.4 shows a schematic figure of the muon target chamber. Downstream of the muon target, a pair of two scrapers collimates the scattered proton beam. The muon target and the scrapers can be positioned with the precision level of 0.5 mm against the beam axis.
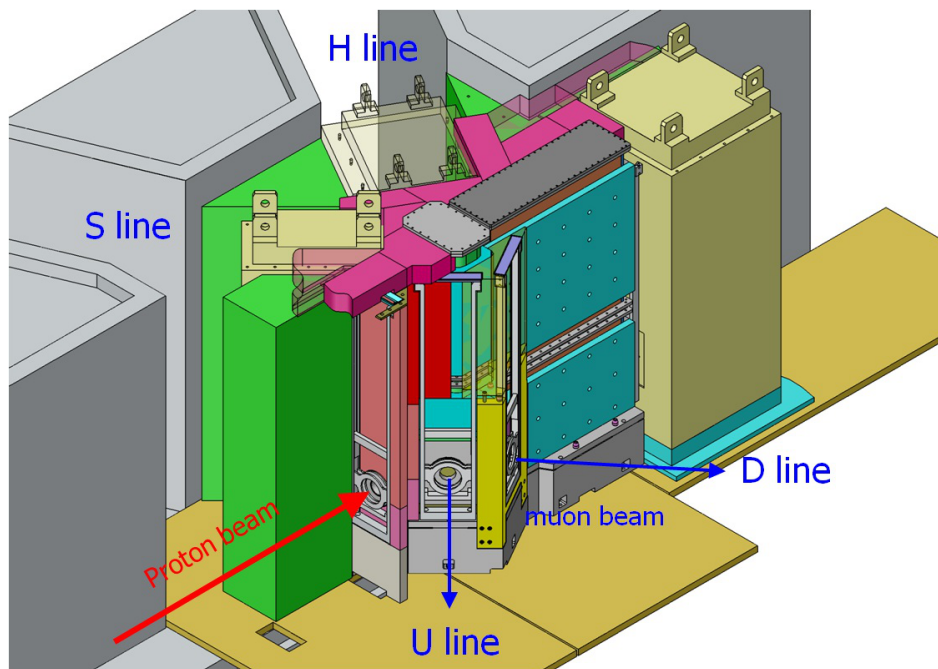

Figure 3.4: *A schematic figure of the muon target chamber.*

Figure 3.5 shows a conceptual design frame of the magnet in M2 tunnel. According to this design frame, all the magnets are designed.

For vacuum connection between the beam ducts in M2 tunnel a inflatable metal seal, a.k.a. pillow seal, is adopted, which is remotely controlled by compressed air. The leak rate of the pillow seal of
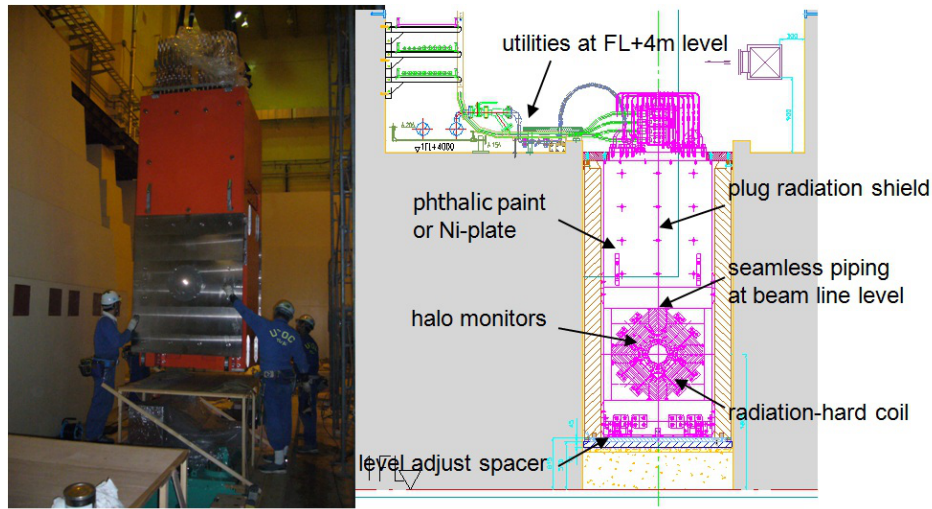
Figure 3.5: *A conceptual design frame of the magnet in M2 tunnel.*

the muon target chamber was 10^{-9} Pa·m^3/s. The out-gassing rate of the chamber itself was measured to be 10^{-7} Pa·m^3/s/m^2. An overall pressure of 10^{-5} Pa was achieved in the beam line.

3.2.2   Surface Muon Production

A surface muon beam is produced when positive pions are stopped near the surface inside the production target and decay into muons, while decay muon beam is produced when positive or negative pions decay in flight along the beamline. We will use a surface muon beam as the primary source of the cold muon beam because a surface muon beam is obtained with higher intensity and higher spin polarization than a decay muon beam. The surface muon intensity can be estimated from the number of pions stopped near the surface. Calculation was done utilizing the measured data on pion production cross sections followed by tracking of the pions with GEANT 3.21.

In order to reduce the CPU time, instead of starting from the proton beam, we generated the pions according to an empirical differential cross section equation (generator) which approximates the data taken for 2.9 GeV protons on a beryllium target [3]. The generator equation was also compared with the recent pion production cross section data taken by the HARP collaboration at CERN [4] shown in Fig. 3.6, and it was confirmed that the generator reproduces the HARP data reasonably well within 20% for low energy regions below 100 MeV. We are concerned mostly with pions with energy below 50 MeV, since the range of a 50 MeV pion is 10 g/cm^2 (5 cm) in the graphite target. Higher energy pions are less likely to be stopped in the target and would have only a small contribution to surface muon production. Even so, pions up to 500 MeV were handled for completeness.

We assumed that pions are produced uniformly along the proton beam path in the target, since the target thickness is much smaller than the proton interaction length. We also assumed the proton beam
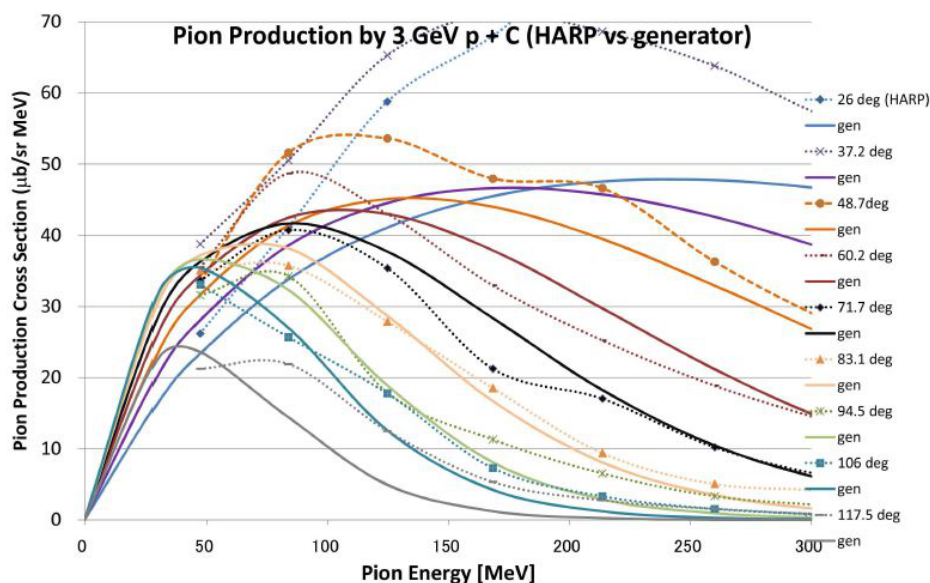
Figure 3.6: *Comparison of pion production differential cross section used in the pion generator (solid line) and that of HARP data (symbols and dotted lines).*

distribution is uniform inside the 24 mm diameter in the production target because of the design value of the primary beam transmission.

By integrating the generator equation for various angles and for pion energies up to 500 MeV, the total cross section for positive pion production is about 90 mb. It is calculated from this cross section that the total yield of positive pions is about 0.016 per 3 GeV proton passing through the 2 cm (3.6 g/cm^2) thick graphite target. This number is converted to 3.2×10^{13} positive pions per second generated for the 333 μA proton intensity at J-PARC.

About 3.2×10^7 pions (1×10^{-6} of the above number) were generated in the simulation to study how many of those pions are stopped near the target surface. The energy and angle of each pion was generated following the distribution of our pion generator as described above. The tracking of the pions, pion interaction in the target, their decay to muons, and the tracking of muons were handled by GEANT 3.21.

Only pions that stopped inside the production target near the surface will contribute to the generation of surface muons, so the number and depth distribution of the stopping pions is the basic information. Figure 3.8 shows the number of π^+ stopped in each depth region in 0.1 mm steps in units of Million/s. The area is limited to inside a 24 mm radius. For example it can be seen that 7,400 M π^+ are stopped within 0.1 mm (1 bins in the figure) from the backward surface. The figure also shows that the number of pions stopping near the surface is about half (although not exactly) of those in the middle plane. This is because stops in the middle have contributions from pions produced in close-by forward and backward regions, while those stopping at the forward (backward) end are caused by pions that were produced toward the downstream (upstream) only.
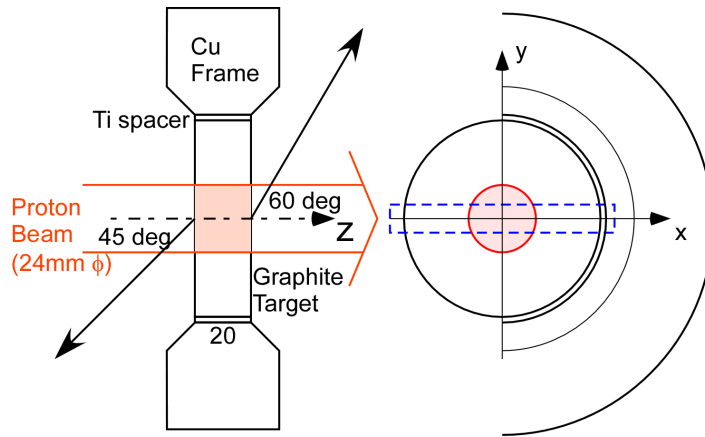
Muon g-2/EDM Experiment, Conceptual Design Report, Revised, December 12, 2011, 11:40 A.M.

Figure 3.7: *Target geometry and proton beam size used for the calculation.*

Figure 3.9 shows the horizontal distribution in the target. It is seen that the main contributions are from inside the 24 mm diameter region which is directly hit by the proton beam. There are also pions stopping outside, which amounts to 40% of those inside.

Detail of the MLF Muon H-line is described in the sections below. Let us assume a typical solid angle of 100 msr for $\sigma_p = 5\%$ beam. With this momentum acceptance, the surface muons in the momentum range from 29.8 MeV/c to 25.2 MeV/c can be collected in $1.5\sigma_p$. Pion stopping within 0.4 mm from the surface will contribute to the muons in this momentum range if the muons are emitted normal to the target surface. If the beamline sees the production target at 60 degrees to the axis, the effective depth from the surface is reduced to 0.2 mm. Thus we expect from our pion stopping simulation that the surface muon rate from the target will be $(7,400 \text{ M/s}/0.1 \text{ mm}) \times 0.2 \text{ mm} \cong 15,000 \text{ M/s}$.

3.3   Muon Beam Line

The muon-production target is inserted 30 m upstream of the neutron target in the proton beam line. From the muon target, we decided to extract four muon beam lines. Each of them provides the world-strongest pulsed muon beam with an individual design concept to be utilized for the variety of muon science. Two of the secondary beam lines are extracted at the angle of 60 degrees to the proton beam line (forward), and the others are at 135 degrees (backward) [5].

The decay muon beam line (D-line) was constructed at first, and this is the existing only beam line. D-line extracts both negative and positive decay muons up to their momenta of 120 MeV/c, as well as 30 MeV/c surface and cloud muons [6]. This high momentum-tune-ability meets the wide demands of user programs. The second beam line to be constructed in FY2011 is the large acceptance beam line, U line, which provides the most intense surface-muon beam among the four secondary lines [7]. This intense beam is used to generate ultra-cold muon beam by the laser resonant ionization method [8]. The rest two beam lines, S and H-line, are located in the east experimental hall, and the construction
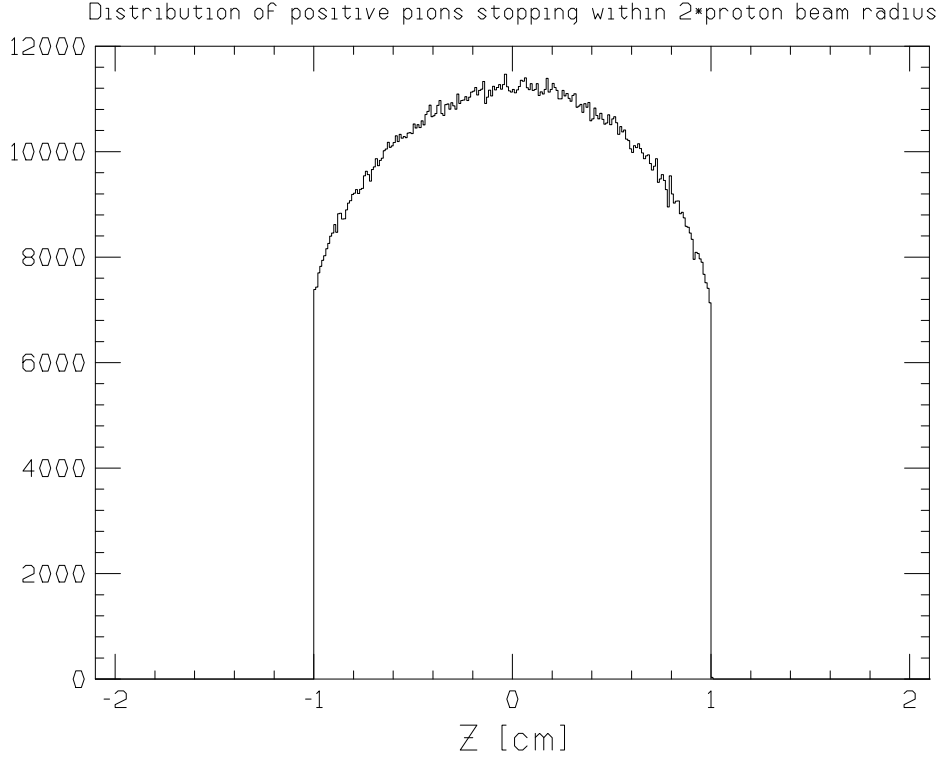
Figure 3.8: *π^+ stopping distribution in the production target along the beam path. Only pions that are stopping inside a 24 mm radius around the center are included. Units for number of π^+ are M/s.*

will start in FY2012. S line is designed to transport surface muons to several experimental areas by using kicker devices to dedicate μSR spectroscopy. Lots of samples are examined simultaneously under a variety of conditions. A typical period of an experiment in S line is a few days because the required statistics, *i.e.* the number of observed μ-e decay electrons, is the order of 10^6. Therefore, a study requiring much higher statistics doesn't match the experimental style of S line as well as D and U lines. The forth beam line, H-line, aims to answer the demands for not only $g-2$/EDM experiment but also the other experiments [9, 10, 11] which need high statistics, *i.e.* use of high intensity beam for a long period.

3.4   H-line

3.4.1   Beam line optics

The intended experiments in H-line require high statistics, *i.e.* high intensity beam. Momentum tune-ability is also needed. Both features will be important for potential experiments in future. The design work on H-line is performed along these two concepts. The basic idea of the beam line optics
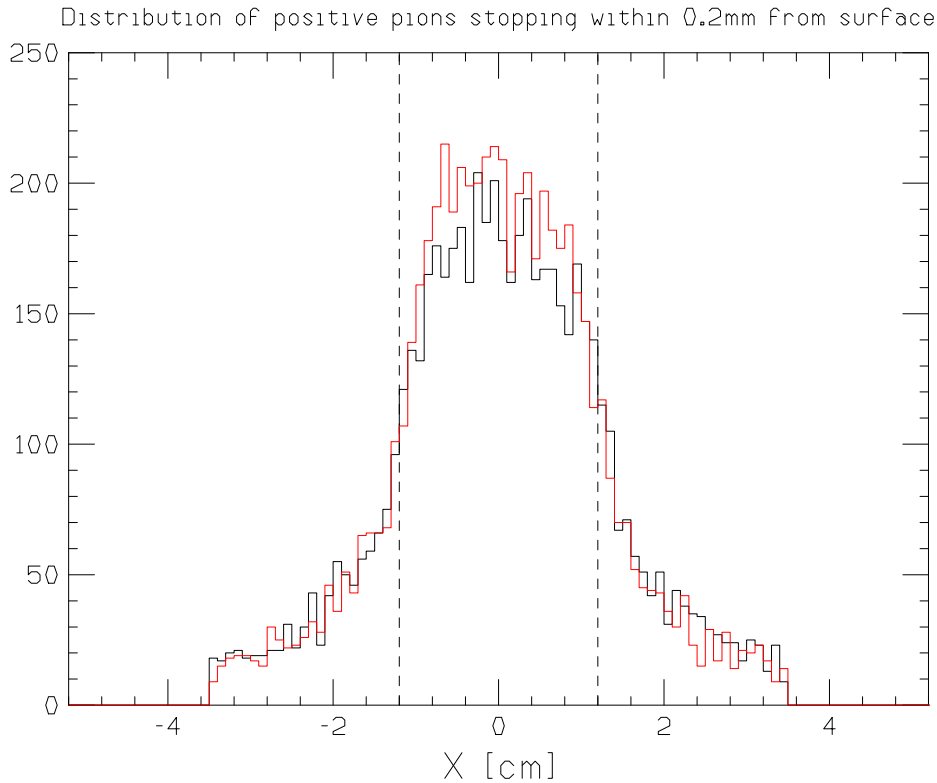
Distribution of positive pions stopping within 0.2mm from surface

Figure 3.9: *Horizontal distribution of pions stopping in the production target. Only pions stopped within 0.2 mm from the backward surface (black) or the forward surface (red) and within ±5 mm vertically from the center level are plotted (see the dashed square in Fig. 3.7). The model is symmetric around the proton beam axis, so a similar distribution is expected for the vertical direction.*

was proposed to use a large-aperture muon-capture solenoid, a wide-gap bending magnet and a pair of two solenoid magnets which have opposite-direction field each other [12]. Conventional matrix calculation is not applicable because the near-axis approximation is not good in a large-aperture solenoid. Thus, G4BEAMLINE [13] is applied for optics calculation, and detailed design work is in progress. The front-end capture solenoid magnet (HS1) consists of 8 coils, and three kinds of currents are supplied to the first, the second and the rest coils, respectively. The first coil makes the main capture field, and by tuning the second and the rest coils, the beam profile is minimized at around the first bending magnet (HB1) and the gate valve (HGV1) which is unavoidable due to the operation. The second solenoid magnet (HS2) make parallel or weak-focusing beam by a weak field, and this enables the installation of a wien filter or other non-transport magnet like kicker magnets proposed in the experiment [10]. The third solenoid magnet (HS3) makes the field the opposite direction of HS2 to cancel the beam-profile rotation by HS2. This canceling function doesn't depend on the momentum, and thus beam loss due to momentum dispersion at the second bending magnet (HB2) is reduced. The final focusing (FF) magnets are discussed in the following section.

Figure 3.11 shows a typical transport calculation, and the beam is delivered to the first experimental
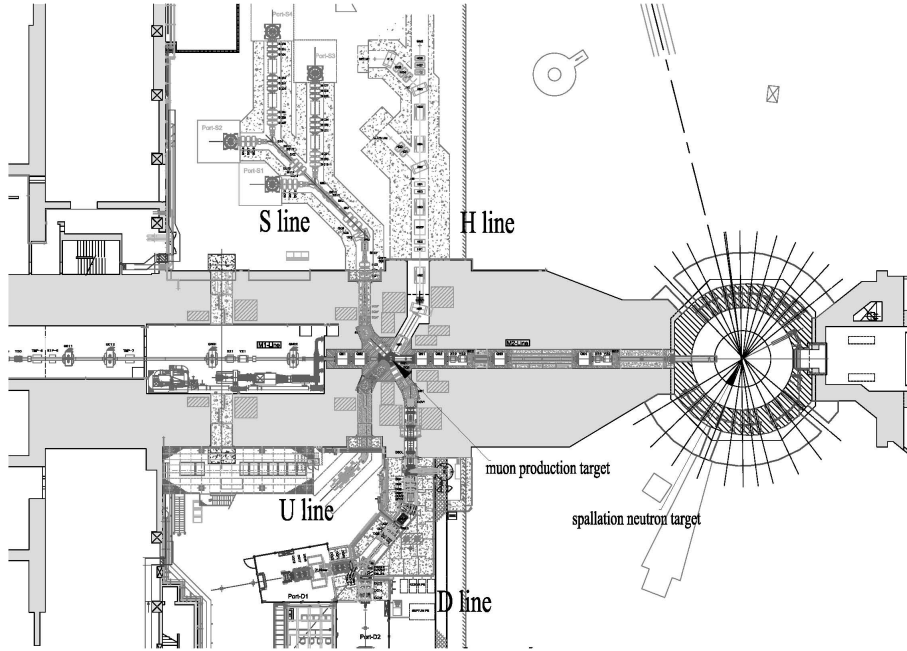
Figure 3.10: *The layout plan of MUSE.*

area which is the nearest to the muon source. Turning off HB2, the beam goes straight, and the beam is able to be transported to the other experimental areas by applying the pair of opposite-direction solenoid field. Namely, H-line can provide the intense beam to a few experiments which use different apparatuses and cannot share the experimental area. For the $g - 2$/EDM experiment, muon beam is required to transport perpendicular to the proton beam transport tunnel because of the ability to install the accelerator in MLF.

3.4.2 $g - 2$/EDM branch optimization

In this section we discuss the $g - 2$/EDM beamline optimization. For this experiment, the following conditions are important to be satisfied.

- *Transmission efficiency should be as high as possible.* Statistics is the most important issue of this experiment.

- *Focus point size should be less than 4 cm in diameter.* This experiment installs a muonium production target at the beamline final focus point. The muonium emitted from the target is irradiated with a laser in order to produce the ultra-cold muon beam. Small beam spot size helps to increase the slow muon intensity.

- *Leakage field at the final focus position should be as small as possible.* The slow muon has a quite low momentum at around the final focus position, and thus the leakage field disturbs the

slow muon trajectory. The other parameters such as x/y beam angle distribution are not so much important. Possible final focus systems are evaluated in the following subsection.

Final focus system with a solenoid

The simplest way to make small beam spot size is to use a solenoid magnet. The solenoid magnet, HS6, is installed just downstream of the last bending magnet of HB3. Transmission efficiency is as high as 87.5% inside 40 mm in diameter at the final focus position. The focus point size is small enough as 1.7 cm for σ_x and 1.8 cm for σ_y. However, leakage field of HS6 is a problem. Figure 3.13 shows the magnetic field along the beam axis. To make small beam spot, the maximum field of HS6 is as high as 0.42 T. This leads to short focal length of 0.4 m, thus leakage field at the final focus point is as high as 0.07 T. To use this option, we need to design magnetic shield for HS6 carefully.

Final focus system with quadrupole triplet magnets

To solve the leakage field problem mentioned in the above subsection, we have an option to use quadrupole triplet magnets for the focusing system. The last beamline component is a quadrupole magnet, and thus the longitudinal leakage field along the beam axis is zero. The maximum field of the quadrupole magnet is lower than that of the solenoid magnet. Therefore, the leakage field at around the beam axis is also expected to be small. As the optimized result, the transmission efficiency is 63.7%, and the beam size is 3.5 cm for σ_x and 1.8 cm for σ_y. This result is not good enough, and we cannot adopt this option.

Final focus system with a solenoid and quadrupole triplet magnets

The smallness of the transmission efficiency of the quadrupole triplet system comes from its small focusing power. The solenoid system has the large leakage field. To solve these problems, we devise the following method as shown in Fig. 3.14. First of all, we make a small focus spot by the strong focusing power of HS6 solenoid magnet. This small focus spot is transported to the final focus position by quadrupole triplet magnets. This method has an advantage of a small focus spot and a small leakage field. The estimated transmission efficiency is as high as 83.4%, and the final focus size is as small as 2.1 cm for σ_x and 1.1 cm for σ_y. This method will be applicable to the $g-2$/EDM experiment.

3.4.3 MuHFS beamline optimization

In this section we discuss the MuHFS beamline optimization. For this experiment, the following conditions are important to be satisfied.

- *Transmission efficiency should as high as possible.* Statistics is the most important also for this experiment.

Muon g-2/EDM Experiment, Conceptual Design Report, Revised, December 12, 2011, 11:40 A.M.

- *Focus point size should be less than 6 cm in diameter.* For this experiment, the beam focusing is not so much serious issue in comparison with $g - 2$/EDM experiment, because we installed the MuHFS solenoid magnet and the strong magnetic field as high as 1.7 T eventually focuses the surface muon beam. This condition is decided to make sure that all muons stop inside good field region of the MuHFS magnet (20 cm in diameter).

- *Leakage field at the final focus position should be less than 1.7 Gauss.* One of the key issues of this experiment is to make a large and homogeneous magnetic field region. The limit of 1.7 Gauss comes from the magnetic-field correction power by the shim coil [14].

- *Muon stopping distribution should be inside of good field region the MuHFS magnet (30 cm long).* This condition will limit the muon momentum spread.

The other parameters such as x/y beam angle distribution are not so much important. Possible final focus systems are evaluated as follows. The most effective way to suppress the leakage field of the beamline magnet is to keep the focal length as long as possible. To achieve this long focusing, we devise the following method. At first, we prepare almost parallel beam by using 3 quadrupole magnets as shown in Fig. 3.15.

Next we put the MuHFS magnet at the final focus point. The created magnetic-field distribution is consistent with Opera calculation. The MuHFS magnet design is described in detail in a reference [14]. One of the possible problems is effect of the leakage field of the strong MuHFS magnet against the muon beam transport. This leakage field is carefully investigated as shown in Fig. 3.16, and the leakage field at a position of the last quadrupole magnet (HQ3) is estimated to be as small as 0.005 T. We also checked the leakage field effect from the MuHFS magnet to the beam profile at the HQ3 exit. It is confirmed that the leakage field does not affect the beam transport seriously. Finally, we estimated the transmission efficiency and the beam profile at the final focus point in the MuHFS magnet. As the result, the transmission efficiency is as high as 93.6% and final focus spot size is as small as 1.3 cm for σ_x and 1.3 cm for σ_y. It is concluded that this method will be applicable to MuHFS experiment.

3.4.4   Construction status

Front-end magnet

The front-end magnets, HS1 and HB1, are under mechanical design work and under fabrication to install during the summer shutdown in FY2012. At present, iron and concrete blocks are placed in H-line for the radiation shield. Because MUSE has been under operation since 2008, and the radiation dose from the accumulated residual activities is evaluated to be close to the order of Sv/h at the hottest point in summer, 2011. Taking the practical work into account, the next summer will be the last chance to install the front-end magnets in H-line.

The design work of the front-end magnets is in progress according to the conceptual design framework of M2 tunnel devices. The materials are carefully selected. For instance, mineral insulation cable and

polyimide insulation are adopted for the HS1 and HB1 coil, respectively. Figure 3.18 shows the layout of M2 tunnel. Not only the magnets but also the other devices, such as the large-aperture pillow seals, the installation guide for the magnets and the gate valve are under mechanical design work and under fabrication. All these synthetic devices are linked mutually, and are required to be installed in the next summer.

The vacuum gate valve, HGV1, will be installed just downstream of HB1. HGV1 has a all-metal body and pillow seals are attached both sides to be operated under high radiation field. In order to reduce the beam loss, a large aperture of 320 mm is adopted for HGV1. A thin polyimide film is attached on the HGV1 to separate the beamline vacuum between the primary and the secondary beamline. This separation is important not to diffuse the tritium produced in the muon production target, and also to make the secondary beamline operation free from the primary one.

Around the front-end magnets and HGV1, the devices for their remote-handling-installation guide are necessary.

All the devices mentioned in this section have to be installed in the next summer shutdown.

Other devices

The magnets and other devices downstream from HGV1 are under conceptual designing. These devices are placed in the experimental hall, and thus they have many design options in senses of material selection, geometrical size and position and so on. In order to provide the satisfactory muon beam to all the planed experiments in H-line, designing work is performed under a consensus of all experiments.

The designing work of the radiation shields is just started. Along the beamline $1 \sim 2$-m-thick concrete tunnel will be necessary to enclose the streaming neutrons and other radiation sources. Especially for $g-2$/EDM experiment, the muonium production target and VUV laser system will be installed in the tunnel, and thus its maintainability should be considered carefully. For the hands-on maintenance, streaming particles have to be blocked at upstream side by a thick plug shield, and then one can access to such devices.

3.5   Summary

The effective surface-muon-emission rate is 15,000M/s, taking into account the extraction angle of H-line, 60 degrees. The beamline acceptance of H-line is evaluated to be about 100 mstr, Although the beamline design is not converged, this value of 100 mstr is not unrealistic. The transmission efficiency in the final focus will be reach 80%. Overall surface muon injection rate to the muonium target is $15,000\text{M/s} \times 0.1/4\pi \times 0.8 \sim 100\text{M/s}$.

The detailed design work of each magnet and other beam-line components is in progress, and the result is fed back to the optics calculation. The muon facility is under operation since 2008. The temporary radiation shields were placed in H-line, and they have been activated. The radiation dose

from the residual activities is evaluated to reach the order of 1 Sv/h in the next year. Thus, first of all, HS1, HB1 and the other front-end devices will be installed in the next year. The mechanical design work is in progress along the design strategy for devices under high radiation field [15]. H-line will be constructed in the world's strongest pulsed muon facility, MUSE. A high intensity muon beam is provided for the proposed experiments in order to observe new physics beyond the standard model.

References for Chapter 3

[1] S. Makimura *et al.* 2009 *Nucl. Inst. Meth.* **A600** 146.

[2] H. Iwase *et al.* 2002 *J. Nucl. Sci. Technol.* **39** 1142. K. Niita *et al.* 2006 *Radiat. Meas.* **41** 1080.

[3] P. A. Piroue and A. J. S. Smith 1966 Phys. Rev. **148** 1315.

[4] HARP Collaboration 2008 Eur. Phys. J. **C53** 177.

[5] Y. Miyake *et al.* 2005 *Nucl. Phys. B* **149** 393.

[6] K. Shimomura *et al.* 2009 *Nucl. Inst. Meth.* **A600** 192.

[7] K. Nakahara *et al.* 2010 *AIP Conf. Proc.* **1222** 420.

[8] P. Bakule *et al.* 2003 *Spectrochimica Acta Part B* **58** 1019.

[9] K. Shimomura *et al.* *NuFact11 proceedings*.

[10] S. Mihara *et al.* *ibid.*

[11] K. Nagamine *et al.* private communication.

[12] J. Doornbos private communication.

[13] http://www.muonsinc.com/

[14] K. Sasaki *et al.* *NuFact11 proceedings*.

[15] N. Kawamura *et al.* 2009 *Nucl. Inst. Meth.* **A600** 114.
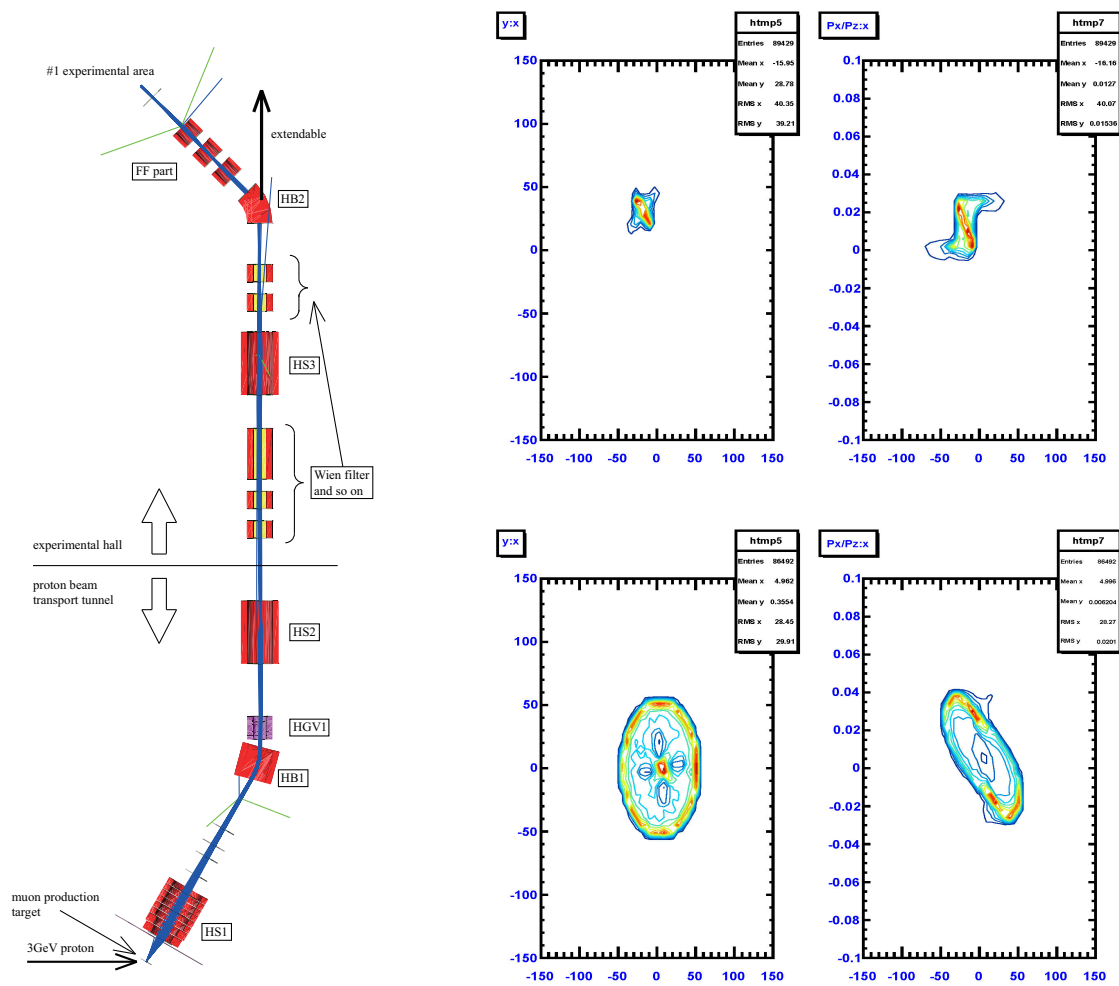
Figure 3.11: *A typical result of G4BEAMLINE calculation. The blue lines are beam trajectories (left). The surface muon beam from a point source is transported to the first experimental area through three solenoid magnets and two bending magnet. The wien filter and the kicker magnets are also shown, but they are not in use in this transmission. The beam profile at the exit of HS2 and HS3 (right).*
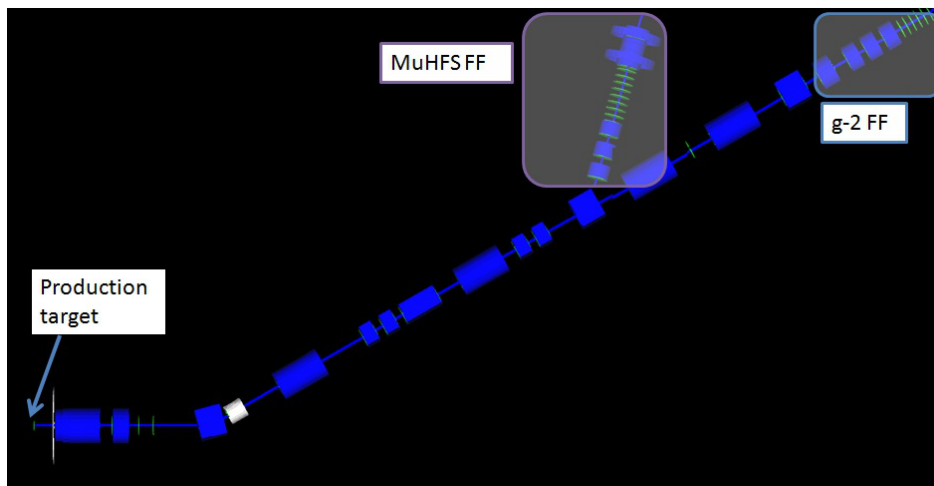
Figure 3.12: *Layout of the J-PARC/MUSE H-line. Purple box shows MuHFS beamline and its area. Blue box shows g − 2/EDM beamline.*
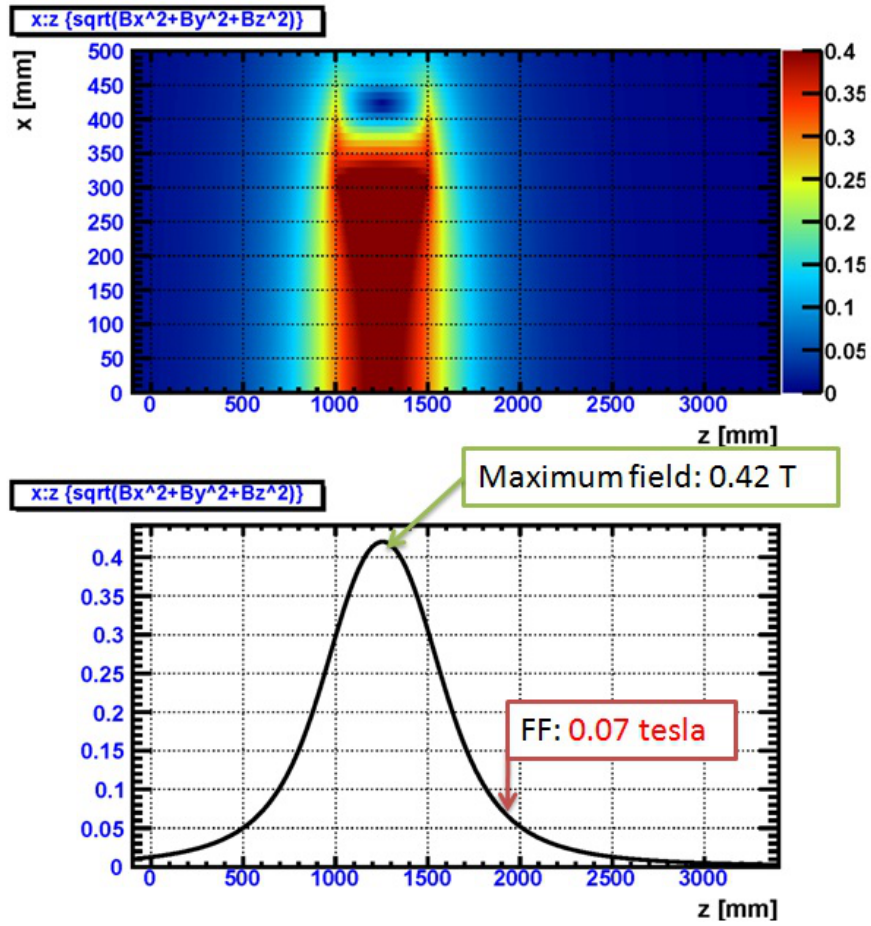
Figure 3.13: *Magnetic field [T] distribution along the beam axis, z [mm].*
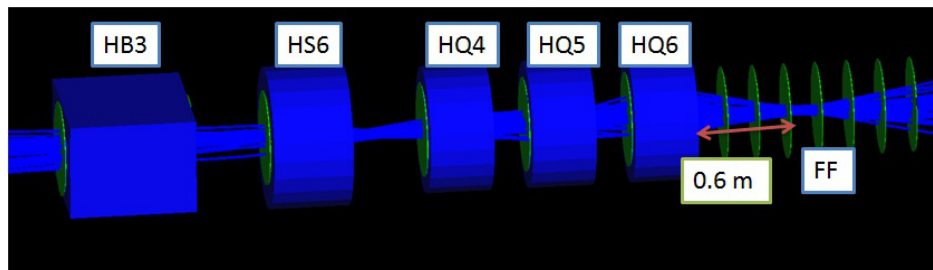
Figure 3.14: *Layout and beam profile with a solenoid and quadrupole triplet magnets.*
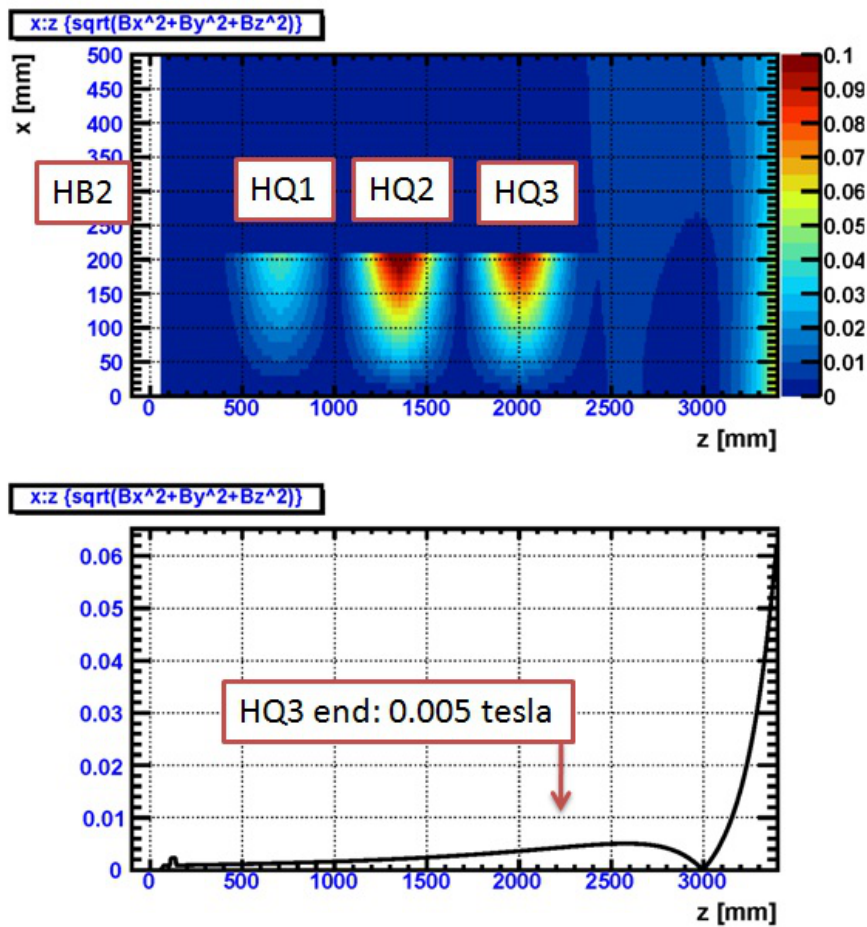
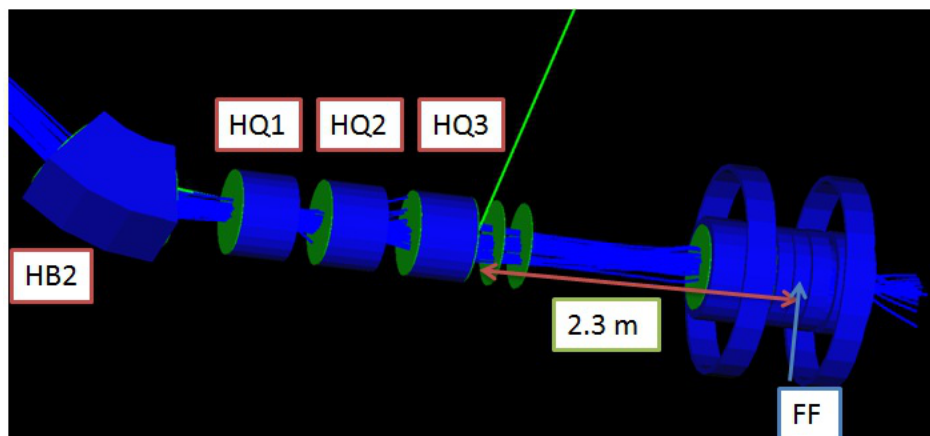**Figure 3.15:** *Layout and beam profile of the MuHFS final focus beamline.*

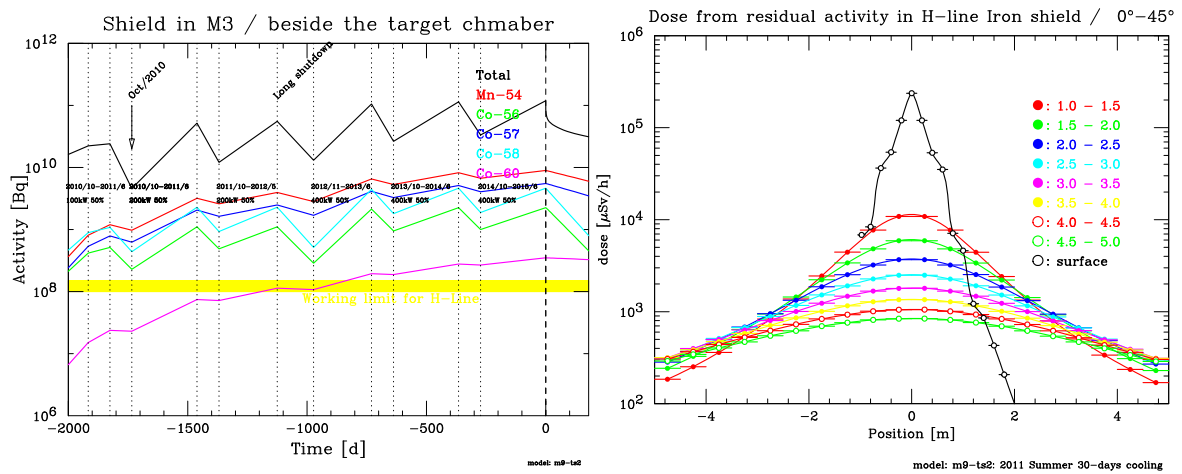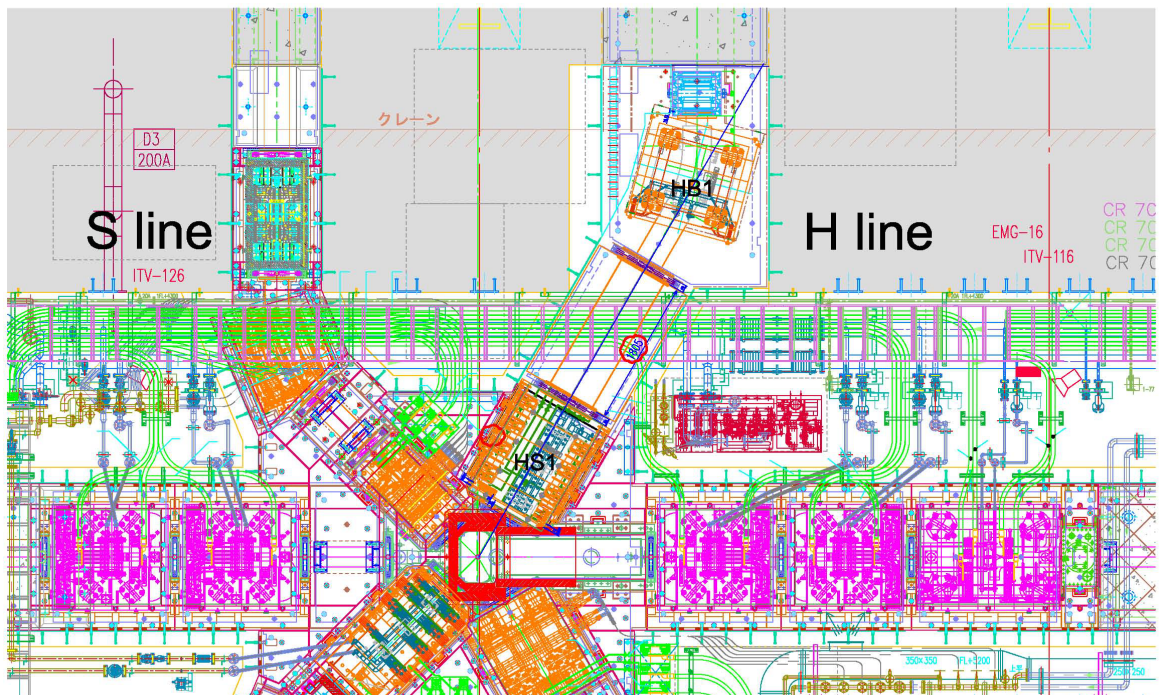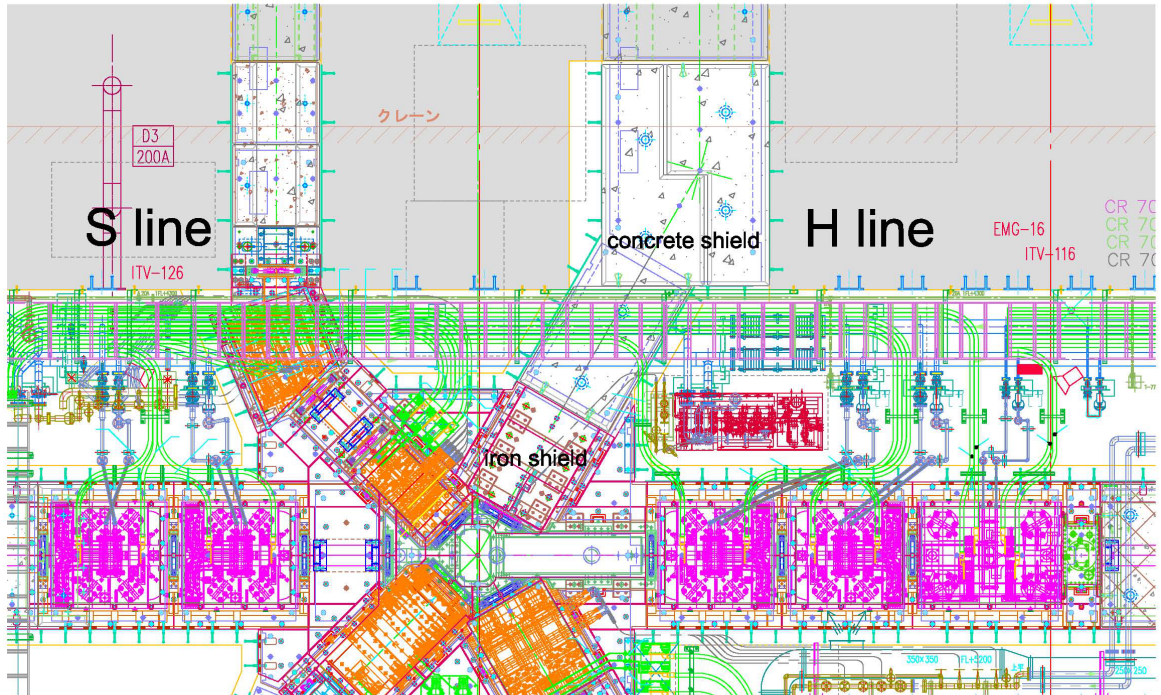**Figure 3.16:** *Magnetic field [T] distribution along the beam axis, z [mm].*

Figure 3.17: *The evaluated accumulated residual activities of the temporary iron shield in H-line (left), and the evaluated radiation dose around it in summer, 2011 (right). The evaluation is based on the operation schedule before the earthquake in 11/Mar/2011.*

Muon g-2/EDM Experiment, Conceptual Design Report, Revised, December 12, 2011, 11:40 A.M.

Figure 3.18: *The layout of M2 tunnel at present (upper) and after the installation of the front-end magnets (lower).*

CHAPTER 4

Ultra-Cold Muon Production

Contents

We describe the method of the ultra-cold muon production in this chapter. The production is based on

1. muonium production and its thermal emission into a vacuum, and

2. its two-step resonant ionization through 1S → 2P, then unbound.

The thermalization process is the key to cool down the muon beam.

When we proposed the experiment, the best knowledge on the ultra-cold muon was from a work jointly performed by RIKEN and KEK at Rutherford Appleton Laboratory (RAL). Since then, we have performed R&D experiments at RAL and at TRIUMF. The main goal of the RAL experiment is to find the laser ionization efficiency as a function of the laser power per unit area, space position, and time. The work is still ongoing at RAL. On the other hand, the goal of the TRIUMF experiment (referred to as S1249) was to search for best possible target for the Mu production and to measure the space-time distribution of the Mu emission into a vacuum.

Basing on the results from the S1249 and from the preparation stage of the RAL experiment, we have decided to take following configuration as our baseline:

- tungsten foil heated up to 2,000 K as a muonium target

- Lyman-α creation at 100 μJ using DFB-LD and nonlinear frequency conversion

- laser exposure area is 5 mm in z direction with a area of 200 mm^2 for 1 ns at 0.6 μs after the second muon pulse (1.2 μs from the first muon pulse) corresponding to a coverage of Mu atoms emitted into vacuum to be 22%.

Overall conversion efficiency from the surface muon beam to the ultra-cold muon is 0.12%, which is a factor 8 below the required number. In the following sections, we will discuss the basis of our estimates, RAL experiment and S1249, and a recovery plan.

4.1 Ultra-Cold Muon Beam at RIKEN-RAL Muon Facility

Our plan for ultra-cold muon production is based on a work jointly performed by RIKEN and KEK at the Rutherford Appleton Laboratory (RAL) in UK [1, 2]. There, we have utilized the fact that thermal muonium with mean kinetic energy of only 0.2 eV can be produced in vacuum with an efficiency of several percent by stopping the muon beam in a hot tungsten foil [3] or in SiO$_2$ powder [4]. Then thermal muonium atoms can be ionized by intense laser irradiation, leaving very cold polarized bare muons to be re-accelerated in the subsequent acceleration stages. The conversion from a 4.1 MeV muon beam to a 10 keV muon beam using this laser ionization method was achieved with an efficiency of about 3×10^{-5} [2]. Although the efficiency achieved here is as low as other methods to provide ultra-cold muons [5], and the scheme has an extra complication associated with the operation of the laser

system, it has a huge potential. The ionization efficiency of muonium atoms depends only on the laser intensity and can theoretically be as high as 100%, which would result in a total conversion efficiency of a few percent (starting from the surface muon). The energy spread as well as the divergence of the re-accelerated beam is much smaller than other methods of producing cold muons.
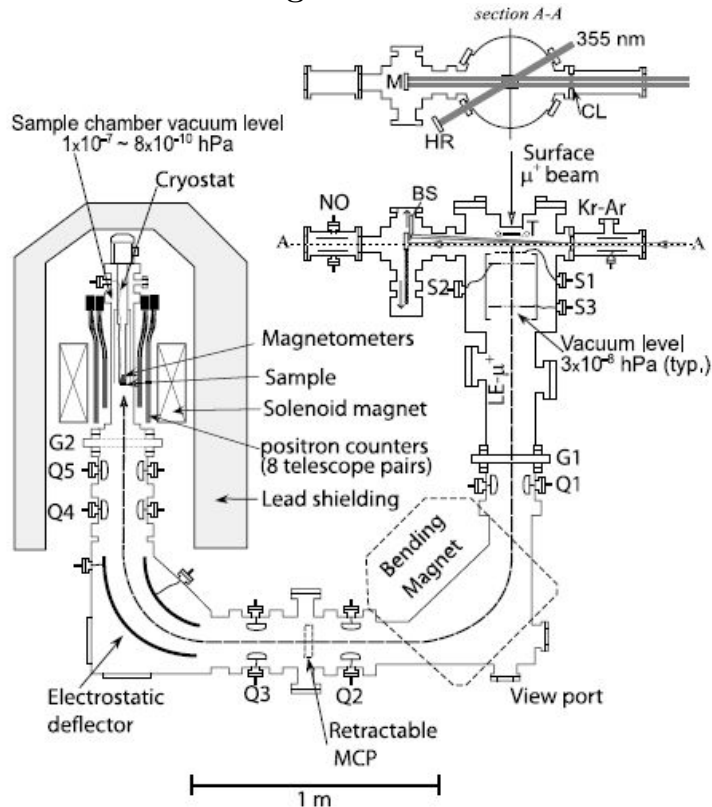
4.1.1   Muonium target

Figure 4.1: *An experimental layout of the ultra-cold muon beam line at RIKEN-RAL muon facility*

Figure 4.1 shows the layout of the target chamber and the ultra-cold muon beam line. The initial muon beam with momentum of 28 MeV/c enters the target chamber through a 50 μm thick stainless window and a 20 μm thick tungsten foil, and is stopped inside a 45 μm thick tungsten foil heated by DC current up to 2,100 K. The muonium can be produced with high conversion efficiency (1∼4%) by stopping high energy, 4 MeV surface muon beam in thin tungsten foil heated to 2,100 K [3]. The muonium is formed by electron capture near the surface of the hot tungsten foil. The muonium atoms can then escape to the vacuum with thermal velocity.

The area of the tungsten foil is 40 mm (W) × 35 mm (H). The total thickness of the foils is optimized to stop the largest fraction of the incident muons near its rear surface, which results in efficient emission of muonium atoms into vacuum.

Muon g-2/EDM Experiment, Conceptual Design Report, Revised, December 12, 2011, 11:40 A.M.

4.1.2 Laser system and ionization of muonium

Binding energy of the electron in a muonium atom is 13.6 eV. The muonium can be efficiently ionized through the 1S-2P single photon transition followed by the 2P-unbound ionization. Thus it requires two laser beams of different wavelengths. Firstly, for the strongly allowed transition from the 1S to 2P state, tunable radiation around 122 nm (Lyman-α) is required. Then for the ionization from the 2P state, a wavelength shorter than 366 nm is required.
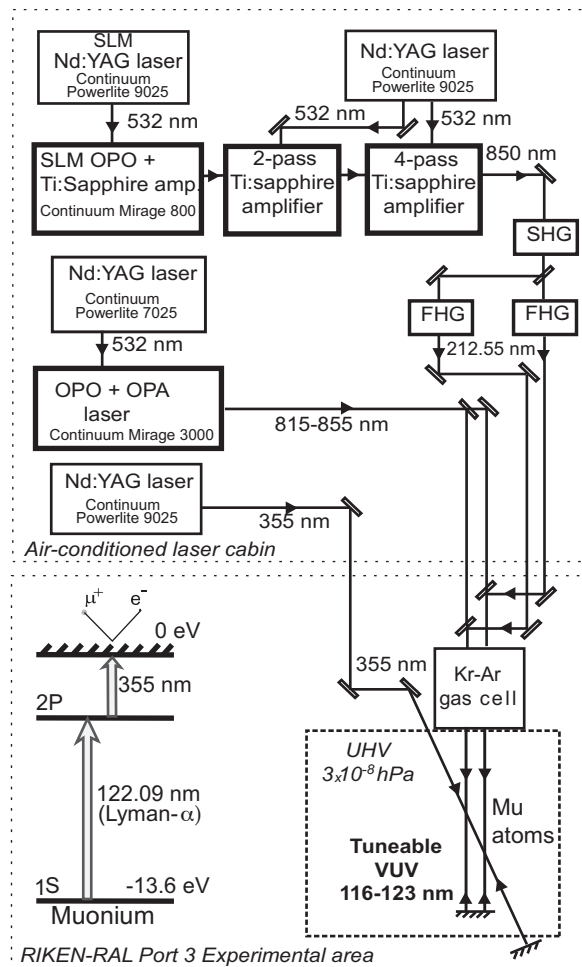

Figure 4.2: *A schematic diagram for the laser system used at the RIKEN-RAL muon facility*

Figure 4.2 shows a schematic diagram of the laser system [6]. The 122 nm radiation is generated through a two-photon absorption difference frequency mixing scheme in a phase-matched krypton/argon mixed gas. This conversion scheme requires two pump lasers: one at 212.55 nm which is matched to a two-photon absorption resonance line in Kr, the other at tunable wavelength from 815 nm to 855 nm. This added complication pays off for the following reasons. Firstly it gives a high conversion efficiency for 122 nm generation ($\sim 10^{-4}$), compared to the conventional third harmonic

Table 4.1: *Summary of the laser output parameters at RAL*

Wavelength	355 nm	212.55 nm	815–855 nm	116–123 nm
Pulse duration	10 ns	4 ns	12 ns	∼4 ns
Pulse energy	380 mJ	10-12 mJ (×2)	12 mJ (×2)	∼0.5 μJ (×2)
Bandwidth	30 GHz	<2 GHz	180 GHz	180 GHz

generation in gaseous media. Second, the tunability of the output wavelength allows one to ionize not only muonium, but also residual hydrogen and deuterium atoms in the target chamber. This provides a useful tool for testing the beam line. Lastly, the bandwidth of the output 122 nm can be controlled by using a properly selected infra-red laser. In this setup, the bandwidth of the output was set to be about 180 GHz in order to cover the Doppler width of the thermal muonium from the tungsten foil heated to 2,000 K. For the ionization from the 2P state, the 355 nm laser light from the third harmonic of a Nd:YAG laser is used.

The most crucial part of the laser system is an optical parametric oscillator (OPO) pumped by the frequency-doubled Nd:YAG laser, which generates single longitudinal mode (SLM) 850 nm wavelength. The output laser pulse is amplified in the Ti:Sapphire amplifiers, and then converted to 212.5 nm by the forth-harmonic generation using BBO crystals. High quality of the 850 nm laser beam results in high quality and intensity of 212.5 nm, which in turn increases the pulse energy of the Lyman-α wavelength. The current output parameters of the laser system are summarized in Table 4.1.

The laser system is operating at a repetition rate of 25 Hz, corresponding to a half of the muon repetition rate at the RIKEN-RAL muon facility. This limitation is due to strong thermal effect associated with operating high power solid-state laser systems. Otherwise, the laser system has a good, long term stability. Stable 24 h/day operation can be sustained for up to 20 days, limited mainly by the lifetime of flashlamps in Nd:YAG lasers.

The two Lyman-α beams are shaped by focusing optics to have a width of only 1–2 mm in horizontal and about 5–8 mm in vertical plane, and introduced parallel to the rear face of the tungsten target at about 5 mm away from the surface. The 355 nm beam is introduced from the top at 30 degrees from the Lyman-α beams and is shaped to have a width of 3 mm by 25 mm. All laser beams are retro-reflected to maximize the ionization yield. Since the retro-reflecting mirrors are placed at a distance of 0.5 m, the width of the ionizing laser pulse is effectively broadened from 4 ns to 7 ns. The overlap of the Lyman-α and 355 nm beams defines an interaction region where muonium atoms are ionized. The volume of the region is approximately 1 cm^3.

4.1.3   Ultra-cold muon beam line

The ultra-cold muons generated by the laser ionization are initially extracted by a low gradient electric field between the tungsten foil held at 9.0 kV and a mesh electrode S1 held at 8.8 kV, separated by 14 mm. S1 is the first of three elements forming an SOA immersion lens, which re-accelerates the

ultra-cold muons to 9.0 keV as well as focuses the muons to a spot of 2.5 mm (FWHM). The muons are then transported by electrostatic quadrupoles, a bending magnet, and an electrostatic deflector, to the sample position at the end. A position-sensitive microchannel plate detector (Roentdek DLD40) can be mounted at the sample position to measure the beam properties.
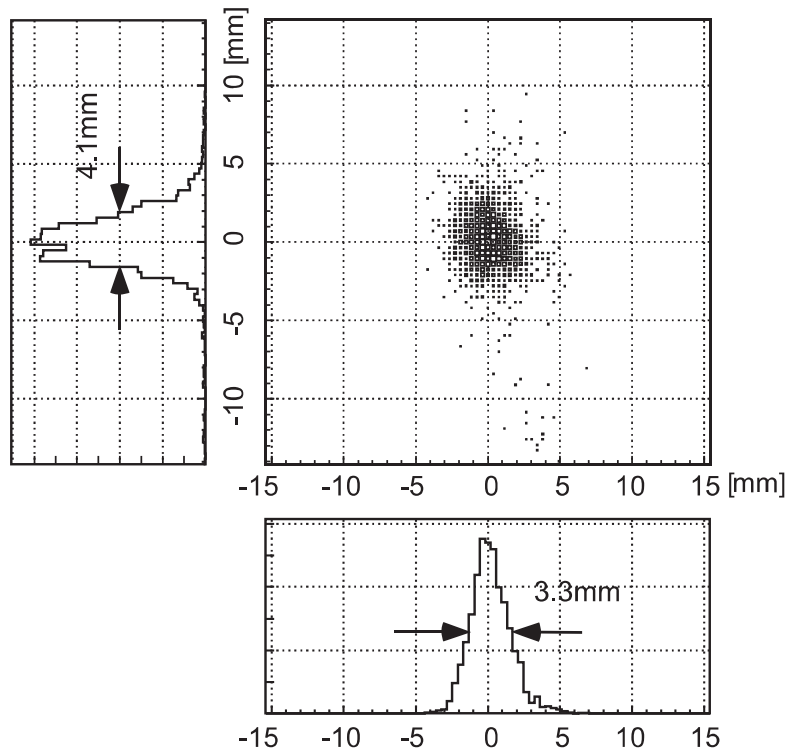
4.1.4 Beam parameters

Figure 4.3: *A beam profile of 9 keV muons at the sample position*

Figure 4.3 shows the beam spot of the re-accelerated 9 keV muon beam at the sample position. While the FWHM diameter of the incident 4 MeV muon beam is 35 mm, the FWHM diameter of the re-accelerated 9 keV muon beam is about 10 times smaller. The superior quality of the re-accelerated beam can be also seen in its time-of-flight (TOF) spectrum shown in Fig. 4.4.

While the incident muon beam has a double-pulse structure consisting of 80 ns pulses separated by 320 ns, the Gaussian fit to the TOF spectrum yields FWHM pulse duration of 7.5 ns. Compared to the effective width of ionizing pulse of 7 ns, the energy variation of the re-accelerated beam is very small. The main source of the energy variation is the width of the ionization region, which is of the order of 2 mm (FWHM). The difference in electrostatic potential over the 14 mm gap between the tungsten foil and S1 is kept at 200 V, which means that the 2 mm width of the ionization region contributes to the standard deviation of the muon energy by ∼13 eV. due to bending of the heated
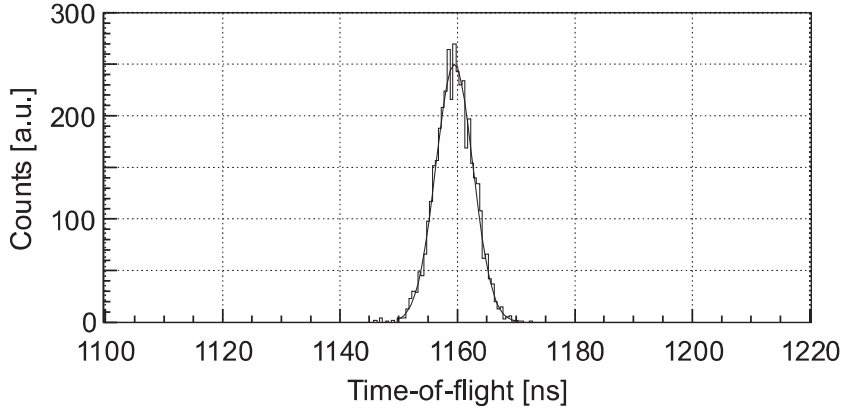
Figure 4.4: *A time-of-flight spectrum of 9 keV muon beam detected by a MCP at the sample position*

tungsten, contributes a few eV. Taking into account other factors, such as the uneven distance between the foil and S1 due to bending of the heated tungsten, the standard deviation of the re-accelerated beam is estimated to be approximately 14 eV. This estimation is consistent with the measured μSR asymmetry in a 40 nm thick Al layer on SiO_2 substrate [2].

With the current laser parameters, we observed $\sim15\mu^+$/s at the sample position, which corresponds to an overall conversion efficiency of 3×10^{-5}. The number of available muons is far below that required for the $g-2$ experiment.

There are three main issues to be addressed to use this scheme for the proposed $g-2$ experiment. Firstly, we need to increase the intensity of the incident muon beam. This can be achieved by constructing an all-solenoid muon capture and transport beam line at the MSL facility. Secondly, we need to study the way to generate muonium in vacuum more efficiently. Lastly, we need to increase the ionizing laser power for the generated muonium. Our measurements show that improvement of the yield can be expected from increases of the pulse energy of the 122 nm and 355 nm beams (Fig. 4.5).

Especially it is worth noting that the power of 122 nm (~1 μJ/pulse) is still below the saturation intensity of 1S-2P transition. In order to address this challenge, we propose to build a new laser system, based on a newly developed $Nd:GdVO_4$ laser.

4.2 Muonium Production

4.2.1 Muonium production target materials

Muonium (μ^+e^-) is an analog of the hydrogen atom, with similar atomic and chemical characteristics, and is often denoted as a chemical species with the name Mu. It is produced with non-negligible probability in a variety of gases, liquids, and solids. As a muon thermalizes, the ionization process may result in the charge exchange interaction whereby a valence electron is captured by the positive
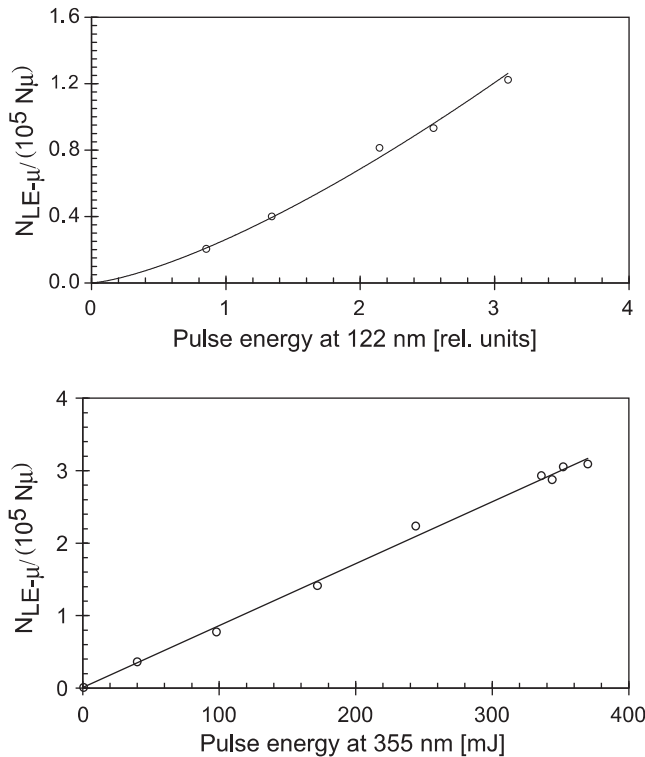
Figure 4.5: *Dependence of the efficiency of ultra-cold muon generation on the laser energies*

muon into an atomic state. Subsequent charge exchange interactions may result in the stripping of this electron, or perhaps in the capture of another electron to form a negative ion [7]. At a kinetic energy of 200 eV, the muon is almost completely neutralized [8]. If the cross section for electron capture to the neutral state is dominant as the energy is further reduced in collisions, the muon can thermalize as muonium. In the muonium state, the spins of the muon and electron are coupled by the hyperfine interaction, just as in atomic hydrogen.

In the case of solids of typical densities, the time required for thermalization of polarized muons from energies of a few MeV to room temperature ($\sim$25 meV) is less than 10^{-12} s. In conducting materials, conduction electrons screen the muon such that no coherent muonium hyperfine-coupled state persists. In many insulating systems, however, the characteristic muonium spin rotation signal at 1.4 MHz per Gauss is evidence of abundant muonium formation and polarization.

For the J-PARC $g-2$ measurement, it is required to produce polarized thermal muonium in vacuum, in order that it can be ionized by laser and the resulting ultra-cold muons can be accelerated while retaining the extremely small transverse momentum components compatible with muon storage in the detector magnet. Two approaches have been developed previously and demonstrated to produce muonium in vacuum. One uses a hot ($> 2,000$ K) tungsten foil; while muonium is not expected to be produced inside the foil, the hot surface provides electrons such that the neutral system is emitted with energies consistent with the foil temperature [3]. The other approach used finely divided room-

temperature insulators, particularly silica (SiO_2) powder, in which muonium formed in the silica was emitted from powder particles and eventually from a layer of the material into vacuum [9, 10, 4].

The direct detection of muonium emitted into vacuum from a room temperature target was first accomplished using silica powders of diameters of a few nm [4]. It was subsequently verified independently [11] and studied further [12]. Muonium is formed with about 60% probability inside silica powder particles [10] and is emitted from the particles with 97% probability [9]. The nominal particle radius is as small as 3.5 nm (Cab-O-Sil EH-5 fumed silica), and can be larger depending on the grade. The powders are characterized by measurements of specific surface areas, up to ~ 400 m^{2}g^{-1}. The high surface area and corresponding small structure size means that muonium does not have to travel far to find the powder particle boundary. The measurements are consistent with the interpretation that muonium, once it finds the void between powder particles, does not re-enter the silica, although temperature dependence found in [10] indicates a muonium interaction at the surface. Diffusion through the voids between particles at thermal speeds allows migration of the polarized muonium atoms over distances of the order of 0.3 mm within the powder in the muon's lifetime. If a target is made with a thin layer of such powders, the muonium may escape the surface of the layer with significant probability, depending among other things on the thickness of the layer.

Several experimental programs have relied on muonium production in vacuum from silica powder. It was originally motivated by early searches at TRIUMF for muonium conversion to antimuonium, which are most sensitive if muonium remains without collisions in a vacuum [13, 14]. It was used at KEK to identify the 1S-2S Doppler-free two-photon laser excitation of muonium [15] and later on at RAL to measure the resonance frequency in that transition [16]. Finally, a silica powder muon target was exploited in the most sensitive search to date for muonium conversion to antimuonium, at PSI [17].

In the J-PARC g–2 measurement, there are several advantages to the use of a room temperature target such as silica powder rather than high temperature targets. The lower energies at room temperature lead directly to a smaller emittance of the ionized source and thus are more compatible with the small transverse momenta required for storage in the detector magnet. In addition, the resonant line for muonium excitation has a smaller Doppler broadening. The reduced velocity distribution also results in a smaller spatial spread of muonium in vacuum, so the available laser power may be utilized much more efficiently.

The powder targets have disadvantages as well. The powder must be placed on a support film that must be at or near horizontal. This makes them difficult to make compatible with typical horizontal muon beams. The powder must be evacuated very slowly and carefully, otherwise it can disperse through a vacuum system easily and is a potential cause of damage to some types of vacuum pumps. The powder is electrostatically active, and being so light, it cannot tolerate any significant static electrical potential. Finally, there is some evidence of deterioration of uniformity and increase in density of powder layers after several days under vacuum, presumably due to the slow evolution of water and hydroxyl molecules at the powder surface that tend to bind the powder constituents into agglomerates that resist packing. All of these issues have convinced us to search for a more stable and self-supporting material for room-temperature muonium production in vacuum.

Silica aerogel is one candidate. Previous measurements on silica aerogel, made 20 years ago, found a rather low emission rate (about 1/4) compared with that from silica powder [18]. We expect that more uniform aerogel samples are now available, for example that used for the Cerenkov counters, where the density of the aerogel has been finely controlled to change the refractive index. Silica aerogel samples with densities of 30, 50, 110 and 200 mg/cm^3 were produced by the Chiba-U/JAXA group for evaluation at TRIUMF.

Another candidates are the materials with porous structure so that the effective surface area of the material is larger than bulk materials. Note that the structure of silica powders and silica aerogels are chains of small SiO$_2$ grains, which has a large effective surface area. One expects larger production rate for porous materials as well if the effective surface area is a key parameter for the emission rate of muonium in vacuum region. In order to study muonium emission from porous-structured materials, alumina plates with porous diameter of 60-270 nm in 100-450 nm pitch, 40-100 μm thickness, were produced at the Prof. Masuda's group at Tokyo metropolitan university. We also produced silica plates with porous diameter of 8 μm in 10 μm pitch, 50 μm thickness in collaboration with Prof. Esashi's group in Tohoku university. Several of these porous samples were tested at TRIUMF which will be described later.

4.2.2   Study of muonium production targets at TRIUMF

There are two major muonium-related questions which prevent us from estimating the ultra-cold muon beam intensity accurately: (1) no self-standing material is known for good muonium emitting material at room temperature so far, (2) calculation of the muonium distribution involves several assumptions in the muonium production model. More information is necessary to answer these questions. We are measuring muonium productions from several room-temperature targets at TRIUMF.

For the purposes of identifying suitable materials for production of muonium in vacuum for $g-2$, there are many advantages to a muon beam from a continuous (high duty factor or continuous wave (cw)) accelerator rather than a pulsed source. It allows identification of decays of individual muons, with correlations of muon decay time, position, etc., that are not possible when the instantaneous rate is high. The cw muon beams at TRIUMF were used in two stages of experiments in order to search for one or more materials that could produce abundant muonium in vacuum at room temperature and perhaps avoid some of the experimental challenges presented by targets of powdered silica. The TRIUMF experiments consisted of two stages.

The schematical overview of the measurement is shown in Fig. 4.6(a). The first stage used the muon spin rotation/relaxation (μSR) technique to provide a quick test of several powdered or porous materials to determine whether they produced polarized muonium, and if so, was it subsequently depolarized by the well-known spin exchange reaction with oxygen added in small concentration to the target volume. Observation of this depolarization indicated that muonium was escaping from the bulk of the material to a region where it could undergo spin exchange collisions.

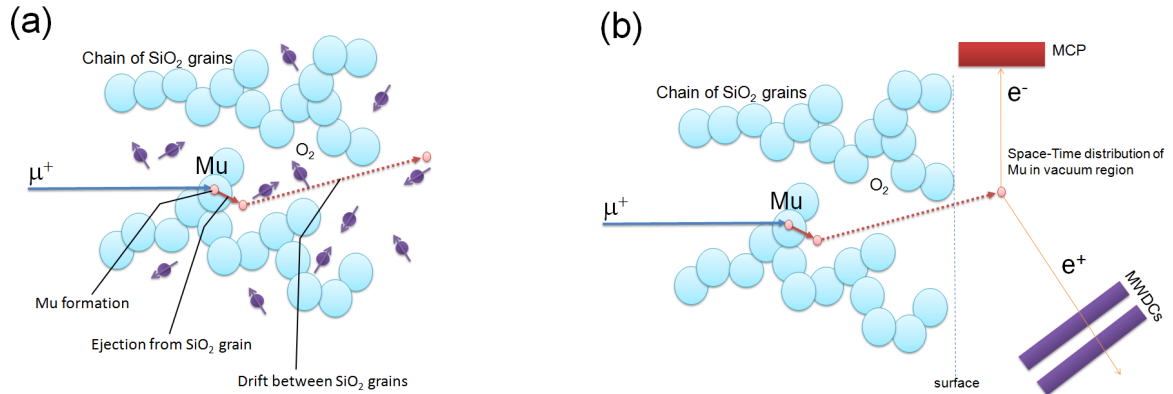If that was observed, the material would be a candidate for the second stage of measurements shown

Figure 4.6: *The schematic overview of the experiment at TRIUMF. The experiment consists of two stages; (a) MuSR measurement with and without O_2 concentration to survey muonium ejection from sample grain or material, (b) muonium imaging by measurement of decay positron and electron for investigation of the space-time distribution in vacuum near the target surface.*

in Fig. 4.6(a), where the decay of muonium was detected directly and identified by the decay positron and in some cases the coincident detection of the remnant atomic electron. The track of the decay positron could be extrapolated to the target region to determine whether muonium was spatially separated from the material used to thermalize the muon beam, while the atomic electron could only be detected if muonium decayed completely outside of the material.
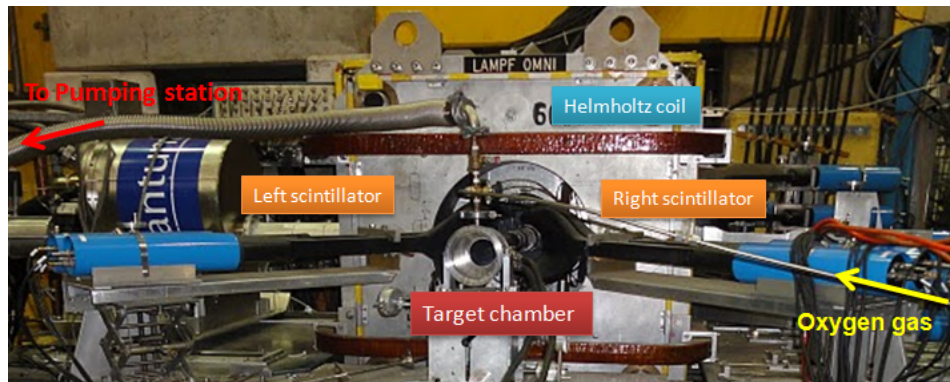

Figure 4.7: *Downstream view of the experimental setup for the MuSR measurement at the TRIUMF M20 beamline.*

4.2.2.1 μSR measurement

The first stage of measurements was carried out for 11 target samples in June 30, 2010. Data were taken with the LAMPF-OMNI muSR spectrometer at TRIUMF M20 beamline (need reference). List of material tested in this measurement are silica quartz, silica powders (Cab-O-Sil EH5, nanogel), silica aerogel ($\rho = 30, 50, 110$ mg/cm^3), porous alumina and porous silica (see Fig. 4.8). The experimental

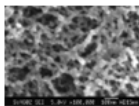| Material	Density (g/cm³)	Thickness (mm)	Structure	
Silica powders (SiO₂)	0.03, 0.075	37.5	Chain of nano-grains	
Silica aerogel (SiO₂)	0.03, 0.05, 0.11	20	Chain of nano-grain	
Porous Silica (SiO₂)	1.1	0.05 – 0.07	Nano-porous (10 µm pitch)	
Porous Alumina (Al₂O₃)	2.9	0.09 ,0.255, 0.4	Nano-porous (60-450 nm pitch)	

Figure 4.8: *Target samples for the S1249 MuSR measurement.*

set up is shown in Fig. 4.7. Transverse (vertical) magnetic field of 6 or 23 G was generated for spin rotation of muoniums and muons in a horizontal plane. The surface muon beam was stopped in the target sample in the target chamber. Decay positrons were detected in two scintillators in left and right to the target sample. For the samples which we observed muonium precession signals in vacuum, oxygen gas was introduced in the target chamber to investigate relaxation of the muonium asymmetry as a function of oxygen concentration in the target chamber. As a cross check, we confirmed that the muonium production rate and relaxation rate with the silica powder (Cab-O-Sil) were consistent with previous study [9].

Figure 4.9(top) is the time spectrum of the raw left-right asymmetry in the aerogel target (50 mg/cm³) with 6 G transverse magnetic field in vacuum. The rapid oscillation with a period of ∼120 ns is due to muonium spin precession which is as strong as silica powder sample. With the oxygen concentration (Fig. 4.9(bottom)), the time spectrum shows strong relaxation, indicating that muonium interacts with oxygen outside of silica grains. Similar trend was seen in other aerogel samples (30 and 110 mg/cm³) as well. This is an encouraging indication that silica aerogels could be efficient muonium emitter, therefore worth studying in the next stage of the experiment (muonium imaging).

4.2.2.2   Muonium imaging

The second stage of muonium production target tests, tracking decay positrons and detecting coincident remnant atomic electrons following muon decay in muonium, used the high luminosity M15 surface muon beam at TRIUMF. Based on selections made in the first stage, the target was one of a selection of sheets of aerogel of different densities but approximately the same mass.
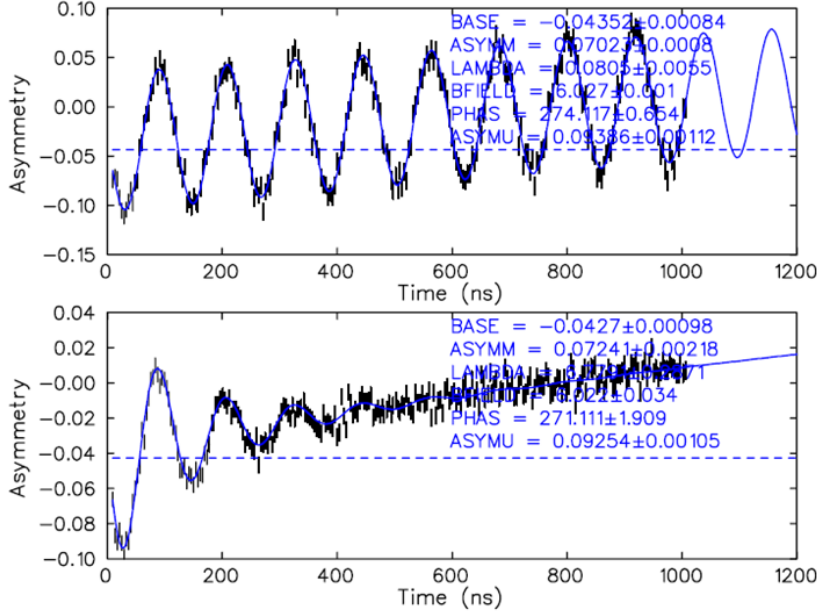
Figure 4.9: *Time spectrum of the raw left-right asymmetry in the aerogel target (50 mg/cm^3) with 6 G transverse magnetic field in vacuum (top), and with oxygen concentration ($20 \times 10^{15} cm^{-3}$) (bottom). Curves are fit to data with the functional form Asymmetry = ASYMM$\times \exp^{-\lambda t} \cos(\mu_{Mu}Bt+PHAS)$ +ASYMU$\times \cos(\mu_{\mu}Bt+PHAS+PHASDIFF)+BASE$ in physica. The first term is for the spin rotation of muoniums and the second term is for the muons not forming muonium.*

The experimental set up is shown in Fig 4.10. We stopped muons in the sample, and detect muonium atoms which has emerged from the surface of the sample by tracking positrons from muon decay by the positron tracker which consists of two sets of multi wire drift chamber (MWDC) [19] followed by trigger scintillators and a NaI calorimeter. In order to increase the sensitivity to the muonium distribution near the target surface, one needs to discriminate them from backgrounds from the decay of muons which stayed in the sample. For this purpose, we have employed an MCP (micro channel plate) to capture an electron left from muonium when the muon decayed. Note that no electron is expected from the free muon decay in the sample.

In order to effectively guide the electron to the MCP we applied a static electro-magnetic field (100 V/cm and 100 G). MCP with delay-line readout has hit point resolution of better than 1 mm. The electron has an initial energy spread of around 8 eV and emitted in random direction, so the overall imaging resolution is limited by its motion in the electro-magnetic field and is estimated to be around 2 mm (RMS) in a GEANT4[20] simulation.

The coincidence measurement will also allow one to have a complete 3 dimensional information of the muonium decay point, since the MCP adds the depth information to the positron tracking by MWDC.
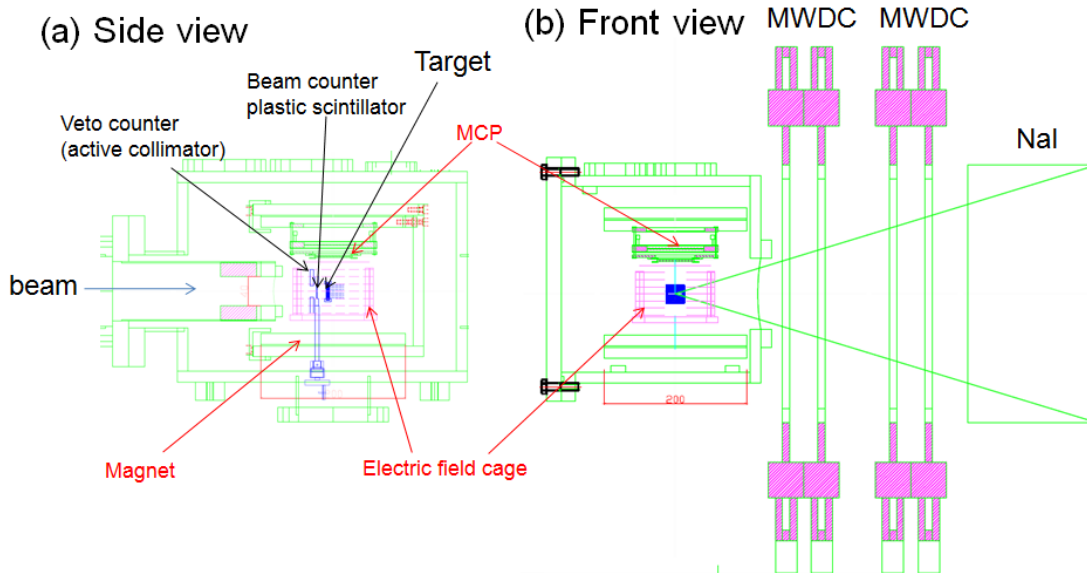
Figure 4.10: *Setup for the muonium imaging measurement at the TRIUMF M15 beamline.*

In the November 2010 Run, we were ready to take data for various samples but because of the beam stop by a failure in the proton beamline, we were able to take data for only one sample. In a measurement in 2011, which was just finished, we took data for four aerogel samples (with density 0.026, 0.049, 0.099, and 0.180 g/cm^3) and one silica glass plate as a reference.

The surface muon beam momentum was lowered from the typical 29 MeV/c to about 22 MeV/c to pass through holes in a collimator and veto counter, then through a beam counter made of a thin plastic scintillator, in order to maximize the number of muons stopping near the surface of the aerogel and presumably the number of muonium atoms emitted from it. We analyze the data to determine both the position and time of each decay observed. The position was measured according to an extrapolation of the drift chamber tracks to the target region, allowing some degree of separation of events corresponding to decays in the vacuum regions adjacent to the target surface from events due to muon or muonium decays inside the target. The time measurement confirms what portion of the decays that seem to originate in the vacuum region are in fact from emission, because there is a time delay due to diffusion from the material plus drift at thermal speed from the surface ($v_{th} \approx 0.6$ cm μs^{-1}). The distribution of the time delay leads to a decay time distribution from decays in vacuum that is very different either from stops in the target or from other backgrounds, both of which show the smooth exponential behavior characteristic of the muon lifetime. We describe here some of the procedures in acquiring and analyzing these data.

The selection of muon beam momentum is important to optimize muonium emission for a particular

thickness of materials in the beam (aerogel target, beam counter, vacuum window, etc.). It is expected that only muonium atoms in a region near the boundary of the silica layer have appreciable chance of emission into vacuum. This means that the stopping density near the surface must be as high as possible. Furthermore, experience has shown that the analysis is most effective if the number of muonium atoms observed to be decaying in vacuum can be normalized to the number of muons stopping within the silica layer, as this accounts reasonably well for corrections to the data that are common to muon decays detected from either region, such as for efficiency, dead time, solid angle, and so on. Thus it is important to know the muon stopping density near the surface as well as throughout the silica in order to estimate diffusion and to normalize consistently to muons stopping and decaying in the target. A necessary ingredients for this is a realistic simulation, to obtain knowledge of the muon beam characteristics and then to predict the stopping distributions.

The drift chamber position distributions make it straightforward to identify decays originating in the silica target. If those decays are counted for different settings of beam momentum, carefully scaled to account for elapsed time, dead time, beam variations, and so on, a curve is obtained for an aerogel target of density $0.099 \, \mathrm{g \, cm^{-3}}$ and thickness $2.4 \, \mathrm{mm}$ as shown in Fig. 4.11. One can easily see that for low and high values of the beam momentum scan, the number is very much reduced. At low momentum, the muons are stopping in materials upstream of the silica target (e.g., the beam counter scintillator) while at high momentum, most pass completely through to stop in materials downstream. For an intermediate momentum, almost all the muons stop in the layer. The shape depends on the target density and thickness, which are known, and the momentum distribution of the beam, which must be determined.
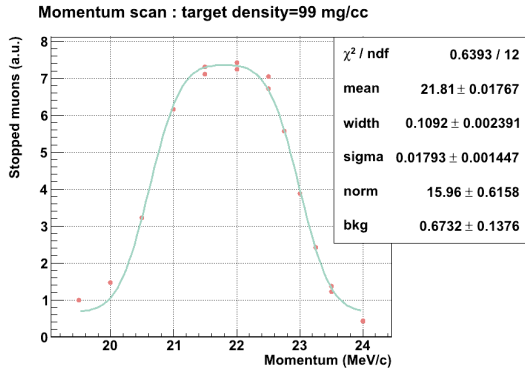

Figure 4.11: *Normalized number of muons decaying in silica aerogel target, as a function of beam momentum.*
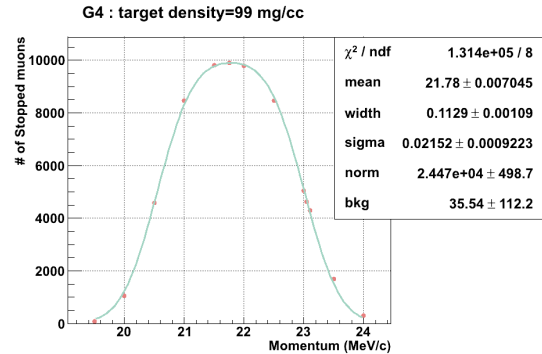
Figure 4.12: *Simulated momentum dependence of muons decaying in silica aerogel target.*

Proven software tools such as SRIM [21] or Geant4 [20] can be used for simulations of these measurements. We have used both, but Geant4 is more easily adapted to the geometry of our beam, vacuum window, scintillator, and target configuration. By varying the simulated beam momentum for some fixed fractional momentum width ($\Delta p/p$), an attempt is made to match the simulation to the data. For the appropriate choice of $\Delta p/p = 1.9\%$ (rms), the results of Fig. 4.12 are obtained to be approximately consistent with experiment.

The shape of the distribution can be fit to a function representing a convolution of a uniform ("box") distribution with mean momentum μ and width $\omega\mu$ with a gaussian distribution of rms width $\sigma\mu$:

$$y = N \frac{1}{2\omega\mu} \left\{ \left[\mathrm{erf}(\frac{x - \mu + \frac{1}{2}\omega\mu}{\sqrt{2}\sigma\mu}) \right] - \left[\mathrm{erf}(\frac{x - \mu - \frac{1}{2}\omega\mu}{\sqrt{2}\sigma\mu}) \right] \right\} + B \qquad (4.1)$$

where the fractional width parameters ω and σ depend on the silica thickness and beam momentum resolution, as well as range and energy straggling. Momentum calibration for data was achieved by scaling beam line magnet currents from the kinematic edge for surface muon production at 29.79 MeV/c; the difference in mean value μ is within the accuracy expected by scaling dipole magnet currents. The normalization (norm) N is arbitrary and the background (bkg) B is slightly above zero for the experimental data. The relatively small disagreement for width and sigma are probably due to the simulation's assumption of a gaussian momentum width; the beam line has a rectangular momentum selection aperture, so a rectangular component to the momentum distribution is expected.

The characteristic depth for diffusion to the surface in the muon's lifetime τ_μ is $\sqrt{D\tau_\mu}$, where D is the diffusion constant. The distance is small (< 1 mm) compared to the thickness of the silica. The beam momentum is thus chosen to match a point on the high-momentum side of the distribution in Fig. 4.11, where only half the muons stop in the target near the downstream surface. For this momentum and for $\Delta p/p = 1.9\%$, the simulation shows a stopping distribution as in Fig. 4.13. One can see that the peak of the stopping distribution is near the aerogel edge at 2.4 mm on this horizontal axis scale.
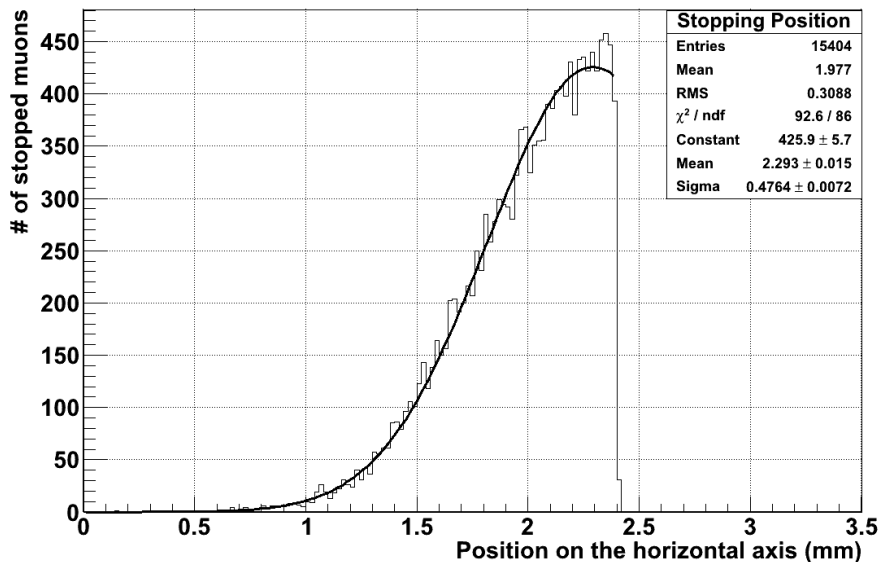

Figure 4.13: *Muon stopping distribution in the aerogel layer, for a beam momentum for which half the muons stop in the layer while half penetrate through. The curve is a fit to Gaussian distribution.*

When the beam settings have been optimized, decay positron track positions and times are recorded by the MWDC array, scintillators, and a NaI calorimeter. The spatial coordinates of each track are extrapolated back to a point on a plane near the track origin at the muon stopping target. Tracks are

selected with small slope, to minimize a parallax uncertainty, and with 30 MeV or greater positron energy deposited in the calorimeter, to select events with smaller multiple scattering uncertainty. Decay times with respect to muon arrival are determined by the scintillators. The correlations between the decay time and the distance from the extrapolation z perpendicular to the surface of the silica layer is shown in Fig. 4.14, while a background data set with a solid silica glass plate in Fig. 4.15 shows no similar correlation.
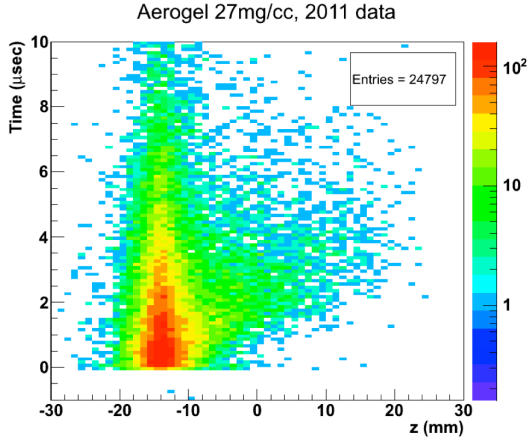

Figure 4.14: *Decay time vs. one coordinate of track extrapolation for $0.027\,\mathrm{g\,cm^{-3}}$ aerogel target. The surface of the aerogel is near $z = -13$ mm. The intense region is due to muons decaying in the target, while the time-correlated distribution for $z > -6$ mm is largely due decay in vacuum.*
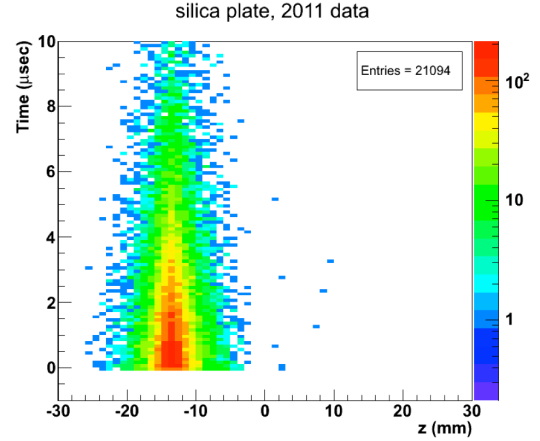
Figure 4.15: *Decay time vs. one coordinate of track extrapolation for a silica plate target. There is no evidence of time correlation with position.*

Distributions obtained from the analysis can be compared to a program that simulates diffusion in the silica layer and emission from the surface of the layer into vacuum. The program is based on a three-dimensional random walk in which each step is taken with a speed v drawn from a Maxwell thermal distribution of mean $\langle v_{\mathrm{th}} \rangle$ and a path length l derived from an exponential distribution with mean l_{mfp}. The time l/v for each step is accumulated until the muon decays at a time taken from an exponential distribution of mean τ_μ. The direction of each step is random. For a room temperature value of the mean $\langle v_{\mathrm{th}} \rangle \approx 0.7\,\mathrm{cm\,\mu s^{-1}}$ and an input value of the diffusion constant D, l_{mfp} is calculated algebraically. A special set of simulations in a uniform material, with no boundaries and with no muon decay, was used to verify that the time dependence of the motion agrees with diffusion theory [22, 23]. One main requirement is that the initial muon position distribution with respect to the layer surface corresponds to the experiment. It is taken from a distribution such as that of Fig. 4.13, which has been verified as previously explained by comparison to the momentum scan data. Different aerogel densities result in different stopping distributions, so the momentum scans must be simulated for each target configuration.

There are some interesting features of the simulation. Unlike some previous routines [12], the passage

of muonium through the boundary of the silica layer into vacuum is treated as a physical process, where the muonium direction and remaining path length are retained from the current random walk step, rather than adding some assumed uncorrelated direction. The distribution of angles with respect to the normal to the boundary surface follows closely but not exactly a proportionality to $\cos\theta$ as has usually been assumed. This allows a much more reliable prediction, within any limitations of the diffusion model, of muonium emitted at large angles that decays too close to the surface to be resolved experimentally.

The simulation ignores some details. The extremely fast relaxation time of a few ns obtained in the μSR experiments leads us to believe that the delay due to migration from the silica structure into the voids is not important on the time scales of emission over the muon lifetime, so it is not taken into account. Each step in the random walk is based on an independent thermal speed, path length, and direction, ignoring any possible correlation from one path to the next. Finally, while we expect that at low temperatures there is a significant dwell time of the muonium at a silica surface between steps [10], we assume the room-temperature estimate of 3 ps is small enough to be ignored. However, this brief surface interaction does support the assumption of a lack of correlation of speed between steps because it is long enough for thermal equilibration of the muonium atom with the silica. In any case, the diffusion model is only a tool to understand the evolution of muonium from a silica layer into vacuum, and to allow prediction of the process for different beam situations such as at the J-PARC H-line.

We can compare the characteristic time distributions of emission as predicted by the simulation to data obtained at TRIUMF. For example, an aerogel target of $0.027\,\mathrm{g\,cm^{-3}}$ and thickness $0.78\,\mathrm{cm}$, with the muon beam optimized as described above, is compared to a simulation with a similar muon stopping distribution using a diffusion parameter $D = 8\,\mathrm{cm^2\,s^{-1}}$ in Fig. 4.16. Background with an exponential time distribution of muon decay has been subtracted from the data for the three vacuum regions (V1, V2, and V3). The simulation is scaled to the data such that muonium decays in the target region (Tgt) are equal after accounting for target muon decays in the data (40% of the total) that are not within the simulation. With this diffusion constant, the agreement is reasonable but not perfect, and is limited by the statistics of the data.

This level of agreement allows the use of the simulation to make a reliable estimate for the muonium yield into the laser ionization region in a simple aerogel target configuration at J-PARC. The simulation is adjusted to reflect the proposed J-PARC H-line muon beam parameters of $(\Delta p/p) = 5\%$ (gaussian rms) with a double pulse structure with separation of 600 ns. Figure 4.17 shows the number of muonium atoms in a laser ionization region between 1 mm and 5 mm from the aerogel surface, as a function of time from the average of the two accelerator beam pulses. The vertical axis has been scaled to represent the rate per second, assuming a muon beam rate of $10^8\,\mathrm{s^{-1}}$.

A preliminary analysis of the Oct 2011 data suggests that the emission is not much dependent on the silica aerogel target density. As the density is increased, the muon stopping density per depth from the surface is increased, thus we can expect more muons to come out from the surface. On the other hand, the diffusion rate may be decreased because of the shorter mean free path length. The new result indicates that the gain by higher stopping density is largely compensated by the slower
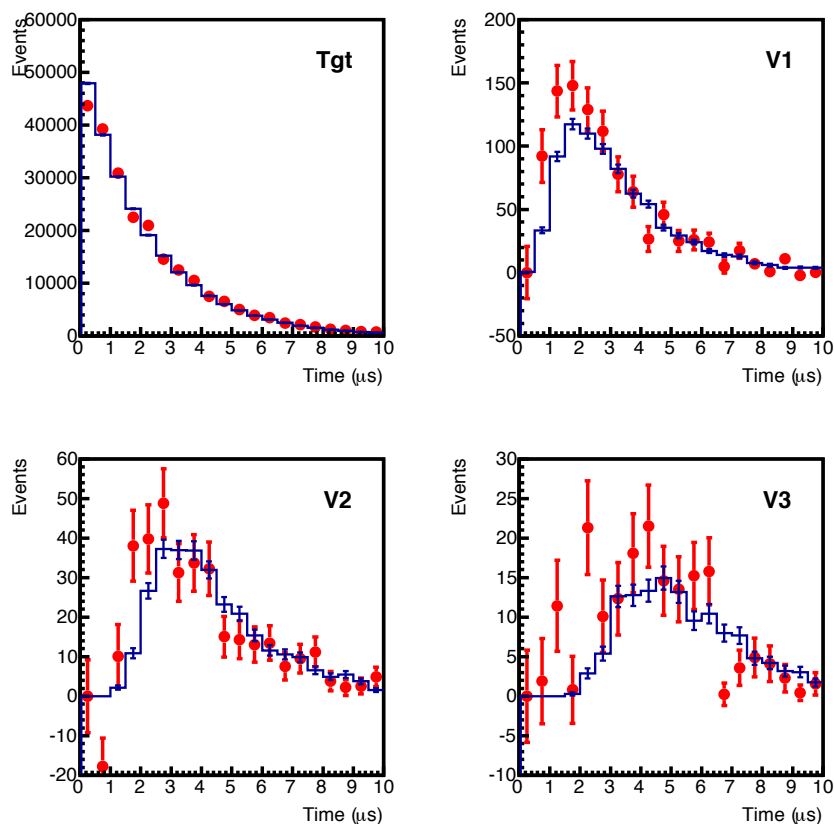
Figure 4.16: *Data (filled circles) and simulation (histogram) showing time distributions for decay positron tracks extrapolated to positions at the aerogel target (Tgt), and for vacuum regions of width 1 cm at distances of 1.0, 2.0, and 3.0 cm from the surface (V1, V2, and V3 respectively). Exponential muon decay background has been subtracted from the vacuum region data and all plots use a single normalization based on the events from the target.*

diffusion constant when the target density is increased.

Although we are not yet ready to fully report about the MCP measurement, online analysis has shown that we have a much cleaner signal (free from background from the muon decay in the target) from the decay of muonium in vacuum by requesting the coincidence of the MCP signal and the MWDC signal. Also we can obtain 3-dimensional information of the Mu decay position as the crossing point of two tracks, which will help us to understand in more detail the Mu emission such as the angular distribution. Detailed analysis is on progress.
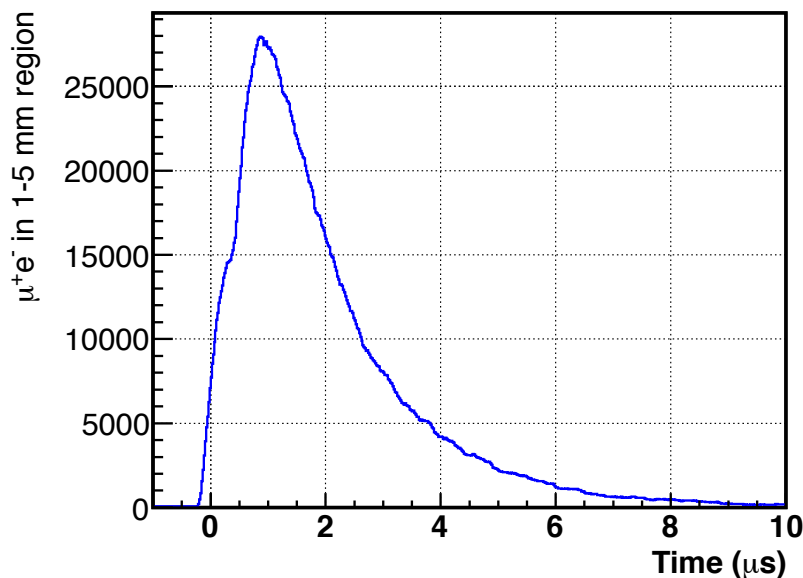
Figure 4.17: *Simulation results for the number of muonium atoms in the laser ionization region, per second, in the J-PARC experiment as a function of time after the mean time of the muon beam pulse pair. See text for more detail.*

4.2.3   Spatial distribution of muonium in vacuum and overlap with laser

From the preliminary analysis of the measurement at TRIUMF, we are quite sure that the diffusion model and the Maxwellian distribution modified with cosθ emission distribution well describes the Mu profile in the vacuum region. We can use this model to design the best irradiation condition by the laser beam and also estimate the expected number of muoniums in the corresponding region. It is possible to use a Monte-Carlo simulation as developed here for this optimization but a Mu profile can also be produced by a numerical integral method quickly for overview of the profile.

Figure 4.18 shows the calculated distribution of the muonium position in vacuum (distance from the target surface) at various timings after the muon stopping. In this calculation, the Maxwell distribution (modified with cos θ emission distribution) of the muonium motion, is convoluted with the timing distribution of muonium emission. If we assume that the muon stopping is almost homogeneous near the rear surface of the target and the muonium emission timing into vacuum is controlled by the timing of the muonium to reach the surface by diffusion, the emission timing distribution is simply proportional to inverse square root of the timing after muon stopping.

In this figure the number of the muons is normalized to all the muon emitted. This figure already takes into account the muon loss by decay with the lifetime (2.197 μs) and also the double pulsed muon beam structure at J-PARC. The timing is shown relative to the second muon pulse.
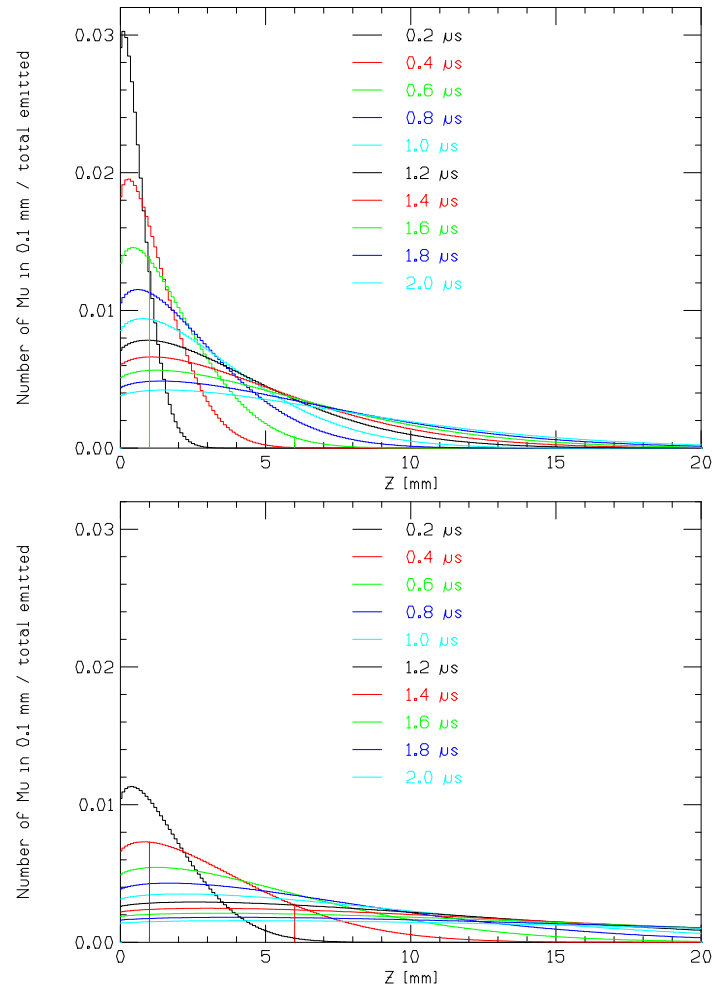
Figure 4.18: *Result of muonium profile simulation based on the diffusion model for two target temperatures (top: 293 K, bottom: 2100K). Each profile shows the muonium distribution in vacuum at every 0.2 μs after muon stopping. Horizontal axis is the distance from the target surface and the vertical axis is the fraction of the muonium in each 0.1 mm region normalized by the total number of emitted muoniums.*

We can use this figure to estimate how much of the muoniums will be covered by the laser shot of a certain spot size and at a certain timing. Let us assume we shoot the laser at a distance of at least 1 mm from the target surface and that the laser beam is spread for 5 mm in the z direction. We can see that the best laser timing will be around 0.6 μs from the second muon beam pulse (1.2 μs from the first pulse) for the room temperature target. In this condition, about 30% of all the emitted muoniums will be inside this region.

The two Lyman–α beams used in the RIKEN-RAL experiment had a beam size of 1–2 mm in the horizontal plane and about 5–8 mm in the vertical plane, thus the two beams together covered only 20 mm^2. It would be possible to increase the laser area to 5 mm $\times$ 40 mm and still have 10 times more luminosity, because the total power of the new laser is designed to be 100 times larger. With this power it will be possible to ionize most of the muonium in the irradiated region as described in the next section.

4.3 Laser System

Muonium atoms evaporated from the production target are photo-ionized by two laser lights: one at wavelength of the Mu Lyman-alpha (Ly-α) photo-excites Mu from the ground to the 2P state, and then another at wavelength of 366 nm (or shorter) ionizes the excited Mu. Although a laser system for the Ly-α generation is not simple (as can be seen below), it is considered that this ionization scheme gives better overall efficiency compared with the other ones such as photo-ionization via the 1S-2S excitation.

4.3.1 Laser Ionization of Muonium

4.3.1.1 1s to 2p excitation

Three transitions rates are involved in the laser excitation from the 1s to 2p state. One is the spontaneous photon emission decay rate from 2p to 1s and the other two are the induced photon emission and the induced photon absorption rates. These rates for muonium atom can be taken from the theoretical rates for atomic hydrogen since the atomic size is quite similar.

The 2p to 1s spontaneous emission rate is written as $A(2p \rightarrow 1s) = (2^{10}/3^{11})(h\omega)^3/(hc)^2 \alpha a_0^2 = 0.627$/ns. The induced transition rate from 2p to 1s is $w(\nu)B(2p \rightarrow 1s)$, where w is the photon spectra intensity and $B(2p \rightarrow 1s) = (c^3/8\pi h\nu^3)A(2p \rightarrow 1s) = A/(9.3 \text{x} 10^{-12} \text{Js/m}^3)$. For a typical band width $\Delta\nu = 80$ GHz (enough to cover Doppler broadening of the absorption line due to thermal motion of muonium), laser irradiation area 2 cm^2 and the laser pulse width of 1 ns, 44 μJ/pulse gives wB comparable to A. The induced transition from 1s to 2p is three times larger than the above rate considering the degenerate factor.
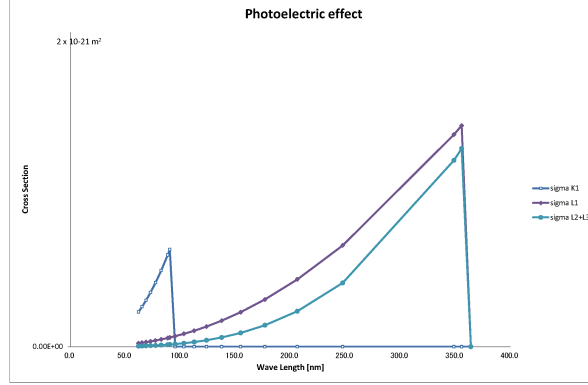
Figure 4.19: *Calculated ionization cross section by photons.*

4.3.1.2   2p to unbound

This ionization process is well known as the photoelectric effect. The cross sections for the photoelectric process from 1s, 2s and 2p states can be found in the textbook of Bethe-Salpeter for example. The photoelectric cross section for 1s electron is:

$\sigma(1s) = (2^9\pi^2/3)\alpha a_0^2(I_1/\hbar\omega)^4 exp(-4\nu_1\, arccot(\nu_1))/[1 - \exp(-2\pi\nu_1)]$ where $\hbar\omega$ is the photon energy, I_1 is the 1s ionization energy and $\nu_1 = \sqrt{(I_1/(\hbar\omega - I_1))}$.
Similarly, $\sigma(2s) = (2^{14}\pi^2/3)\alpha a_0^2(I_2/\hbar\omega)^4(1 + 3I_2/\hbar\omega)exp(-4\nu_2\, arccot(\nu_2/2))/[1 - \exp(-2\pi\nu_2)]$
and $\sigma(2p) = (2^{14}\pi^2/3^2)\alpha a_0^2(I_2/\hbar\omega)^5(3 + 8I_2/\hbar\omega)exp(-4\nu_2\, arccot(\nu_2/2))/[1 - \exp(-2\pi\nu_2)]$
where I_2 is 2s or 2p ionization energy and $\nu_2 = 2\sqrt{(I_2/(\hbar\omega - I_2))}$

Figure 4.19 shows the photoelectric cross section as a function of the wave length. Largest efficiency is obtained for the photon energy just above the threshold. The cross section at the 2p to unbound threshold is $\sigma(2p) = 1.26$ x 10^{-21} /m^2.

Let's assume the following parameters for the 355nm laser (power per pulse 300 mJ, pulse length 1 ns, spot size 2 cm^2). Then the laser intensity is 1.5 x 10^{12} W/m^2 and the number of 3.6 eV photons is 2.7 x 10^{30} photons/m^{2}s. Combining with the above cross section $\sigma(2p)$, $\lambda(2p\rightarrow$unbound$) = 3.0$ /ns. This is larger than 2p→1s decay rate (0.627 /ns), so 300 mJ would be enough to ionize muonium from 2p before it decays back to 1s state.

4.3.1.3   Ionizing efficiency

The rate equations for the muonium state population under laser radiation are

$dP_{1s}(t)/dt = -3\lambda P_{1s}(t) + (\lambda_{\mathrm{nat}} + \lambda)P_{2p}(t)$

Muon g-2/EDM Experiment, Conceptual Design Report, Revised, December 12, 2011, 11:40 A.M.
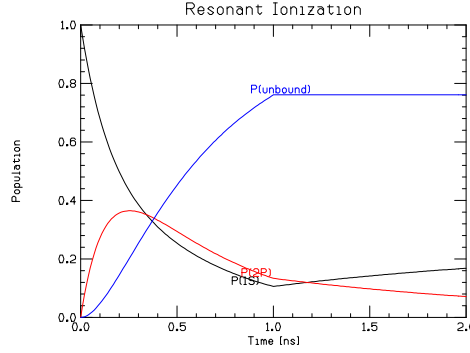
Figure 4.20: *Calculated time development of the muonium state populations under laser irradiations at J-PARC with new Lyman-α laser.*

$dP_{2p}(t)/dt = 3\lambda P_{1s}(t) - (\lambda_{\mathrm{nat}} + \lambda + \lambda_u)P_{2p}(t)$

$P_u(t) = 1 - P_{1s}(t) - P_{2p}(t)$

where λ_{nat} is the spontaneous 2p decay rate, λ is the 2p to 1s induced transition rate, λ_u is the rate for 2p→unbound, and P_{1s}, P_2, P_u are the populations of 1s, 2p and unbound states.

The time development of the muonium state populations for a typical laser intensity is shown in Fig. 4.20. The 2p state population first increases with 122 nm laser, then the 355 nm laser ionize the muonium from 2p state. Here we assumed both 122 nm and 355 nm lasers have the pulse width of 1 ns and are irradiated at the same timing. It is also possible to delay the 355 nm laser timing by, for example, 0.3 ns relative to the 122 nm timing so we can wait until the 2p population is fed enough. However, the relative gain with delay was only about 4 %, so the delay was set to zero in the following calculations for simplicity.

Table 4.2 shows the muonium ionization efficiency for various laser intensities. Here the laser beam size is assumed to be 2 cm^2. The 100 μJ/pulse and 1 ns Lyman-α laser which we are developing is intense enough to ionize about 76 % of the muonium in the laser irradiated region. Since the ionization efficiency is nearly saturating with this power, the laser power may be more efficiently used by dividing the laser beam to cover multiple targets, for example.

4.3.2 New laser system

Generation of the Ly-α laser is not simple because there are no non-linear frequency conversion crystals in wavelength shorter than 200 nm. Therefore historically researchers applied non-linear frequency conversion processes in gaseous atoms, such as Kr, Xe, and Hg, to generate coherent vacuum UV (VUV) light. Therefore we use one of the most commonly applied technique, the two-photon resonant absorption four-wave difference frequency mixing in a Kr atom. This method requires two pump laser lights (Fig. 4.21): firstly 212.55 nm (ω_1) excites Kr atom from 4p^6 to 4p^{5}5p state by two-photon absorption, then secondly 820 nm light (ω_2, tunable 815 $\sim$ 850 nm) generates the Ly-α light by the

Table 4.2: *Ionizing efficiencies of muonium for various combinations of 122 nm Lyman-α (top, in μJ) and 355 nm ionizing (left, in mJ) laser power*

	20	40	60	80	100	120
50	0.110	0.169	0204	0.226	0.241	0.252
100	0.192	0.294	0.354	0.391	0.415	0.433
150	0.254	0.388	0.464	0.512	0.543	0.564
200	0.301	0.459	0.548	0.601	0.636	0.660
250	0.339	0.514	0.611	0.669	0.706	0.732
300	0368	0.56	0.660	0.721	0.759	0.785
350	0.392	0.590	0.698	0.761	0.800	0.825
400	0.411	0.617	0.728	0.792	0.831	0.856

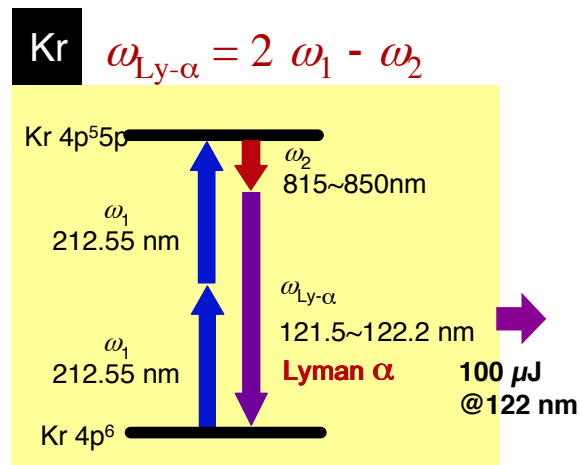**Figure 4.21:** *Schematic diagram of four-wave mixing process in Kr*

difference frequency generation. A key issue is how to increase the Ly-α power to be sufficient for the ultra-cold muon production i.e. the conversion efficiency of VUV generation in gaseous medium is generally very low. So far the conversion efficiencies of this method have been $\sim 10^{-4}$ to 10^{-5}, resulting in the output power of 10 μJ/pulse at most, even though the Ly-α light is such an important wavelength. Here we set our goal to 100 μJ, 1 ns, 80 GHz linewidth, and $25 \sim 50$ Hz repetition rate pulsed Ly-α output by having high-intensity pump lasers (especially for ω_1), and the conversion efficiency of 10^{-3} by performing experiments and simulations to find the best conditions for the non-linear frequency conversion process.

4.3.2.1 ω_1 and ω_2 laser

The Ly-α power is proportional to

$$N^2\chi^{(3)}(2\omega_1 - \omega_2)^2 P_1^2 P_2 F' \tag{4.2}$$

where N is the number density of Kr atom, $\chi^{(3)}$ is the third-order susceptibility of Kr atom for $2\omega_1$-ω_2 process, P_1 and P_2 are the laser power for ω_1 and ω_2 respectively, and F' is the phase-matching factor. To obtain the high-power Ly-α, it is necessary to not only increase the power of ω_1 and ω_2, but also increase the gas pressure (N) and optimize the phase-matching factor. To achieve the above-mentioned goals, it is estimated that both P_1 and P_2 need to be approximately 100 mJ/pulse provided that we can achieve the 10^{-3} conversion efficiency. A light source of 100 mJ/pulse of 212.55 nm seems already challenging, but it is technically feasible by applying the following state-of-the-art laser schemes:

ω_1 laser system

fundamental for the ω_1 laser To generate high-intensity 212.55 nm laser light we use the fifth-order harmonic of 1062.75 nm (fundamental), which is an output of a distributed feedback laser diode (DFB-LD) that enables oscillation at the single longitudinal mode with narrow linewidth ($\sim$2 GHz). The fine tuning on the central wavelength of the DFB-LD by changing the LD temperature is very important in this application because the two-photon resonant absorption in Kr has a well-defined excitation energy. Since the LD has relatively short optical cavity length, it has less jitter. The temporal shape of the input electric current directly appears as the laser output. Therefore it is possible to change the laser repetition rate and pulse duration just by controlling the input electric circuit. To obtain sufficient power of ω_1 laser after the nonlinear frequency conversion, it is necessary to have enough power of the fundamental, which we estimate to be approximately 1 J/pulse considering conversion efficiency of the nonlinear crystal. To amplify the seed from the DFB-LD we need multiple amplification stages as shown on Fig. 4.22.

Fiber amplifier The seed output from the DFB-LD is first amplified by the fiber amplifier to 10 μJ/pulse. For the non-linear wavelength conversion it is important to keep the linear polarization
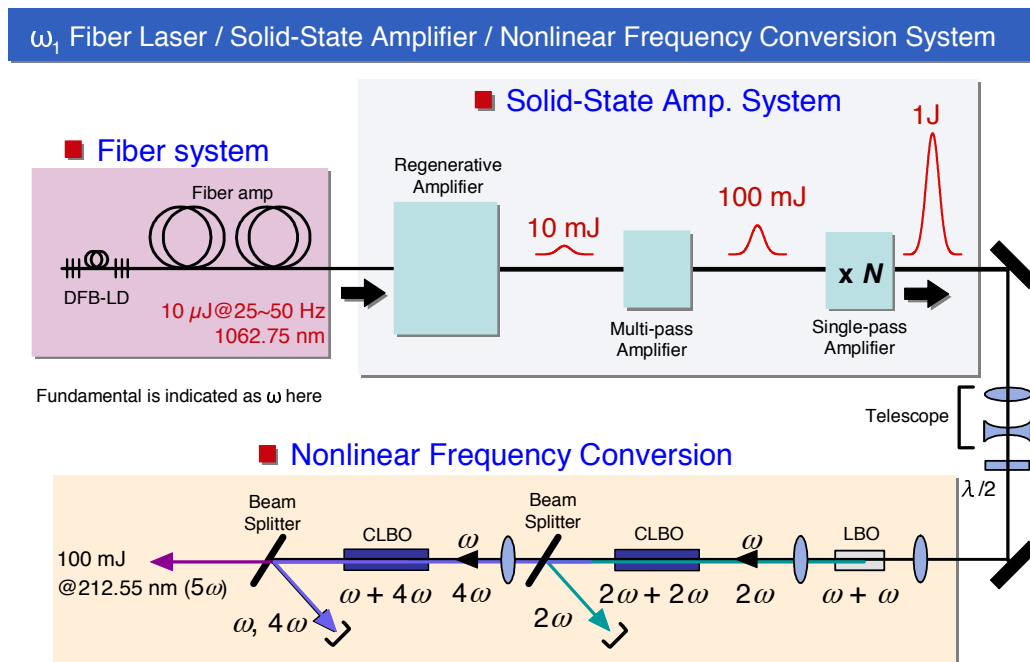
Figure 4.22: *laser system for generating ω_1, 212.55 nm*

Figure 4.23: *DFB-LD + Fiber Amplifier system for 1062.75 nm*

and avoid spectral broadening due to the self-phase modulation in the fiber medium. Currently we have completed the DFB-LD and the fiber amplifier with the expected power output (10 μJ /pulse) as shown on Fig. 4.23.

Regenerative amplifier The second amplification stage is a regenerative amplifier with a Nd:YGAG crystal as a gain medium, which resembles the traditional Nd:YAG crystal but has Ga substituting part of the Al atoms, so that the central gain spectrum is tuned to the fundamental wavelength (1062.75 nm). We are currently working on this part to characterize the gain profile in detail. If the amplification turns out to be not sufficient with the regenerative amplifier only, we will consider an additional multi-pass amplifier.

Nd:GdVO$_4$ single pass amplifier Finally the pulse train is amplified by a series of single pass amplifiers with Nd:GdVO$_4$ crystals as the gain medium which we have recently developed [24]. Its gain spectrum is peaked at 1062.9 nm with 2 nm bandwidth, so it can amplify the fundamental very close to the center of its gain spectrum. If the amplification turns out to be still not sufficient we will add one more stage for further amplification.

Non-linear wavelength conversion The amplified fundamental pulse (1 J, 1 ns pulse duration) is now converted to ω_1 by the nonlinear frequency conversion system as show in Fig. 4.22. We utilize an LBO crystal for the second harmonic generation, and CLBO crystals for the forth- and fifth-order harmonic generation, with overall 10% conversion efficiency (thus results in 100 mJ/pulse of 212.55 nm). An important point here is the use of CLBO crystals, which gives high conversion efficiency, although a low damage threshold has prevented it from being practical. We have studied the characteristics of the crystal in detail and found an approach for long-term stable operation.

ω_2 **laser system** For the ω_2 laser we use the DFB-LD as an oscillator in the similar way as the ω_1 laser system, and then amplify the output pulse by the optical parametric amplification (OPA) with an LBO crystal. In this case the pump laser for OPA is a left-over green (531 nm) after the forth harmonic generation in the ω_1 process (see section 4.3.2.1). Our goal here is 100 mJ, 1ns pulse duration of 815 $\sim$ 850 nm. This output level should not be so difficult because the technology is more established in this wavelength region.

4.3.2.2 Lyman-α laser light generation using Kr gas

ω_1 and ω_2 lasers are collimated and incident on a gas cell for the Ly-α generation. The gas cell contains Kr/Ar gas mixture with a certain ratio for optimized conversion efficiency. Here Ar is necessary to satisfy the phase-matching condition, $\Delta k = 0$, where k indicates a wave vector and $\Delta k = k_{Ly-\alpha}$ - $(2k_{\omega_1} + k_{\omega_2})$. Since Kr has negative dispersion at the wavelength of Ly-α, it is necessary to have Ar to give a positive dispersion so that the system satisfies $\Delta k = 0$ and to maximize the F' factor in the equation above. Unfortunately there were no works so far that systematically studied the conversion

efficiency as a function of the relevant parameters such as ratio of the partial gas pressure, absolute pressure, beam intensity, and so on. We need to start by measuring fundamental optical parameters such as the third-order susceptibility of Kr at Ly-α wavelength, therefore it requires a serious R&D to achieve the 10^{-3} conversion efficiency.

So far the simulation revealed importance of the dielectric breakdown of the gas i.e. the strong electric field due to the focused pump beams causes the breakdown of gas molecules, resulting in breaking the phase-matching condition[25]. The dielectric breakdown becomes more serious when the beam is tightly focused in high-pressure gas, although focusing and high-pressure gas drastically enhance the conversion efficiency as can be seen in the equation above. To avoid the gas breakdown we will need a long, loosely focused beam in a ultra-pure gas mixture. According to the simulation, 100 μJ/pulse of Ly-α is achievable with the assumed pump energies.

As for the second UV light (< 366 nm) for ionizing the excited Mu, we will use the third harmonic (355 nm) of Nd:YAG laser for now because it is easy to create high-power laser pulse. In future, however, we will make 366 nm since the absorption cross section of 2P-state Mu is several times higher for 366 nm than 355 nm.

4.4   Spin Polarization

4.4.1   Muon spin in muonium

Muonium is a bound state of a muon and an electron. Its hyperfine splitting between the spin singlet state and the triplet state has been measured as $\nu_{\mathrm{HFS}}(= 2\pi\omega_{\mathrm{HFS}}) = 4.463$ GHz [26].

Suppose the incident surface muon is 100% polarized, and the electron it captures is unpolarized, then half of the muonium ensemble is formed in the state where the spin of the electron is parallel to that of the muon, denoted as $|++\rangle$, and another half of the ensemble is in the state with spin anti-parallel, $|+-\rangle$. Since the $|++\rangle$ state is a spin-triplet energy eigenstate, the total spin of muonium and the muon spin are stationary. Therefore, the muon polarization in the $|++\rangle$ state is kept. On the other hand, the $|+-\rangle$ state is not an energy-eigenstate, but a mixture of a spin singlet and a triplet states. The $|+-\rangle$ state oscillates to the $|-+\rangle$ state in a time scale of $1/(4.463$ GHz$) = 0.224$ ns [27]. The average thermal velocity of the muonium at room temperature is 8 mm/μs. It takes at least a hundred ns for muonium to diffuse/drift to the region of the laser beam (about 1–2 mm from the target surface). Therefore, by the time muonium is ionized, the $|+-\rangle$ state and the $|-+\rangle$ state are equally populated, resulting in zero polarization of the muon. Since the initial ensembles of the $|++\rangle$ and the $|+-\rangle$ states are equal, the polarization of the ultra-cold muon is $(100\% + 0\%)/2 = 50\%$.

4.4.2   Recovery of spin polarization

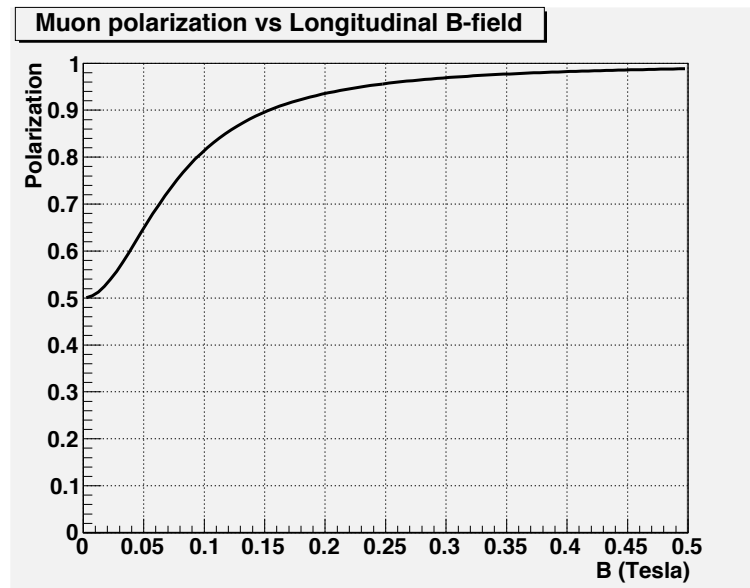Two possibilities of recovery of muon polarization are being considered.

Figure 4.24: *Muon polarization in muonium as a function of the longitudinal magnetic field*

Longitudinal magnetic field If the magnetic field is applied parallel to the initial muon polarization, total muonium spin is no longer a good quantum number. In the limit of the strong magnetic field, the spin component along the magnetic field becomes a good quantum number. Thus, the muon spin in the $|+-\rangle$ state will also be "locked". The dependence of the muon polarization P_μ with the magnetic field strength B can be written as [27]

$$P_\mu = \frac{1 + 2x^2}{2(1 + x^2)}, \tag{4.3}$$

with

$$x = \frac{(g_e\mu_e + g_\mu\mu_\mu)}{2\hbar\omega_{\mathrm{HFS}}}B = 13[\mathrm{T}^{-1}]B. \tag{4.4}$$

Figure 4.24 shows P_μ as a function of B in the region $0 < B < 0.5$ T. The muon polarization increases from 50% to 96% with a longitudinal magnetic field of 0.3 T in the region of the muonium target and laser ionization.

The primary challenge of this method is the muon beam transport after the ionization under the circumstance of the magnetic field. The muon transport in the initial acceleration must be carefully designed so that transverse kick to the muons from the fringing field of the spin holding magnet is sufficiently small to preserve the transverse dispersion. Preliminary estimation of the disturbance is given as follows. We assume a cylindrically symmetric holding field along the axis of the beam extraction z, which seems most of the case. Most reasonable choice will be to reduce the longitudinal field as soon as possible so it would not affect the following optics. The reducing field cause the field line to expand so a transverse magnetic field component will appear naturally. This component will give transverse kick to the muon momentum. If the field is low enough and we assume the muon trajectory is reasonably straight, the integral of the kick can be written $P_x = e \int_0^{z1} v_z B_y(0, a, z) dt = e \int_a^{z1} B_y(0, a, z) dz$. For a

cylindrical case, from div B = 0 condition, $2\pi a \int_a^{z1} B_y(0, a, z)dz = \int B_z(x, y, z1)dS - \int B_z(x, y, 0)dS$ where dS is the surface integration for the area $x^2 + y^2 < a^2$. Assuming the magnetic field is designed to disappear to almost zero at $z1$ and the field value does not change much in region S, the kick can be simply written $P_x = e(a/2)B_z(0, 0, 0)$. The most severe criteria would be to ask this component to be smaller than the thermal value of the transverse component. The corresponding field is estimated to be 3 G. Preliminary judgment is that 3 kG is too large to meet this criteria.

One possible solution avoiding this problem would be to use a pulsed magnetic field so that the 3 kG holding field is switched off just after the ionization, thus minimizing its effect on the extraction optics. We plan to study such feasibility and the beam transport configuration to increase the muon polarization.

Narrow band laser The singlet state and triplet states are selectively ionized if the laser bandwidth is narrower than the hyperfine splitting ν_{HFS}=4.463 GHz. The narrow band laser can be used to sweep out the depolarized muons in the unfavorable singlet state in advance to the normal ionization scheme. This way, the polarization increases from P =50% to (100%+0%)/1.5 = 66%, and we lose 1/4th of muons by sweep out. We gain the figure of merit ($\propto NP^2$) by a factor of 1.33.

4.5 New Measurement of Laser Ionization at RIKEN-RAL

4.5.1 Laser ionization test at RIKEN-RAL

New measurements are planned at RIKEN-RAL to establish our scheme so far explained. We plan to improve the previous measurement at RIKEN-RAL in several ways so we establish the production method of ultra-cold muons and are sure about the efficiency when we install a new ultra-cold muon source J-PARC. The plan is described below. We started the new measurement in April 2011, and had planned to have more data in 2011. However, due to a serious delay because of the failure of the target heater power supply, most of the measurement had to be postponed to early 2012.

4.5.1.1 Upgrade of the RIKEN-RAL Ultra-Cold Muon Beamline

As described in the first section of this chapter, we have been using the ultra-cold muon beam line at RIKEN-RAL for almost 10 years. Since several small inconveniences have built up after the step by step development in long years, we have carried out a major upgrade of the ultra-cold beamline to clear these problems. The refurbishment work consisted of (i) moving the electric rack outside the experimental port, so we have more working space around the beamline, (ii) replacing the beamline power supplies so that they are more stable and 20 keV acceleration instead of 9 keV is possible, and (iii) installing a LabView based beamline control system so the operation and adjustment of the ultra-cold beam is easier. The upgrading work of the beamline was completed and the commissioning with the muon beam was carried out in April 2011.

4.5.1.2 Measurement of the incoming muon beam intensity

It is important to know the number of incoming muons in order to exactly know the efficiency of the conversion to ultra-cold muons. Although we had this number in the previous publications, we tried to improve the number to an accuracy better than 10%. A beam profile monitor made of scintillator hodoscopes was used for this purpose. It is not straightforward to count the number of muons in one bunch of the pulsed beam, because lots of muons pass a counter at the same time and thus one by one muon counting is not possible. So we used a pulse height integration method where the signal by energy deposit by a muon pulse is considered to be proportional to the number of passing muons. The relation between the pulse height and the deposit energy by a single muon was separately measured by deliberately decreasing the muon beam intensity. The number of muons in the area of 4 cm x 4 cm was measured to be 1.5×10^6 per double pulse.

4.5.1.3 Upgrade of the present RIKEN-RAL laser system

We are upgrading the existing RIKEN-RAL laser system also so that we will have better ionization efficiency, which results in more ultra-cold muons. The key improvement is the replacement of the old OPO system with an OPG/OPA system. The wave length is the key of the four photon resonance in the krypton gas. The new system will stabilize the frequency and the spatial mode. So we have less mode hop or hot spot problem which has limited increasing the laser power because of the possible damaging to the optical component. The replacement work was completed and we are now gradually increasing the laser intensity. We expect we can eventually achieve ten times more Lyman-α laser power with this upgrade.

4.5.1.4 Measurement of the absolute Lyman-alpha laser power

It is essential that the laser power is well known so that we can use the measurement of the ultra-cold muon yield to extract the ionization efficiency. The power was so far measured only by NO ionization signal. The advantage of the NO ionization measurement is that it is only sensitive to the Lyman-α and is much less affected by other laser lights [28]. However, it is difficult to estimate the absolute power scale with this method because of saturation effect of the NO ionization and dependence of the signal strength to the laser position etc.

In order to make an absolute power measurement of the Lyman-α, we have installed a calibrated photo diode in the laser path downstream of the target region. It is important that the 212 nm and 820 nm laser lights, which are the source of the Lyman-α generation (and far more intense than Lyman-α itself), should stay away from the photo diode. Figure 4.25 shows the schematic layout of the detection system. The 212 nm and 820 nm lights are bent by a cylindrical lens that is placed just after the krypton cell. Lyman-α light will be separated from these lights by 10 mm at the photo diode position due to the difference in the deflection angle. The deflected 212 nm and 820 nm lights will then enter a prism and will be swept away. We installed a filter (80% transmission for Lyman-α and 1/100 for others) and a shield to cover the photo diode so even the scattered lights will not reach the

photo diode. By combining the laser power measurement and the previously measured Mu emission yield, the ionization efficiency versus laser power will be studied.
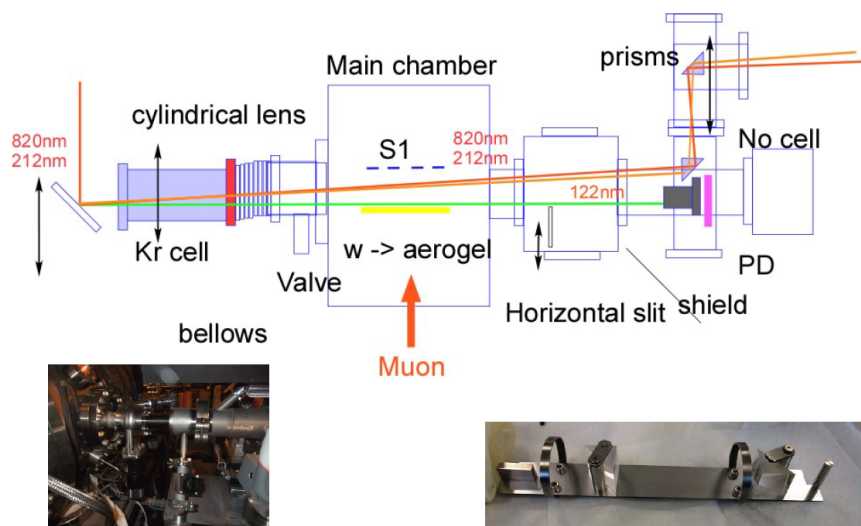

Figure 4.25: *The schematic figure of the absolute Lyman-α intensity measurement with a photo diode (PD). The photos are for the device to move the laser position and for the prisms deflecting unwanted lights for laser power measurement.*

4.5.1.5   Study of linear increase or saturation of the muonium ionization with laser density

So far we observed increase of the ultra-cold muon yield linearly with the laser power as in Fig. 4.5. As is shown from the calculation of the laser ionization process, with the new high power Lyman-α laser, we will soon saturate the ionization efficiency. Such an effect could be observed even with the upgraded laser power based on the present laser system. For this study, the laser power and the laser spot size will be carefully measured because the laser luminosity (power divided by the area) is relevant to the saturation.

From these studies we expect to obtain information about the ionization efficiency versus laser power, and this will optimize the use of the laser power. If we are to see a clear saturation, the extra laser power may better be used by expanding the laser spot size to cover more muoniums

4.5.1.6   Mu profile measurement

We also installed a device to sweep the laser position near the target surface. By measuring the ultra-cold muon yield as a function of the laser distance from the target surface and also the laser timing

Muon g-2/EDM Experiment, Conceptual Design Report, Revised, December 12, 2011, 11:40 A.M.

Table 4.3: *Efficiencies from surface to ultra-cold muon*

	Silica Powder[4]	Silica Powder[11]	Silica Aerogel (S1249)	Hot W[3]
Momentum bite (RMS)	3%(FWHM) $1.3\%/5\% = 0.26$	7.5%(FWHM?) $3.3\%/5\% = 0.66$	2%(RMS) $2\%/5\% = 0.4$	5%(RMS) $5\%/5\% = 1.$
Struggling	$(20\text{MeV}/28\text{MeV})^{3.5}$ $= 0.31$	$(20\text{MeV}/28\text{MeV})^{3.5}$ $= 0.31$	$(23\text{MeV}/28\text{MeV})^{3.5}$ $= 0.50$	$(23.2\text{MeV}/28\text{MeV})^{3.5}$ $= 0.52$
Half-stop	0.5	0.5	0.5	0.5
Mu formation	0.6	0.6	0.6	-
(total emission)/ (Mu in target)	0.19	0.33	0.016	0.04
(Mu in laser region) /(total emission)	0.30	0.30	0.30	0.22
Ionization efficiency	0.76	0.76	0.76	0.54
Product of efficiencies	0.1E-2	0.46E-2	0.02E-2	0.12E-2
Expected Ultra-Cold Muon Yield (/s)	0.1E6	0.46E6	0.02E6	0.12E6

after the muon stop we can measure the Mu profile (position and timing) in the vacuum region. This will enable us to select the optimum laser irradiation condition.

This method gives us information similar to the imaging measurement done at TRIUMF. The advantage of this method is that the apparatus is a nearly permanent setup (though depending on laser availability) and could be used for an urgent quick study such as a new sample or various sample conditions such as temperature. Also this will readily give us information on the hot tungsten target, for which we do not have profile data from TRIUMF measurement. A possible disadvantage is some uncertainty about the change of the laser beam profile and the laser power when the laser position is moved. We will make a systematic study of the laser power versus position to minimize this effect.

The device was already installed and we plan a measurement in late 2011 or early 2012.

4.6 Ultra-Cold Muon Production Yields

4.6.1 Expected yield of ultra-cold muons: single target case

We have summarized in Table 4.3 various efficiencies in the production of ultra-cold muons using results on several targets reported in references and the new result at TRIUMF. The expected ultra-cold muon yield for the J-PARC H-line surface muon beam (intensity of 1 x 10^8 /s and 28 $\pm$ 1.8 MeV/c momentum bite) is shown in the bottom line.

The stopping density near the surface depends on the surface muon beamline parameters such as the central momentum and the momentum bite. The efficiency was normalized to that of the J-PARC muon beam line. The stopping efficiency is inversely proportional to the momentum bite and to the

inverse power of 3.5 of the central momentum. The beam parameters for each condition was taken from the publications. The designed value for the H-line (surface muon momentum of 28 MeV/c and momentum bite 5% RMS) was used to calculate the scaling factor.

The values for "Mu in laser region" and the "ionization efficiency" was taken from the model simulation which we have described in this section in detail.

Among the several target options, silica powder gives the best yield. However, we are yet reluctant to use this as the muonium source because of the handling difficulties.

We get only one eighth of the required yield with hot tungsten. This is partly because of the larger Doppler broadening and larger spread of the muonium in vacuum (and thus requires higher laser power).

We get even less for the silica aerogel, for which we just finished the measurement at TRIUMF. We are not sure yet why we only got such a low yield for the silica aerogel, while the previous report [18] for some silica aerogel samples indicates only a factor of 4 reduction compared with the silica powders. Concerning the use of room temperature target such as silica aerogel, porous silica and porous aluminum, we have not yet observed enough muonium emission in vacuum. We would need more investigation on the target candidates. Artificial mesoscopic channels to the surface in the aerogel, for example, would increase the overall diffusion rate. We will keep studying these materials. Even though, this cannot be the primary candidates of the $g-2$ muon source at the moment.

Our present choice is hot tungsten. The estimated ultra-cold muon yield still lacks a factor of 8 to our goal, so we are studying method to fill this gap.

4.6.2   Multiplication schemes

One of the key would be the use of multiple target surfaces. So far we have considered only one target layer as a source of ultra-cold muons. Actually most of the primary muons are lost just because they stop deep inside the target or pass through the target without stopping. If we use multiple target layers in the passage of the muon beam, the number of muoniums will linearly increases with the number of surfaces. If we can simply increase the number of the laser beam to cover all the target surfaces, the total ultra-cold muon yield is just proportional to the number of target layers. Even if we need to limit the total laser power, we can still increase the number of by dividing the laser power and distributing for each surface layer, since the laser nearly saturating the transition would be more efficiently used by covering larger region sacrificing the luminosity.

How to combine the ultra-cold muons from multiple targets and accelerate as an ultra-cold muon beam needs consideration. We could stack them into a chain of pulses so that each pulse arrive at the same phase relative to the rf and is accelerated together. Though we need more detailed design, real gain is expected in this scheme.

4.7   Summary

The proposed $g-2$ experiment utilizes the ultra-cold muon source which can be produced by the laser ionization of the muonium thermally emitted from a target surface. The laser ionization technique has been developed by KEK and RIKEN, and continuously improved at the RIKEN-RAL muon facility. By increasing the ionizing laser power by two orders of magnitude, we expect to significantly increase the muonium ionization efficiency and to cover more muoniums in the expanded laser region. Optimization is in progress about the laser coverage area and laser luminosity as well as the number of laser beams. For these optimization, test measurement as well as predictions based on theoretical calculations are essential. We have carried out the profile measurement of muoniums emitted in vacuum with good accuracy at TRIUMF. The comparison of the result with the simulations made us convince that we can use the combination of the diffusion limited emission and the Maxwellian velocity distribution as a base for understanding the muonium profile in vacuum. We have started a new measurement of the ultra-cold muon yield at RIKEN-RAL using an increased laser power to study where the saturation effect will start to be seen and whether it is consistent with theoretical predictions.

A realistic estimate of the ultra-cold muon yield has been made based on previous measurement as well as new data and the new beamline design parameters of the J-PARC H-line. The yield for the primary candidate, hot tungsten, seems not sufficient by itself. It is to be noted that the number of muonium emission is limited by the number of muon stopping near surface and not by the total number of incoming muons. Considering this fact, a natural solution would be to place several thin targets in the beam to increase the number of surfaces and to extract ultra-cold muons from each vacuum region near the surface.

References for Chapter 4

[1] K. Nagamine, et al., Phys. Rev. Lett., 74, 4811 (1995)

[2] P. Bakule, et al., Nucl. Instrum. Meth. B., 266, 335 (2008)

[3] A.P. Mills, Jr et al., Generation of Thermal Muonium in Vacuum, Phys. Rev. Lett. 56 (1986) 1463.

[4] G.A. Beer et al., Emission of muonium into vacuum from a silica-powder layer, Phys. RevLett. 57 (1986) 671.

[5] E. Morenzoni et al., Generation of very slow polarized positive muons, Phys. Rev. Lett. 72, 2793 (1994).

[6] P. Bakule, Y. Matsuda, Y. Miyake, P. Strasser, K. Shimomura, S. Makimura, K. Nagamine, Slow muon experiment by laser resonant ionization method at RIKEN-RAL muon facility, Spectrochim. Acta B 58 (2003) 1019.

[7] M. Senba, Charge exchange collisions in the presence of competing processes: an integral equation approach, J.Phys.B.At.Mol.Opt.Phys. 22 (1989) 2027.

[8] J.H. Brewer et al., Positive Muons and Muonium in Matter, in Muon Physics", Vol. III, eds. Vernon W. Hughes and C.S. Wu, Academic Press, New York (1975).

[9] G.M. Marshall et al., Production of thermal muonium in the vacuum between the grains of fine silica powders, Phys. Lett. 65A (1978) 351.

[10] R.F. Kiefl et al., Muonium and positronium production in oxide powders, Hyp. Int. 6 (1979) 1857.

[11] K.A. Woodle et al., Measurement of the polarization of thermal muonium in vacuum, Z. PhysD 9 (1988) 59.

[12] A.C. Janissen et al., Muonium production from
ne silica powder, Phys. Rev. A 42 (1990) 161.

[13] G.M. Marshall et al., A search for muonium to antimuonium conversion, Phys. Rev. D25 (1982) 1174.

[14] T.M. Huber et al., Search for mixing of muonium μ^+e^-) and anti-muonium ($^m u^-e^+$), PhysRev. D41 (1990) 2709.

[15] S. Chu et al., Laser excitation of the muonium 1S-2S transition, Phys. Rev. Lett. 60 (1988) 101

[16] V. Meyer et al., Measurement of the 1S-2S energy interval in muonium, Phys. Rev. Lett. 84 (2000) 1136.

[17] L. Willman et al., New bounds from a search for muonium to antimuonium conversion, Phys. Rev. Lett. 82 (1999) 49.

[18] W. Schwarz, et al., Journal of non-crystalline solids 145 (1992) 244.

[19] R. S. Henderson et al., Nucl. Instrum. Meth. A, 548 (2005) 306.

[20] http://geant4.cern.ch

[21] http://www.srim.org

[22] A. Einstein, Ann. Physik 17 (1905) 549.

[23] S. Chandrasekhar, Rev. Mod. Phys. 15 (1943) 1.

[24] T. Ogawa, Y. Urata, S. Wada, K. Onodera, H. Machida, H. Sagae, M. Higuchi and K. Kodaira, Opt. Lett. 28, (1994) 2333.

[25] O. Louchev, P. Bakule, Norihito Saito, S. Wada, K. Yokoyama, K. Ishida and M. Iwasaki, Phys. Rev. A 84, 033842 (2011).

[26] W. Liu et al., Phys. Rev. Lett., 82 (1999), 711

[27] V. W. Hughes, C. S. Wu, "Muon Physics volume III", Academic press, New York (1975).

[28] J.A.R. Samson, D.L. Ederer, Vacuum ultraviolet spectroscopy, Experimental Methods in the Physical Sciences, Academic Press, London, 2000.

Muon Linac

Contents

5.1 Re-acceleration

The ultra-cold muons created in the muonium target region must be reaccelerated to around 300 MeV/c in momentum (210 MeV kinetic energy) to then be injected into the muon $g - 2$ storage ring. To suppress muon loss in the course of reacceleration, the muons should be accelerated in a sufficiently short period of time compared with the muon life time of 2.2 μs. To realize fast reacceleration, we plan to build a linac dedicated for this purpose. A linac has an overwhelming advantage over circular accelerators in shortening the reacceleration time.

Another essential requirement for the reacceleration is the suppression of transverse emittance growth. The ultra-cold muons will have an extremely small transverse momentum of around 30 keV/c with a transverse spacial extent of around 10 mm. Assuming an ideal acceleration to 300 MeV/c, the typical transverse divergence angle of muons becomes 10^{-5} rad. These are the requirements for injection into the storage ring. Therefore, the beam at injection should have essentially the same normalized transverse emittance as that of the muon source. Consequently, the transverse emittance growth in the linac should be suppressed as much as possible to meet this requirement.

In the design consideration of this linac, we separate the acceleration into some sections, namely, a bunching section including the initial acceleration, a low-β section, a middle-β section and a high-β section as shown in Fig. 5.1.
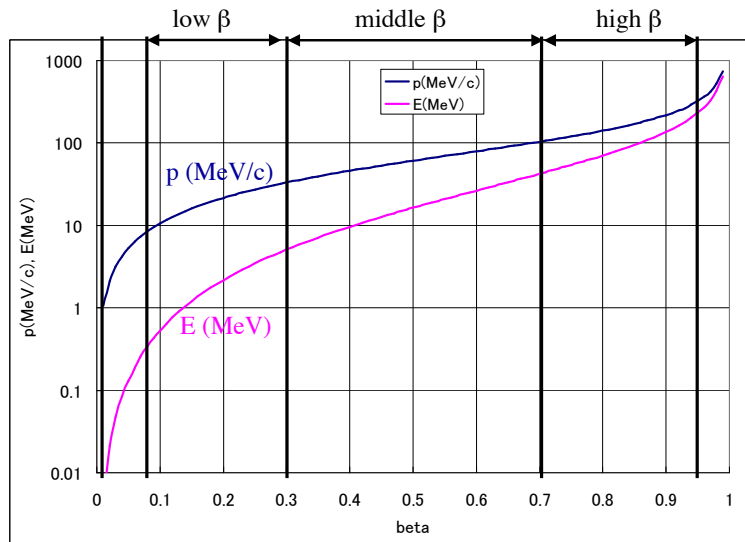
Figure 5.1: *β region for re-acceleration.*

Figure 5.2 shows the plans of the muon re-acceleration.

The bunching section is designed for the β region from 0.01 to 0.08, since the RFQ of the J-PARC proton linear accelerator was designed for this β region as one candidate of the bunching section. This

corresponds to the kinetic energy from 5.7 keV to 340 keV. Additional two bunching methods were also considered for the bunching section.

In the low-β and the middle-β section, we assume the β region from 0.08 to 0.7. This corresponds to acceleration from around 10 keV to 43 MeV or in kinetic energy. Finally the muon beam is designed to further accelerated to 210 MeV through high-β region.

In the low-β and middle-β section, the particle β increases rapidly with kinetic energy. Accordingly, it becomes very important to adopt an adequate accelerating structure matching β. The DTL and ACS based on the J-PARC proton linear accelerator is a candidate for the low-β and middle-β section. Further the Interdigital-H structure is much better candidate since the I-H structure has much higher shunt impedance.

To the contrary, the β variation in the high-β section is modest. Then, its design emphasis is naturally shifted to achieving a high accelerating gradient to realize sufficiently fast reacceleration.
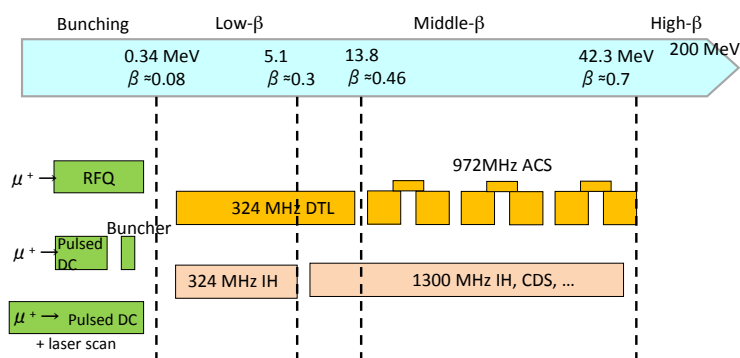
Figure 5.2: *Plans for re-acceleration.*

In the following subsections, we review the proposed design for the bunching section including the initial acceleration, the low-β section, the middle-β section and the high-β section of the linac, respectively.

5.1.1 Bunching section

The designed longitudinal muonium spread is around 5 mm and the bunch length becomes much longer than the excitation laser pulse duration due to the longitudinal muon distribution. Thus the bunching section is required to accelerate the muon beam using the RF accelerating structures. There are three following candidates for this bunching section.

- Bunching section using RFQ.

- RF Buncher.

- Laser scan method.

The bunching section using RFQ and the laser scan method were designed as following.

RFQ

The RFQ (Radio-Frequency Quadrupole linac) is most popular candidate for the bunching section in the proton linear accelerator where a continuous beam injected from an ion source is gradually bunched and RF captured for acceleration.

This bunching capability and the focusing field against the space charge effect greatly improves the transmission efficiency of a proton linac compared with a classical Cockcroft-Walton injector. Thus the RFQ is over specification for the muon accelerator since the muon charge is much less than the proton accelerator.

However there is an upgrade plan of the current RFQ for the J-PARC proton linac, and it is possible to use this retired RFQ for J-PARC proton linac. The electric field of the RFQ is linear to the mass ratio. Thus the operating electric field of the RFQ for the muon accelerator becomes approximately 1/9 of the current proton accelerator. Further the required power becomes only 4.5 kW. Figure 5.3 shows the RFQ structure for the J-PARC proton linac. This RFQ is designed to operate under 324 MHz.

Figure 5.4 shows the result of the muon tracking through the RFQ.

Meanwhile, an RFQ is known to have a substantial nonlinear component of the RF field due to unavoidable deviation of its vane shape from the ideal one [3]. The nonlinear component can be a source of transverse emittance growth, which should be strictly suppressed for our purpose. While we need further study on the effect of the nonlinear component,

Pulsed DC injector and RF Buncher

A pulsed DC injector is another candidate for an alternative option of the front-end. To adopt a pulsed DC injector, it is required to have an additional RF cavity for bunch compression. We need
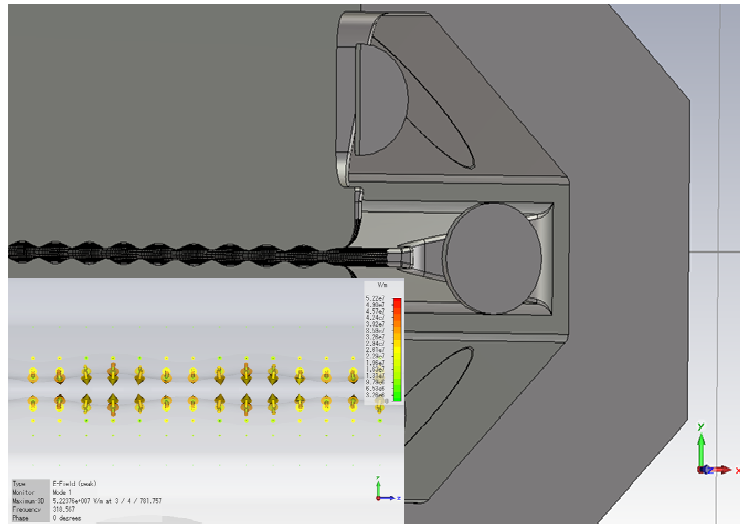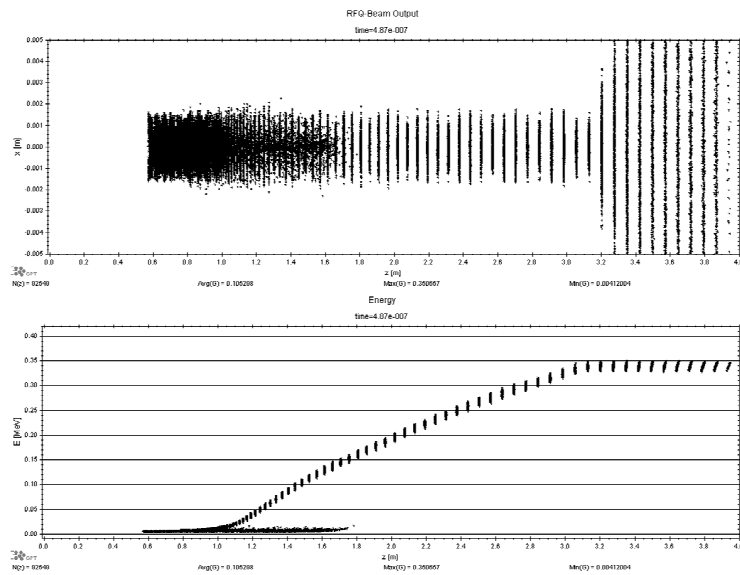
Figure 5.3: *RFQ.*

Figure 5.4: *The muon beam tracking simulation of the RFQ.*

to perform bunch compression before injecting into the low-β section using the 324 MHz RF cavities. To this end, we plan to have a buncher cavity between the pulsed DC injector and the low-β section.

In the early design of the initial muon beam excited by the laser, we assumed 100 ps of the bunch length as same as the laser pulse duration. However the bunch length becomes around 7 ns which is much longer than the laser pulse duration due to the longitudinal muonium spread. Thus a low frequency single-gap cavity of around 40 MHz is required for this purpose.

Laser scan method

The another smart bunching method was considered through the laser excitation and the initial acceleration electric field. The longitudinal muonium spread is around 5 mm and the bunch length becomes much longer than the excitation laser pulse duration due to the longitudinal muon distribution. However it is possible to bunch the muon beam if the longitudinal position of the laser excitation is moved from the upstream to the downstream corresponding to the accelerating electric field strength as shown in Fig. 5.5.
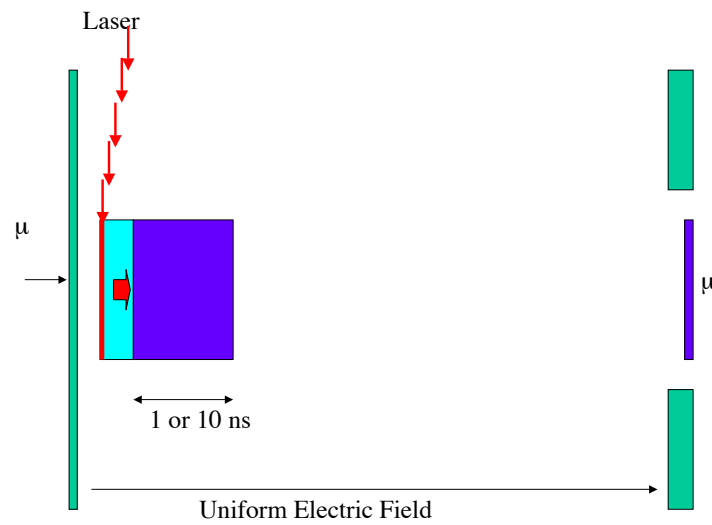
Figure 5.5: *laser scan method for the muon beam bunching.*

Figure 5.6 shows the simulation result through the initial accelerating field with the laser scan method.

As the simulation result, the 100 ps bunch length is expected.
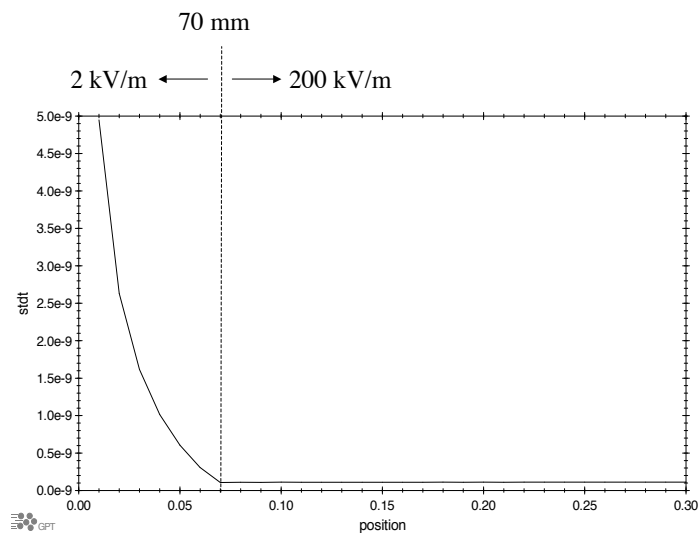
Figure 5.6: *laser scan method.*

5.1.2   Low β and middle β section

DTL and ACS

As mentioned above, the particle β changes rapidly in the low-β section as its kinetic energy increases. Then, a suitable accelerating structure should be chosen for each β range. This situation is essentially the same as in a usual proton linac. Therefore, we basically follow the conventional configuration for a proton linac in the design of the low-β section. In addition, we put the emphasis on making the best use of J-PARC experience to reduce the R&D burden. It should also be noted here that the space-charge effect is not an issue for the linac even at its lowest energy, because the number of muons assumed per bunch is as small as around 50,000. This is an important difference from a usual proton linac, where the design emphasis is often put on suppressing the space-charge effect.

We here divide the low-β section into three parts, namely, the front-end part ($\beta < 0.08$), the low-β part ($0.08 < \beta < 0.45$), and the medium-β part ($0.45 < \beta < 0.7$). For the low-β part, we plan to adopt a DTL (Drift Tube Linac) of Alvarez type with the operating frequency of 324 MHz. This operation frequency is chosen to be the same as the J-PARC DTL [1]. With this choice, we can use the existing J-PARC klystron for its RF source avoiding an R&D burden.

As for the medium-β section, we plan to adopt an ACS (Annular Coupled Structure linac) [2]. The ACS is a variation of a CCL (Coupled Cavity Linac), and adopted for the energy upgrade of the J-PARC linac. The ACS is advantageous in suppressing the dipole component of the RF field, having an annular symmetry for the coupling cell [2]. The operation frequency for the ACS is chosen to be 972 MHz with a three-fold frequency jump from DTL. This frequency is again the same as J-PARC ACS to utilize 972-MHz klystrons developed for it [1].

It should be noted that both the DTL and the ACS are standing-wave structures, and it is a conventional choice for a proton linac. This is contrasted with the high-β section where a traveling-wave structure is assumed.

In the linac design, it is important to optimize the particle β where the accelerating structure is switched from one to another. We here assume the transition β of around 0.45 between DTL and ACS. While it is a conventional choice for a proton linac, there still remains room for further optimization. We should note here that the transition β is usually determined to optimize the effective shunt impedance. In other words, we will have wider flexibility by tolerating inefficient use of RF power. As efficient power consumption is not such a pressing requirement for our purpose, the choice of the transition β will be subject to further optimization in the coming design work.

Figure 5.7 shows the proposed configuration of the low-β linac. Plan A shows the present baseline design with a Cockcroft-Walton injector, and Plan B shows an alternative plan with an RFQ as the front-end. In both plans, we can adopt the same design for DTL and ACS. In the baseline design, the low-β linac consists of a 0.34-MeV Cockcroft-Walton injector, a single-gap buncher cavity, a 13.8-MeV DTL, and a 43-MeV ACS. The DTL section consists of one DTL tank driven by a 324-MHz klystron. Meanwhile, the ACS section consists of six ACS tanks. Two neighboring ACS tanks are connected

with a bridge coupler, and driven by a 972-MHz klystron. We plan to adopt klystrons of J-PARC type both for 324 MHz and 972 MHz. The saturation power for the klystrons is 3.0 MW for both 324 MHz and 972 MHz. As for the buncher cavity, we plan to adopt a solid state amplifier as its RF source. The required RF power for the buncher cavity is estimated to be kW level or even less, and is easily fed by a solid state amplifier.

Table 5.1 and 5.2 show the main parameters for the DTL and ACS, respectively. It is readily seen in these tables that the main parameters are comparable with the J-PARC design except that the muon DTL and ACS cover a little wider β range. This difference arises because we omit the SDTL (Separate-type DTL) [4] section in the low-β linac to reduce the number of transitions. On the other hand, SDTL is adopted in J-PARC to improve the power efficiency in the β range between DTL and ACS [1].

As shown in these tables, we plan to adopt the synchronous phase of -30 degree to attain sufficient acceptance in the longitudinal phase space. With this choice of the synchronous phase, the RF field provides the muon beam with longitudinal focusing, but in turn it defocuses the beam transversely. Accordingly, it is required to provide transverse focusing to compensate the RF defocusing force. In the DTL, we plan to equip each drift tube with a quadrupole magnet as in a conventional DTL. The transverse focusing is provided with these DTQ's (Drift Tube Quadrupole magnets) with a so-called FODO lattice.

In the ACS section, a quadrupole doublet is placed at each inter-tank spacing to provide transverse focusing. An additional solenoid magnet is also assumed before the DTL injection to match the beam size by focusing the beam from the pulsed DC injector.

For this baseline design, proper beam transport through the low-β section is confirmed with the Trace3D code [5] as shown in Fig. 5.8. In this figure, the calculation is performed from the exit of the pulsed DC injector to the exit of ACS. We assume a 2.4-m long matching section between the injector and DTL, and a solenoid magnet and a buncher cavity are assumed there for transverse focusing and bunch compression, respectively. The Trace3D code calculates the time-evolution of the phase-space beam ellipses, and hence beam envelopes, along the linac. The top left figures in Fig. 5.8 show the phase-space beam ellipses assumed at the injector exit, and the top right figures those obtained at the ACS exit. The bottom figure shows the calculated beam envelope along the beam line from the injector exit (at the left end) to the ACS exit (at the right end). It is seen in this figure that the beam can be matched with a rather simple configuration of a solenoid magnet and a buncher cavity. Then, the beam envelope through the low-β linac is sufficiently controlled.

Proper beam acceleration is also confirmed with a preliminary particle simulation. The simulated particle distribution at the ACS exit is shown in Fig. 5.9. In this simulation, an initial Gaussian distribution is generated at the DTL entrance with 50,000 simulation particles. Then, they are tracked through DTL and ACS assuming a realistic RF field and a hard-edge quadrupole magnetic field. For this tracking, the IMPACT code [6] is utilized turning off the space-charge calculation. An RMS emittance growth of around 7% is observed in the simulation. This growth is believed to be induced by the nonlinear nature of the RF defocusing force. While the shape in the transverse phase space also shows some distortion in this figure, it is assumed to be at a tolerable level.
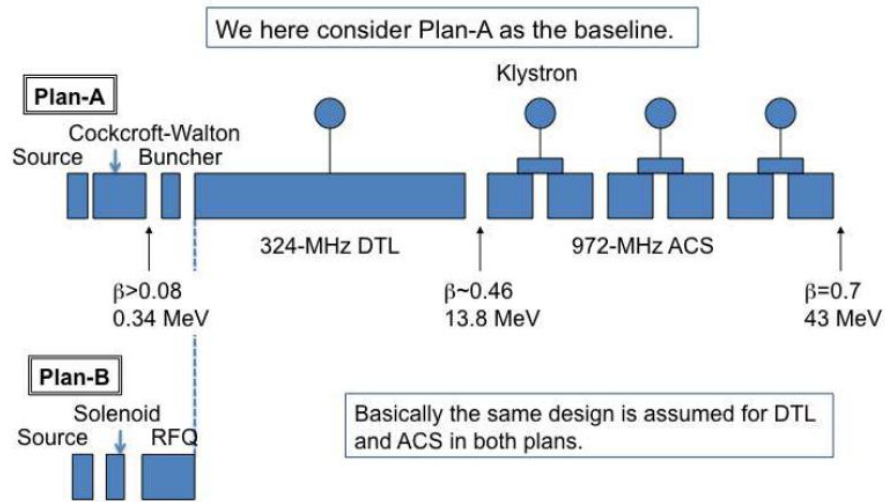
Assumed layout for low-β section

**Figure 5.7:** *Schematic layout of low-β linac.*

Table 5.1: *Main parameters for DTL.*

	Muon DTL	J-PARC DTL
Number of cells per tank	33	146
Number of tanks	1	3
Operating frequency	324 MHz	324 MHz
Cavity type	Alvarez-type	Alvarez-type
Averaged accelerating field E_0	2.5 MV/m	2.5 MV/m
Synchronous phase ϕ_s	-30 degree	-30 degree
Kinetic energy at the entrance	0.34 MeV	3.0 MeV
Kinetic energy at the exit	13.8 MeV	50.1 MeV
β at the entrance	0.080	0.080
β at the exit	0.462	0.313
Wall loss per tank	0.83 MW	1.1 MW
Total length	8.82 m	27.1 m
Traversing time	99 ns	

Table 5.2: *Main parameters for ACS.*

	Muon ACS	J-PARC ACS
Number of cells per tank	17	17
Number of tanks	6	42
Operating frequency	972 MHz	972 MHz
Cavity type	ACS	ACS
Averaged accelerating field E_0	4.36 MV/m	4.12 MV/m
Synchronous phase ϕ_s	-30 degree	-30 degree
Kinetic energy at the entrance	13.8 MeV	190 MeV
Kinetic energy at the exit	43 MeV	400 MeV
β at the entrance	0.465	0.555
β at the exit	0.703	0.712
Wall loss per tank	0.82 MW	0.73 MW
Total length	14.76 m	107.1 m
Traversing time	80 ns	
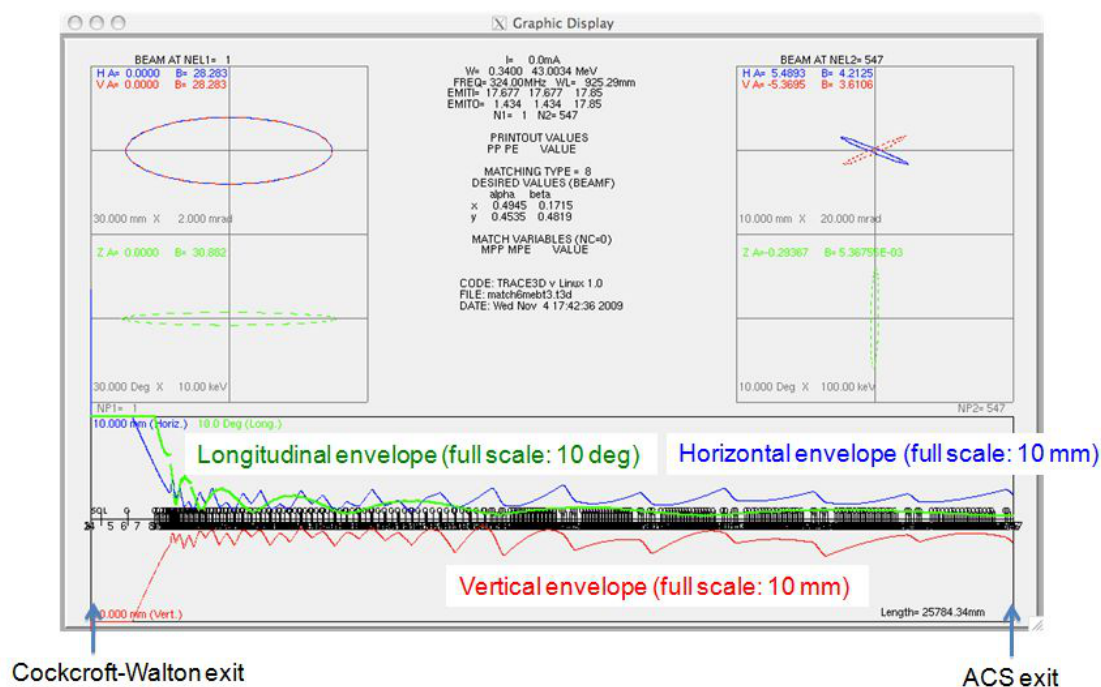
Figure 5.8: *The beam envelope along the low-β linac calculated with Trace3D.*
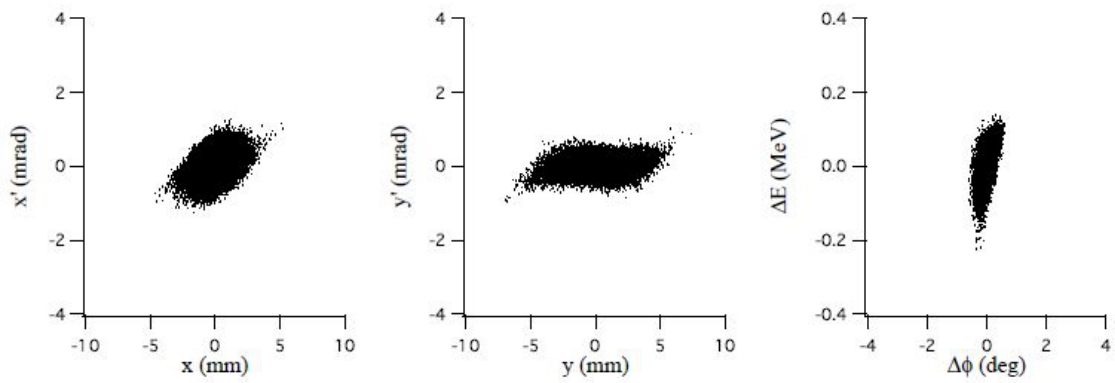
Figure 5.9: *The particle distribution at the exit of the low-β linac simulated with IMPACT*

Interdigital-H

Muon beam, which is pre-accelerated up to 300 keV with a RFQ linac, is boosted up to 3MeV with an Interdigital-Hdrift tube linac (IH),as shown in Fig. 5.10, as low-beta acceleration. Generally, the IH has been used for low energy heavy ion acceleration, and it has high shunt impedance in low-beta region.

For the J-PARC $g-2$ experiment, the adoption of the IH realizes saving of the installation space of an accelerator and manufacturing cost.An Alvarezdrift tube linac studied as a muon accelerator before excites an acceleration electric field by the TM_{010} mode and carries out the 2 -mode beam acceleration, as shown in Fig. 5.11 and 5.12. On the other hand, the IH uses the TE_{111} mode. When the cylindrical cavity resonator which defined the z axis as the beam acceleration direction is considered, from the character of the TE mode, the TE_{111} mode does not have an electric field component in the z direction, therefore it cannot use for beam acceleration.If accelerating electrodesare arranged interdigitally along the z direction, it can produce the electric field, i.e., the acceleration electric field. Then, since the electric field of adjacent acceleration gaps become the opposite direction, it is able to accelerate beam by the π-mode. Compared with the linac of 2π-mode type, the accelerator length can be shortened in an about half.

About the fabrication structure of an IH, we can consider the conventional style that attaches drift tubes into a cylindrical cavity and the three pieces type that attaches two semi-circle shells to a center frame. In the latter, a center frame and drift tubes can be machined by monobloc, and it realizes the improvement of manufacture accuracy, and cost-cutting. Moreover, a long cavity can also be fabricated easily. For these reasons, we will adopt the three pieces type as the IH for muon. Acceleration field distribution is adjusted with the metal plate called a ridge. The electric field in the TE111 mode in a cylindrical cavity is concentrated around the center.In the IH, many drift tubes are set at the beam injection side because the particle energy is lower, and this causes concentration of the electric field distribution by the increase of capacitance. However, from point of heat generation and electric discharge, flat electric field distribution is desirable. The ridge is extended in the z direction of the cylindrical cavity, and adjusts magnetic flux distribution.In the case where the ridgesare arranged to the upper and lower sides in the cavity, the transverse component of the magnetic flux will be blocked near the center, and the magnetic field distribution will be spread to both ends. Therefore, the flatness of electric field distribution can be achieved. Moreover, by cutting the base end of the ridge, fine tuning of the magnetic field distribution is possible, and it can adjust electric field distribution indirectly.

Since an IH has been developed as a heavy ion accelerator, the operating frequency has been chosen in the range of 30-200 MHz.We considered the frequencies of 81,108,162 and 324 MHz for muon acceleration. The lower frequency is more desirable in order to keep practical cell length as a low-beta accelerator. However, because we will use the J-PARC RFQ as the first accelerator in the new plan, the IH has been designed with the operating frequency of 324 MHz to standardize a RF power source system.

Another advantage of the I-H structure is the alternative phase focus(APF). In such a muon accel-

erator, the bunch charge is too small for the beam position monitor. Thus the mis-alignment of the quadrupole magnet is fatal for the beam commissioning. However the APF leads to focus the muon beam to the center of the cavity. We can design the I-H structure with the suitable cell spacing for the APF.
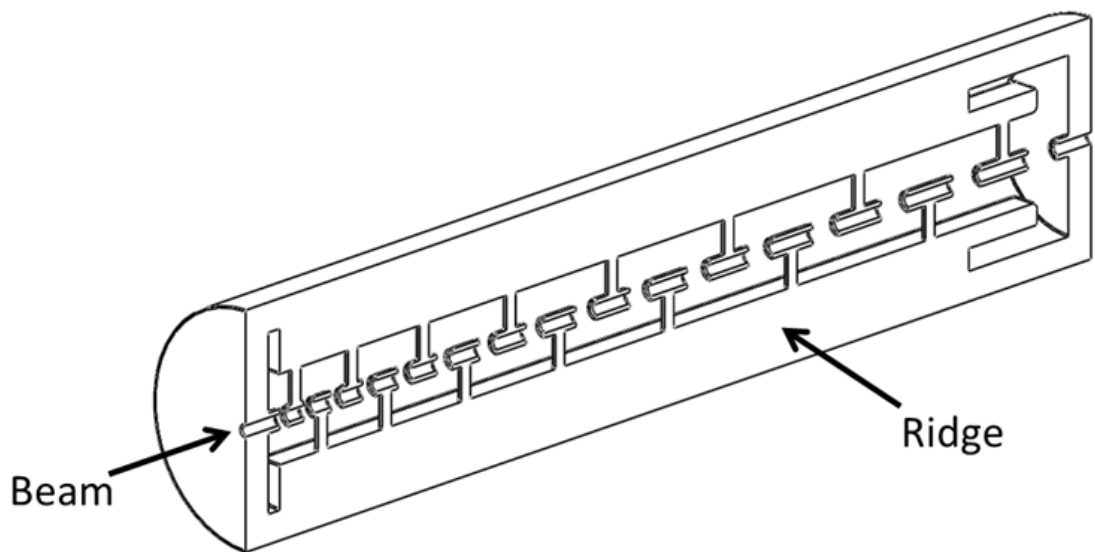

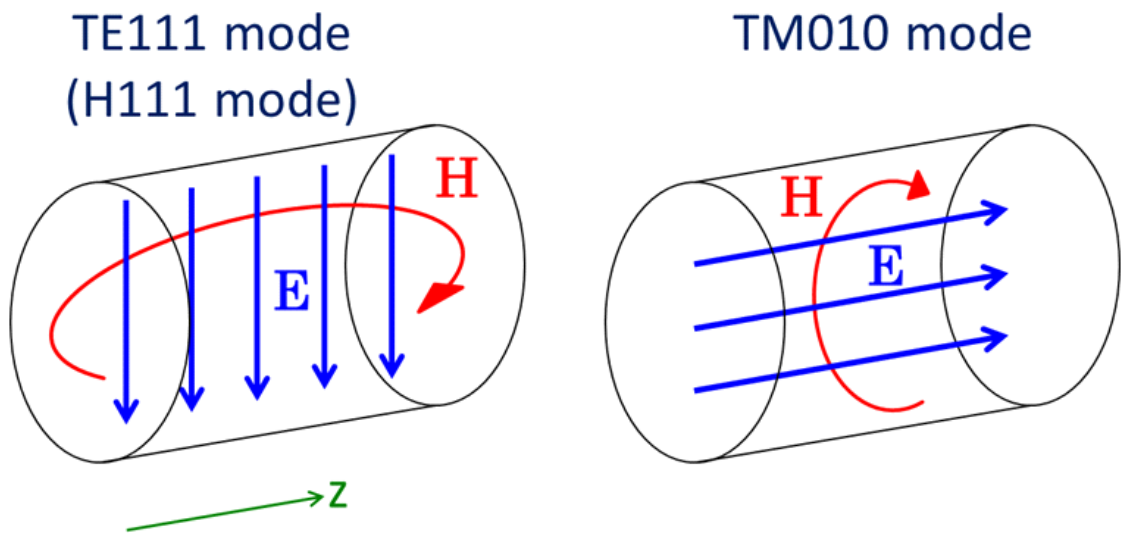**Figure 5.10:** *Schematic drawing of IH linac.*

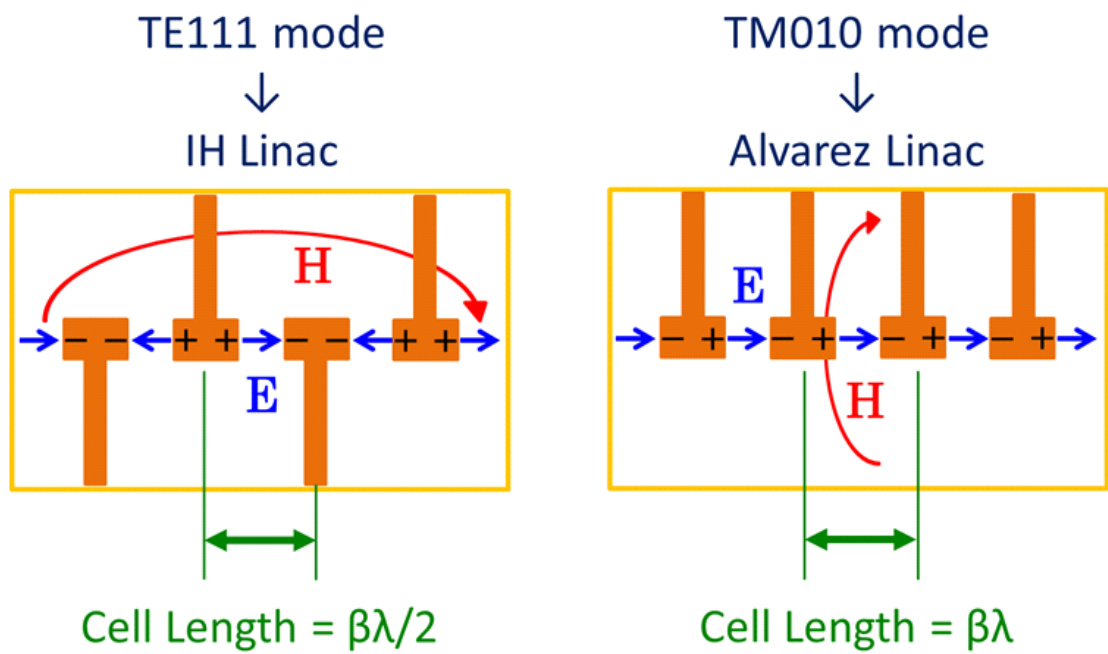**Figure 5.11:** *Electromagnetic field distributions of TE_{111} and TM_{010} mode.*

Figure 5.12: *Comparison of acceleration field between IH and Alvarez.*

For middle-β section, there are some candidates of the alternative accelerating structure as followings.

- Disk and washer (DAW).

- Cut disk structure (CDS).

- Interdigital structure.

All structures requires to fabricate the 3D shape for cells. However the interdigital structure has an great advantage for the fabrication using the monoblock plate for the inner structure. Thus we will develop the 0-mode or π-mode linac with the operating frequency of 972 or 1300 MHz as shown in Fig. 5.13.
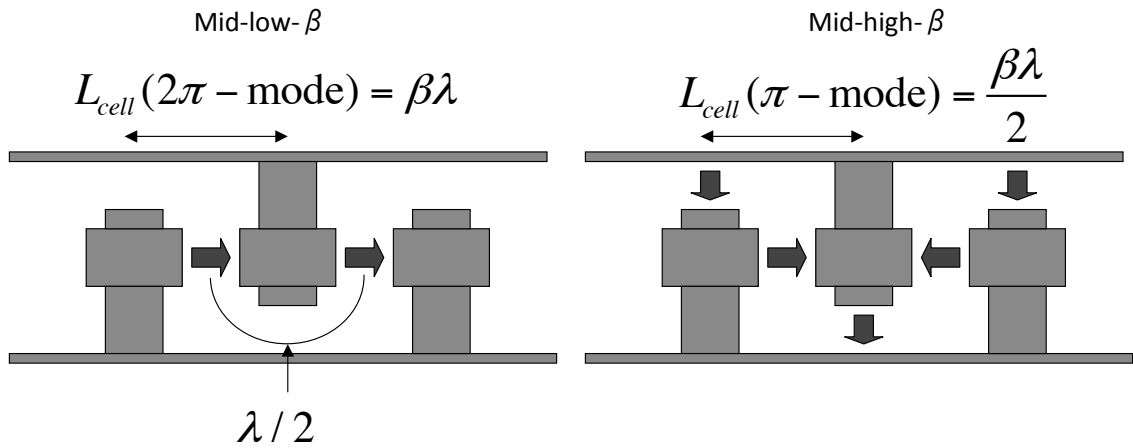
Figure 5.13: *Middle-β interdigital structure.*

5.1.3   High β section

The high β section of the muon linear accelerator is designed to re-accelerate from 100MeV/c to 300MeV/c. As the basic design of the high β section, a disk-loaded traveling wave accelerating structure, which is similar to an electron linear accelerator, was selected. The advantage is its high electric field of around 20MV/m to shorten the accelerator length. Figure 5.14 is the typical accelerating structure of the electron linac. The emittance and bunch length of the muons are small enough to accelerate using such a disk-loaded structure, though the available phase space becomes less due to the higher frequency. However we have to evaluate the phase stability and determine the frequency to minimize the emittance growth.
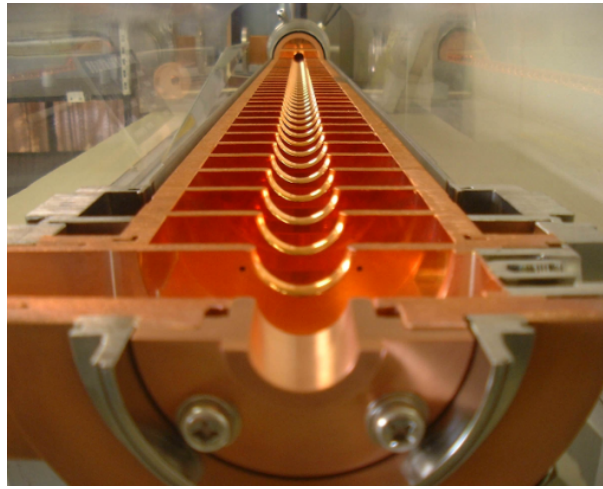
Figure 5.14: *Disk-loaded accelerating structure.*

The particular design item of the disk-loaded structure for the muon acceleration, which is different from the general accelerating structure for the electron accelerator, is the variation of the disk spacing corresponding to the muon velocity.

The design procedure of the phase velocity matched disk-loded structure is as followings,

- The disk spacing is generated in turn to pass the center of each cavity at a given RF phase for a test particle.

- The test particle is tracked through the electromagnetic field of the cavity which is calculated utilizing the series expansions and impedance matching method [8] without mesh.

- The particles at the end of the low β section are tracked in the cavity chain.

The RF frequency of 1300 MHz is adequate for the wider phase space, where the klystrons and other waveguide components for this frequency band were already developed by the KEK electron-positron linear accelerator group.

Muon g-2/EDM Experiment, Conceptual Design Report, Revised, December 12, 2011, 11:41 A.M.

Further the constant gradient structure was adopted, the input power is 8MW for each accelerating structure and the ratio of the power attenuation constant usually described as τ is selected to 0.5. Figure 5.15 shows the disk spacing and the length of the accelerating structure corresponding to the muon momentum. It consists of only four accelerating structures and the total length is around 10 m.
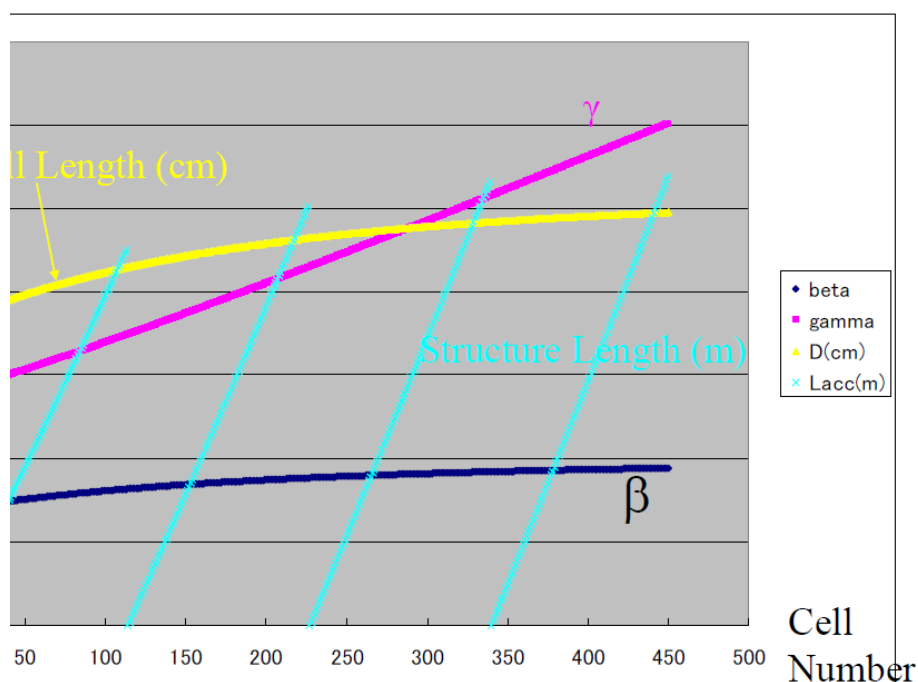

Figure 5.15: *Cell length corresponding to the muon velocity.*

The total system based on this design of the high β linac is shown in Fig. 5.16. One 50 MW class klystron can drive four accelerating structures to accelerate muons from 100MeV/c to 300MeV/c.

The muons from the end of the low β section are tracked through these accelerating structures generated for the center RF phase of 80 degree.

Figure 5.17 is the longitudinal distribution at the end of the high β section.

As a result, the 98 % of muons are passed in the accelerating phase.

References for Chapter 5

[1] Y. Yamazaki ed., "Accelerator Technical DesignReport for J-PARC", KEK-Report2002-13.

Muon g-2/EDM Experiment, Conceptual Design Report, Revised, December 12, 2011, 11:41 A.M.

One 50 MW Klystron can drive 4 accelerating structures.
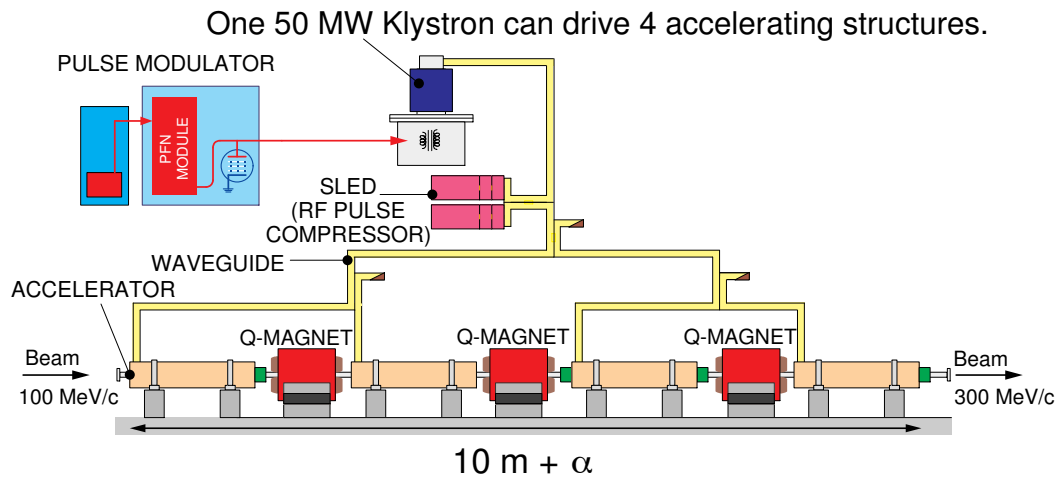
Figure 5.16: *Schematic diagram of the high β section of the muon re-acceleration.*
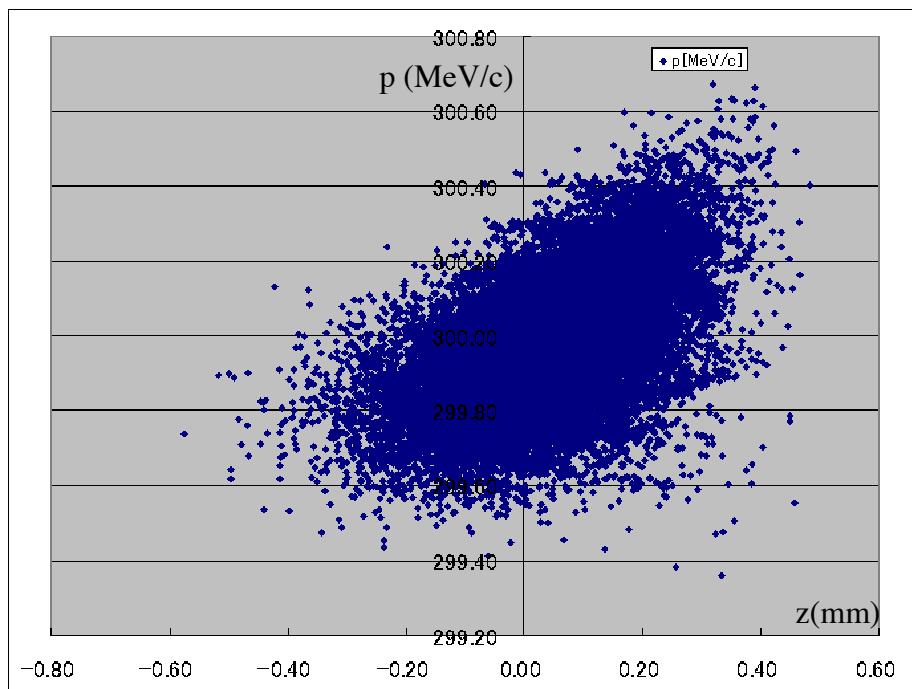
Figure 5.17: *The particle longitudinal distribution at the exit of the high β linac.*

[2] T. Kageyama, et. al., "Development of Annular Coupled Structure", Procs. of LINAC'94, Tsukuba, 1994, p. 248 (1994).

[3] K. R. Crandall et. al.,"RFQ design codes", LA-UR-96-1836.

[4] T. Kato, "Proposal of a separated-type proton drift tube linac for a medium-energy structure", KEK Report 92-10 (1992).

[5] K. R. Crandall, D. P. Rusthoi, "TRACE-3D Documentation", Los Alamos National Laboratory Report, LA-UR-97-886, 1997.

[6] J. Qiang, R. D. Ryne, S. Habib, V. Decyk, J. Comput. Phys. 163, p. 434 (2000).

[7] I. Abe, et al., "The KEKB injector linac", Nuclear Instruments and Methods in Physics Research A 499 (2003) 167.190

[8] Masao Nakamura, "A Computational Method for Disk-Loaded Waveguides with Rounded Disk-Hole Edges", Japan Journal of Applied Physics, Vol.7, No.3, March, 1968.

Muon Storage Field and Injection

<hr>

Contents

6.1 Muon storage ring magnet and injection

The muon storage ring for this experiment will be a precession field 3 Tesla solenoid with cylindrical iron poles and return yoke. The solenoid is being designed now in collaboration with a private company to a specification of < 1 ppm variation of the field locally within the storage region. The storage region, which is defined on the mid-plane, with a radius of 33.3 ± 1.5 cm and height of ± 5 cm, is applied bf weak focusing magnetic field to keep vertical motion of the beam within few cm. An engineering study is discussed in different section. In this section, we would introduce five major topics.

- Outline of the Muon Injection strategy,

- Configuration of beam trajectory and magnetic field,

- Acceptance of the beam at Injection Point,

- Weak focusing magnetic field in the storage volume, and

- Beam control from injection field to storage field.

6.1.1 Outline of the Muon Injection Strategy

For injection, the muon beam must be injected into the storage ring with minimum interference to the storage field. In the BNL $g - 2$ experiment, as displayed in Fig. 6.1, a device called an inflector was used to inject the muon beam, to avoid deflection by the fringe field. As the beam crossed the storage region, the beam was kicked horizontally by the kicker to move to the central orbit through an angle large enough to prevent the beam from striking the inflector after one turn. This procedure works only if the radius of the storage ring is large enough compared to the inflector wall thickness. The limitation comes from the required kick-angle within the first turn in the storage ring (within 149.2 ns) to avoid hitting the inflector itself. In the BNL $g - 2$ experiment, the radius of storage ring was 711 cm and the wall thickness was ~ 1 cm. Therefore the kick angle was ~ 1.5 mrad.

In our experiment, the radius of the central beam orbit is 33.3 cm. This corresponds to a required horizontal kick angle of 30 mrad within the first turn in the ring (within 7.4 ns). The kick angle would be an order of magnitude larger than a kick with any existing technology. The horizontal kick does not work for our case.

Therefore, we have chosen a **spiral injection scheme** instead as displayed in Fig. 6.2. The beam will be separated from the injecting point by $\sim$10 cm *vertically*, so there would be no disturbance in the beam trajectory.

A solenoidal magnet is suitable for this injection scheme. An unique point of this scheme is to build in a radial fringe field to replace the role of the inflector. The beam will enter the solenoid through a hole in the return yoke iron. (Note that BNL E821 used a similar hole in the iron return yoke, which was easily compensated for by adding additional iron beside the hole.)

The beam momentum is deflected vertically by a radial magnetic field, which will be built in the solenoid fringe field, which is shown as B_R on Fig. 6.2. The magnetic field should be carefully shimmed not only for the vertical field for the muon storage but also for the radial field so that only a small vertical momentum remains when the spiraling beam reaches the beginning of the storage region.

The injected beam will then spiral through the good field (B_R) storage region and a magnetic kicker will be used to deflect the beam into a stable orbit at the center of the storage region. The duration of the kick can be for a number of cyclotron (or revolution) periods, since a longer kicker pulse allows a low kicker voltage and more stability. A multi-turn-kick by the longer pulse shape kicker would be easier.

Then finally, the beam is stored into the storage region. In order to control vertical beam motion, that is vertical envelope size, we apply **weak focusing magnetic field**.
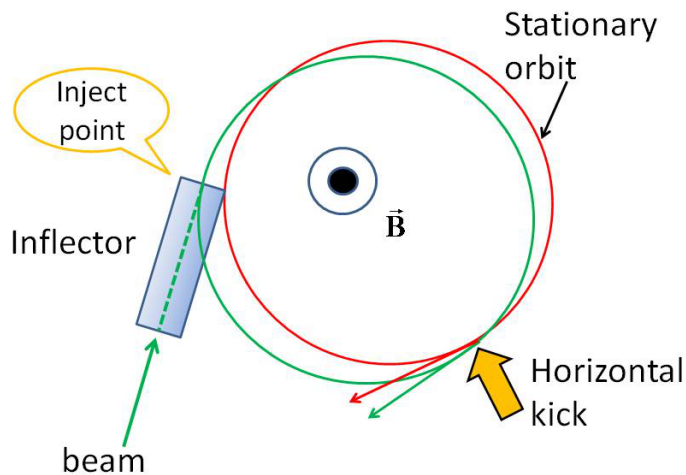
Figure 6.1: *Injection scheme for previous experiment (BNL g − 2) from top view. They use an inflector and horizontal kicker system.*
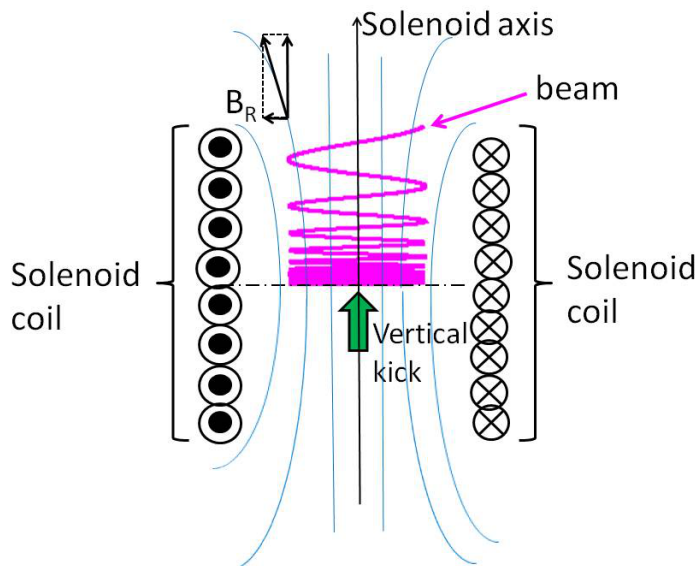
Figure 6.2: *Schematic representation of spiral injection for our case. A radial fringe field, shown as B_R, deflects the vertical component of the beam momentum to the horizontal component.*
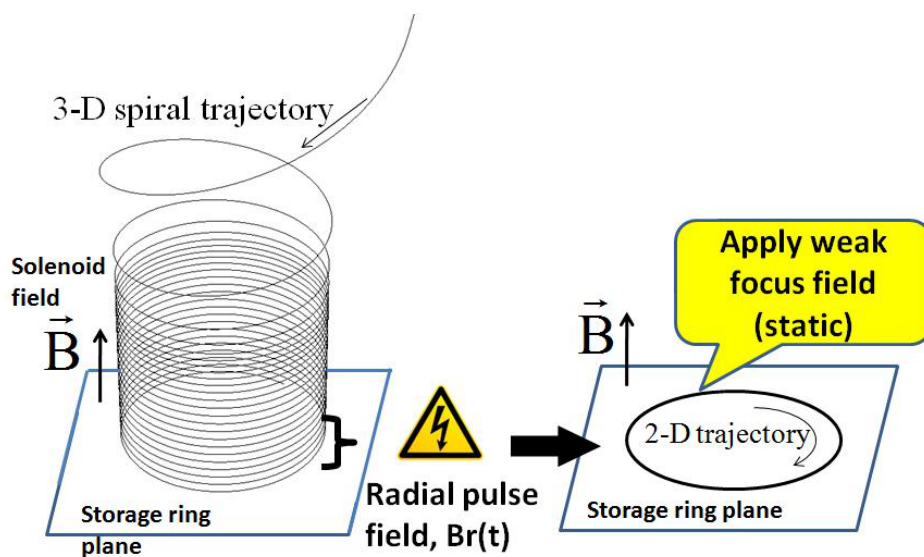
Figure 6.3: *Outline of three-dimensional injection scheme. A radial fringe field deflects the vertical component of the beam momentum to the horizontal component. Pulsed radial magnetic field removes the residual vertical motion down to 10^{-4} [rad], and then weak focusing field keep the beam inside storage area.*
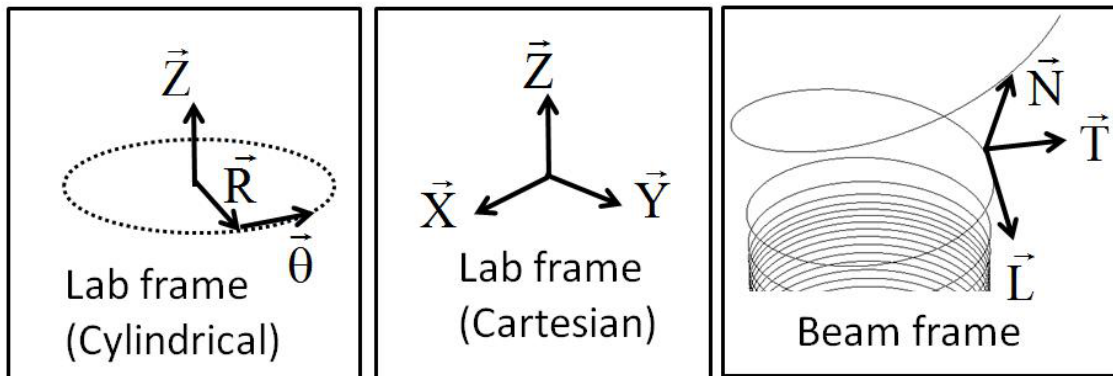
Figure 6.4: *Explanation of coordinates we use in this document.*

6.1.2 Configuration of beam trajectory and magnetic field

Figure 6.5 introduces the magnet configuration planned for the storage ring. Note that we will discuss the muon injection scheme in a conceptually designed magnetic field in this section. More practical design is in progress collaborating with a private company. The upper picture depicts a cut view of solenoidal conductors (red), iron pole tip (cylinder shape, light green), iron return yoke (green circle plate and blue cylindrical wall). The middle picture depicts the calculated three-dimensional muon beam injection trajectories(100) with this magnet configuration. The bottom plot displays beam trajectories(100) projected to the X-Y plane.

5/Dec/2011 16:34:41

Opera
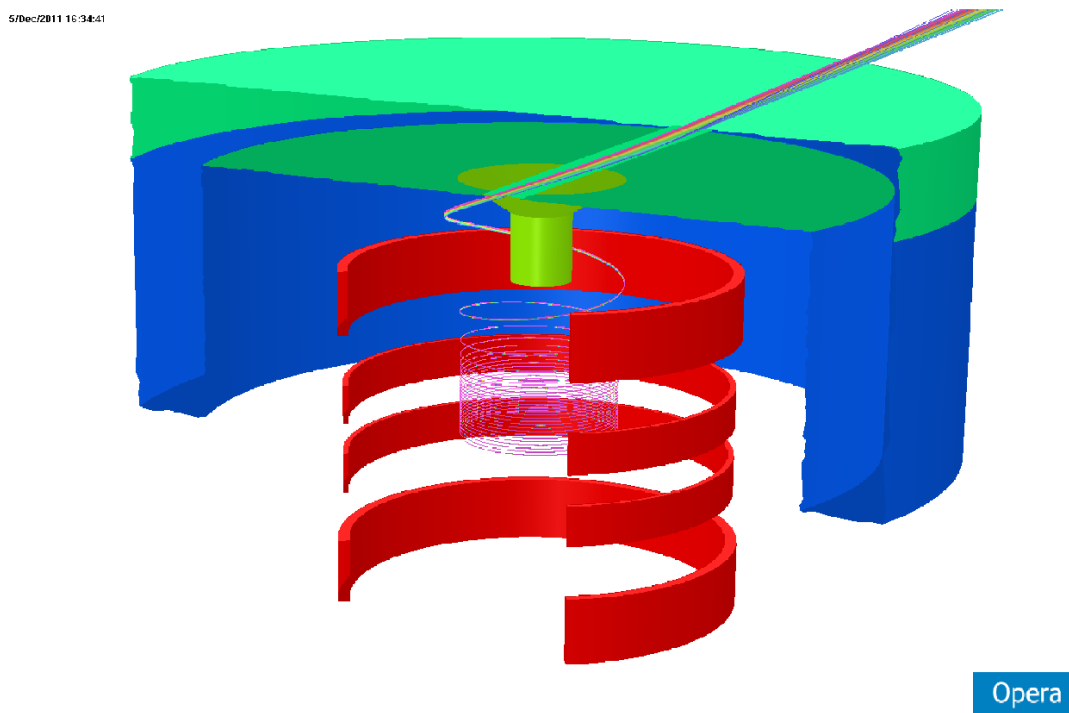
Figure 6.5: *A conceptual illustration of the storage ring magnet: solenoid coils, iron pole tip and return yoke together with* 100 *of muon beam.*

Figure 6.7 displays a volume of Z$\leq$ 30 cm (upper) and a cut of X-Y plane at Z=0.1 cm (lower). Although beam size at Z$\sim$ 95 cm is rather large, beam shape at Z$\sim$ 0 cm is well-focused in vertically **and** horizontally. Note this is the second advantage to adopt solenoidal field for this injection scheme. Fringe field of Solenoidal magnet acts as a unit focusing system for vertical **and** radial direction **at a time**.

A projection of X$-$Z plane of bottom plot of Fig. 6.5 is shown in the left side of Fig. 6.8. Right plot of Fig. 6.8 displays the vertical (along the solenoid axis, Z-axis) and radial components of the trajectories. These trajectories are almost axial symmetry.

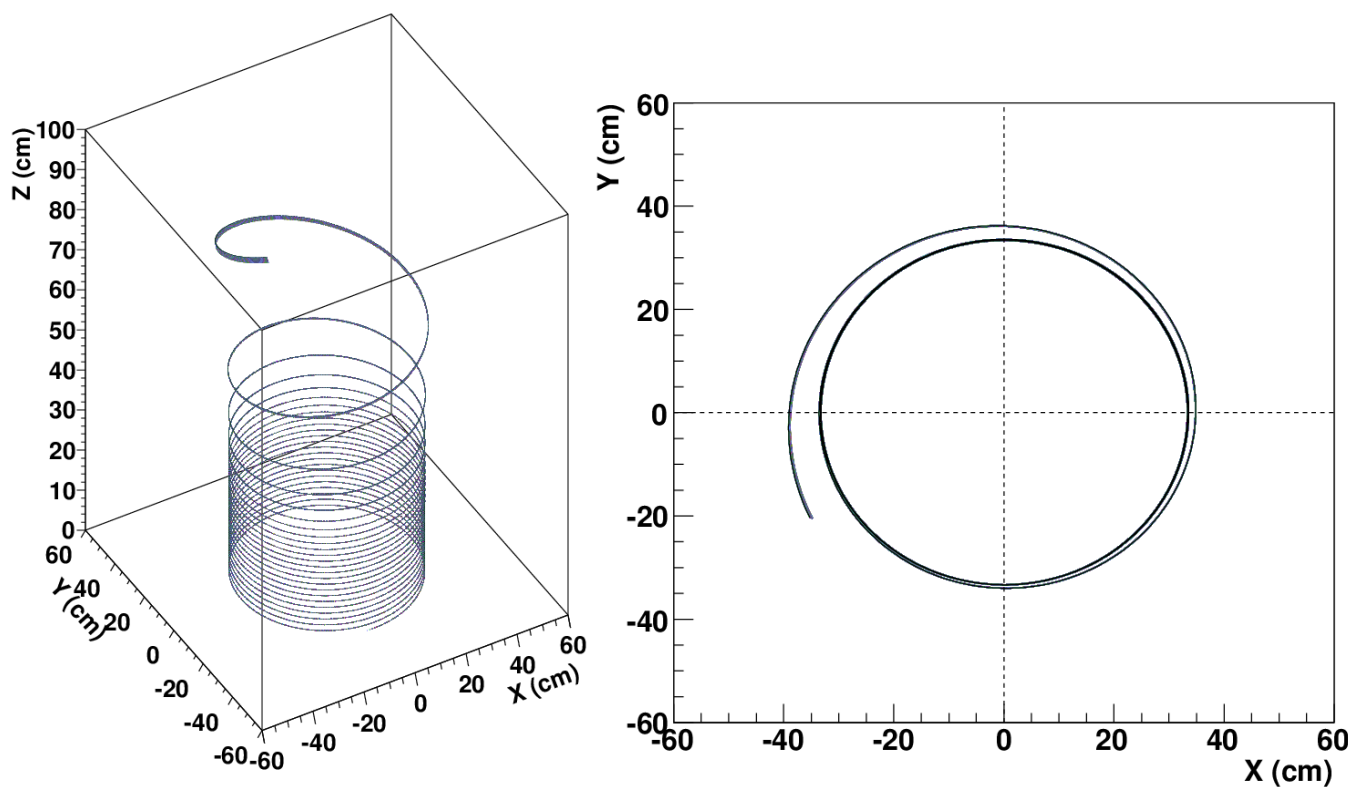Figure 6.9 depicts deflection of pitch angle ($=V_Z/V$) as a function of Z position. As introduced

Figure 6.6: *Top: Calculated spiral trajectory of 100 muon particle with $\gamma_\mu = 3$ by* OPERA *inside of the return yoke volume. Bottom: Projected beam trajectories on the $X-Y$ plane.*
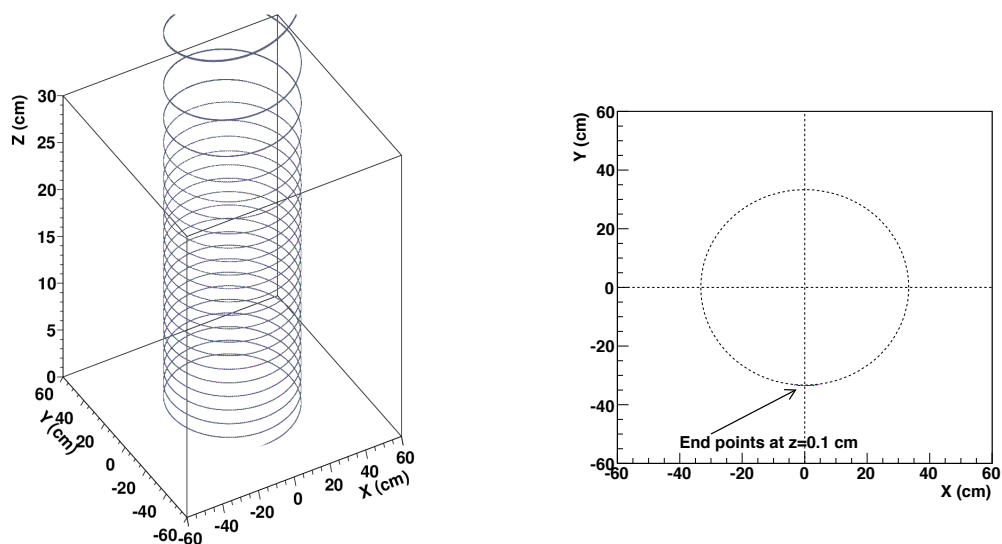

Figure 6.7: *Closeup view of three-dimensional trajectories in $Z \leq 30$ cm (upper) and a cut plane at $Z=0.1$ cm (lower) Beam shape at $Z \sim 0$ cm is well-focused in vertically* **and** *horizontally.*
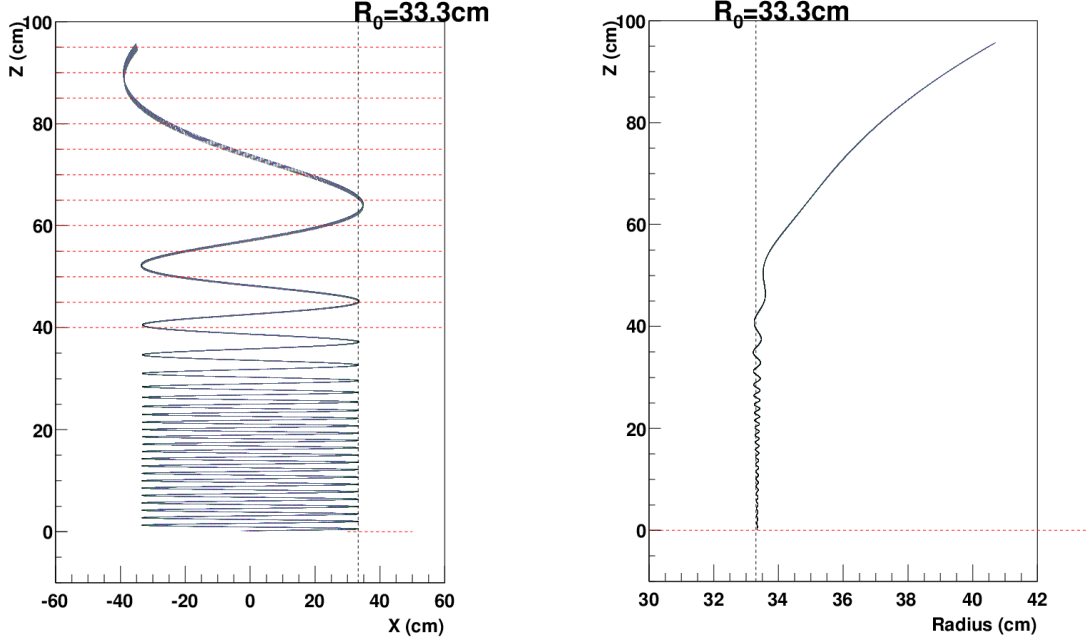
Figure 6.8: Left: A projection of X−Z plane. Red dotted horizontal lines indicate vertical positions of slice points, discussed in the next subsection. Right: Radial and vertical positions of the trajectories introduced in Fig. 6.5 (bottom).

in subsection 6.1.1, we deflect beam direction by the fringe field. Pitch angle is reduced down to −6.9 mrad at Z¡10 cm region. We apply **kicker** to decrease pitch angle down to zero, which discuss later.

Analytical approach to design magnetic field   Acceleration of motion of charged particle ($\vec{a}$) with velocity, $\vec{V}$, in the presence of magnetic field, $\vec{B}$, is written as

$$\vec{a} = \frac{q}{m_\mu} \vec{V} \times \vec{B}, \tag{6.1}$$

here, velocity is $\vec{V} = (V_x, V_y, V_z)$, and magnetic field is $\vec{B} = (B_x, B_y, B_z)$ in the lab frame, which we take solenoid axis is the Z-axis. Therefore, main solenoid field is B_Z and radial field is $B_R = \sqrt{B_X{}^2 + B_Y{}^2}$. Velocity on the X-Y plane (that is, horizontal component) is $V_{xy} = \sqrt{V_x{}^2 + V_y{}^2}$. Z component of velocity V_z changes as a function of Z position, but absolute value of velocity $|V| = \sqrt{V_{xy}{}^2 + V_z{}^2}$ never change in the magnetic field.

Derivation of vertical and horizontal components are expressed as:

$$\begin{aligned}
\frac{\Delta V_z}{\Delta t} &= \frac{q}{m_\mu} V_{xy} B_R, \\
\frac{\Delta V_{xy}}{\Delta t} &= \frac{q}{m_\mu} \sqrt{V_z B_R{}^2 + V_{xy} B_Z{}^2}.
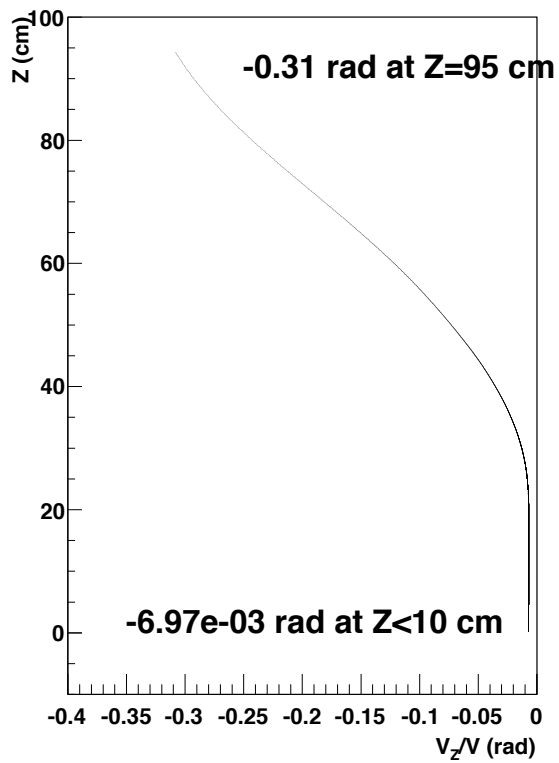\end{aligned} \tag{6.2}$$

Figure 6.9: *Pitch angle (=V_Z/V) as a function of Z position. At injection point, Z=95cm, pitch angle is 0.31 rad. And it is deflected down to 6.9 mrad at Z$\leq$ 10 cm region.*

By use of this equation connect time-derivative terms and space-derivative terms are connected:

$$
\begin{aligned}
\frac{\Delta V_z}{\Delta t} &\cong \frac{\Delta V_Z}{\Delta z}\frac{\Delta z}{\Delta t} \\
&\cong \frac{\delta V_Z}{\delta z}V_z, \\
\frac{\Delta V_{xy}}{\Delta t} &\cong \frac{\Delta V_{xy}}{\Delta z}\frac{\Delta z}{\Delta t} \\
&\cong \frac{\delta V_Z}{\delta z}V_z.
\end{aligned}
\tag{6.3}
$$

Then we get

$$
\begin{aligned}
\frac{\delta V_z}{\delta y} &= \frac{q}{m_\mu}\frac{V_{xy}}{V_z}B_R, \\
\frac{\delta V_{xy}}{\delta t} &= \frac{q}{m_\mu}\frac{\sqrt{V_z B_R{}^2 + V_{xy}B_Z{}^2}}{V_z}.
\end{aligned}
\tag{6.4}
$$

In this way we confirm a relationship between a trajectory (V_Z, V_R, Z and R) and magnetic field along a trajectory ($B_Z(Z,R)$ and $B_R(Z,R)$).
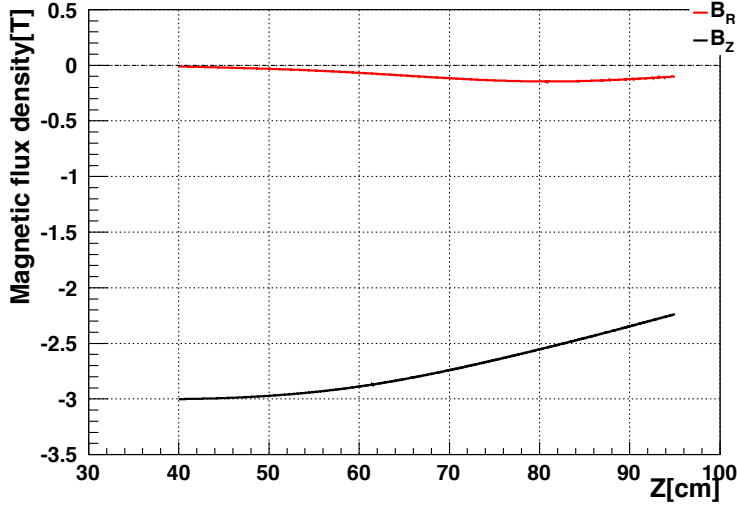

Figure 6.10: *Magnetic field along the muon beam trajectory as a function of vertical axis (solenoid axis). Note that the magnetic field changes smoothly as the muon moves. Upper iron cover is at Z=100 cm.*

Figure 6.10 displays B_Z and B_R along a trajectory as a function of Z position. Red and black thin lines are from OPERA output, and gray thick lines are calculation from trajectory information using Eq. 6.3. From this study, we learned two important points for magnetic field configuration (Injection volume);

- $B_R \times B_Z$ should positive along the trajectory,

Muon g-2/EDM Experiment, Conceptual Design Report, Revised, December 12, 2011, 11:41 A.M.

- B_R should always same sign and smoothly changed along the trajectory for smooth V_Z.

These are quite natural results, but very important fact. Because, once we decide an *ideal* trajectory, we can design magnetic field configuration to meet our ideal trajectory!

Lastly we would mention a way to decide *ideal* trajectory briefly:

- decide V_Z as a function of Z,

- obtain V_{xy} as a function of Z by use of $V_{xy} = \sqrt{V^2 - V_{xy}{}^2}$,

- obtain radial position $R(= \sqrt{x^2 + y^2})$ as a function of Z by use of

$$R(Z) = \int_0^{Z_{max}} V_R(Z) \cdot dt, \qquad (6.5)$$

  here, initial value of R_0 is 33.3cm.

then, we have a trajectory information: V_Z, V_R, Z and R.

As long as we think about a **single** trajectory and its magnetic field configuration, there is no necessarily to care about **Maxwell Equation**. However, magnetic field should satisfy **Maxwell Equation** all the time. If we think about a **group** of particles (=beam), which distribute a certain volume in the magnetic field, we need **Maxwell Equation** as well as Eq. 6.2.

6.1.3 Acceptance of the beam at Injection Point

In this subsection, we would introduce how to estimate the optimal correlation between position displacement and duration of angle. At first, we pick a single trajectory as a reference trajectory, and define a specific reference plane at a certain point along this reference shown in Fig. 6.11. Here, we pick twelve points along this reference trajectory as shown in the left plot of Fig. 6.8. And then we slice beam bundle by each reference plane. Figure 6.12 and 6.13 are correlations obtained with respect to that twelve planes.
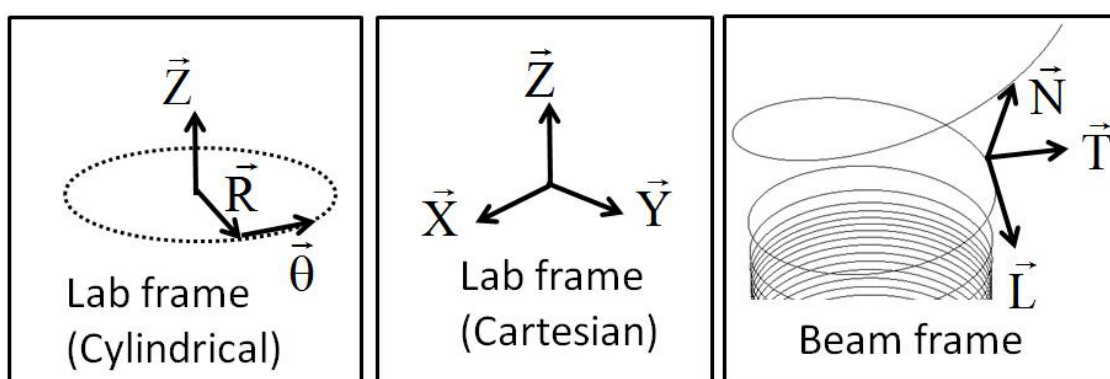
Figure 6.11: *Example of an orthogonal coordinate axis of a specific plane with a base trajectory. Correlation between position displacement and duration of angle are taken with respect to the $\vec{T}$, $\vec{N}$ and $\vec{L}$ axes.*

Figure 6.14 and 6.15 also depict correlation at twelve different vertical position. These are same data as shown in Fig. 6.12, but they are shown in independent plots.

There are strong correlations between position displacement and duration of angle in $\vec{N}$ and $\vec{T}$ directions.

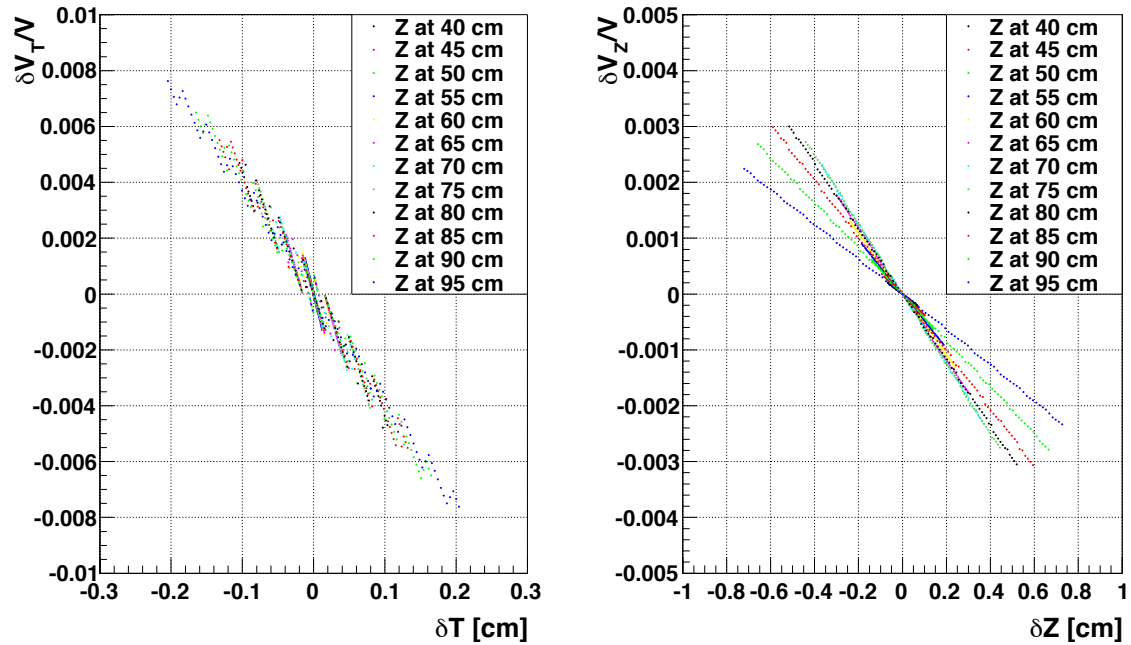It is clear that a fringe field acts as *local focus* for a proper set of beam injection conditions.

Figure 6.12: (Left: Correlation between T and $\frac{V_T}{T}$ at several vertical position. Right: Correlation between N and $\frac{V_N}{N}$ at several vertical position.
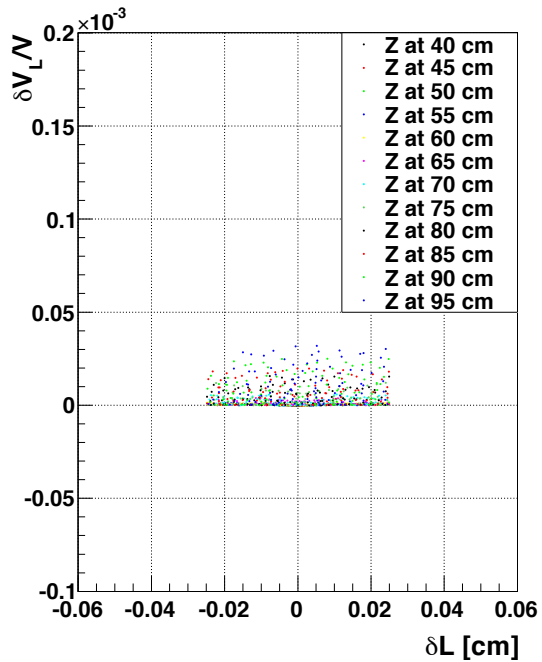

Figure 6.13: Correlation between L and $\frac{V_L}{L}$ at several vertical position.
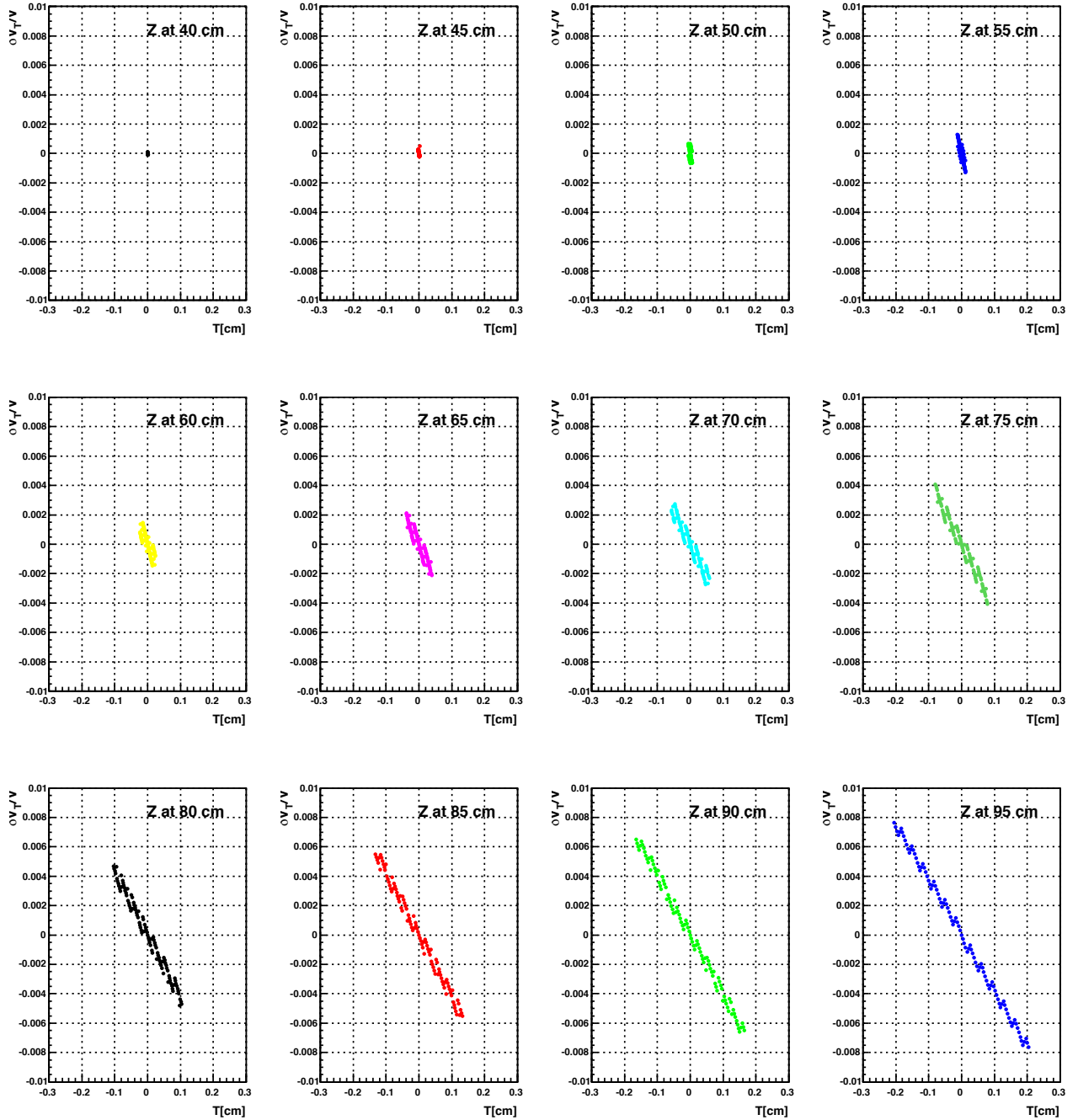
Figure 6.14: *Correlation between T and $\frac{\Delta V_T}{V}$ at several vertical position. Same as left plot of Fig. 6.12 but correlations are plotted separately.*
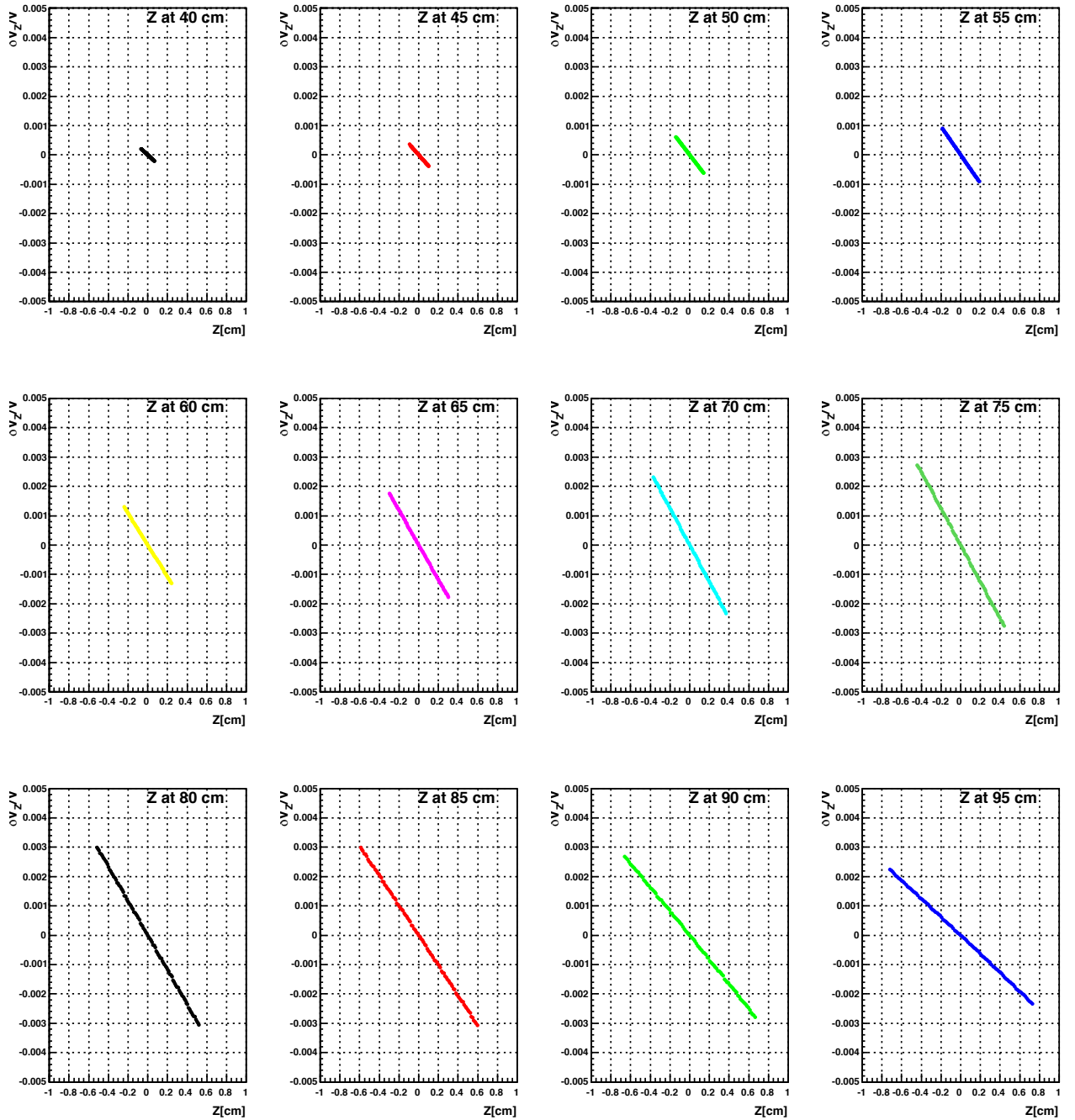
Figure 6.15: Correlation between N and $\frac{\Delta V_N}{V}$ at several vertical position. Same as right plot of Fig. 6.12 but correlations are plotted separately.

Analytical approach to obtain strong correlation For more detailed study, we obtain slopes and width of horizontal region from Fig. 6.15, and summarized in Table 6.1.

Table 6.1: *Slopes at twelve different points.*

Vertical position Z (cm)	slope (rad/cm)	horizontal width (cm)
40	-0.003073	0.08
45	-0.003775	0.1
50	-0.004388	0.09
55	-0.004817	0.1
60	-0.005318	0.1
65	-0.005883	0.1
70	-0.006280	0.07
75	-0.006297	0.07
80	-0.005928	0.07
85	-0.005192	0.07
90	-0.004233	0.07
95	-0.003184	0.07

Equation of motion of charged particle with velocity, $\vec{V} = (V_x, V_y, V_z)$, in the presence of magnetic field, $\vec{B} = (B_x, B_y, B_z)$, is written as

$$\vec{a} = \frac{q}{m_\mu} \vec{V} \times \vec{B}. \tag{6.6}$$

in the lab frame. Note that absolute value of velocity $|V|$ do not change in the magnetic field.

Vertical component of acceleration is,

$$\frac{\Delta V_z}{\Delta t} \cong a_z = \frac{q}{m_\mu} V_{xy} B_R. \tag{6.7}$$

here $V_{xy} = \sqrt{V_x{}^2 + V_z{}^2}$ and $B_R = \sqrt{B_x{}^2 + B_y{}^2}$.

By use of these two equations:

$$\begin{aligned} \frac{\Delta V_z}{\Delta t} &\cong \frac{\Delta V_Z}{\Delta z} \frac{\Delta z}{\Delta t} \\ &\cong \frac{\delta V_Z}{\delta z} V_z, \end{aligned} \tag{6.8}$$

and

$$\frac{V_N}{N} = \frac{\delta V_z}{\delta Z}, \tag{6.9}$$

we obtain slope in the analytically:

$$\frac{V_N}{N} \cong \frac{q}{m_\mu} \frac{V_{xy}}{V_z} B_R. \tag{6.10}$$

Figure 6.16 depicts slopes in table 6.1 (red points) and results of Eq. 6.10 (black line) as a function of vertical position. These numbers are well consistent.
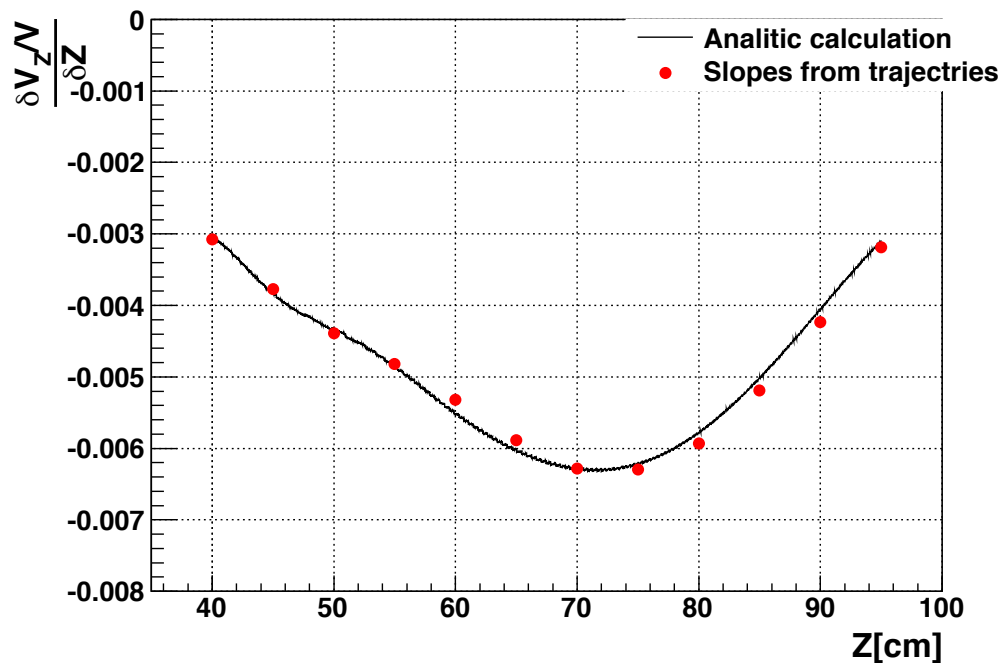
Figure 6.16: *Slopes from Fig. 6.15 and Table 6.1 as a function of vertical positions (red points). Results from Eq. 6.10 are also shown in black solid line. 6.10*

Note that results from Eq. 6.10 in black line are obtained from reference trajectory. On the other hand, red points are from Fig. 6.15 which includes information of 100 of trajectories. Therefore we can determine required conditions for a **group** of trajectories from a **single** reference trajectory.

Acceptable deviation from the ideal correlation   As introduced above, ideal correlation between position displacement and duration of angle in $\vec{N}$ is a very narrow line. Instead of trying *a tightrope act* for beam production, we should try to wide area.

We expand area in direction of N and try injection calculation for 100 trajectories for two cases: one is (A) $\sigma_Z = 100$ μm and the other is (B) $\sigma_Z = 100$ μm. Two plots in Fig. 6.17 depict (A) and (B). There are trajectories reflected by fringe field like a magnetic mirror in (A). Therefore, we should find criteria to avoid mirror reflection between $\sigma_Z = 10$ μm and $\sigma_Z = 10$ μm.
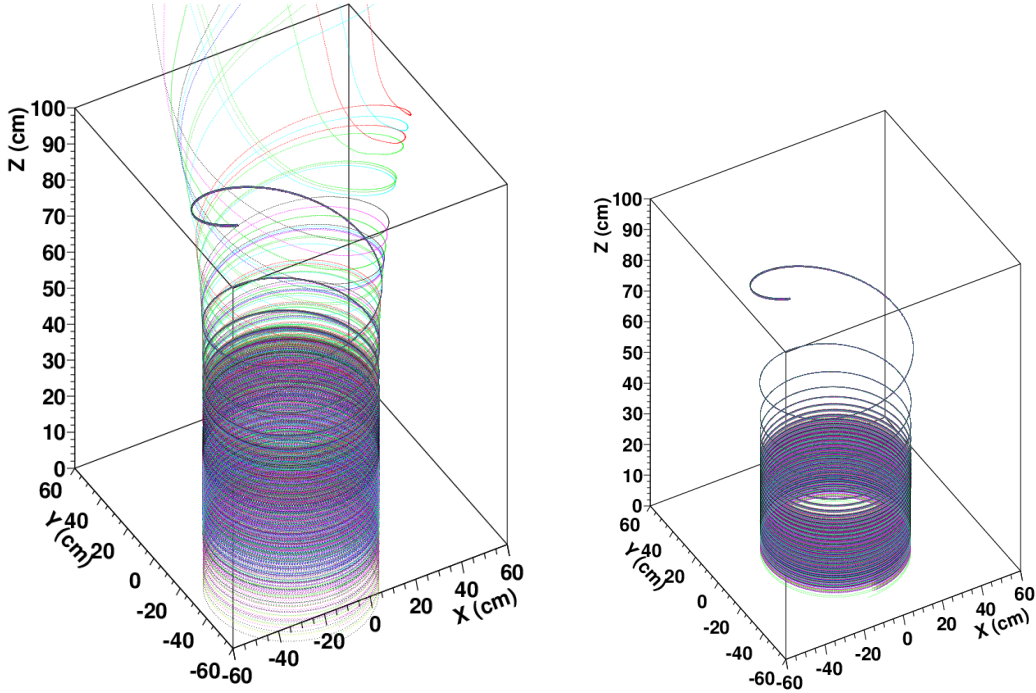

Figure 6.17: *Examples of 100 trajectories for two initial cases. Left: (A) $\sigma_Z = 100$ μm. Right: (B) $\sigma_Z = 10$ μm. There are trajectories reflected by fringe field like a magnetic mirror in (A). We should find criteria to avoid mirror reflection between $\sigma_Z = 10$ μm and $\sigma_Z = 100$ μm.*

At the end of injection point, we apply vertical kick to storage beam as discussed in 6.1.1. Therefore, we also need to think about another selection criteria to meet **Weak Focusing Field** and **Kicker Field** configuration:

- limit rotation number is 25 ± 1 at Z=0.1cm point,

- limit pitch angle (vertical angle V_Z/V) duration within 5%.
  Note that pitch angle at Z=0 cm is 6.9 mrad. Therefore, we choose pitch angle of 6.9±0.35 mrad.

Figure 6.18 and 6.19 depict selected trajectories for case (A) and (B). In case (A), only 9 trajectories are chosen (probability of survival is 9%). In case (B), 49% trajectories are survived. Reversely, we can estimate acceptance of
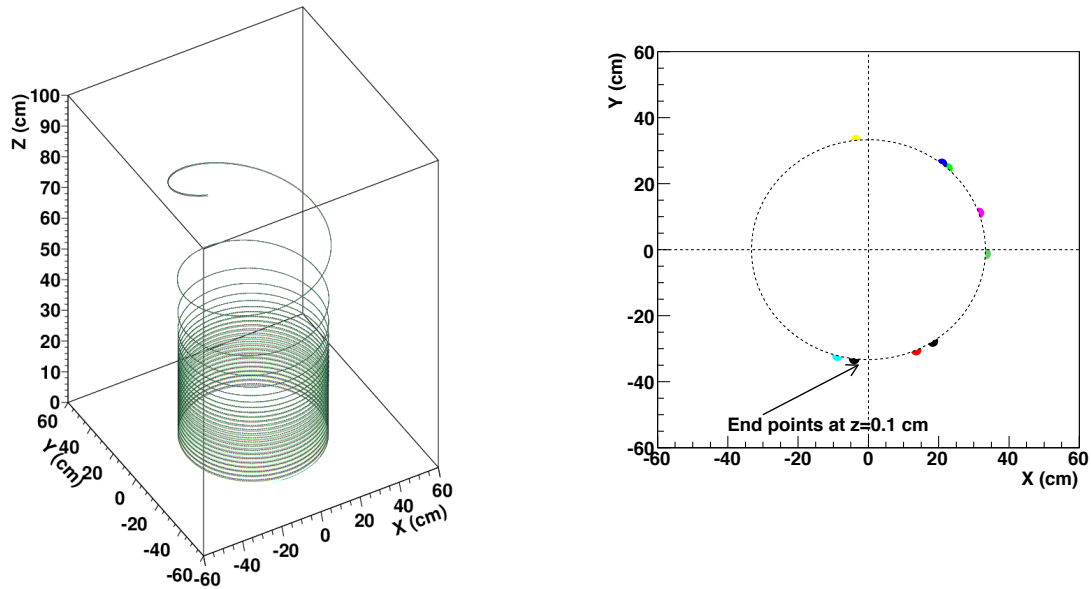
Muon g-2/EDM Experiment, Conceptual Design Report, Revised, December 12, 2011, 11:41 A.M.

Figure 6.18: *Applying proper selections (rotation number and pitch angle) to case (A; left plot of Fig. 6.17), only 9 acceptable trajectories are survived out of 100.*
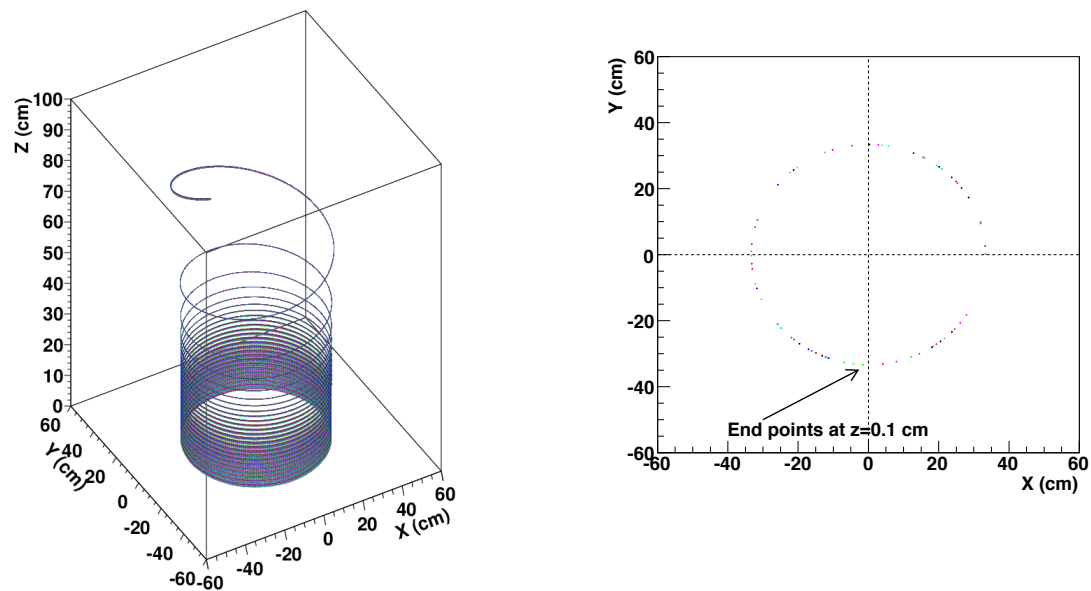

Figure 6.19: *Applying proper selections (rotation number and pitch angle) to case (B; right plot of Fig. 6.17), 47 acceptable trajectories are survived out of 100.*

In this section, we showed a strategy to estimate a phase-space distribution of a single reference trajectory. Next step is to study how to increase area of phase-space acceptance. We will try additional phase-space of another reference trajectories, and sum them up.

6.1.4 Weak focusing magnetic field in the storage volume

To keep the beam within a storage region, we need to focus beam horizontally and vertically at a time by a single unit system. Therefore, we employ **Weak Focusing Magnetic Field System** to the beam. In this section, we use cylindrical coordinate shown in Fig. 6.4.

Weak focusing magnetic field is expressed as:

$$B_Z = B_0\left(1 - n\frac{\Delta R}{R}\right),$$
$$B_R = -n\frac{Z}{R}B_0, \tag{6.11}$$

here $B_0 = 3$ Tesla is main solenoidal field at Z=0 cm. $R_0 = 33.3$ cm and $r = R - R_0$. Field index n is

$$n = -\frac{R_0}{B_0}\frac{\delta B_Z}{\delta R} \tag{6.12}$$

Focus condition is obtained when we set $0 < n < 1$. ($n < 1$; for radial focus. And $n > 0$; for vertical focus.)

Figure 6.20 depicts a example case of $n = 8 \times 10^{-5}$ in Eq. 6.11. Note that B_R does not change as a function of R, but changes by Z. B_Z, on the other hand, does change as a function of R, but does not change by Z.
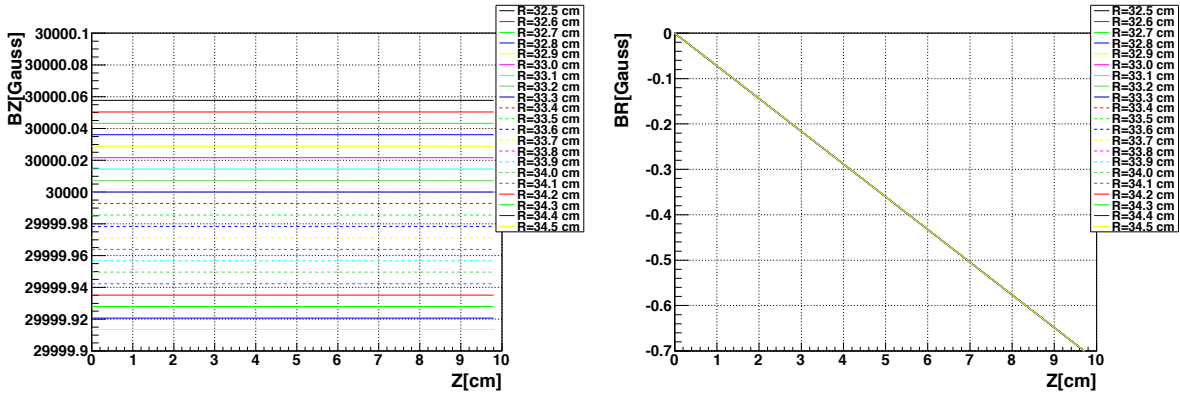

Figure 6.20: *Example field of $n = 8 \times 10^{-5}$ case in Eq. 6.11.*

We introduce horizontal (radial direction) and vertical (Z direction) transfer matrix for a single turn:

$$M_R = \begin{pmatrix} \cos\left(\frac{s}{R_0}\sqrt{1-n}\right) & \frac{R_0}{\sqrt{1-n}}\sin\left(\frac{s}{R_0}\sqrt{1-n}\right) \\ -\frac{\sqrt{1-n}}{R_0}\sin\left(\frac{s}{R_0}\sqrt{1-n}\right) & \cos\left(\frac{s}{R_0}\sqrt{1-n}\right) \end{pmatrix} \tag{6.13}$$

and

$$M_Z = \begin{pmatrix} \cos\left(\frac{s}{R_0}\sqrt{1-n}\right) & \frac{R_0}{\sqrt{1-n}}\sin\left(\frac{s}{R_0}\sqrt{1-n}\right) \\ -\frac{\sqrt{1-n}}{R_0}\sin\left(\frac{s}{R_0}\sqrt{1-n}\right) & \cos\left(\frac{s}{R_0}\sqrt{1-n}\right) \end{pmatrix} \tag{6.14}$$

here, s is a path length and $s = 2\pi R_0$.

Matrix at $s = 0 = 2\pi R_0$ is also expressed by use of twiss parameters $\beta(0), \alpha(s), \gamma(0)$ and phase advance $\mu(0)$ as follows:

$$M = \begin{pmatrix} \cos\mu(0) + \alpha(0)\sin\mu(0) & \beta(0)\sin\mu(0) \\ -\gamma(0)\sin\mu(0) & \cos\mu(0) - \alpha(0)\sin\mu(0) \end{pmatrix} \tag{6.15}$$

Set $n = 8 \times 10^{-6}$, and comparing Eq. 6.15 and Eq. 6.13 or Eq. 6.14, we obtain $\beta(0)$, $\alpha(0)$, $\gamma(0)$ and tune $\nu(0) = \mu(0)/2\pi$ for horizontal motion.

$$\begin{aligned} \beta_R(0) &= \frac{R_0}{\sqrt{1-n}} \cong 33.3\text{cm} \\ \alpha_R(0) &= 0 \\ \nu_R(0) &= \sqrt{1-n} \cong 1 \end{aligned} \tag{6.16}$$

Similarly, parameters for vertical motion is

$$\begin{aligned} \beta_Z(0) &= \frac{R_0}{\sqrt{n}} \cong 37.23\text{m} \\ \alpha_Z(0) &= 0 \\ \nu_Z(0) &= \sqrt{n} \cong 8.9 \times 10^{-3} \end{aligned} \tag{6.17}$$

Momentum dispersion is:

$$\begin{aligned} \eta(s) &= \frac{2R_0}{1-n} = 66.6\text{m} \\ \eta'(s) &= \frac{2R_0}{1-n} = 0 \end{aligned} \tag{6.18}$$

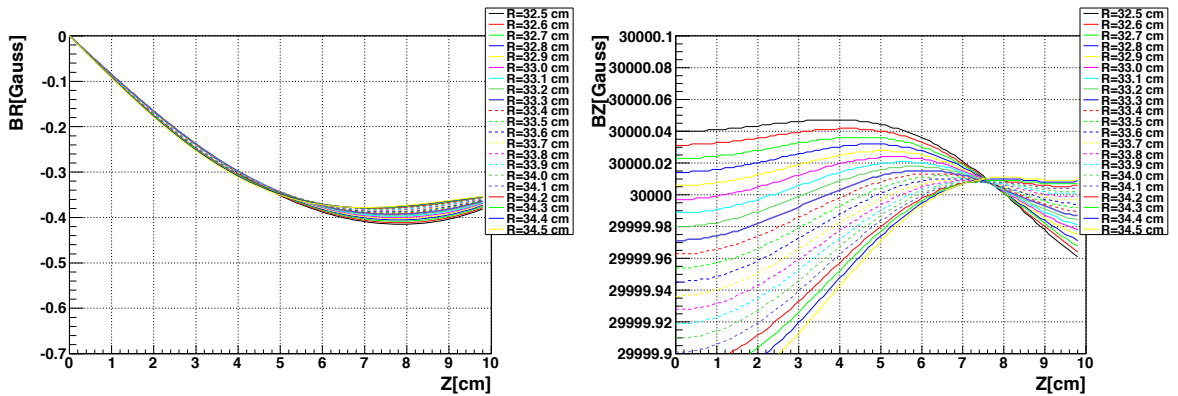Figure 6.21 depicts a realistic weak focus field designed by a private company H.

Figure 6.21: *Realistic example field designed by Private company H.*

Applying this field information, beam phase-spaces in the storage area are estimated by beam tracking calculation (GEANT4). Results are shown in Fig. 6.22. Residual vertical motion in order of 0.35 mrad is possible case to increase acceptance of beam injection. In this case, vertical envelope becomes ±15 mm We also estimate tunes from Fig. 6.21 for both horizontal and vertical from a realistic field. They are consistent with Eq. 6.16 and 6.17.
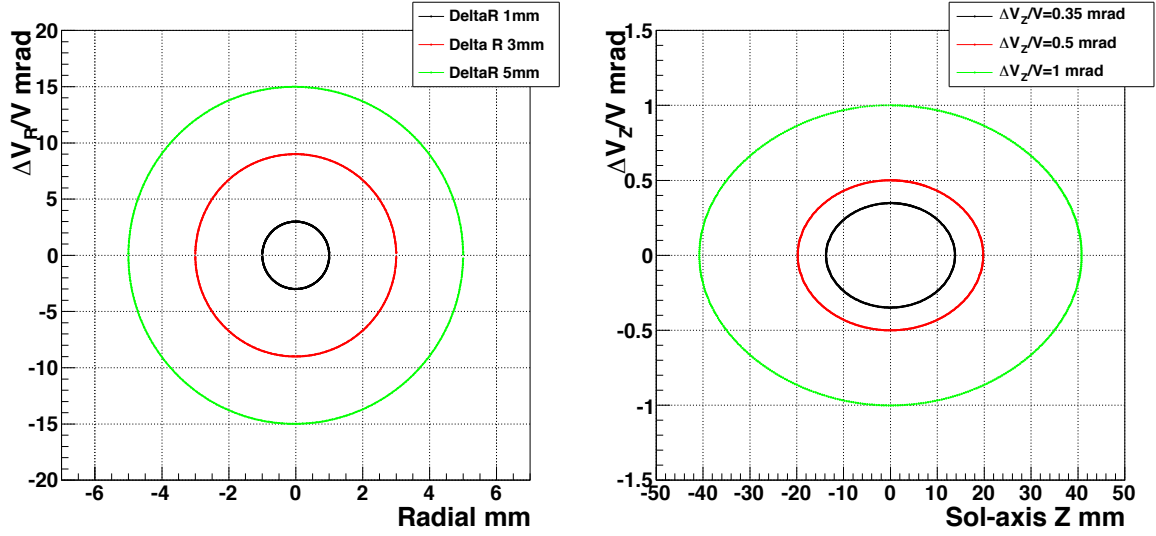

Figure 6.22: *Phase-space estimation with realistic weak field in Fig. 6.21 with several initial condition. Left: radial direction. Even residual momentum in radial direction is 15 mrad (very big compared to design), radial beam size is 5 mm. Right: vertical direction. Possible residual pitch after kick is estimated to 0.35 mrad at Z=0cm. In this case, vertical envelope is ±15 mm.*

Horizontal error field estimation   Horizontal transfer matrix shown in Eq. 6.13 is rewritten as

$$M_R \cong \begin{pmatrix} \cos\frac{s}{R_0} & R_0\sin\frac{s}{R_0} \\ -\frac{1}{R_0}\sin\frac{s}{R_0} & \cos\frac{s}{R_0} \end{pmatrix} \tag{6.19}$$

here we use $n \cong 0$. We assume the presence of horizontal error field in a certain small region δl along the orbit. This error field gives a horizontal kick to beam for every turn beam passes. As shown in left side of Fig. 6.23, horizontal momentum direction is changed for every turn by horizontal kicks as bellow:

$$\theta_{kick} \equiv \frac{\Delta B_Z}{B} \frac{\delta l}{R_0}. \tag{6.20}$$

Since horizontal tune$\cong 1$, beam is kicked every turn in the same region. In this case, displacement from the ideal orbit becomes large at two points: $\phi = \pi/2$ and $\phi = 3\pi/4$ as shown in right side of Fig. 6.23.
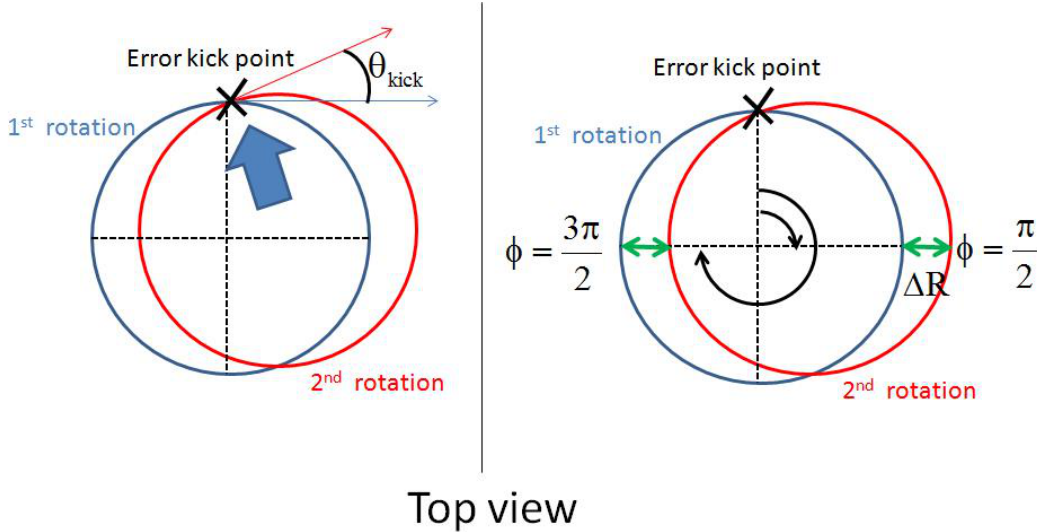

Figure 6.23: *Left: horizontal momentum direction is changed for every turn by horizontal kicks. Right: displacement from the ideal orbit becomes large at two points:$\phi = \pi/2$ and $\phi = 3\pi/4$.*

Therefore displacement ΔR is then,

$$\Delta R = R_0 \Delta \theta_{kick} \tag{6.21}$$

for a single turn. To control displacement Δ_{kick} within 5 mm up to $m = 5000$ turns, $mR_0\theta_R \leq 5$ mm, kick angle for each turn should be $\theta_{kick} \leq 3 \times 10^{-5}$. Therefore, we have

$$\frac{\Delta B_Z}{B} \frac{\delta l}{R_0} \leq 3 \times 10^{-5}. \tag{6.22}$$

Finally we get

$$\frac{\Delta B_Z}{B} \leq 1 \times 10^{-6} \text{ for } \delta l = 10\text{cm}. \tag{6.23}$$

Vertical error field estimation Vertical transfer matrix shown in Eq. 6.14 is rewritten as

$$M_Z = \begin{pmatrix} 1 & s \\ -\frac{ns}{R_0^2} & 1 \end{pmatrix} \tag{6.24}$$

here we use $n \cong 0$. This matrix is approximately drift matrix in free space. Error kick for a single turn for vertical direction is

$$\theta_{kick} \equiv \frac{\Delta B_R}{B} \frac{\delta l}{R_0}. \tag{6.25}$$

Vertical displacement after mth turns becomes

$$\Delta Z \cong 2\pi R_0 \theta_{kick} \frac{m-2}{2}. \tag{6.26}$$

Since vertical tune is 8.9×1^{-3}, beam turns 112 times horizontally during one cycle of vertical beam motion. That is, vertical direction of beam motion flipped at every 56 turns as shown in Fig. 6.24.
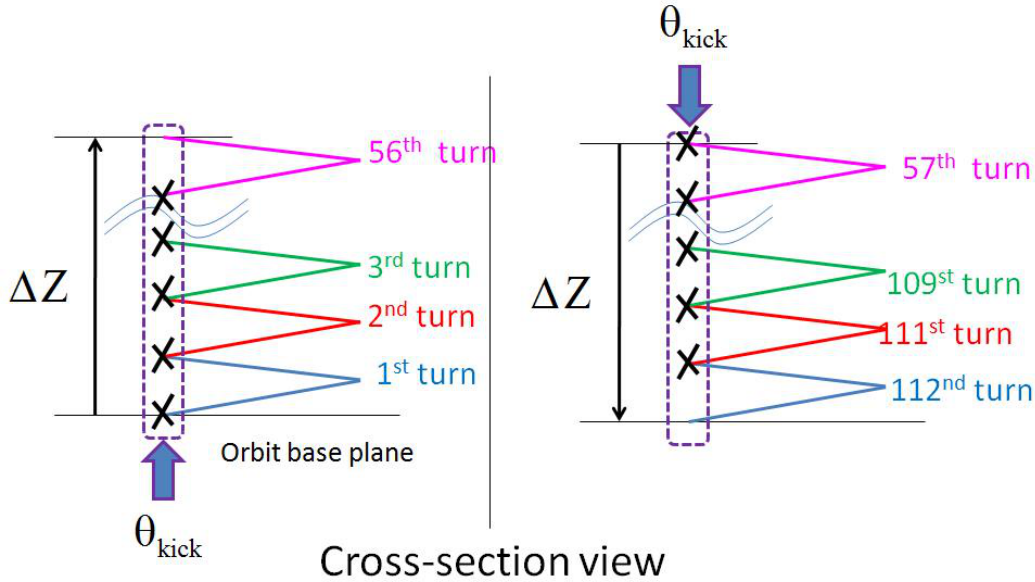

Figure 6.24: *Vertical direction of beam motion flipped at every 56 turns since vertical tune is 8.9×10^{-3}. Beam turns 112 times horizontally during one cycle of vertical beam motion.*

To control displacement ΔZ within 5 mm up to $m = 56$ turn $mR_0\theta_{kick} \leq 5$ mm, kick angle for each turn should be $\theta_{kick} \leq 1.52 \times 10^{-6}$. Therefore, we have

$$\frac{\Delta B_R}{B} \frac{\delta l}{R_0} \leq 1.52 \times 10^{-6}. \tag{6.27}$$

Finally we get

$$\frac{\Delta B_R}{B} \leq 4.8 \times 10^{-6} \text{ for } \delta l = 10 \text{cm}. \tag{6.28}$$

For both horizontal and vertical, weak focusing field should be controlled in order of 1 ppm level.

6.1.5   Beam control from injection field to storage field

The role of the kicker is to move the muon beam onto a stationary orbit. In our case, the muon beam will be guided to the good field region by the solenoidal field only which includes a small radial field above the good field region, reducing the pitch angle of the incoming beam to zero degrees. The pitch angle of the beam in the good field region is planned to be the order of a few mrad. Therefore the required vertical kick is a few mrad, which is achievable. We plan to apply the kick for several cyclotron periods along the orbit. This allows us to apply a lower kicker voltage without strict jitter requirements, and with better stability.

Figure 6.25 depicts one of candidates for the kicker set-up in the storage ring: An anti-Helmholtz type coil system, which is not satisfied exact Helmholtz condition, shown in red, has four loops. Figure 6.26 depicts a zoom on the cross-section of a kicker system. Pairs of coils above and below the storage region have different radii and are separated 6 cm vertically. The upper and lower coils are separated by 24 cm and do not interfere with the storage and detector volumes.

The current direction of the pair of upper coils and the pair of lower coils is the same, but the current is opposite between upper and lower coils. Such a coil system generates mainly a radial field around the region of $|y| < 10$ cm as shown in Fig. 6.26. This radial field is cylindrically symmetric in the radial direction and applies a vertical kick to the muon beam.
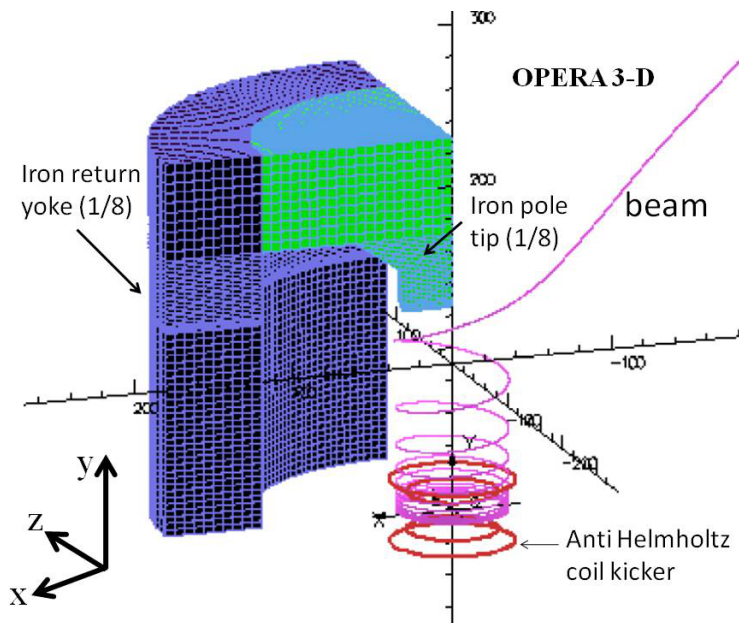

Figure 6.25: *A kicker system (Anti-Helmholtz type coil system) is shown in red lines, in the storage ring magnet. To give an idea of its size, the expected muon beam trajectory, circular iron pole tip and return yoke are also shown.(Solenoid coil is not shown.)*

Figure 6.27 displays an example electrical circuit to drive the kicker coils. In this case, the system can apply a 3.5 mrad kick vertically with a half-sine shaped pulse within a 150 ns (20 cyclotron periods).
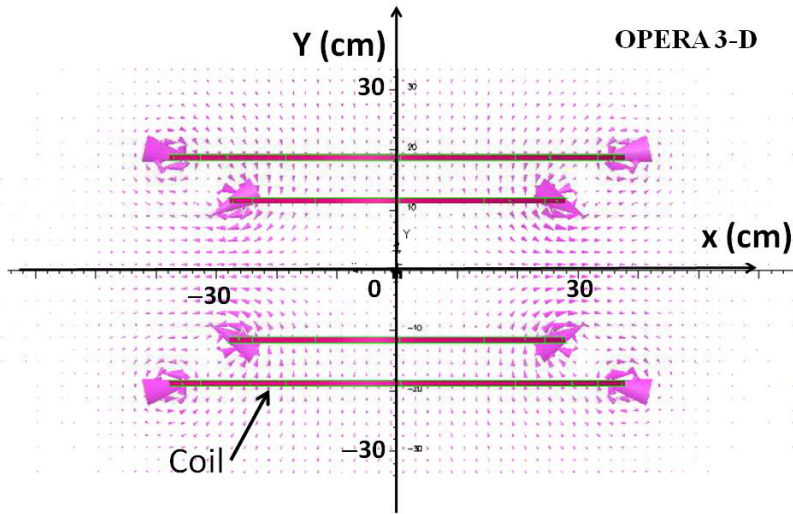
Muon g-2/EDM Experiment, Conceptual Design Report, Revised, December 12, 2011, 11:41 A.M.

Figure 6.26: *Cross-section view of the kicker system (zoom up). Pink triangles depict the direction of the magnetic field.*

$$B_{kick}(t) = B_{peak} \cdot \sin(\omega t), \tag{6.29}$$

here,

$$B_{peak} = 1.3 \times 10^{-4} \text{ T},$$
$$\omega = \frac{\pi}{T_{kick}},$$
$$T_{kick} = 150 \text{ ns}.$$

The simulated current shape as a function of time is displayed in the lower plot in Fig. 6.28. During 150 ns, the vertical drift length of the muon beam is about 7 cm.
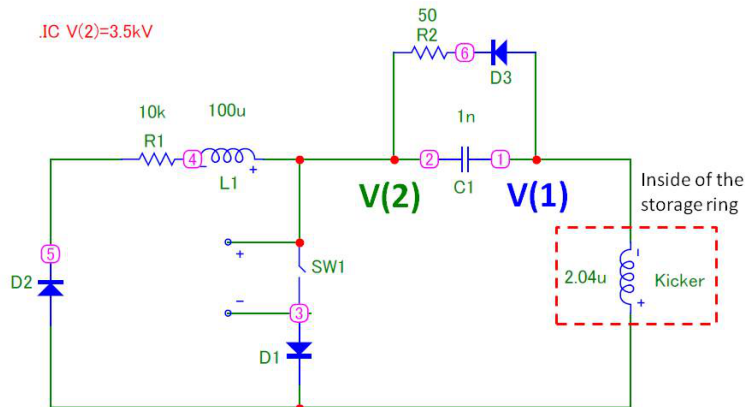
Figure 6.27: *Example circuit for the kicker. Pairs of two ring coil system the storage ring is indicated as the red dotted box.*
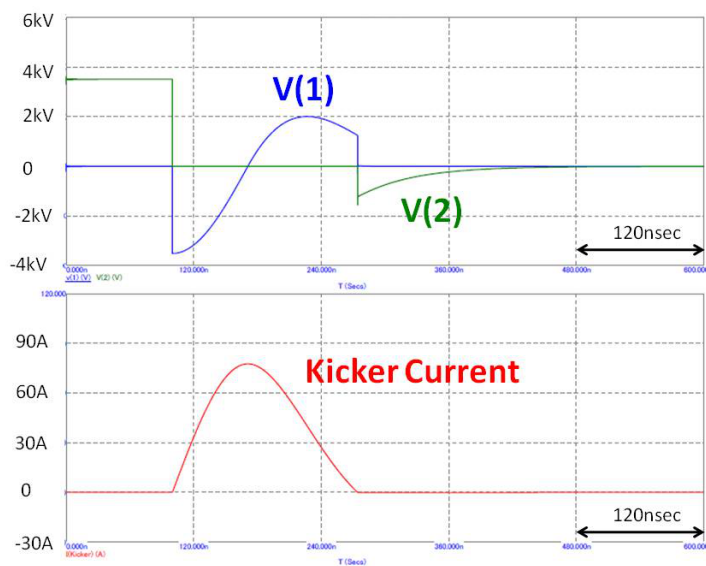

Figure 6.28: *Top: Voltage as a function of time. V(1) and V(2) correspond to pickup points in the circuit. Bottom: Kicker current as a function of time. Half-sin shape can be seen as introduced in Equation 6.29.*

Major two issues for the kicker are eddy currents and induced voltage in quench.

Eddy currents generated in the cryostat wall causes an *error field* and needs to be considered carefully. In the current example circuit, the residual voltage V(2) in Fig. 6.28 remains for ~ 100 ns after the kicker-pulse. We estimated the field from eddy current on the Cryostat wall at the radius=60cm.

We tried two types of materials for the Cryostat wall; one is SUS316 and the other is Aluminum. Figure 6.29 displays total eddy current in Cryostat wall as a function of time. Eddy currents from both materials are nearly identical and cannot separate on the plot.
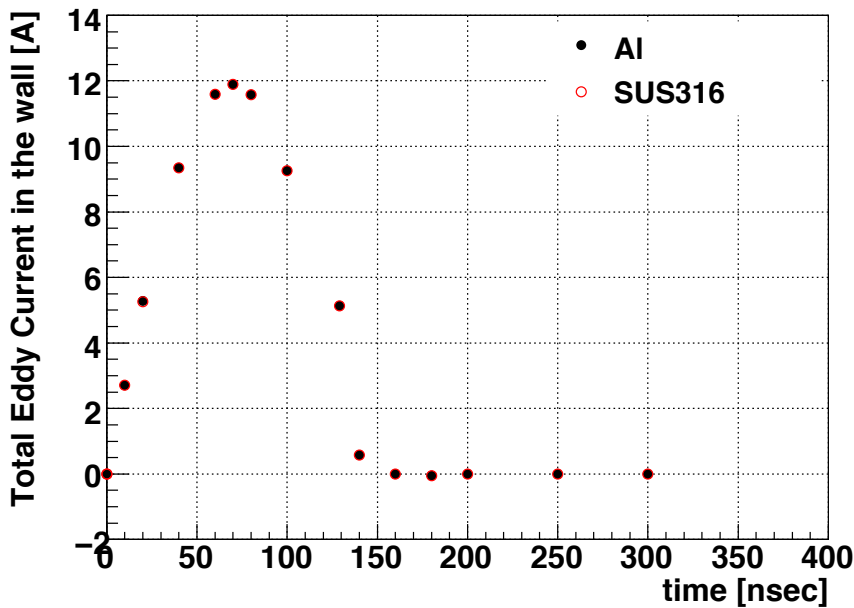

Figure 6.29: *Total eddy current in the wall as a function of time. Time=0 ns is the rise edge of kicker current. Eddy currents from both materials does not change much. Profile of eddy current is similar to that of kicker current ($T_{kick} = 150$ ns, see Fig. 6.28) and do not stay in the wall.*

Profile of eddy current is similar to that of kicker current ($T_{kick} = 150$ ns, see Fig. 6.28) and do not stay in the wall more than 10 ns after the kicker pulse. Figure 6.30 displays the current density profile at t=160 ns. The strength of field changes as a function of time, while density profile on the wall surface is not change much and the dominant component of current direction is parallel to the kicker coils. By use of this profile, we estimate the *residual* field strength from the kicker around the region of the muon orbit as displayed in Fig. 6.31. Horizontal axis corresponds to vertical position. The plot covers $|y| < 10$ cm region where the muon beam stays in the first few hundreds ns. Note that the residual field for the solenoid axis and radial components ΔB_R and ΔB_Y are negligible compared to the main field ($B_Y = 3$ Tesla) from the main coils in the level of 0.1 ppb at t$\geq$ 160 ns. From this study, we conclude that the field from eddy current on the Cryostat wall goes off t$\geq$ 160 ns in the level of 0.1 ppb.
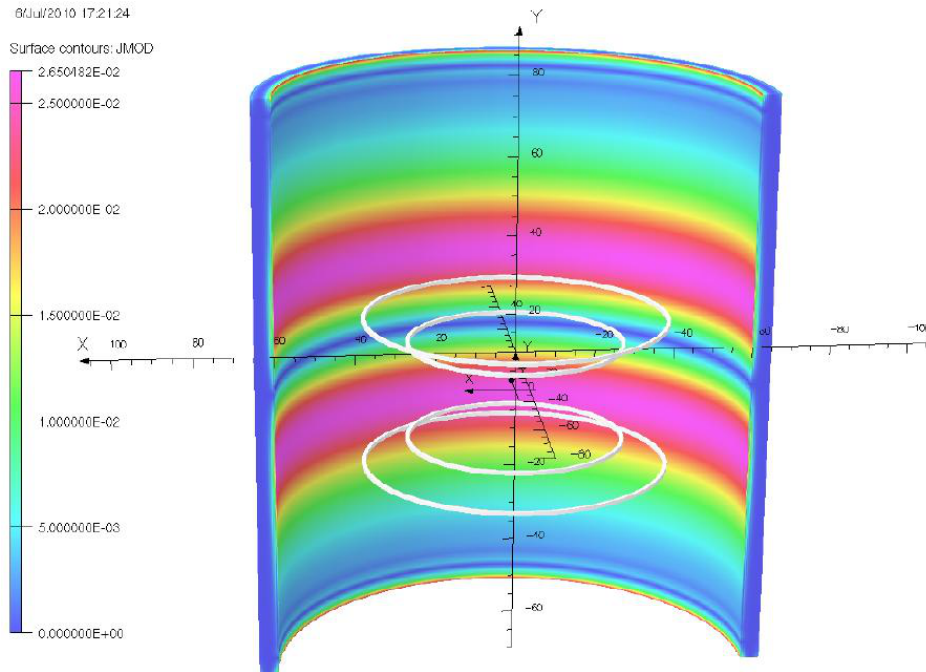
Figure 6.30: *Eddy current density on the SUS316 surface at radial=60 cm at the time t=160 ns. Two pairs of kicker coils are shown in white.*

As for the quench effect on the kicker system, it turns out that this effect is quite small and negligible, because decay time from the maximum field strength B=3 Tesla is the order of few seconds. For example, in case of decay time $\Delta t = 1$ s, dielectric voltage V per kicker coil (radius=0.5m, area S=0.785 m^2) from quench is

$$V = -\frac{\Delta \Phi}{\Delta t} = 2.5 \text{ (V)}. \tag{6.30}$$

Here,

$$\Delta \Phi = B \cdot S = 3 \cdot 0.785 \text{ (Tesla} \cdot \text{m}^2). \tag{6.31}$$

Induced voltage from quench effect can be easily consumed by normal registers R1 and R2 shown in the kicker circuit in Fig. 6.27.

Other major issues for the kicker are the following:

- Kicker field flatness as function of radial position,

- Residual voltage in the circuit may cause an electric field in the space,

We are determining to the best configuration for the coils and expect to achieve sufficient field flatness.
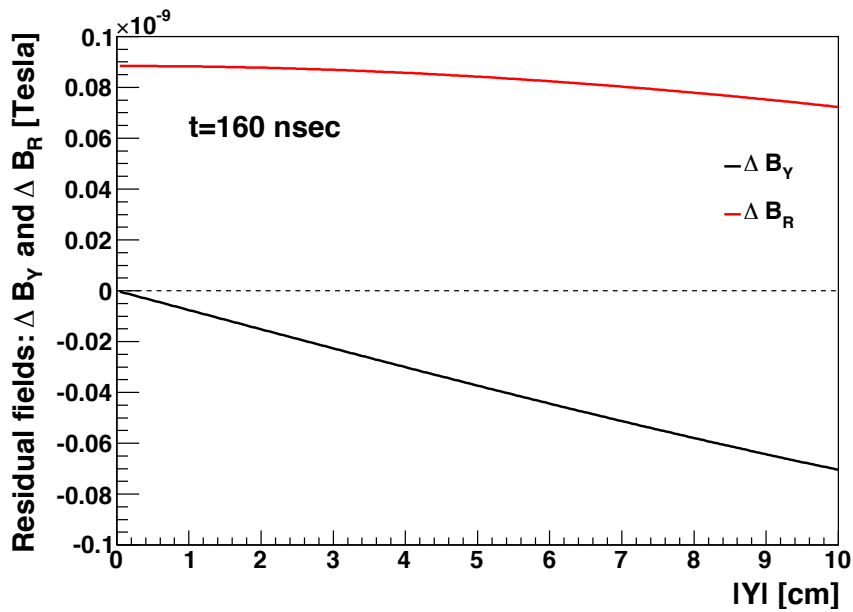
Figure 6.31: *Residual magnetic field strength (Tesla) from the eddy current as a function of vertical position (solenoid axis direction). Black solid line corresponds to field component along the solenoid axis $DeltaB_Y$. Red dotted line corresponds to Radial field $DeltaB_R$. Horizontal axis corresponds to vertical position. This plot covers $|y| < 10$ cm region where the muon beam stays in the first few hundreds ns. Note that these ΔB_R and ΔB_Y are the residual field from eddy current. We have $B_Y = 3$ Tesla from the main coils. Therefore the residual field from eddy current goes off $t \geq 160$ ns in the level of 0.1 ppb.*
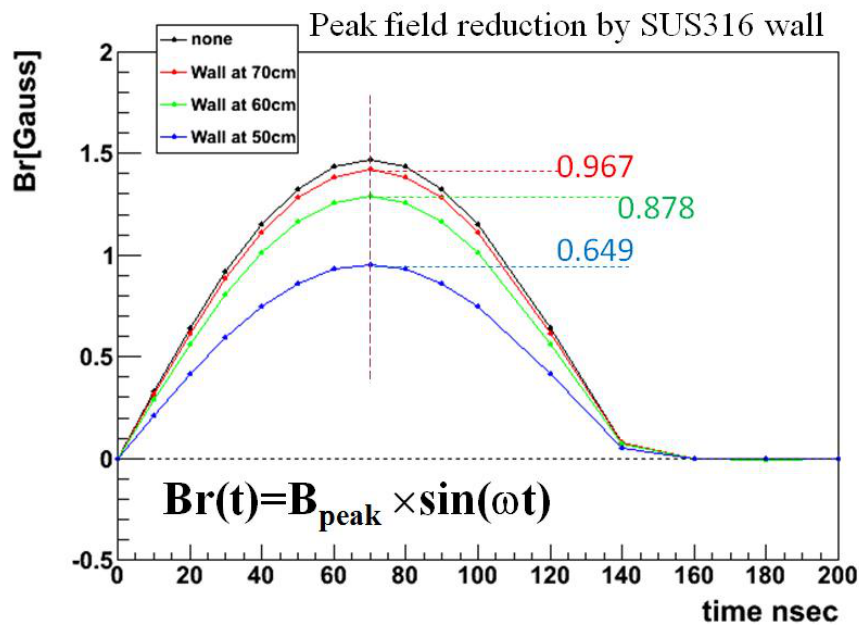
Figure 6.32: *Kicker field as a function of time. Different colors correspond to different positions of SUS316 surface at radial=50, 50 and 70 cm.*

Lastly in this section, we would mention about test bench of kicker system. We have started research and development for high voltage power supply system as shown in Fig. 6.33. By use of dummy coil, which is same inductance of kicker coils, we confirmed measured current on kicker coils satisfies our design. The next step is to build prototype kicker coils and make an adjustment for the high voltage circuit.

Figure 6.33: *Brief status of research and development of high voltage power supply system. By use of dummy coil, which is same inductance of kicker coils, we confirmed measured current on kicker coils satisfies our design.*

CHAPTER **7**

Detection of Decay Positrons

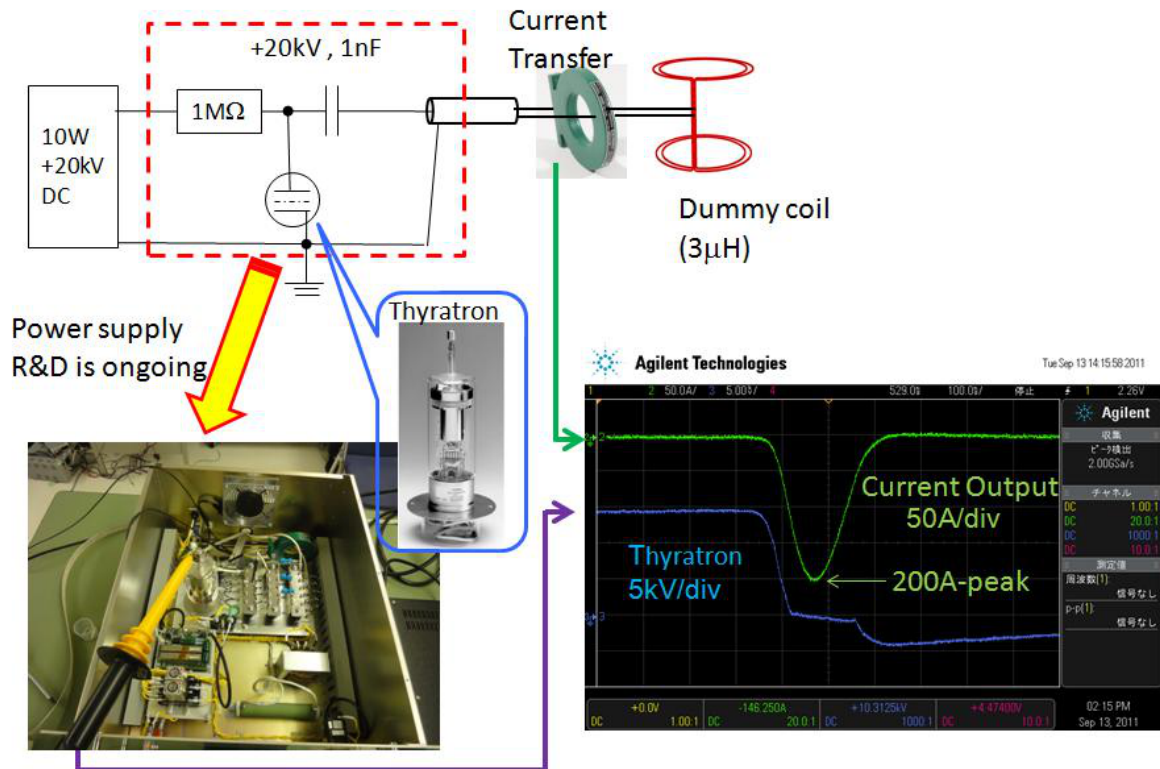Contents

7.1 Requirements

7.1.1 Principle of the measurement

Polarized muon decay

The positive muon decays into a positron, a neutrino and an anti-neutrino; $\mu^+ \to e^+ + \bar{\nu}_\mu + \nu_e$. Parity non-conservation in the weak decay and helicity conservation lead to an asymmetry in the angular distribution of the decay positrons with respect to the direction of the muon spin (θ_S). Viewing the decay in the muon rest frame, the decay positron (e^+) has its maximum momentum and is 100% polarized when the $\bar{\nu}_\mu$ and ν_e are emitted to the opposite direction of the positron. Here, e^+ and $\bar{\nu}_\mu$ are right-handed, ν_e is left-handed. The maximum value of the positron momentum is approximately half of the mass of the muon; $p_{max}^* = m/2 = 53$ MeV/c. [1] We define η as the decay electron momentum relative to its maximum,

$$\eta = \frac{p^*}{p_{max}^*}. \tag{7.1}$$

The probability for a positron in a momentum range dη to be emitted into a solid angle dΩ at an angle θ_S is given by the $V - A$ theory[1, 2];

$$
\begin{aligned}
\mathrm{d}\mathcal{M}(\eta, \theta_S) &= n(\eta)[1 + a(\eta)P_\mu \cos\theta_S]\mathrm{d}\eta\mathrm{d}\Omega, \\
n(\eta) &= 2\eta^2(3 - 2\eta), \\
a(\eta) &= \frac{2\eta - 1}{3 - 2\eta},
\end{aligned}
\tag{7.2}
$$

where θ_S is the angle between the muon spin vector $\vec{S}$ and the positron momentum vector $\vec{p^*}$, and P_μ is the polarization of the muon. The $n(\eta)$ and $a(\eta)$ are displayed in Fig. 7.1. It can be seen that decay positrons tend to be emitted to the muon spin direction ($\cos\theta_S \sim 1$) with their highest energy ($\eta \sim 1$). The number of decay positron can be expressed from Eq. 7.2 and decay factor:

$$N_e(t) = N_0 \cdot \exp\left(-\frac{t}{\gamma\tau}\right) \int\int \mathrm{d}\mathcal{M}(\eta, \theta_S), \tag{7.3}$$

where N_0 is the initial number of muon, $\tau = 2.197\ \mu s$ is the muon life time.

Anomalous $g - 2$ precession in the magnetic field

In the presence of a static and uniform magnetic field, $\vec{B}$, the muon circulates on the plane perpendicular to $\vec{B}$ (Cyclotron motion). The spin vector also rotates in the magnetic field due to its magnetic moment. In this chapter, we assume that both the electric field and the electric dipole moment are zero. We discuss those effects in subsection 7.1.2 and chapter 10.

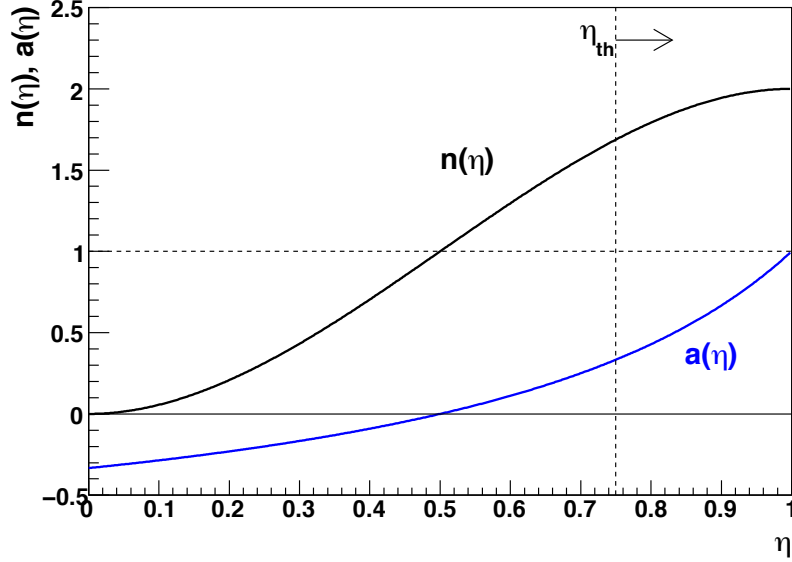[1]In this chapter, variables with the symbol $*$ denotes ones defined in the muon rest frame.

Muon g-2/EDM Experiment, Conceptual Design Report, Revised, December 12, 2011, 11:41 A.M.

Figure 7.1: *Analyzing power $a(\eta)$ and event fraction $n(\eta)$ as functions of η, the positron energy fraction in the muon rest frame. η_{th} is the optimal threshold to measure the spin precession.*

The frequency of the Cyclotron motion in the magnetic field $\vec{B}$ (Cyclotron frequency, $\vec{\omega}_c$) is expressed as

$$\vec{\omega}_c = -\frac{e\vec{B}}{m\gamma}, \tag{7.4}$$

where e is the electric charge of muon, $\gamma = \frac{E}{m}$ is the Lorentz gamma factor. Similarly, the spin precession frequency $\vec{\omega}_S$ is expressed as

$$\vec{\omega}_S = -\frac{ge\vec{B}}{2m} - (1-\gamma)\frac{e\vec{B}}{m\gamma}, \tag{7.5}$$

where g is the g-factor of the muon. The anomalous spin-precession frequency $\vec{\omega}_a$ is defined as a difference of these frequencies, i.e. frequency of spin precession relative to the momentum;

$$\vec{\omega_a} = \vec{\omega_S} - \vec{\omega_c} = -\frac{e\vec{B}}{m}\left(\frac{g-2}{2}\right) \equiv -\frac{e}{m}a_\mu\vec{B}. \tag{7.6}$$

In the proposed experiment, where $\gamma = 3$ ($p_\mu = 300$ MeV/c) and $B = 3$ T, we obtain the cyclotron period $T_c = 2\pi\omega_c = 7.387$ ns and the anomalous spin-precession period $2\pi\omega_a = 2111$ ns.

We measure the anomalous spin-precession frequency (Eq. 7.6) by utilizing the correlation between the muon spin and the positron decay angle (Eq. 7.2). In the following, we show how the anomalous spin-precession frequency (Eq. 7.6) and positron decay distribution (Eq. 7.2) can be related.

In the muon rest frame, we define x coordinate along the muon momentum in the laboratory frame, z coordinate along the direction of the magnetic field, and y coordinate being perpendicular to x and

z coordinates. The magnetic field vector is expressed as $\vec{B} = (0, 0, B)$. The muon spin vector $(\vec{S})$ rotates with the frequency of $\vec{\omega}_a$

$$\vec{S} = (\cos(\omega_a t), \ \sin(\omega_a t), \ 0). \tag{7.7}$$

We define a polar angle χ^* and a azimuthal angle ψ^* of the positron direction in the rest frame with respect to the direction of the magnetic field (z axis). The unit vector of the decay positron momentum is expressed as

$$\overrightarrow{p^*}/|\overrightarrow{p^*}| = (\sin\chi^* \cos\psi^*, \sin\chi^* \sin\psi^*, \cos\chi^*). \tag{7.8}$$

The $\cos\theta_S$ can be written as,

$$
\begin{aligned}
\cos\theta_S &= \vec{S} \cdot \frac{\overrightarrow{p_e^*}}{|\overrightarrow{p_e^*}|}, \\
&= \sin\chi(\cos\psi^* \cos(\omega_a t) + \cos\psi^* \sin(\omega_a t)), \\
&= \sin\chi \cos(\omega_a t - \psi^*).
\end{aligned}
\tag{7.9}
$$

Substituting Eq. 7.9 into Eq. 7.3, one find:

$$N_e(t) = N_0 \cdot \exp\left(-\frac{t}{\gamma\tau}\right) \int\int n(\eta)[1 + a(\eta)P_\mu \sin\chi \cos(\omega_a t - \psi^*)]\mathrm{d}\eta\mathrm{d}\Omega. \tag{7.10}$$

When the angle ψ^* is constant over time, number of positron changes with time at a frequency of ω_a. We will discuss in next section that a requirement of high energy positrons in the laboratory frame would effectively select forward-going positrons in the muon rest frame. Thus, ω_a can be extracted from the time spectrum of the positron decay.

Lorentz boost to the laboratory frame

From Eq. 7.10, it is clear that higher the asymmetry, it is more sensitive to ω_a. However, statistics of decay positrons become poorer since we are limited only within a narrow η-bin in the muon rest frame. There is an optimal energy threshold to measure ω_a shown as $\eta_{th} = 0.75$ in Fig. 7.1. However, applying this threshold requires reconstructing the decay in the muon rest frame, which may not be possible due to an uncertainty in the positron momentum direction in the muon rest frame. We consider the decay, instead, in the laboratory frame.

The muon rest frame is rotating in the laboratory frame, as displayed in Fig. 7.2. Transformation to the laboratory frame is straightforward by the Lorentz boost along the direction of muon momentum. Figure 7.3(top) displays the mapping of positron momentum from the muon rest frame to the laboratory frame. After the Lorentz boost, the maximum momentum of the positron increased from 52 MeV/c to 309 MeV/c. Positrons in the higher momentum region in the laboratory frame comes only from those decayed in forward direction with large η in the muon rest frame , while lower momentum positrons comes from wider η region with more population in the lower η region. This correlation implies that the selection of the higher momentum positrons in the laboratory frame would
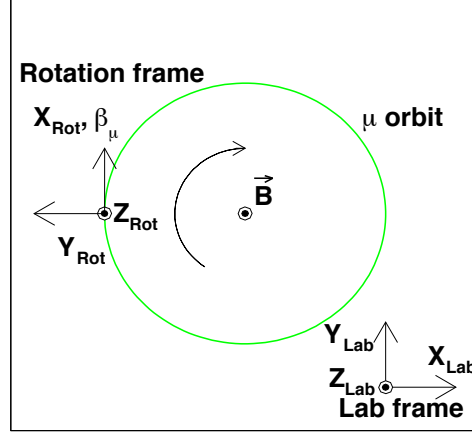
Figure 7.2: *Definitions of the rotation frame (muon rest frame) and the laboratory frame. The origin of the rotation frame is the muon decay point*

bring us a forward-going positron sample with large η without transforming back to the muon rest frame.

The positron time spectra for 65 M simulated events is shown in Fig 7.4 for twelve positron energy ranges in the laboratory frame. It can be seen that the sign and amplitude of the modulation in the time spectrum due to the anomalous precession ω_a changes with the positron energy.

We select higher energy positrons by applying a proper minimum-energy threshold in the laboratory frame. The fraction of decay positrons above the energy threshold (E_{lab}^{th}) and effective analyzing power in the laboratory frame are derived as follows.

We describe the fraction of events above an energy threshold of $E_{lab} \geq E_{lab}^{th}$ as C^{th}. The Cth and effective analyzing power A weighted by the yield are expressed by using Eq. 7.2 and Eq. 7.10:

$$C^{th} = \frac{\int n(\eta)\mathrm{d}\eta \int \mathrm{d}(\cos\chi^*) \int \mathrm{d}\psi^*}{\int \mathrm{d}\eta \int \mathrm{d}(\cos\chi^*) \int \mathrm{d}\psi^*}. \tag{7.11}$$

The analyzing power for $E_{lab} \geq E_{lab}^{th}$ is expressed as:

$$C^{th} \cdot A = \frac{\int \int \int n(\eta)a(\eta)\{\sin\chi^* \cos(\omega_a \cdot t - \psi^*\}\mathrm{d}\eta\mathrm{d}(\cos\chi^*)\mathrm{d}\psi^*}{\int \mathrm{d}\eta \int \mathrm{d}(\cos\chi^*) \int \mathrm{d}\psi^*}. \tag{7.12}$$

In the limit of $\gamma \ll 1$, these integrations become

$$\begin{aligned}
C^{th} &= \left[1 - \frac{5b}{6} + \frac{b^3}{8} + \frac{b^4}{48}\right], \\
C^{th} \cdot A &= \left[\frac{b}{6} - \frac{b^3}{8} + \frac{b^4}{24}\right],
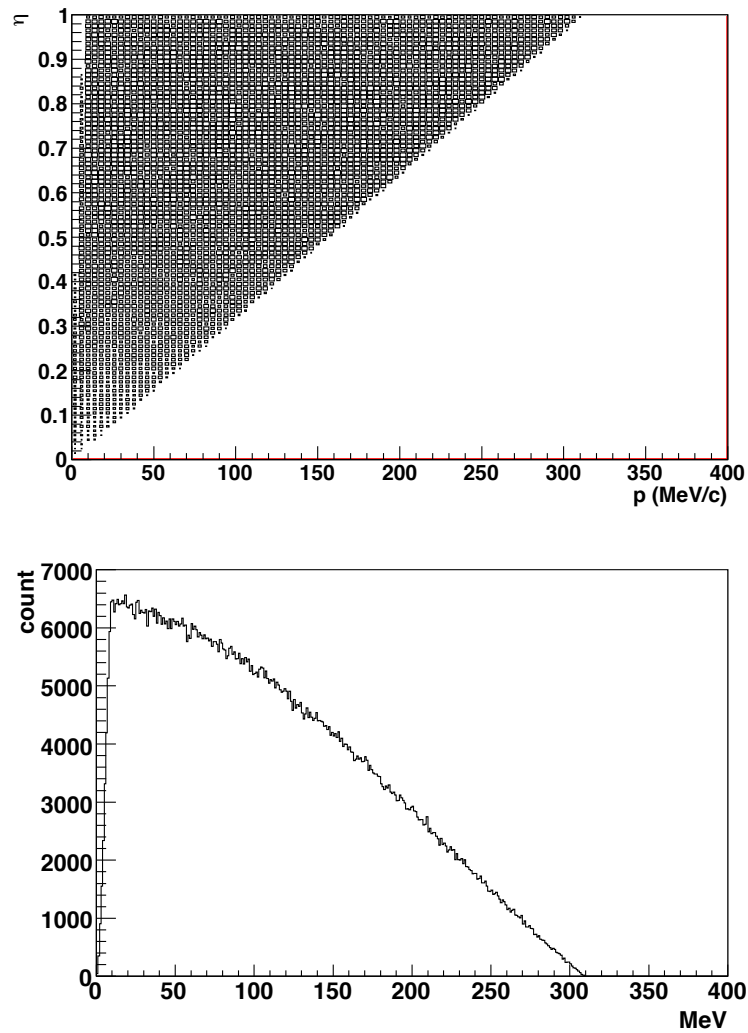\end{aligned} \tag{7.13}$$

Figure 7.3: *Simulated positron energy spectra. Top: Normalized positron momentum in the muon rest frame η vs positron momentum in laboratory frame. Bottom: Energy spectrum of the positrons in the laboratory frame.*
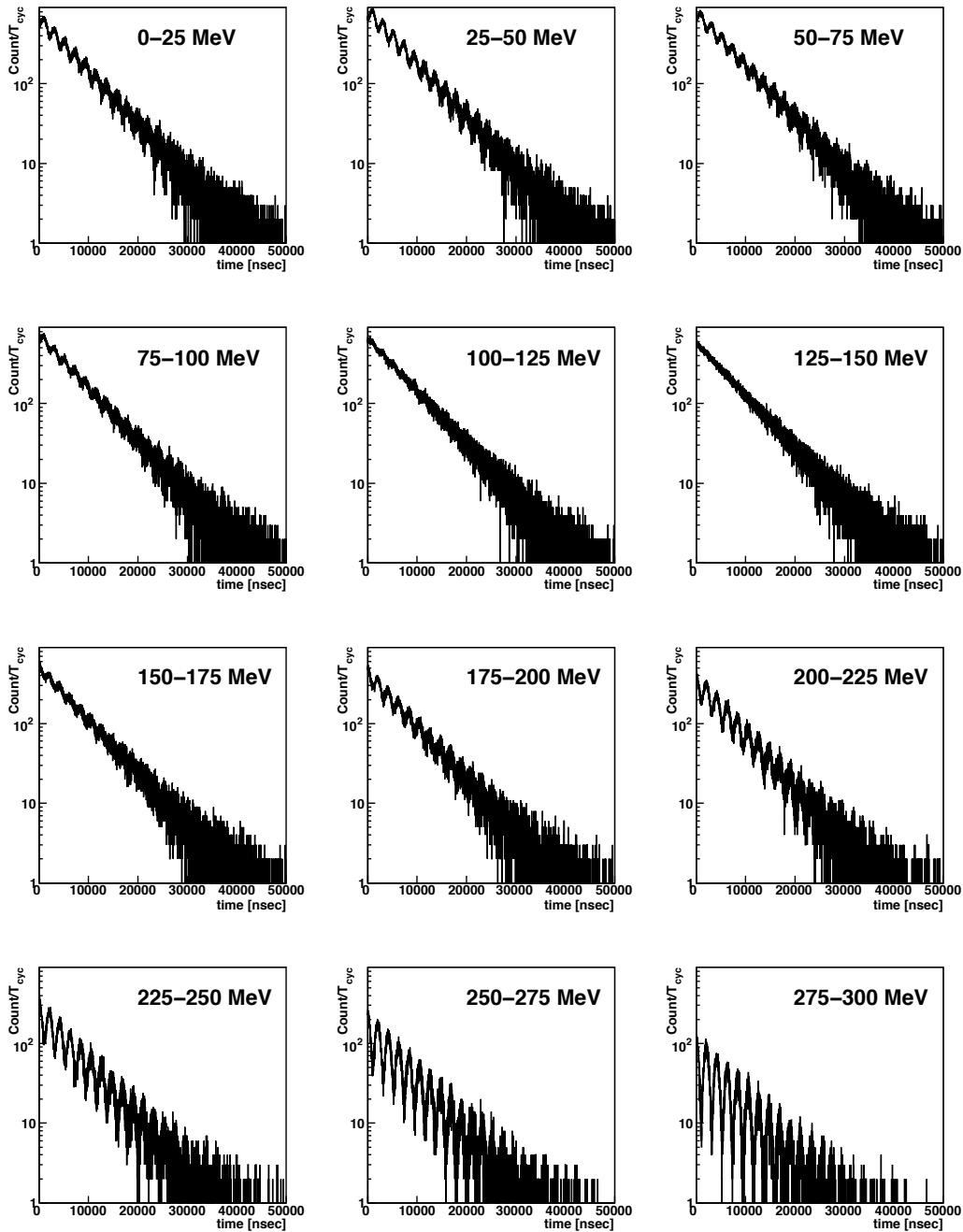
Figure 7.4: *Positron time spectra generated by* GEANT4 *for 65M events for several energies. Muon polarization is assumed to be 100 percent* $(P_\mu = 1)$.

where $b = \frac{E_{lab}^{th}}{\gamma(m/2)}$. The figure of merit (FOM) for the measurement of ω_a is $C^{th} \cdot A^2$. Figure 7.5 displays C^{th}, A, and FOM as a function of b. The E_{lab}^{th} at the maximum FOM is $E_{lab}^{th} = 1.27 \times 3 \times 106/2$ MeV = 200 MeV for $\gamma = 3$. The optimum E_{lab}^{th} was confirmed by the full Monte Calro simulation without any approximation. More detailed description on the derivations are given in the proposal [3].
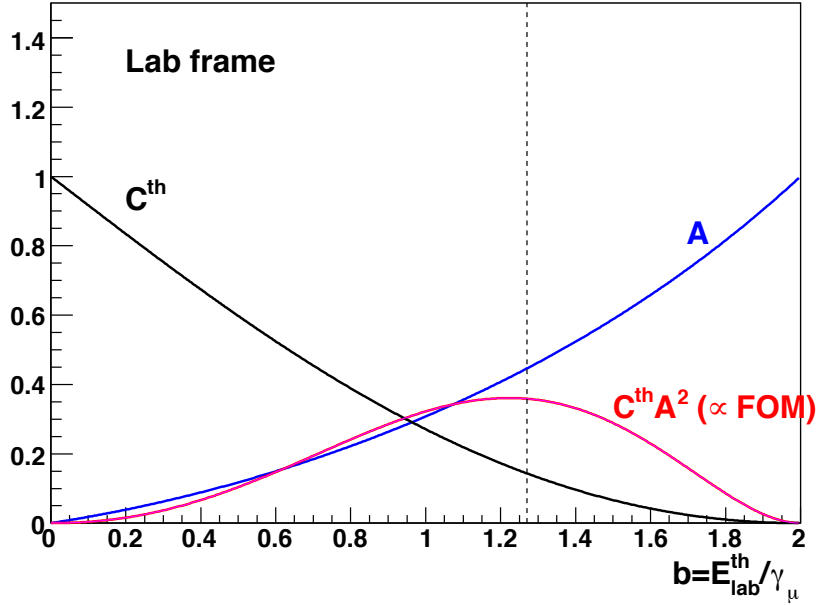
Figure 7.5: *The fraction of decay positron above E_{lab}^{th} (C^{th}) and the effective analyzing power A as a function of normalized threshold $b = \frac{E_{lab}^{th}}{\gamma(m/2)}$. The FOM is shown in red curve. At $b = 1.27$, the FOM is maximum, where effective analyzing power is 0.46.*

At the optimum $E_{lab}^{th} = 200$ MeV, fraction of positron decay above the threshold is $C^{th} = 0.13$, and effective analyzing power is $A = 0.46$. The positron emission angle has its maximum at 250 mrad. The positron momentum components perpendicular to the magnetic field (p_{xy}) has to be greater than 194 MeV/c for $E_{lab}^{th} = 200$ MeV.

We summarize relevant parameters of muon beam characteristics and properties of decay positron in Table 7.1. The positron time spectrum for proposed data-taking period (1×10^7 s) is shown in Fig. 7.6.

Figure 7.6: *Simulated positron time spectrum with the optimum energy threshold $E_{lab}^{th} = 200$ MeV.*

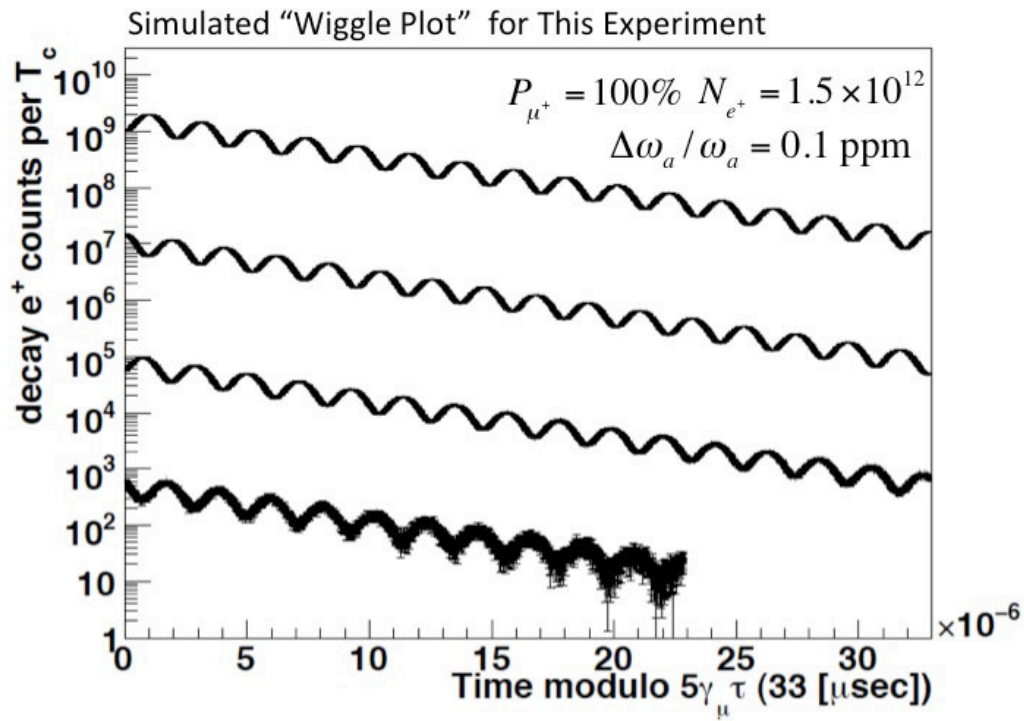| Section	Parameter	Value
Muon Beam	Mass	105.658 367(4) MeV/c^2
	Momentum	300.0 MeV/c
	Energy	318.1 MeV
	β	0.943
	γ	3.011
	Dilated life time	6.615 μs
	Radius of Cyclotron motion	33.33 mm
	Cyclotron period $2\pi/\omega_c$	7.387 ns
	Anomalous spin precession period $2\pi/\omega_a$	2111 ns
		285.7 turns
	Polarization	>0.9
	Intensity	1×10^6/s (4×10^4/spill)
	Pulse repetition rate	25 Hz
Positron	Mass	0.510 998 910(13) MeV/c^2
	Maximum energy (muon rest frame)	52.83 MeV
	Maximum energy (laboratory frame)	309.0 MeV
	Optimum energy threshold E_{lab}^{th}	200 MeV
	Fraction C^{th} at $E_{lab}^{th} = 200$ MeV	0.13
	Effective A at $E_{lab}^{th} = 200$ MeV	0.46
	Maximum emission angle at $E_{lab}^{th} = 200$ MeV	250 mrad (14.3 deg)
	Minimum p_{xy} at $E_{lab}^{th} = 200$ MeV	194 MeV/c

Table 7.1: *Relevant parameters of muon beam characteristics and decay properties*

7.1.2   Requirements on positron detector

Magnetic field

The positron detector is located under the 3 T magnetic field. The detection sensor and readout electronics should be operational under the 3 T field. Detector components should not disturb the magnetic field in the muon storage region. In order to achieve the target precision of $\Delta a_\mu = 0.1$ ppm, the magnet will be carefully shimmed to achieve the local precision of 1 ppm, which would lead uncertainty of integrated B-field down to $\Delta B/B \ll 0.1$ ppm level. The magnetic field change up to 10 ppm level could be taken care by the active shimming coils. Detector component should not change the magnetic field beyond 10 ppm (30 μT).

Electric field

Detector components should not generate electric field in the muon storage region. A simple relation between ω_a (Eq. 7.6) and a_μ is realized when there is no electric field. If electric field is present, ω_a becomes

$$\begin{aligned}
\vec{\omega_a} &= -\frac{e}{m}[a_\mu \vec{B} - (a_\mu - \frac{1}{\gamma^2 - 1})\frac{\vec{\beta} \times \vec{E}}{c}], \\
&\equiv -\frac{e}{mc}[\vec{\theta_B} - \vec{\theta_E}].
\end{aligned} \tag{7.14}$$

Substituting $a_\mu = 1 \times 10^{-3}, \gamma = 3, B = 3$ T, and $c = 3 \times 10^8$ m/s, one obtain

$$|\vec{\theta_B}| \sim (3 \times 10^8\ [m/s]) \times (1 \times 10^{-3}) \times 3\ [T] = 9 \times 10^5 [V/m], \tag{7.15}$$

$$|\vec{\theta_E}| \sim \frac{1}{3^2 - 1}E, \tag{7.16}$$

$$\frac{|\vec{\theta_E}|}{|\vec{\theta_B}|} \sim 1.4 \times 10^{-7}E[m/V]. \tag{7.17}$$

We note that precision of the magnetic field is $\Delta B/B = \Delta|\vec{\theta_B}|/|\vec{\theta_B}|$ is less than 0.1 ppm. Relative electric-field strength $|\vec{\theta_E}|/|\vec{\theta_B}|$ should not exceed 0.1 ppm. The electric field in the muon storage region should be $E \ll 1$ V/m (10 mV/cm).

Kinematic and geometrical coverage

The positron detector should detect positrons efficiently with sufficient acceptance. Muons decay at the radial coordinate r=333 mm. The maximum momentum of positron is 309 MeV/c which is larger than the muon momentum 300 MeV/c. However, most of positrons has their momentum less than the muon momentum (see Fig. 7.3). These positrons curls into the inner region of the muon storage region (r <333 mm).

The radial and axial distributions of positron tracks for their first turn in the magnetic field are shown in Fig. 7.7 for the radial coordinate from r=50 mm to 300 mm. At larger radial coordinate, all positrons

pass though, while smaller radial coordinate, positrons with the energy range $50 < E < 250$ MeV can access. As for the axial coordinate, the distributions are not strongly depend on the energy as they are predominantly determined by the vertical component of momentum which is a small fraction of total momentum. Most of positrons are contained within ± 200 mm in the axial coordinate. The sensitive volume of the detector should cover these coordinates.

As discussed in the previous section, positrons of interest ($E > 200$ MeV) are emitted along the direction of muon within a cone of the polar angle less than 0.25 rad. At the optimum energy threshold of 200 MeV, the minimum momentum in a plane perpendicular to the magnetic field is 194 MeV/c. The detector should be efficient for such positrons.
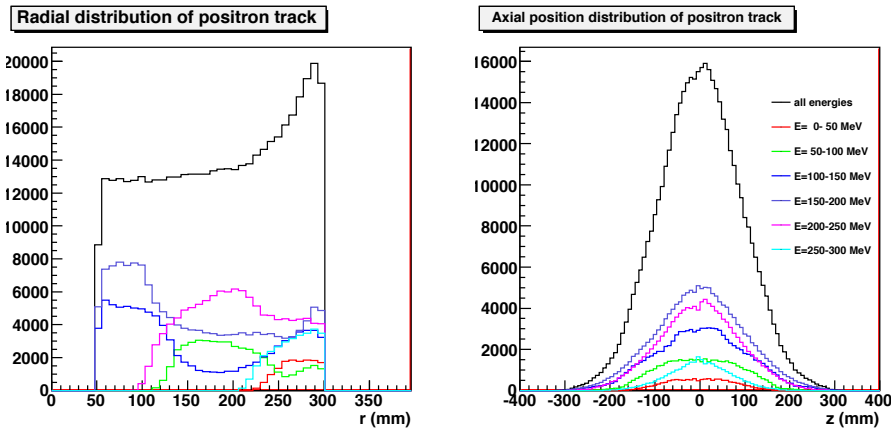

Figure 7.7: *Distributions of positron track in radial (left) and axial direction (right). The positions of positions are sampled for their first turn in the magnetic field.*

Accuracy and resolution of the time measurement

The muon decay time is measured by positron measurement by the detector with a time-to-digital converter (TDC).

In the TDC measurement, the clock system determines the precision of the time stamp. The precision of time stamp ΔT relative to the $g - 2$ precession period T_{g-2} should be $\frac{\Delta T}{T_{g-2}} \ll \frac{\Delta\omega/}{\omega} = 0.1$ ppm. Thus, $\Delta T \ll 0.1$ ppm $\times$ 2.1 μs $= 0.2$ ps. The time stamp must be stable within required precision ($\Delta T \ll 0.2$ ps) over a cycle of the measurement $T_M = 41\mu s$. Therefore, required stability of the clock frequency should be $\frac{\Delta f}{f} = \frac{\Delta T}{T_M} \ll 0.2 \ ps/41 \ \mu s = 5 \times 10^{-9}$.

Resolution of time is determined by jitter in TDC clock and timing resolution of the detector. The clock jitter is usually much better than detector timing resolution. The finite resolution of time measurement would smear the positron time spectrum. The smearing effect on the amplitude of $g - 2$ precession signal is a cosine effect as shown below.

As discussed in the previous section (Eq. 7.10, the positron time distribution has a modulation due

to $g - 2$ precession at a frequency of ω_a with the amplitude A. Dropping irrelevant decay factor for the moment, the timing distribution of the positron becomes $n(t) = n_0(1 + A\cos\omega_a t)$. The smeared timing spectrum $\bar{n}(t)$ with a time resolution σ_t is expressed as a convolution integral:

$$
\begin{aligned}
\bar{n}(t) &= \int \frac{1}{\sqrt{2\pi\sigma_t^2}} e^{-\frac{(t'-t)^2}{2\sigma^2}} n(t')dt', \\
&= \frac{n_0}{\sqrt{2\pi\sigma_t^2}} \int e^{-\frac{(t'-t)^2}{2\sigma_t^2}} (1 + A\cos\omega_a t')dt', \\
&= \frac{n_0}{\sqrt{2\pi\sigma_t^2}} \int e^{-\frac{\Delta^2}{2\sigma_t^2}} (1 + A\cos(\omega_a t + \omega_a\Delta))d\Delta, \text{ (where } t' = t + \Delta) \\
&= \frac{n_0}{\sqrt{2\pi\sigma_t^2}} \int e^{-\frac{\Delta^2}{2\sigma_t^2}} (1 + A\cos\omega_a t \ \cos\omega_a\Delta)d\Delta, \\
&= \frac{n_0}{\sqrt{2\pi\sigma_t^2}} \int e^{-\frac{\Delta^2}{2\sigma_t^2}} \left(1 + A\left(1 + \frac{(\omega_a\Delta)^2}{2}\right)\cos\omega_a t\right)d\Delta, \text{ (if } \omega_a\Delta \ll 1), \\
&\cong n_0\left(1 + A\left(1 - \frac{(\omega_a\sigma_t)^2}{4}\right)\cos\omega_a t\right). &\text{(7.18)}
\end{aligned}
$$

in the last two equations, we assumed a relation $\omega_a\sigma_t \ll 1$. The last equation shows that smearing effect effectively reduces the analyzing power by a quadratic factor of $\frac{(\omega_a\sigma_t)^2}{4}$. The precession precession period $(\frac{2\pi}{\omega_a})$ is 2.1 μs. For example, if the detector has 10 ns time resolution, the analyzing power would be reduced by a 2×10^{-4}, which has no impact on the ω_a sensitivity.

In summary, the time stamp needs to be accurate better than 5×10^{-9} accuracy, while requirement on the detector timing resolution is not stringent in the context of extracting ω_a from the positron timing spectrum.

Energy resolution

The energy resolution of the positron would primarily affect sharpness of the energy threshold. The figure-of-merit (FOM) as a function of the positron energy threshold was discussed in the previous section (Fig. 7.5). At the optimum threshold where the FOM is maximum, the derivative of the FOM is zero. From Fig. 7.5, one can see that the energy threshold at 10% lower FOM is 24% below and 12% above the optimum threshold. The energy resolution of 10% level would reduce the FOM (and overall sensitivity) by a minor factor less than 10%.

Early-to-late stability

The muon beam spill comes every 40 ms synchronously with the J-PARC proton beam. The intensity of the muon beam is $10^6/\text{s} = 40\text{k}$ muons per spill. The number of positron decay is decreased by the dilated life time of 6.6 μs. There are 15.6 anomalous precessions during 5 times dilated lifetime, 33 μs. During this period, the instantaneous rate of positron changes by a factor of $e^{-5} = 1/150$.

The detector must keep their performance (timing/position resolution, efficiency, response function)

stable as a function of time in order not to introduce any undesired bias in the timing distribution which in turn will be a source of systematic uncertainty.

One of major sources of early-to-late effects is the pile-up. Here is an example that the measurement of positron time is systematically shifted due to pile up effects. When two detector signals piles up, the time of the first pulse would systematically be shifted to earlier time. Probability of pile-up per hit is proportional to the instantaneous rate. We model that average time-shift due to the pile-up is proportional to the instantaneous rate, i.e. the positron time distribution $n(t)$ would be modified to

$$
\begin{aligned}
\tilde{n}(t) &= n(t'), \\
t' &= t - \Delta t \left(\frac{n(t)}{n(0)} \right), \\
n(t) &= n_0 \mathrm{e}^{-\frac{t}{\gamma\tau}} (1 + A \cos \omega_a t).
\end{aligned}
\tag{7.19}
$$

The correlation between Δt and ω_a is studied in terms of chi-square χ^2 (Fig. 7.8(left)). The $\frac{\Delta \omega_a}{\omega_a}$ at the minimum χ^2 is shifted with Δt, which is a measure of the systematic error. There is a negative correlation with the time shift parameter Δt as shown in Fig. 7.8(right). In order not to spoil anticipated statistical uncertainty of 0.1 ppm, the timing shift Δt should be less than 8 ps from early to late. We note that this level of stability was achieved in the BNL E821 experiment in which timing shifts were found to be limited to less than 4 ps from early-to-late times [4].
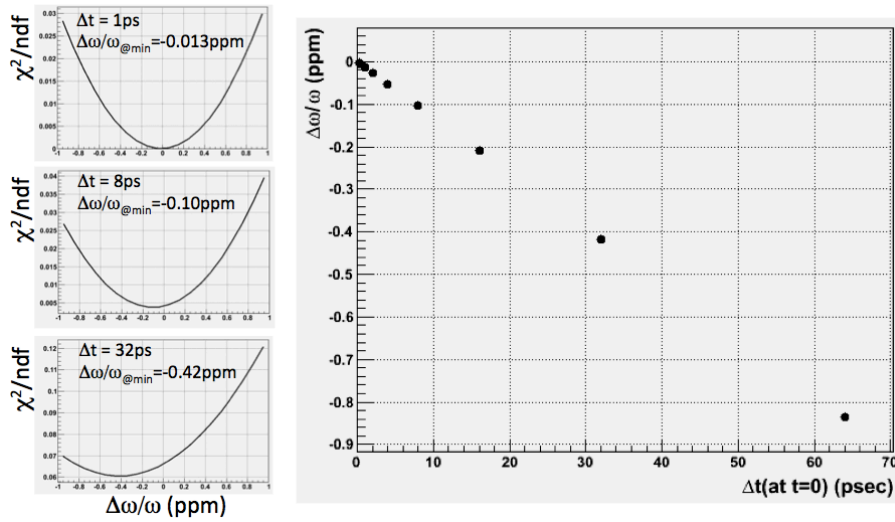

Figure 7.8: *(left) Distributions of χ^2/ndf for three different cases of timing shift scenario. (right) Shift in ω_a as a function of the timing shift parameter.*

The pile-up of positrons could result in early-to-late change of detection efficiency. This effect could be suppressed by taking a ratio of several positron samples with different initial phases in the anomalous

spin precession. This can be realized in following cases, (1) data randomly divided by four subsets and give offsets of half of the $g-2$ precession period as was done in the E821, (2) data taken with alternative muon spin orientation at injection (forward/backward, or left/right), and (3) data divided by subsets of positrons decaying left-hand-side and right-hand-side of the muon momentum.

For the option (3), there is an additional requirement for the detector to distinguish left and right decay of muons. The positron track makes a circular trajectory in the xy-plane (a plane perpendicular to the magnetic field). There are two points where the track-trajectory projected on the xy-plane crosses the muon orbit. One of the crossing point corresponds to muons decaying in-word (right decay), the other corresponds to muons decaying out-word (left decay). The separation of the left decay and the right decay can be made if one can distinguish these two candidates by using the 3-dimensional extrapolation to the muon orbit.

This requires sufficient track angle resolution $(d(r\phi)/dz)$, and the vertex position resolution along the muon orbit $(\Delta(R\phi))$, where r and ϕ represents radius and azimuthal rotation angle of positron track, and R represents radius of the muon orbit. The emission angle of positrons of interest $(E > 200$ MeV$)$ in the laboratory frame distributes in the range of ± 250 mrad. Monte-Calro studies shows that 90% of those positron can be separated to left and right decays if the detector has vertex angle resolution of 2.5 mrad(σ) and vertex position along the muon orbit of 6 mm(σ).

7.2 Detector configuration

7.2.1 Detector concepts

The number of muon tracks which are injected into detection volume per 1 beam spill will be 40k track/spill. If the sampling time is assumed to 5 ns, the track rate at injection is 30.5 track/5ns. Thus, high granularity is desired to suppress systematic uncertainty from pile-up. Tracking the positrons with position sensitive detectors is beneficial in a sense that effects of pile-up can progressively be suppressed by requiring hit-to-hit correlations in the track reconstruction. The existence of the strong magnetic field in the detection volume provides for momentum analysis. On the other hand, the detectors and their readout electronics must operate in a 3 T magnetic field. In addition, any electric field from the detector and readout electronics should be sufficiently small so that the electric field in the muon storage region is negligible for the measurement (10 mV/cm for 0.1 ppm systematic uncertainty).

On the basis of these requirements, silicon strip detectors are considered for the tracking detector since these detectors are compact, highly segmented, available in a magnet field, have stable gain, and do not introduce high electric field in the detection volume. As shown in Fig. 7.9, we plan that silicon strip detectors will be radially placed in the detection volume to efficiently detect the circular tracks of the positrons. In order to detect positrons efficiently with sufficient acceptance, the sensitive area in the axial coordinate is set to ± 200 mm (see 7.1.2). To detect positrons with middle-energy range $(200 < E < 280$ MeV$)$ efficiently, the sensitive area in the radial coordinate is set to from r=70 mm

to r=290 mm. At energies below 50 MeV, the tracking detector is less sensitive to these unwanted positrons because the radius of curl-up is so small. We note that the detector is not sensitive to positrons with the high energy (E >280 MeV) since the radius of the positron track is similar to that of muons. Furthermore, lead tungsten is put in the center region to absorb positrons with middle energy, i.e. it avoids many turns of positron passing through the center region. The silicon detector consists of a double-sided AC-coupled rectangular silicon sensors with radial and axial strips with 188 μm and 255 μm pitches, respectively. The size of the sensor is 7.4 cm wide and 10 cm high. 1 unit module is composed of 6 sensors placed in a 2×3 matrix. Present design is shown in Fig. 7.10. There are 48 modules to form a set of vanes in the upper half of the detection volume, and another 48 units for the lower half. There are 4608 strips (p-side and n-side) per unit, and 442k strips in total.

Because total number of hits is to be 2.2M hits/spill from Monte-Carlo simulation, the hit rate per strip per 1 beam spill is 2.2M/442k=5.0 hits/strip/spill. Thus, the hit rate at injection is 5.0/6.6μs=0.76MHz. The strip occupancy which is defined by hit rate per strip per 1 sampling time in 1 beam spill was calculated as a function of time with Monte-Carlo simulation as shown in Fig. 7.11. In this figure, sampling time was assumed to 5 ns. The occupancy is less than 0.5%.

In the following sections, we discuss the feasibility of the positron tracking with such a radial vane silicon detector system using Monte-Carlo simulation and new tracking tool.
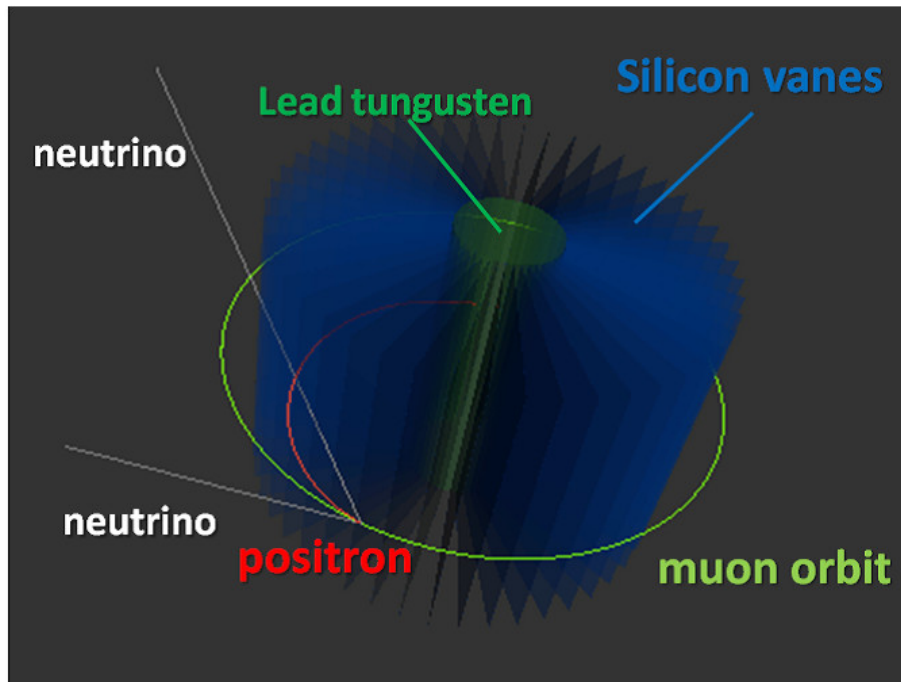

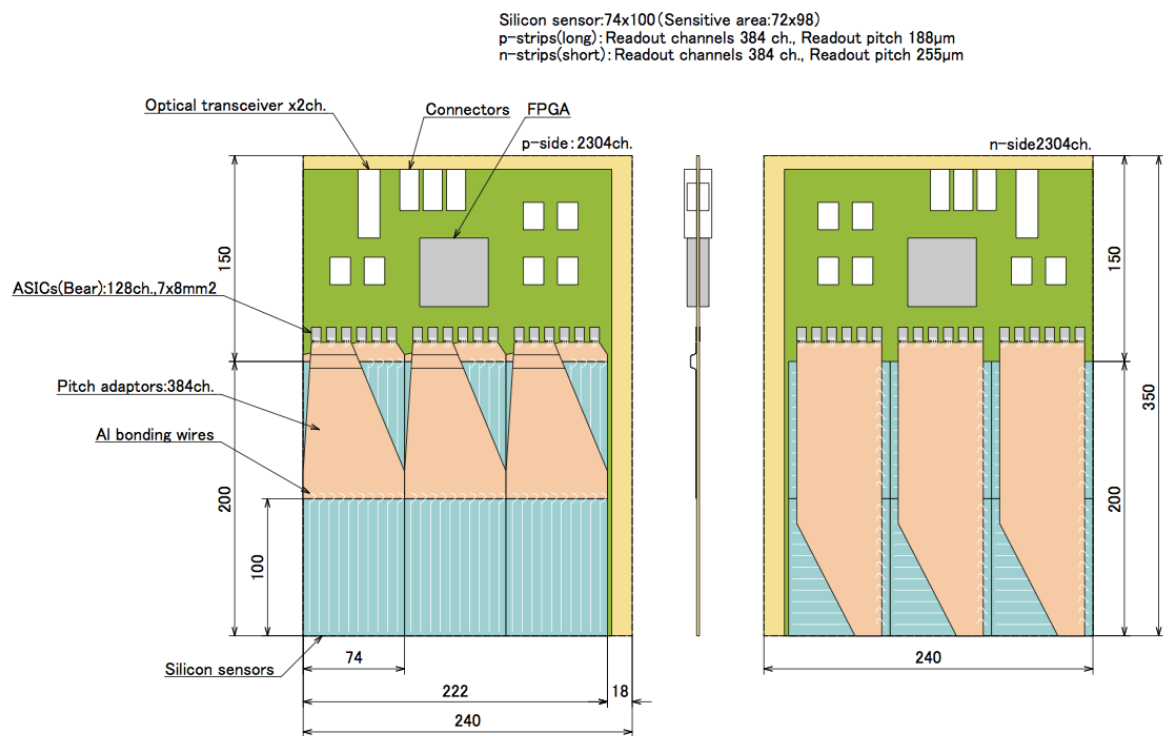**Figure 7.9:** *Layout of the positron detector system.*

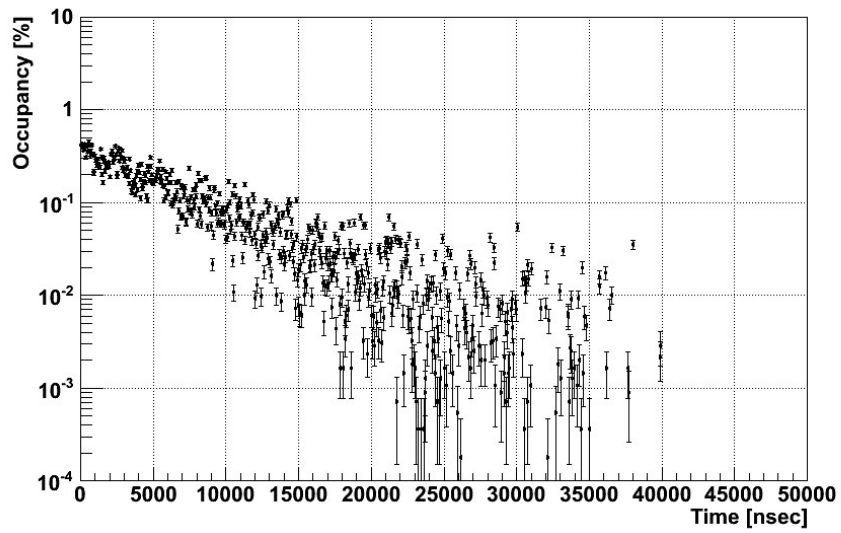**Figure 7.10:** *Layout of the silicon-vane module*

Figure 7.11: *Strip occupancy as a function of time.*

7.2.2   Detector simulation

A simulation model of the detector system has been developed based on the GEANT4 package [5]. It fully simulates the spacial and spin motion of muons, decay, and interactions of positrons in detector materials. Optimum detector size, number of vanes, timing and spacial resolutions, as well as potential backgrounds are being studied in Monte-Carlo data generated by the simulation model, step by step. As a first step, we constructed the simulator in the ideal condition and investigated the event structures. On the basis of the event structure, we have confirmed the feasibility of the positron detection, and considered the track finding algorithm.

We have constructed a simulator based on GEANT4 version 9.4.p01. For the validation of low energy interaction between positron and detector materials, low energy packages of physics lists (G4eMultipleScattering, G4eBremsstrahlung, G4eIonisation, G4eplusAnnhilation, and G4Synchrotron -RadiationMat) were adopted and G4StepLimiter (10 μm, which is much less than the thickness of silicon detector) was also added in the physics list to obtain detail hit information.

To confirm the validation of the positron interaction in the simulator, energy loss of positron in silicon was investigated with a simple model. Positrons which have the energies from 10 to 1000 MeV were injected to the silicon with the thickness of 300 μm as shown in Fig. 7.12, and then the obtained energy loss was compared with the one from NIST [6]. In this result, the difference of energy loss between GEANT4 and NIST was less than 5% in the energy range up to 300 MeV, which is good enough to use for our study.

Figure 7.13 shows the geometry of the silicon vane tracker. Coordinate system in this study is also defined in Fig. 7.13. As a first step, ideal condition (P_μ=300 MeV/c, B = 3 T, and E = 0 V/m) was adopted. In order to simplify the model as a first step, the size of one silicon vane was set to 220 $\times$ 400 $\times$ 0.3 mm^3 and strip pitch was assumed to be 200 μm. Numbers of vanes were 48. In the center region, lead tungsten was put for absorption of low energy positrons. All materials were put in vacuum.

A typical rate to generate a single muon decay event in the simulation model is 1 event per second with a relatively-recent single CPU. In order to produce simulation data with required statistics, computing clusters at RICC (the RIKEN Integrated Cluster of Clusters) and KEKCC (KEK Central Computing System) have been configured in addition to local computers. These two computing systems allows batch job entries into several tens of CPUs at a time, and we currently can generate ten millions of events of the muon decay within a day. There are rooms to improve our computing power by a factor of two.

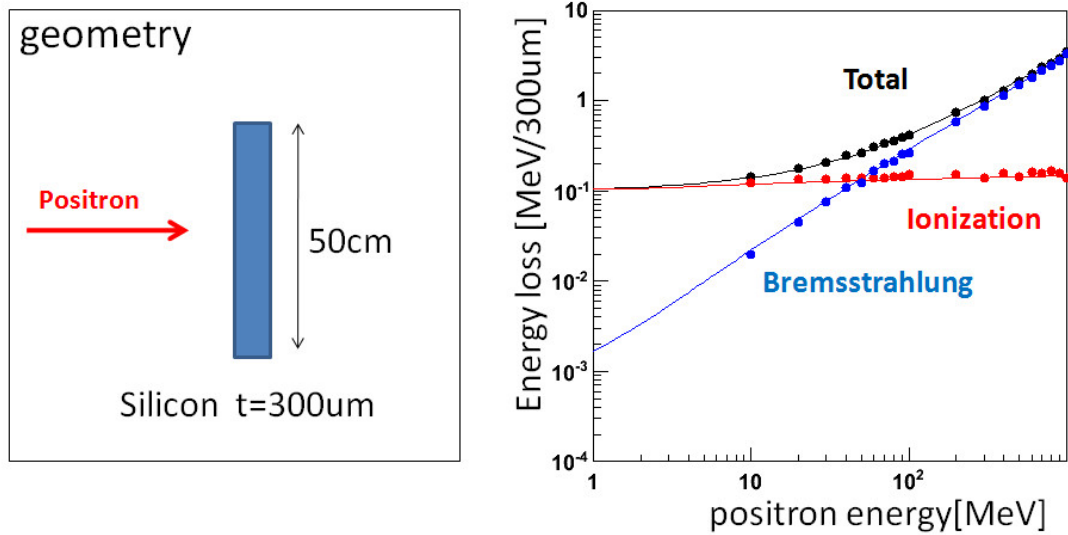**Figure 7.12:** *Geometry of validation test (left) and energy loss of positron in silicon as a function of energy (right). Plots and lines are from GEANT4 and NIST, respectively. Black, red, and blue show the total energy loss, the one of ionization, and the one of bremsstrahlung, respectively.*
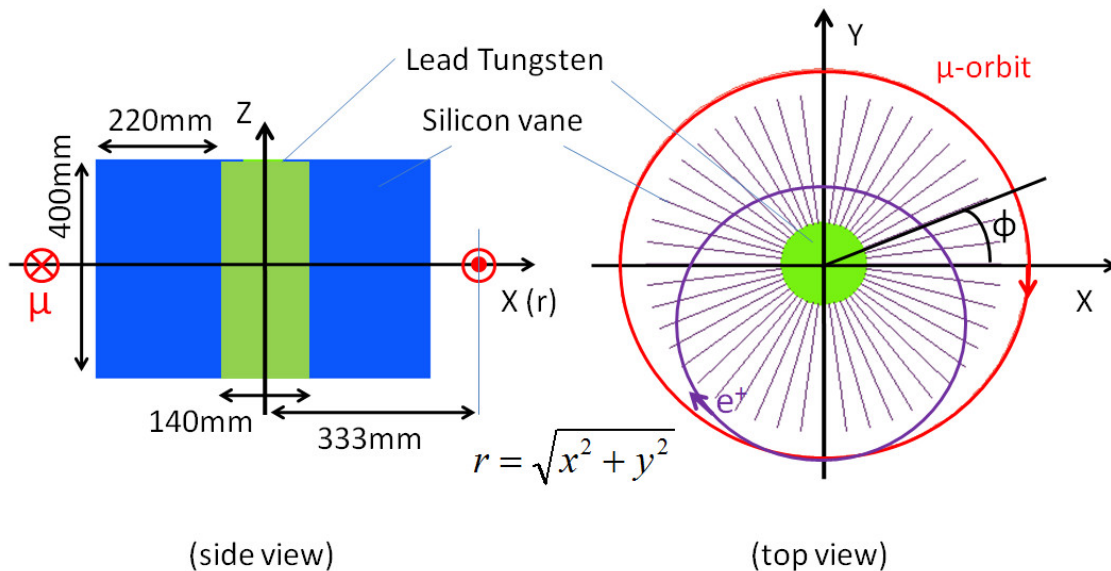

Figure 7.13: *Side view (left) and top view (left) of geometry of the silicon vane tracker in simulator.*

7.2.3   Event Display for $G - 2$/EDM (EDGE)

EDGE is a 3D display program based on Eve, a very powerful environment using ROOT [9]. It has been chosen to be the g-2/EDM simulation and reconstruction analysis toolkit. The geometry files are built using the ROOT geometry package and the TGeo classes. EDGE will be used for event visualization and for navigating through the detector material for the track simulation and reconstruction.

The detector geometry displayed in Fig. 7.14 shows the sensors in magenta and the central part in gray. The 48 vanes can be clearly identified in Fig. 7.14, one can also notice the positron in blue, the electron in red and the photon in green. Figures 7.14 and 7.15 show the simultaneous visualization of 40 GEANT4 simulated events. Note that average number of muon decay in the first 5 ns is 30. Typical events are visible in Fig. 7.16 and 7.17 with a well defined positron track.
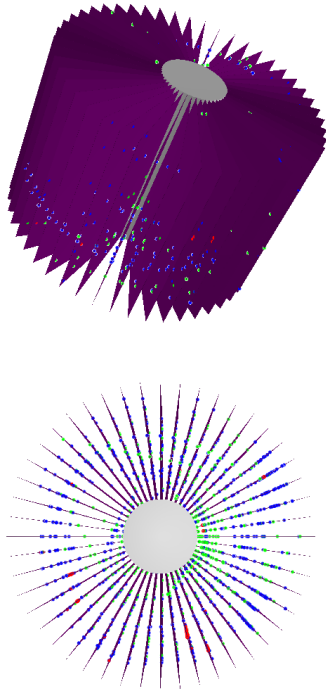
Figure 7.14: *40 GEANT4 simulated events - positron in blue, electron in red and photon in green - (upper) detector structure : sensors in magenta and central part in gray - (lower) top view.*

Figure 7.15: *40 GEANT4 simulated events without detector structure - (upper) front view - (lower) rotated view.*

Figure 7.16: *top view of two GEANT4 simulated events with detector structure (upper) 225 MeV positron - (lower) 257 MeV positron.*

Figure 7.17: *front view of two GEANT4 simulated events without detector structure - (upper) 200 MeV positron - (lower) 257 MeV positron.*

7.2.4   Event structure

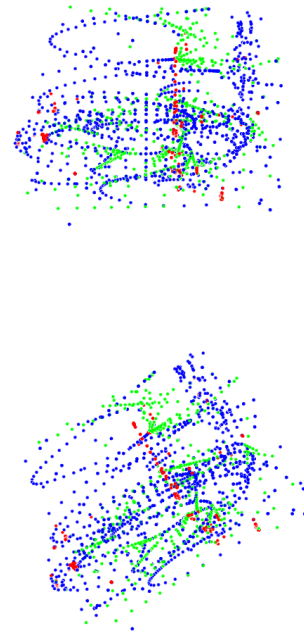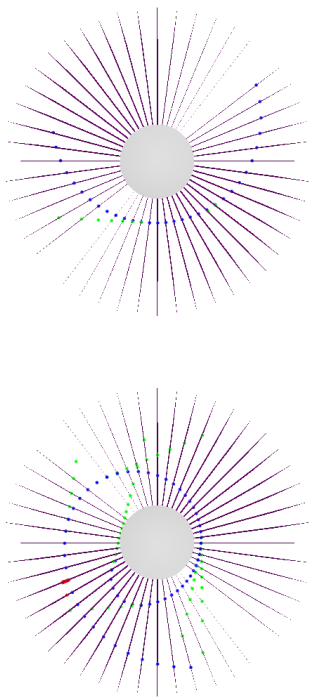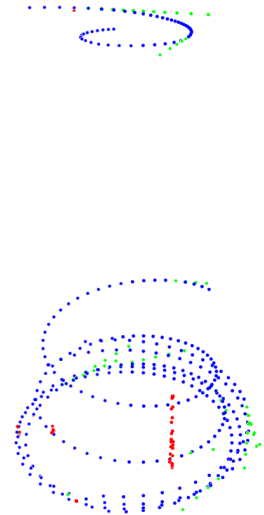Structure of hits from decay positron in the silicon-vane tracker was investigated. The signal positron track has the energy of larger than 200 MeV due to the figure of merit (Section 7.1.1). In what follows, signal and background tracks are defined with the tracks in the energy ranges larger than 200 MeV and others, respectively.

Figure 7.18 shows the typical hit structures for initial 5 ns from beam injection. The 5 ns time window is the readout sampling time. Typically, there are 15 signal positron tracks and 27 background tracks in one sampling time during the initial 50 ns. In this example, there are 14 signal positron tracks and 33 background tracks in one sampling time. In the Fig. 7.18, we can see that distinction between signal and background tracks is made in the ϕZ-plane due to low hit density. An algorithm extracting a line from a 2-dimensional plane can be used to find tracks because the signal track has straight line-like shape in ϕZ-plane. Figure 7.19 shows the same hit structures in XY-plane for four Z-regions. Because the first hit of positron in silicon vane tends to exist near Z=0 (see Fig. 7.7), the Z-dependency of hit structure is useful for the track finding algorithm. In Fig. 7.19, we can see that the Z-sliced hit positions in the XY-plane is actually helpful in track finding.

In order to investigate details of positron track and to develop the tracking algorithm, we scanned events by eye, and events were categorized in 12 categories as follows:

(1) Clear event : It is the easiest event to find the signal track. Only algorithm searching the straight line-like shape in the ϕZ-plane can be used (Fig. 7.20 (1)).

(2) Only secondary electrons : This category has the event like category (1). In addition to this, the event has the hit points which stems from δ-ray in silicon vane or electromagnetic shower in center region as shown in Fig. 7.20 (2). The hit points from δ-ray and electromagnetic shower are the noise events. Thus, an algorithm with rejection of δ-ray or shower hits is needed.

(3a) Small curls : The positron curls in silicon vane, which does not get to the center region. Such event tends to have low energy, thus almost all the events in this category are to be background events. The algorithm insensitive to the events in this category is favorable (Fig. 7.20 (3a)).

(3b) Small curls with secondary electrons ((3a)+(2)) : The event has both the small curl like category (3a) and the hit points from secondary electrons like category (2). This event is also to be background as in category (3a) (Fig. 7.20 (3b)).

(4a) Middle curls : The positron curls in silicon. The track in this category turns around the center region without hits in the center region and passing through the vanes. Such event tends to have middle energy, thus almost all the events in this category are to be signal track events. In this category, some straight line-like shapes can be seen in ϕZ-plane. The algorithm which can distinguish the initial hit points from others is desired (Fig. 7.20 (4a)).

(4b) Middle curls with secondary electrons ((4a)+(2)) : The event has both the middle curl like category (4a) and the hit points from secondary electrons like category (2). This event is also
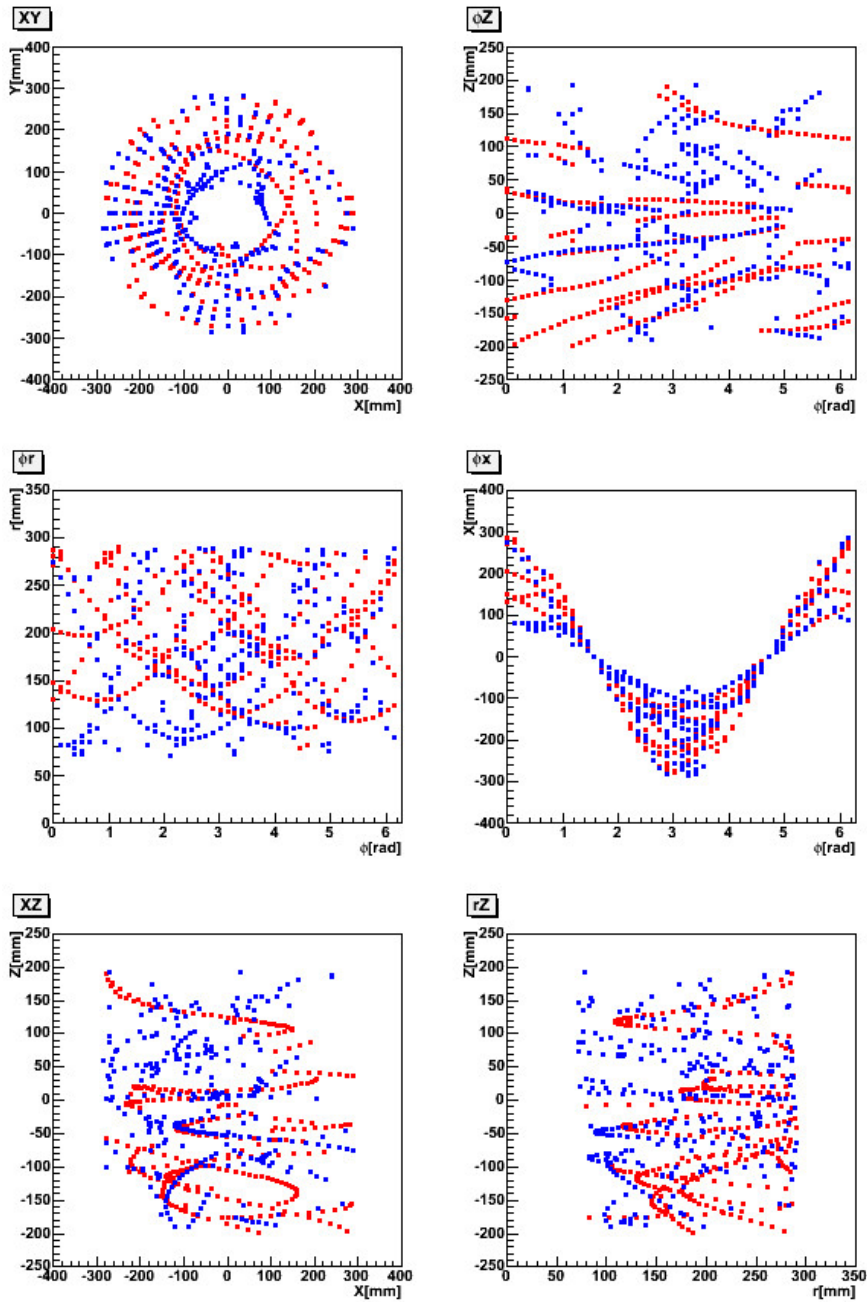
Figure 7.18: *Typical positron hit distributions. Top left, top right, center left, center right, bottom left and bottom right show the hit structures in XY-plane, ϕZ-plane, ϕr-plane, $X\phi$-plane, XZ-plane, and rZ-plane, respectively. Red points show the signal tracks which have the initial energy of larger than 200 MeV. Blue ones show the back ground tracks.*
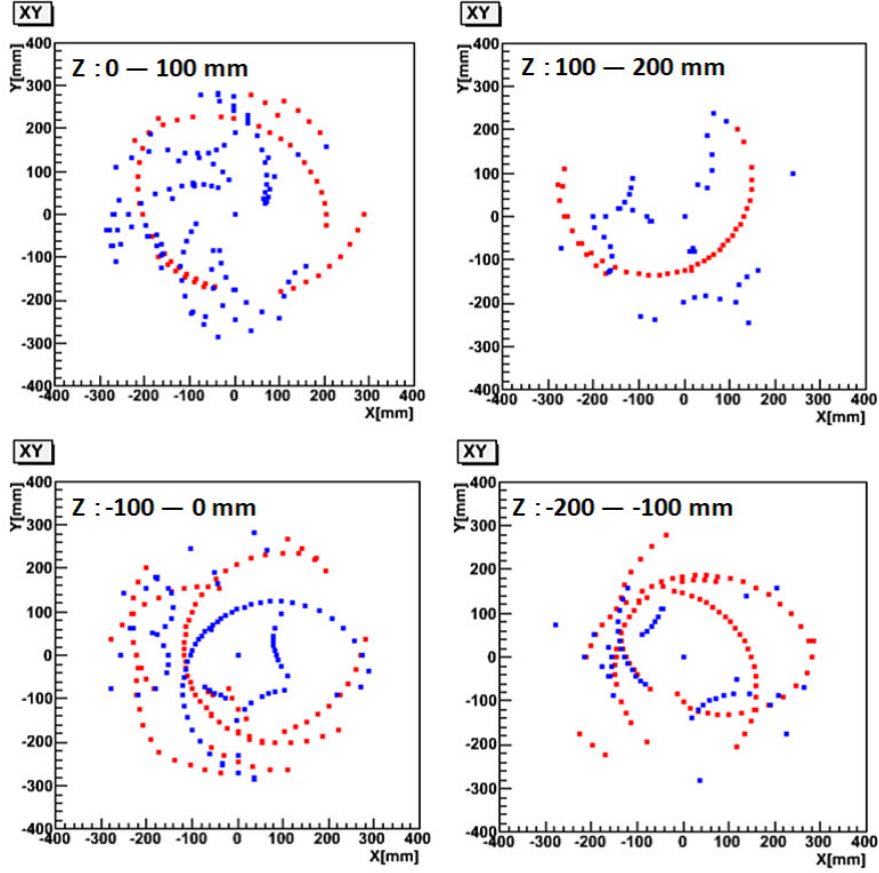
Figure 7.19: *Typical Z-sliced positron hit structure in XY-plane. Top left, top right, bottom left, and bottom right show the hit structure in XY -plane at 0≤Z<100 mm, 100≤Z<200 mm, -100≤Z<0, and -200≤Z<-100, respectively.*

to be signal track as well as category (4a). To this category, the algorithm which can separate signal track from the background one is needed (Fig. 7.20 (4b)).

(5a) Large curls : As well as category (3) and (4), the positron curls. The track turns around the center region with passing through the vanes. Such event tends to have middle energy, thus almost all the events in this category are to be signal track events. In a similar way to category (4), some straight line-like shapes can be seen in the ϕZ-plane (Fig. 7.20 (5a)).

(5b) Large curls with secondary electrons ((5a)+(2)) : The event has both the large curl like category (5a) and the hit points from secondary electrons like category (2). This event is also to be signal track as well as category (5a) (Fig. 7.20 (5b)).

(6a) Only multiple scattering : The positron is scattered with large angle in the silicon vane. The broken straight line-like shape can be seen in ϕZ-plane. In order to find such event, the algorithm which can detect the lines with a kink is needed. (Fig. 7.20 (6a))

Muon g-2/EDM Experiment, Conceptual Design Report, Revised, December 12, 2011, 11:41 A.M.

(6b) Multiple scattering and another ((6a)+ (2-5)) : In addition to the event in category (6a), the event has either hit points from secondary electrons like category (2) or many turns like category (3), (4), and (5) (Fig. 7.20 (6b)).

(7) Others (ex. (2)+(3)+(4)) : The event does not belong to any of categories (1) - (6). For example, the event in this category has the hit points from secondary electrons like category (2), the small curl like category (3), and the middle curl like category (4) (Fig. 7.20 (7)). Such event is most complicated to find signal track. In addition to the algorithm searching straight line-like shape, sampling time window can be used because the events in this category tend to drift in silicon vanes during much longer time than that of sampling window.

(8) No hit : The event does not leave any hits in vanes. If the positron has very low (E <50 MeV) or high (E >280 MeV) energy, the curl is smaller or larger than the sensitive area of the silicon vane. Thus, the event has no hit.

Following above definition of categories, 1000 events were categorized by eyes as shown in Fig. 7.21. At low energy region, the largest events were in category (3). At middle energy range, category (1) and (2) are dominant. The events in categories (4)–(7) increase with the energy. Based on these results, we have developed the track finding algorithm, which is described in next subsection.
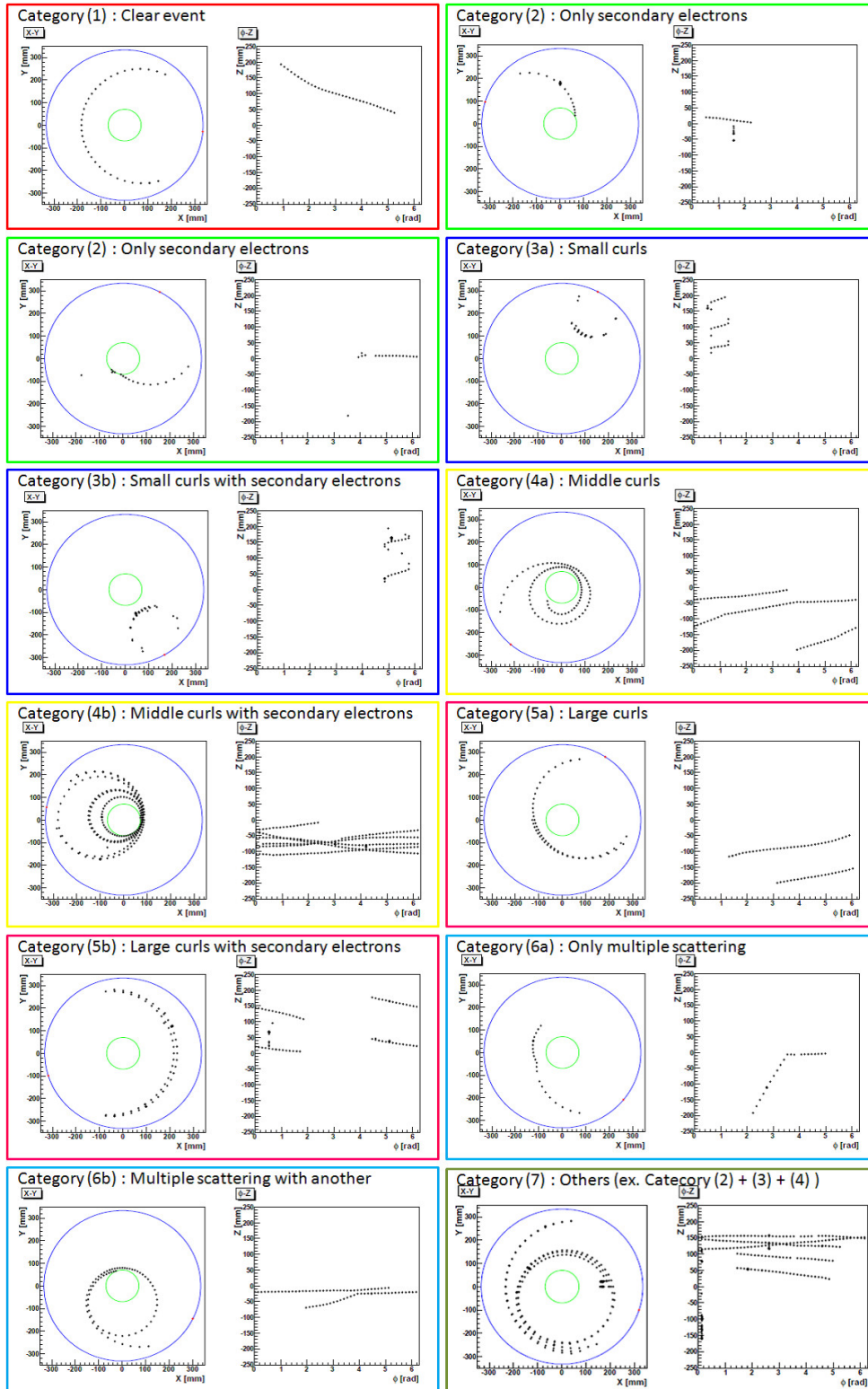
Figure 7.20: *Category of positron track. Figures from top left to bottom right show the category (1) to (7), respectively.*
Muon g-2/EDM Experiment, Conceptual Design Report, Revised, December 12, 2011, 11:41 A.M.
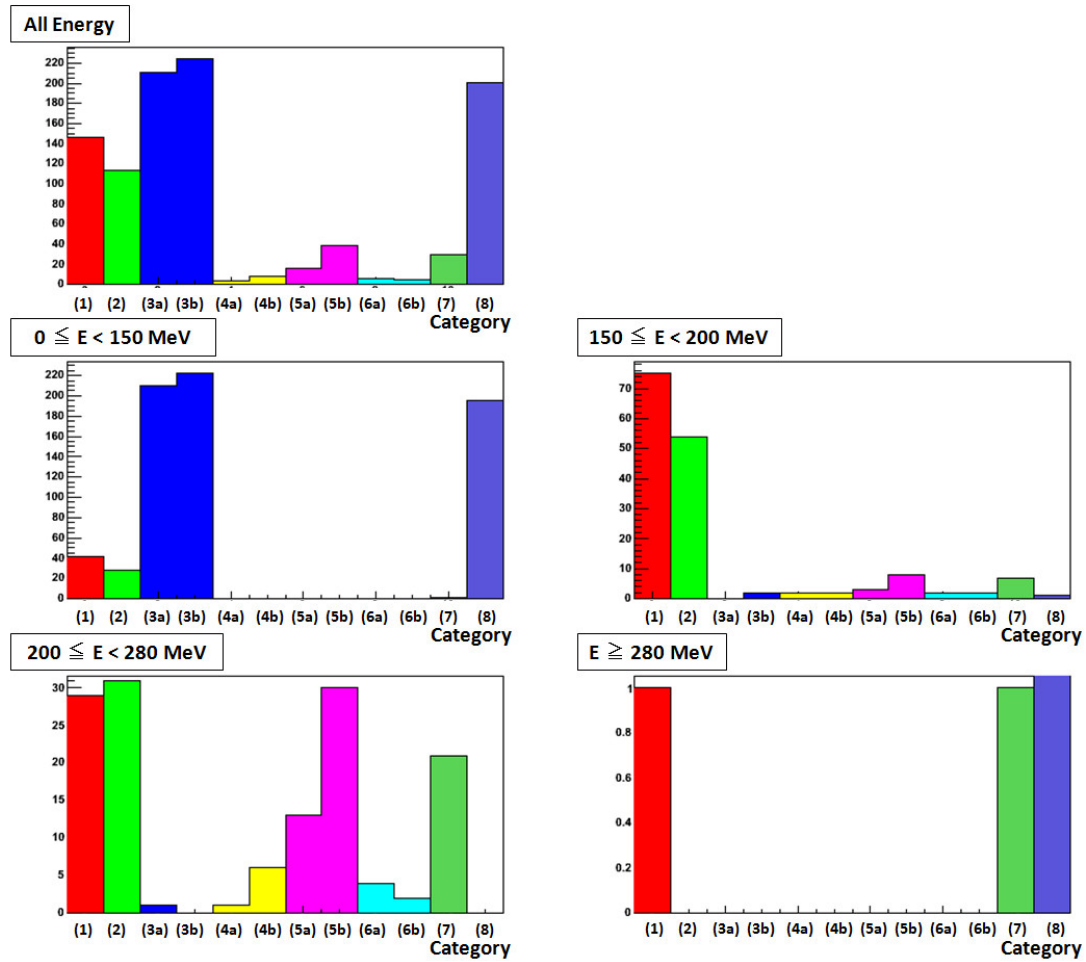
Figure 7.21: *Categorized tracks using 1000 generated events. Top figure shows the number of tracks in all energy range for each category. Center left, center right, bottom left, and bottom right ones show the ones in the energy range of 0≤E<150 MeV, 150≤E<200 MeV, 200≤E<280, and 280 MeV≥E, respectively. Colors are corresponding to ones in Fig. 7.20.*

7.2.5 Track reconstruction

Track reconstruction of the positron track from hit points in the silicon vane consists of track finding and track fitting.

Track finding

Because positron tracks in the silicon tracker had the straight-line trace in the ϕZ-plane, the algorithms which can distinguish such shapes from many hit points were helpful for track finding. We adopted the Hough transform [7, 8], for the algorithm to find such tracks. Hough transform is one of the feature extraction technique used in digital image processing. In order to confirm the feasibility of the track finding, we have developed the track finding tool using the Hough transform step by step. As a first step, we developed the track finding tool for a single track and estimated the track finding efficiency. We examined the detail information on track and investigated the validity of the tool using the Hough transform. On the basis of the results of the first step, we are developing the track finding tool for multi tracks as a second step.

Figure 7.22 shows the flow chart of the track finding in the simulation data. Firstly, the obtained event is digitized with strip pitch of 200 μm. Then, the track finding starts with searching for 3 or more hits in silicon vanes because such hits are needed for the track fitting. We call this selection Nhit cut. Next, hit points near z=0 plane are selected for searching initial ones from the Hough transform, which is called Z-search. Because muon decay point is near z=0 plane, initial hit points tend to be near z=0 region. Then, the Hough transform is applied to selected hit points in the ϕZ-plane and maximum peak in the Hough space is searched ((r,θ) search). Using this peak, fit line is obtained. If the slope of this fit line is larger than 89.9 degree in the ϕZ-plane, hit points near this line is removed and the Hough transform is applied again because the hit points near such fit line stems from secondary electrons (Slope cut). From the fit line which is equal to or smaller than 89.9 degree, residuals between the line and hit points are calculated. In order to distinguish the hit points whether the ones belong to positron track or not, the standard deviation (σ) of the residual distribution is used. We cluster the hit points which satisfy |residual| $<3\sigma$ (Hough cut). Next, we reduce the hit points in the cluster to "right" cluster in order to remove hit points from secondary electrons. Specifically, we select continuum points along ϕ-direction for the cluster which has no overlapping along z-direction (Clustering cut). Finally, cluster is expanded with the steering method. The steering method is as follows: the vector in the ϕZ-plane is calculated using two points in edge of cluster, and then a point which is nearest one to the vector line is added in the raw cluster only if the one exists nearby the edge of raw cluster. Repeating this expansion on both sides of cluster until no adding point remains, we obtain the track cluster. If the obtained track cluster has the same initial 3 points as the answer, this event is considered as a found track. Figure 7.23 shows the typical event display using the track finding tool.
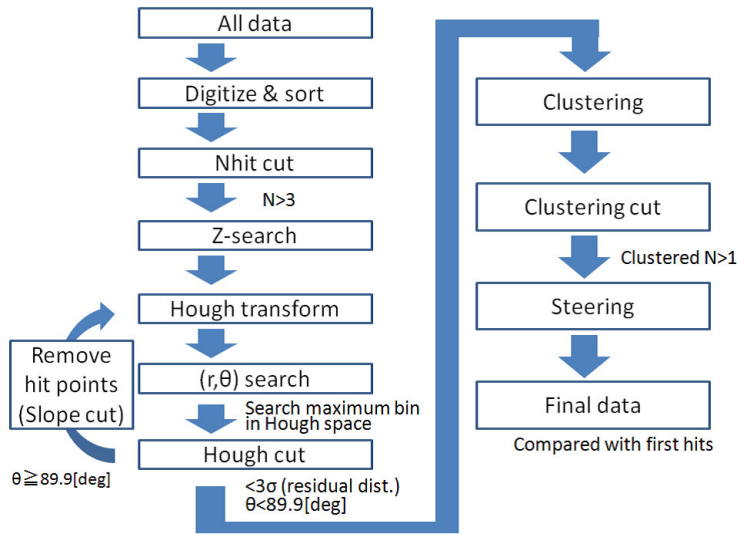
Figure 7.22: *Flow chart of track finding for a simulated track.*
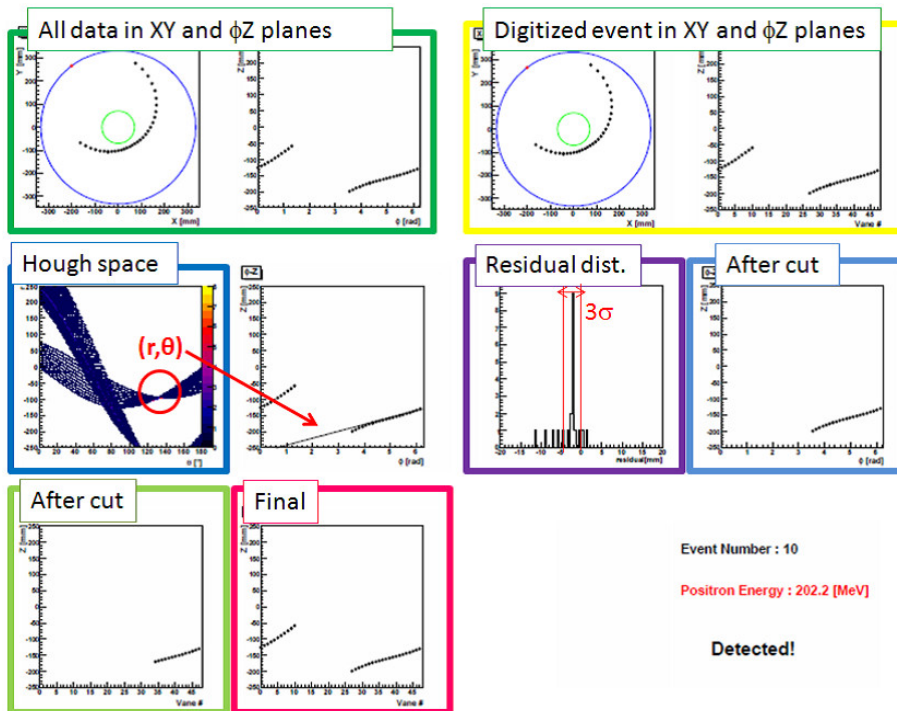
Figure 7.23: *Example of typical event display. In this display, the signal event which has the initial energy of 202 MeV was used. Top left and right two figures show the raw events and digitized events in XY and φZ-planes, respectively. Center figures show the events in Hough space, Hough fit line, residual distribution, and clustered events in order from left to right. Bottom left and bottom right figures show the events which is applied with clustering cut and final obtained event, respectively.*

7.2.6   Track fitting

We have studied a track fitting based on Kalman Filter. Kalman Filters are widely used for track fitting and also some time for track finding in HEP experiments [10]. It is based on an iterative least square fit of the track state vector in all measurement layers. Two main steps are repeated. The first step is the prediction step. We extrapolate the state vector to the next layer. This is done using a track model which is the track propagator from one surface to another surface, adding up multiple scattering and subtracting energy loss. The second step is an update step. We combine the predicted state with the current measurement. A good initial state (a seed) is important and also a precise modelling of material effects in track reconstruction is necessary to obtain the best estimates of the track parameters. This is particularly relevant for reconstruction of positrons where ionization energy loss affects both tracking (averages) and error propagation (covariance matrix), multiple Coulomb scattering affects error propagation and energy losses due to the bremsstrahlung (radiative energy loss) affects both tracking and error propagation. We have to notice that the Kalman Filter is proved to be optimal only when all probability densities involved are Gaussian. Other method such the Gaussian Sum Filter methods is thus mandatory to treat correctly the non gaussian energy loss [11].

In order to perform the Kalman Filter the GENFIT [12] software is being considered. It is a generic toolkit for track reconstruction in particle and nuclear physics experiments which consists of three modular components. This allows to decouples the algebra of the regression algorithm from the hit representation and track representation. The GENFIT track fitting algorithm is currently a Kalman Filter but other algorithm modules can be added easily to the needs. GENFIT is distributed with two well-tested track representations and the hit dimensionality and the orientation of planar tracking detectors can be chosen easily and freely.

The track representation used is the detector system representation $(q/p, u', v', u, v)$ where (u, v, w) is an orthonormal reference system with the uv plane coinciding with the detector one and the derivatives u' (slope) , v' (slope) indicate the momentum direction variation for the particle of charge q and momentum p. The track propagation model, taking into account the effects of materials and magnetic fields, uses the TGeo classes from ROOT for the geometry interface.

For the moment the track fitting is studied with the help of a fast simulation based on the full simulation Geant4 output and the GENFIT software. Fast simulation detector design studies can be employed in a first stage when a high event rate production is needed and detailed simulations such as GEANT4 and detector responses with full digitization simulations are too slow. The fast single-track simulation and reconstruction tool could also help in the process of the optimization of tracking detector design. It allows investigation of the track parameter resolution for the purpose of detector setup optimization.

The position and the momentum of a positron when it enters the detector is generated with the UNU.RAN software (Universal Non Uniform Random number generator for generating non uniform pseudo-random numbers, an extensive online documentation are available at the UNU.RAN Web Site)

according the full simulation GEANT4 result. The trajectory of the positron is computed with the help of the track representation tacking in account the material effects and magnetic fields. The intersection points between the positron trajectory and the detector are smeared according to a gaussian of width $\sigma_{hit} = \frac{pitch}{\sqrt{12}} = \frac{200\ \mu m}{\sqrt{12}}$ in order to reproduce the digitization. Theses smeared points are used in the fit as reconstructed hits. We run the GENFIT Kalman Filter on this reconstructed hits in order to obtain the track fitting. As example result we show in Fig. 7.24 the generated momentum distribution of the positron and the distribution of the momentum track fitting extrapolated where the positron enters the detector and in Fig. 7.25 the pull of coordinate u defined as $(u_{\text{fit}} - u_{\text{true}})/\sigma_u$.
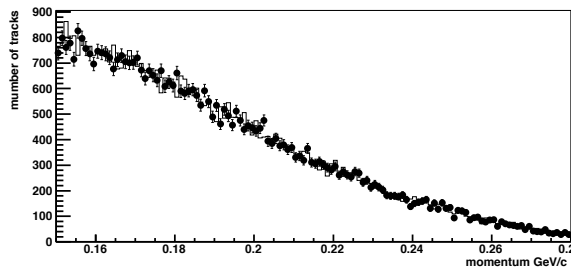

Figure 7.24: *Fast simulation result - Generated momentum (continuous line) - Track fitting momentum (points).*
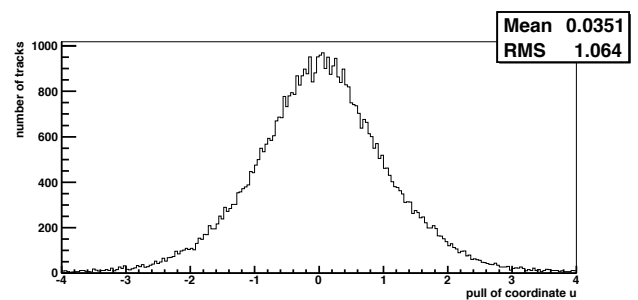
Figure 7.25: *Fast simulation result - pull of coordinate u.*

7.2.7   Expected performance

Using the simulator and the track finding tool, we have estimated the track finding efficiency for a single track.

We applied the track finding tool to 40000 events from simulator. Using the results, we estimated the track finding efficiency. The efficiency was defined with as follows:

$$Efficiency = \frac{N_{found}}{N_{all}}, \tag{7.20}$$

where N_{found} and N_{all} are the numbers of events with a track found and of all events, respectively. We note that events with the energy larger than 200 MeV has enough number of hit points in silicon vane. The efficiencies was 96.9±2.7% for those events. Figure 7.26 shows the found events categorized as well as Fig. 7.21, in which the same 1000 events were used. In the energy range from 150 to 280 MeV, we can see that almost all the events were found. Especially, the efficiency is good enough in the middle energy range (200 < E < 280 MeV). For the lower energy (150 < E < 200 MeV) events, about 10% of the events were not found, while the efficiency is still greater than 90%. This is because the unfound events have small hit numbers (≤ 3 hits) or have hit points from secondary electron events more than once. In the former case, we can collect such unfound events if the parameter of Nhit cut is changed simply. In the latter case, it is thought that the unfound events can be found if the repetition of Slope cut is increased. Figure 7.27 shows the track finding efficiency for single track as a function of the energy of positron. From not only the results described above, but also this figure, we can see that the efficiency in the middle energy range is good enough. In the energy range around 100 MeV, the efficiency is very low because the events belonging to category (2) are dominant.

On the basis of the results described above, we are developing the track finding tool for multi tracks. As a next step, we will plan that one track finding using the finding tool for single track with a little improvement will be applied to about 40 overlapping tracks. If it is useful, i.e. track finding efficiency is good enough, almost all the positron tracks will be found with the track finding tool during beam cycle. On the other hand, if it is complicated, the information of Z-slice will be used for the track finding tool for multi tracks.
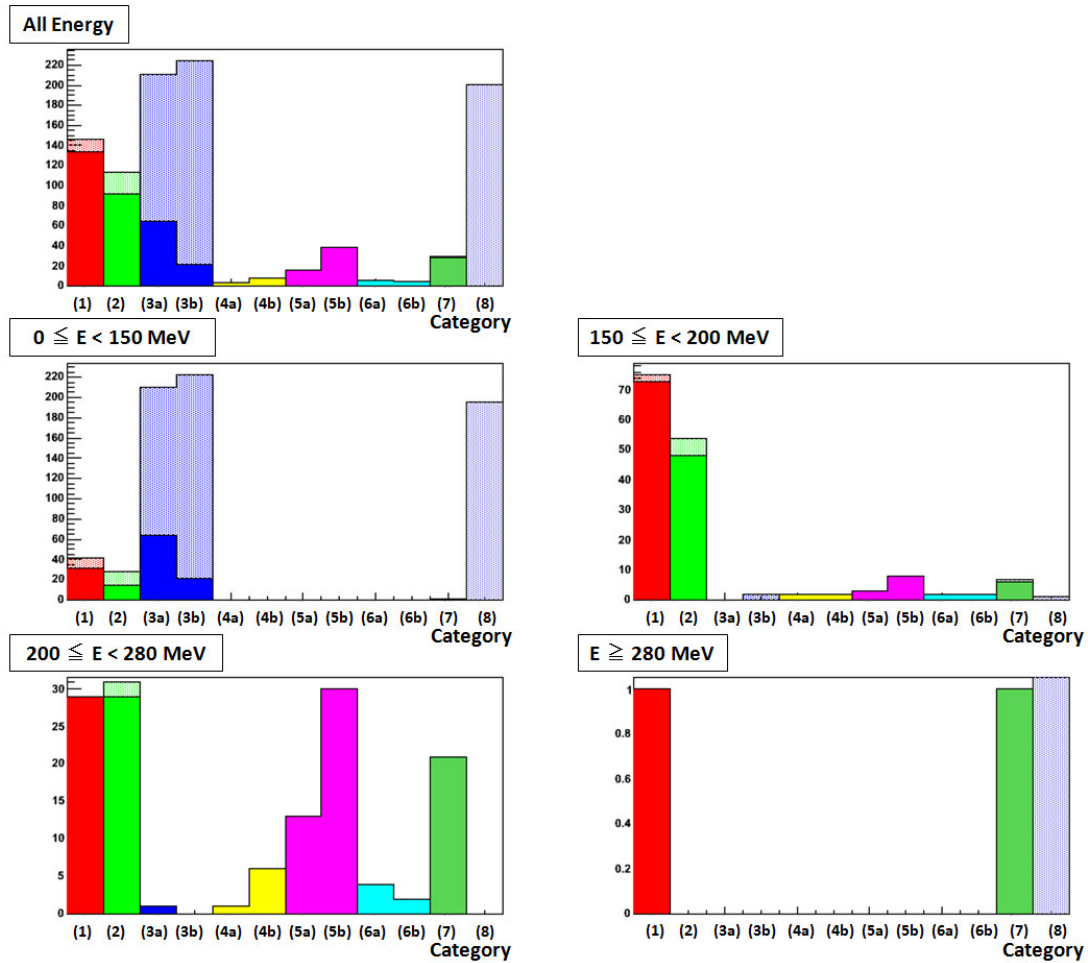
Figure 7.26: *Categorized found tracks using same 1000 events as Fig. 7.21. Top figure shows the number of found tracks in all energy range for each category. Center left, center right, bottom left, and bottom right ones show the ones in the energy range of 0≤E<150 MeV, 150≤E<200 MeV, 200≤E<280, and 280 MeV≥E, respectively. Colors are corresponding to ones in Fig. 7.20. For comparison, number of all tracks (Fig. 7.21) are also shown by shaded colors.*
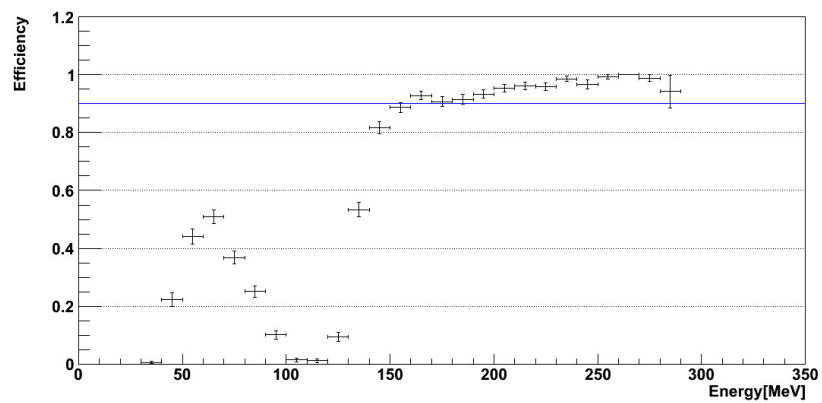
Figure 7.27: *Energy dependence of track finding efficiency.*

7.3 Silicon sensor

7.3.1 Overview of silicon-strip sensor technology

Silicon strip/pixel detectors have been used in the inner tracking detector for the measurement of a charged particle's track precisely to provide location of the particle's origin, i.e. colliding vertex and decay vertex. High granularity is commonly achieved as the silicon sensor is manufactured with micro-electronics technologies. Silicon sensor offers reasonably low material budget for momentum analysis, e.g. 3×10^{-3} radiation length for a 300 μm-thick silicon sensor. Another advantage of silicon sensors for our application is that sensor is immune to 511 keV gamma rays from positron decay. The photon absorption rate is 6×10^{-3} for 300 μm-thick Silicon. In the context of our application, a particularly important property of the silicon detector is that anticipated stability of gain (number of electron-hole pairs per a positron hit) against early-to-late change in the hit rate.

A double-sided silicon-strip detector sensor (DSSD sensor) is considered as a sensor for the the silicon tracker. The DSSD sensor is made of n-type bulk substrate with implantation of p^+ in the p-side and n^+ in the n-side of the sensor plane.

The energy needed for creation of an electron-hole pair in the sensor is 3.6 eV. Total number of electron-hole pairs created by the minimum ionization particle in a silicon sensor of 0.32 mm thickness is about 25k pairs (4 fC). Signal is read out by an AC coupling capacitor made of a thin silicon dioxide film implanted on the strips. A typical duration of the electron and hole currents is about 10 ns for electron and 20 ns for hole, respectively [15]

Hamamatsu photonics co. (HPK) will be able to supply a double-sided strip sensor from a 6 inch wafer with 0.32 mm thickness. The Belle-II SVD [16] has developed a DSSD sensor with a dimension of 120 mm × 60 mm with the HPK's manufacturing process. The silicon sensor for this experiment has a dimension of 100 mm in height and 74 mm in width, which can be produced in the same manufacturing technology as the Belle-II sensor. The depletion voltage of the sensor is 120 V with a typical leakage current of 2 μA at 20 degrees Celsius. The breakdown voltage is about 180 V.

The readout strips are 99 mm long at 188 μm pitch for p-side, and 72 mm at 255 μm pitch for n-side. Orientation of strips in the p-side is orthogonal to that in the n-side. The detector capacitance is in a range of 15–30 pF per strip. There are 384 strips in each side of the sensor. The total number of strip is 768 strips per sensor. There are 6 sensors per module (see Fig. 7.10). There are 48 vanes. Each vane consists of two modules. Thus, total number of sensor is 576 sensors.

7.3.2 Evaluation of DSSD sensor

The DSSD sensor is evaluated with an emphasis on the timing response and its rate dependence. As discussed in Section 7.1.2, stable timing response against the rate change by a factor of 160 is one of the critical requirements for the detector. This particular question has not been addressed in the past researches and experiments as this is rather special requirement for the silicon strip detector. We have

been conducting a series of studies to learn the stability of timing response of the silicon strip sensor.

The HPK's DSSD sensor for the Belle-II SVD was used for the evaluation. The size of sensor is 124.9 mm × 59.6 mm with thickness of 320 μm. There are 1535 and 1023 strips in p-side and n-side, respectively. Strip pitches are 75 μm (p-side) and 240 μm (n-side). Every other strip is readout being half of strips floating. Readout strip is AC coupled with a coupling capacitance of 100 pF. The sensor is fully depleted at 120 V with a typical leak current of 2 μA at 20 degrees. Typical yield of good strip is 98% on average and 97% minimum. These specifications are similar to what is planned for the $g - 2$ silicon sensor in the positron detector.

The set up for the sensor evaluation is shown in Fig. 7.28. In this evaluation, the signal from the DSSD sensor is read by a fast preAmplifier-Shaper-Discriminator (ASD) which was originally developed for the ATLAS thin-gap chamber [17]. The ASD consists of a charge-sensitive preamplifier with a gain of 0.8 mV/fC, followed by a main amplifier with 7 times amplification, and comparator with external threshold setting. The ASD has a peaking time of 10 ns. Equivalent noise change is 2000 e^- at 20 pF. Four ASD chips are assembled in a PCB board with a 16 ch input connector (ASD board). The ASD board is connected to each side of the silicon sensor. In total, 32 strips are readout in the test system.

The test DSSD module is mounted on a xy-stage in the support box as shown in Fig. 7.29. An infra-red (IR) laser (wavelength = 1060 nm) is injected to the sensor with a multi-mode optical fiber guided from a hole on the top cover. The attenuation length of 1060 nm laser photon is 1 mm in Silicon. Photons are absorbed almost uniformly along the laser beam path in the sensor (320 μm). The laser pulse with a width of 50 ps(FWHM) is drived by the Pico-Quant PDL800-B and LDH1060 with a repetition rate up to 80 MHz.

The pulse shape of the strip is measured with a oscillo-scope by triggering on a synchronized-trigger output from the laser driver.

The response to the test pulse on the ASD, and IR laser pulse is shown in Fig. 7.30. A clear signal is observed above typical noise level of about 5 mV (RMS) (2500 e^-). The average pulse shapes of the strip signal are shown in Fig. 7.31(left) at ten different bias voltages. The pulse height is saturated above 120 V which indicates full depletion of the sensor. The laser power was calibrated with a photo diode as shown in Fig. 7.31(right). The pulse height of the central strip is calculated from the photon absorption length, gain of amplifiers, and beam spot size. A consistency between the calculation and the measured pulse height is reasonable.

The timing resolution of the silicon strip signal was evaluated from the timing difference between the leading-edge timing of the strip pulse determined at 50% of the pulse height and synchronized trigger output from the laser driver. The timing resolution is obtained from a Gaussian fit to the leading edge timing distribution. The resolution (σ) is shown in Fig. 7.32 as a function of noise-to-signal ratio. The resolution ranges from 1–5 ns for the noise-to-signal ratio for 0.1–0.5. Note that difference in noise-to-signal ratio between n-side and p-side is not intrinsic, but due to the large laser spot size ($\sigma \sim 200$ μm) and different strip pitch (240 μm for n-side, 75 μm for p-side). This result demonstrate that 1 ns resolution is obtained if the noise-to-signal ratio is 0.1 (signal-to-noise ratio 10).
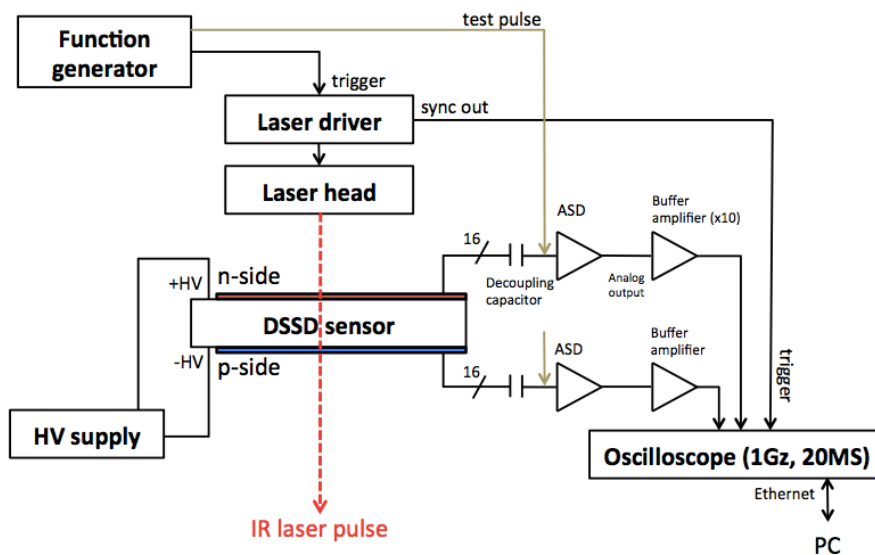
Figure 7.28: *Diagram of the silicon sensor test set up*
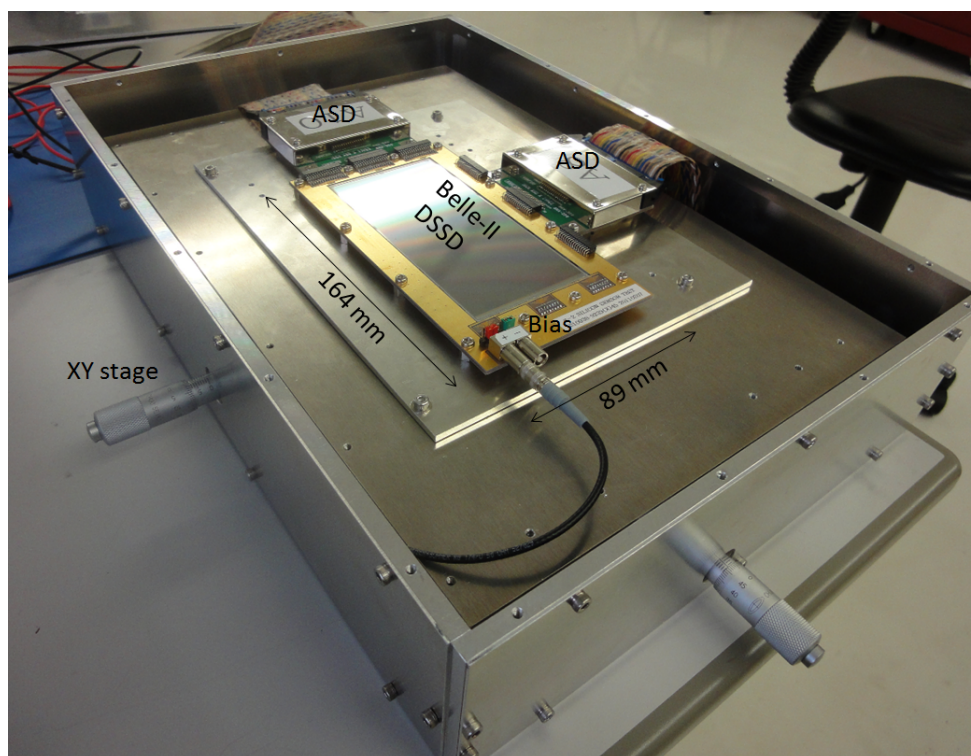
Figure 7.29: *The DSSD test module on the support box*
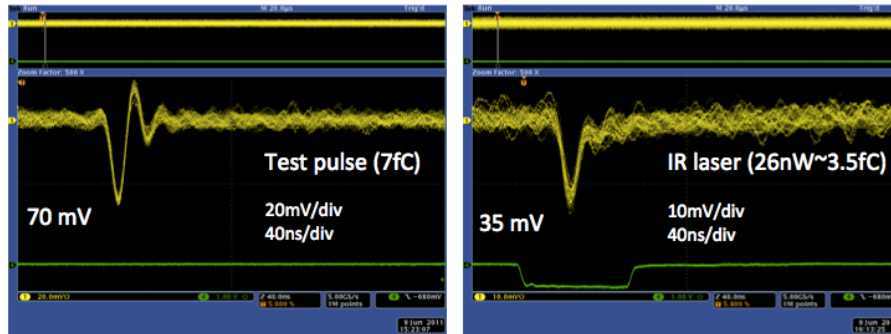
Figure 7.30: *The pulse shape for the test pulse input (left) and the IR laser (right).*
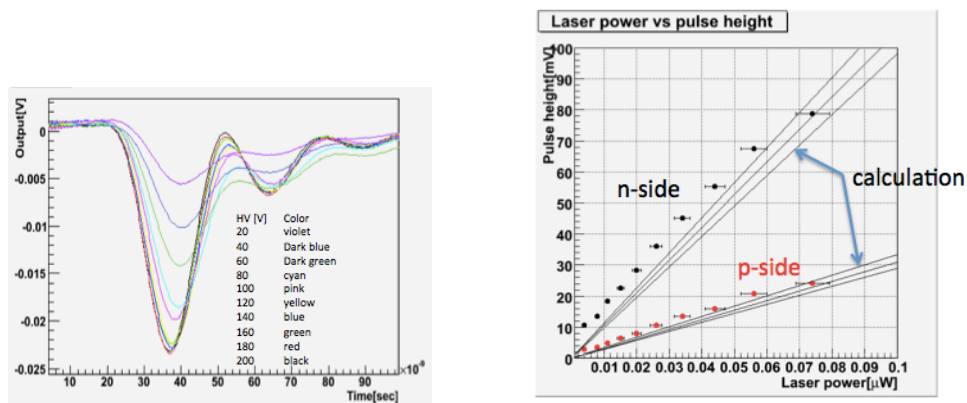
Figure 7.31: *(left) The average pulse shape after the amplifier with the IR laser injection. (right) The average pulse height vs laser power. Solid lines are calculation based on absorption length and repetition rate of the IR laser pulse in the sensor.*

We use this result to estimate the timing resolution with real readout ASIC which is under development. From Fig. 7.31(left), the slope of the leading-edge pulse in this evaluation is 23 mV/15 ns = 1.5 mV/ns. The new readout ASIC will have a pulse height of more than 50 mV with a peaking time of 50 ns for MIPs (see next chapter for detail), thus the leading edge slope will be 1 mV/ns which is a factor of 0.67 shallower than that in the present evaluation. Taking into this difference, we would expect timing resolution of $\sigma_t = 1$ ns/0.67 = 1.5 ns for noise-to-signal ratio of 0.1 with the ASIC in the $g - 2$ experiment. This would be sufficient resolution to distinguish the tracks in the 5 ns time stamp.

This evaluation set up would allow us to study rate effects and pile-up effects as the laser injection rate and pattern is under control as high as 80 MHz. It also allows to test the position dependence as well as temperature dependence of the timing performance. Such studies are under preparation.
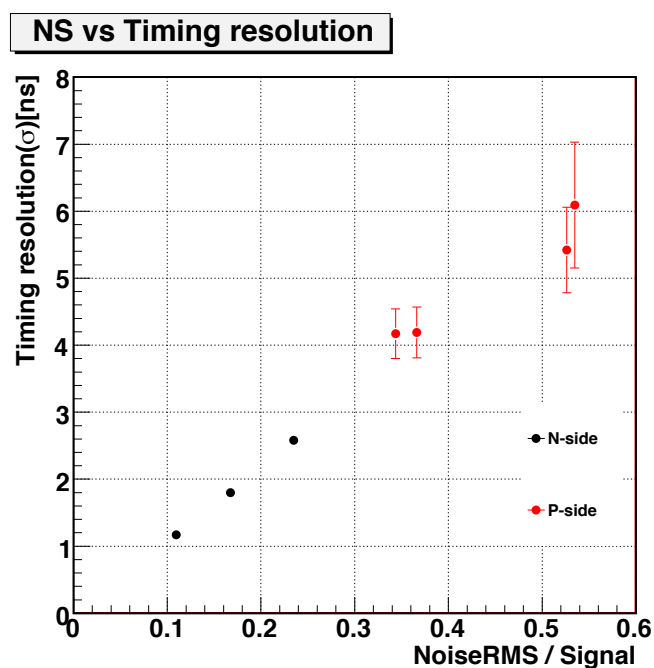
Figure 7.32: *The timing resolution of the silicon strip signal evaluated with the IR laser injection as a function of noise to signal ratio.*

7.4 Influence of magnetic and electric fields in the muon storage area

In general, material with magnetic susceptibility induces additional magnetic field under external field:

$$\Delta \vec{B} = (1 + \chi_m)\vec{B}, \tag{7.21}$$

where χ_m is the magnetic susceptibility of material (volume susceptibility). When a piece of material is localized, the induced magnetic field can be expressed as a field induced by a magnetic dipole:

$$\frac{\Delta B}{B} = \frac{\chi_m dV}{4\pi r^3}, \tag{7.22}$$

where dV is the volume, and r is the distance from the material.
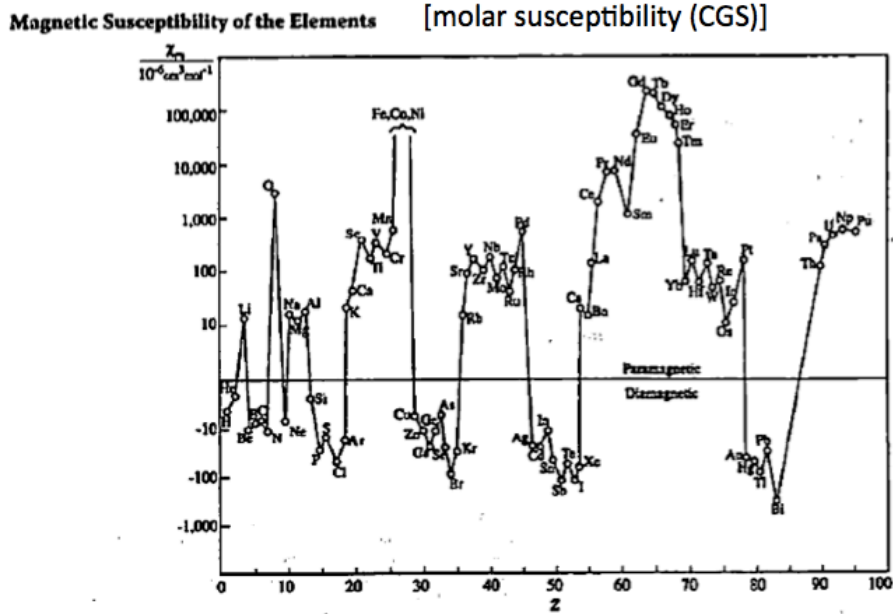
Figure 7.33: *Magnetic susceptibility of metal in CGS unit (Moller susceptibility). Ref [18].*

Metal elements and many of non-metal material have non-zero magnetic susceptibility (Fig. 7.33) [18] [2].

A careful design of the detector structure is necessary to minimize use of ferro-magnetic material. In many cases, information on the material used in the detector components is not disclosed, especially for the integrated-circuit components, such as FPGA, optical transceiver, etc. The evaluation of effective magnetic susceptibility of those components may be required to check these components meet the requirement.

---

[2]the volume susceptibility χ_m (MKS) and the moller susceptibility χ_{moller} (CGS) has following relation : $\chi_m = 4\pi\chi_{mollor}\frac{\rho}{A}$ (ρ is density of material, A is atomic number).

The magnetic field change in the vicinity of various material were measured with a NMR probe under the 1.6 T superconducting solenoid magnet in the cryogenic center at KEK to test if these components meet the requirement. Results for metals and electronic parts are shown in Fig. 7.34. Note that sensitivity of the NMR probe and stability of the magnetic field in these measurement are about 1 ppm level. The finite field changes are observed for Titanium, Tungsten, Brass, SUS with negative change. The field change become less than 5 ppm beyond 120 mm away from the NMR probe. Most of electric parts which are commonly be used in front-end electronics boards were tested. The field change is less than 5 ppm beyond 60 mm away from the probe even with a large amount of pieces. There are several exceptions, such as the optical transceiver, capacitor (not shown), and DC-DC converter (not shown). These items needs to be placed as longest distance as possible from the muon storage region.

The field change in the vicinity of the silicon sensor was measured in the distance range from 30 mm to 150 mm. No detectable change beyond sensitivity of the measurement was observed. There was no field change when the bias voltage was turned on up to 180 V. Thus, it is concluded that the silicon-strip sensor satisfy the requirement of magnetic field change.

These results will be used to evaluate the effect of field change with the actual detector module.
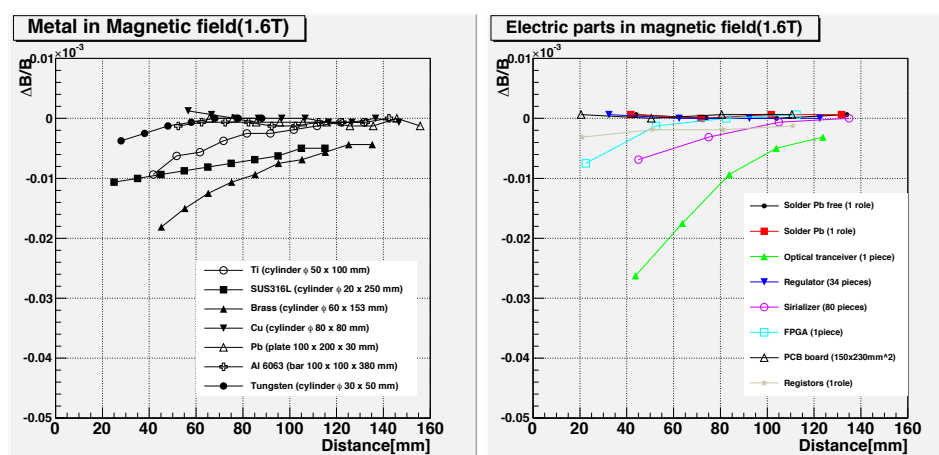

Figure 7.34: *Magnetic field change in the vicinity of metals (left) and electronic parts (right) under 1.6 T magnetic field.*

References for Chapter 7

[1] E. J. Konopinski,Annu. Rev. Nucl. Sci. 1959.9: 99-158.

[2] F. Combley and E. Picasso, Physics Report (Section C of Physics Letters)

[3] The J-PARC $g - 2$ collaboration, proposal submitted to J-PARC PAC (P34), 2009

[4] G.W. Bennett *et al.* Muon $G - 2$ Collaboration, Phys. Rev. **D73** (2006) 072003.

[5] S. Agostinelli et al., GEANT4- a simulation toolkit, Nucl. Instr. Meth. A 506 (2003) 250-303

[6] NIST estar, http://physics.nist.gov/PhysRefData/Star/Text/ESTAR.html

[7] P. V. C. Hough, Method and means for recognizing complex patterns, U. S. Patent 3 069 654, Dec. 18, 1962

[8] R. O. Duda and P. E. Hart, Use of the Hough Transformation to Detect Lines and Curves in Pictures, Comm. ACM. 15 (1972) 11-15

[9] Matevz Tadel, EVE - Event Visualization Environment of the ROOT framework, XII Advanced Computing and Analysis Techniques in Physics Research, November 3-7, 2008, Erice, Italy.

[10] R. Mankel, Pattern Recognition and Event Reconstruction in Particle Physics Experiments, arXiv:physics/0402 .**10** 399(1969), JETP Letters **10** 254(1969)

[11] R. Fruhwirth, A. Strandlie, Track and vertex reconstruction : From classical to adaptive methods, Rev. Mod. Phys. 82, 14191458 (2010).

[12] http://genfit.sourceforge.net/Main.html

[13] C. Hoppner, S. Neubert, B. Ketzer, S. Paul, A Novel Generic Framework for Track Fitting in Complex Detector Systems, arXiv:0911.1008v3 and Nucl. Instrum. Meth. A 620, Issue 2-3, pp. 518-525 (2010).

[14] V. Blobel, "A new fast tracfit based on broken lines", N.I.M. A 566 october 2006, pp.14-17

[15] M. Friedl, et al., Nucl. Inst. Meas. A461, 192 (2001).

[16] M. Friedl, et al., in the proceedings of Vertex 2011

[17] O. Sasaki, et al. (ATLAS TGC Collaboration), http://atlas.kek.jp/tgcelec/ASD/ASD-PRR.pdf

[18] Handbook of Chemistry and Physics 89th edition, CRC press (2008)

CHAPTER 8

Readout Electronics and DAQ System

Contents

8.1   Overview

Figure 8.1: *Overview of the readout and DAQ system*

The overview of the readout electronics and DAQ is shown in Fig. 8.1. The data from the silicon strip sensors are readout by the frontend board on detector, followed by readout boards with VME interface, then collected by the PC farm through a Gigabit Ethernet switch. The system clock is provided by the GPS/Rb clock generator, and it is distributed with real time control signals to the readout boards and the frontend board through the timing control/monitor board.

8.2   Sequence of data acquisition

The muon beam spill comes every 40 ms (25 Hz) in synchronous to the J-PARC accelerator RF signal. The beam spill contains 4×10^4 muons. The detector system starts the measurement of the decay positrons after the beam spill is injected to the storage region by the kicker. The measurement will continue for five time-dilated lifetimes, i.e. 33 μs. The long time interval (40 ms) between the measurement and the subsequent spill enables to send all the data after their proper processing to a back-end DAQ system. The time sequence of the data acquisition is shown in Fig. 8.2.

A binary readout scheme is considered as a readout electronics of the silicon tracker. The front-end readout electronics consists of Amplifier-Shaper-Discriminator (ASD), Time-to-Digital Converter (TDC) with 5 ns resolution, buffer memory, and readout blocks.

Muon g-2/EDM Experiment, Conceptual Design Report, Revised, December 12, 2011, 11:41 A.M.
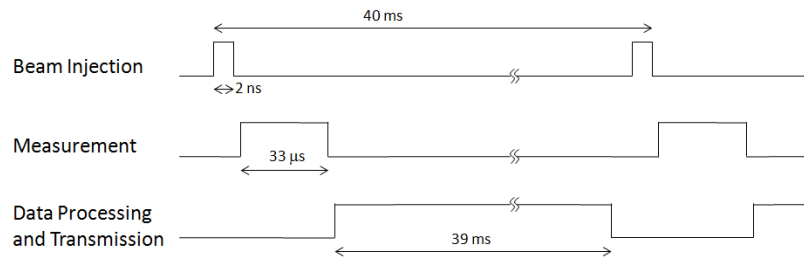
Figure 8.2: *Time sequence of the data acquisition*
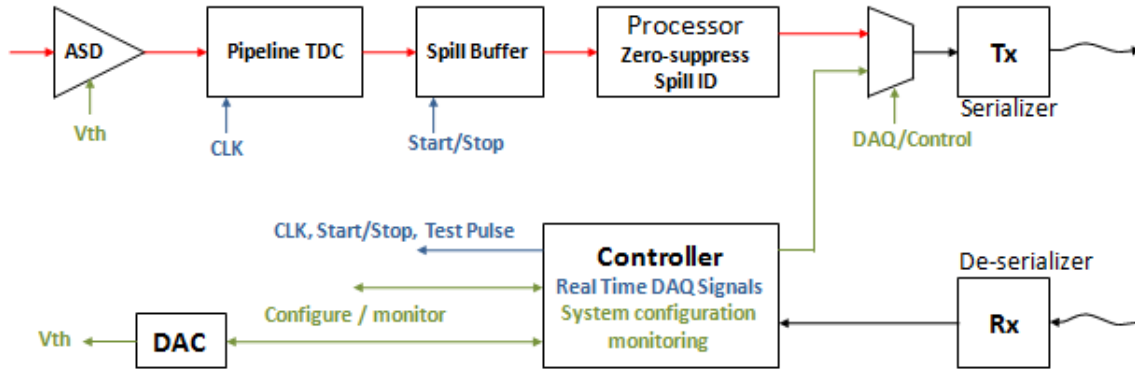
Figure 8.3: *Block diagram of the front-end board.*

8.3 Front-end board

Figure 8.3 shows a block diagram of the front-end board. Signals from the silicon detector enters the ASD with an external voltage threshold. The binary signal outputs from the ASD are then sampled by a 200 MHz clock (5 ns interval). The binary hits for each time stamp are saved in the buffer memory (spill buffer). The spill buffer starts storing data in the memory after receiving the "START" signal and stops either at the end of the preset period or receiving the "STOP" signal. When the measurement stops, the front-end processor circuit starts data processing. The processor reads raw data from the spill buffer, and performs zero-suppression and formatting for the data compaction. A set of spill data fragments, which includes a fragment header and trailer, is prepared and sent to the back-end DAQ system using a set of a high speed serializer and an optical transmitter (TX) via an optical fiber. The fragment header and trailer contains Board Number Identifier (BNID), Spill Number Identifier (SNID), status of the board, the data size, etc. and Cyclic Redundancy Check (CRC). The real time control signals, e.g. Clock, Start, Reset and Test Pulse Trigger, are provided from a set of an optical receiver and a de-serializer (RX). The bidirectional links (a set of TX and
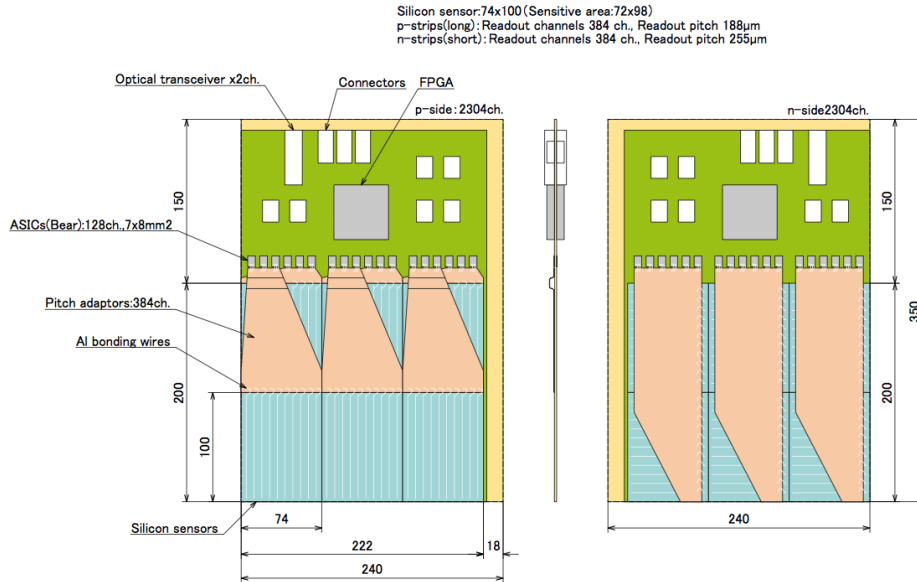
Figure 8.4: *Layout of the silicon-vane module*

RX) are also used for system configuration, control and monitoring of a front-end board.

The front-end board is operated under two operation modes. The "DAQ mode" is an operation mode for normal data acquisition. The "control mode" is an another operation mode for system configuration and monitoring. One of these operation modes is alternatively selected.

8.3.1 Layout of the silicon-vane module

A conceptual design of the silicon-vane module is shown in Fig. 8.4. A six silicon-strip sensors are placed in a 2×3 matrix. Two frontend boards are glued back-to-back. Each frontend board reads one side of the silicon-sensor strips. Readout strips on each sensor are connected to the frontend ASIC through flexible cables and pitch adapters. The silicon sensor has 384 readout strips in each sides. Six frontend ASICs are used to readout one side of the silicon sensor. There are 18 ASICs on the frontend board to readout three sensors. A FPGA collects outputs from ASICs and transmit merged data to the backend readout electronics via an optical fiber.

8.3.2 Front-end ASIC

The front-end ASIC consists of the ASD, the TDC, and the spill buffer (Fig. 8.5). Number of channels in the ASIC chip is 128. The ASIC has serial readout and semi-serial control lines.
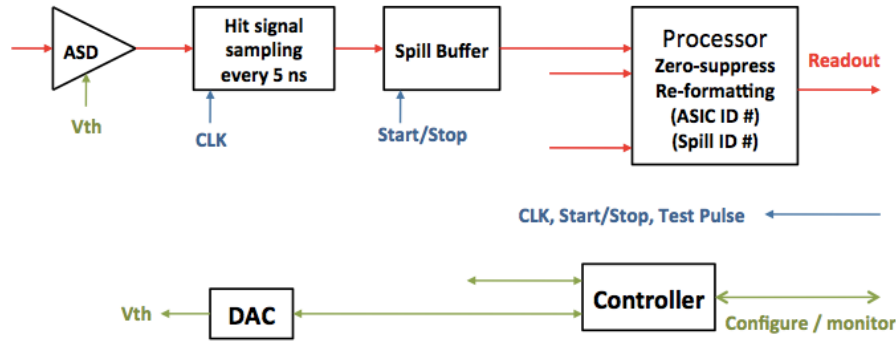
Figure 8.5: *Block diagram of the front-end ASIC*

The ASD receives signals from the silicon strip sensor. The silicon strip sensor is a n-type silicon with double-sided strips. The minimum-ionizing particles (MIPs) generates about 4 fC (25k electrons) in 320 μm-thick silicon-strip sensor. Negative charges are induced in n-side strips, and positive charges are induced in by p-side strips. The anticipated detector capacitance is about 30 pF. The design strategy for the ASD is to pick up precise timing information with fast pulse shaping.

A block diagram of the ASD is shown in Fig. 8.6. The ASD consists of 64 (or 128) arrays of a preamp and a shaper, followed by a comparator with DAC. The output of comparator is plugged into the memory (spill buffer). The DAC on the ASD set the voltage threshold on the comparator for each channel. Control signals, such as test pulse, analog monitor, DAC control are stored in the internal register. The preamplifier has conversion gain of 5–10 mV/fC with the dynamic range of -16 MIP to +16 MIP. The shaper has a gain of 50 mV/fC in the range of -3 MIP to +3 MIP. It generates a pulse with peaking time of less than 50 ns and width of about 100 ns. The anticipated power consumption is less than 5 mW per channel. Figure 8.7 shows simulated signal traces at the preamplifier, shaper, and comparator. The target noise level is less than 3000 e^- for the detector capacitance C_d=30 pF. The voltage levels for the ASD power and ground level is $\pm$1.25 V and 0 V, respectively. Specifications for the ASD are summarized in Table 8.1.

The output of the discriminator in the ASD is passed to the digital part of the ASIC which consists of the TDC and the spill buffer. The block diagram of the digital part of the ASIC is shown in Fig. 8.8. An externally-provided 200 MHz clock drives the digital part of the ASIC. The clock frequency is down converted to two out-of-phase 100 MHz clocks in the 2-phase clock generator to reduce the speed of
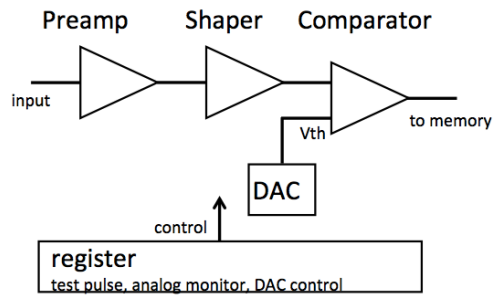
Figure 8.6: *Block diagram of the ASD block*
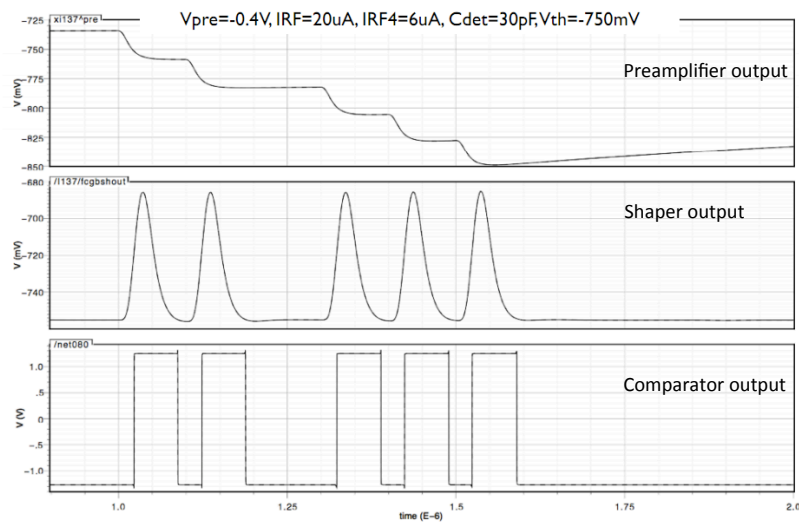
Figure 8.7: *Simulated pulse shape in the ASD*

Block	Parameter	Value
Preamplifier	conversion gain	5–10 mV/fC
	dynamic range	-16 MIP to +16 MIP
Shaper	pulse width	100 ns
	gain	50 mV/fC
	dynamic range	-3 MIP to +3 MIP
	peaking time	50 ns
Others	power consumption	<5 mW/ch
	noise	$< 3000 \ e^-$ (C_d=30 pF)
	number of channel	128

Table 8.1: *Specifications of the ASD*

signal processing. Upon the request of "START write", the states of the signal levels on the 128 input bus are latched by the 100 MHz clocks in the memory write controller. They are then written in the two memory blocks with the 10 ns time stamp provided by the 100 MHz clocks. The each memory block has depth of 4k words. The memory write controller fills the memories for 4k times each with opposite-phase clocks. Thus, these memories store the strip hits with 5 ns time stamps for 41 μs after "START write" signal arrives.

The memory read controller retrieves data from the memory when it receives "START readout" signal. The retrieved data is compressed in the zero suppressor. The zero suppressor provides a list of hit channels and their time stamps. These compressed data is transmitted to a serial data transport link through a serializer with a information on the ASIC ID number, spill ID number, a data header word, and a trailer word.

The ASIC has functions for system diagnostics and calibration with test pulses and test data write/send. A four-wires serial interface receives slow control signals, and monitor the status of the ASIC.

The ASIC is being designed by the electronics system group in KEK and Open Source Consortium of Instrumentation (Open-It)[1]. The UMC 0.25 μm CMOS technologies provided by the United Microelectronics Corporation Japan (UMCJ) is used in the production.

The FPGA in the frontend board collects data from 18 ASICs with serial links. The FPGA merges and reformat the data with sensor and strip address information. The FPGA receives slow control signals as well as real time control signals from the backend readout board, and distributes them to each ASICs.
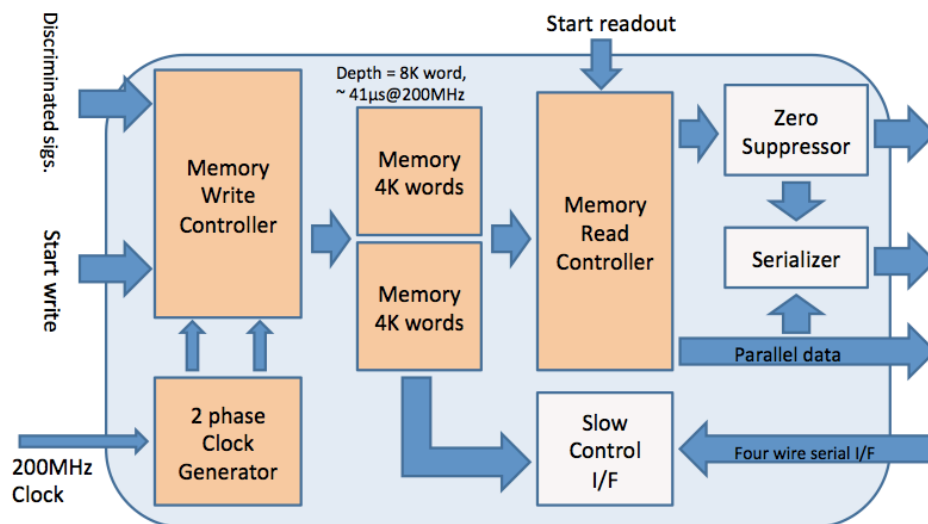
Figure 8.8: *Block diagram of the TDC and readout parts in the ASIC*
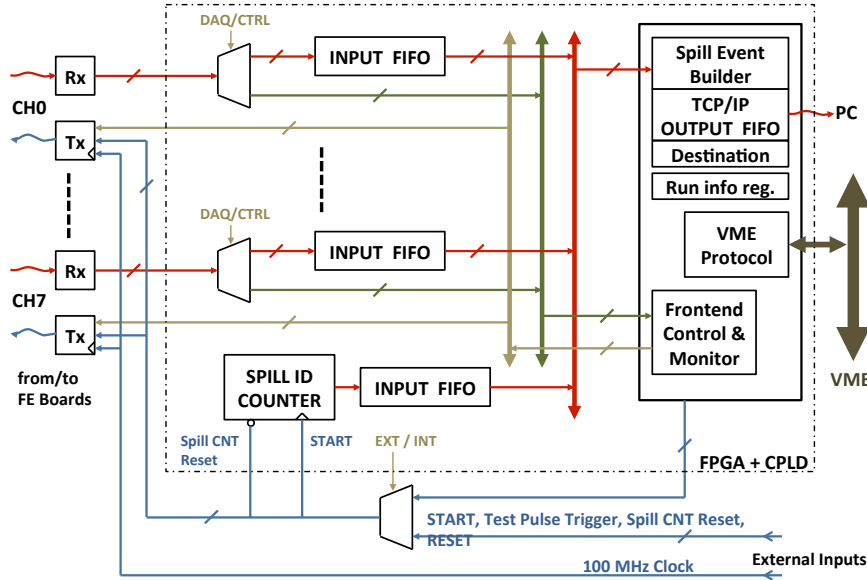
Figure 8.9: *Block diagram of the backend readout electronics*

8.4 Backend readout board

The data from the frontend board is received by the backend readout board. The block diagram of the backend readout board is shown in Fig. 8.9. The backend readout board is connected to 8 front end boards with the bi-directional optical serial link. The baud rate per optical link is 2 Gbps. The data processing and slow control tasks are programmed in the FPGA and CPLD. The incoming data is stored in the input FIFO for each channel. The data fragments from each channel are merged by the spill event builder. The run information is stored in the run information register. The spill ID is computed in in the spill ID counter which starts counting up upon the "START" signal. The merged data is combined with run information and the spill ID. The combined data is transmitted to the PC farms from the TCP/IP output FIFO by utilizing the SiTCP technology [2] via a Gigabit Ethernet network switch.

The configuration and frontend control signals are passed through the VME interface. During the normal data taking, the DAQ mode is selected. The control mode is selected when the frondend board needs to be configured or monitored.

The real-time signals, such as start, test pulse trigger, spill counter reset, reset, are provided either from the VME instructions or external inputs (timing control board). The serial links to the frontend boards are synchronously locked by the 100 MHz clock which is provided from the external input (timing control board).
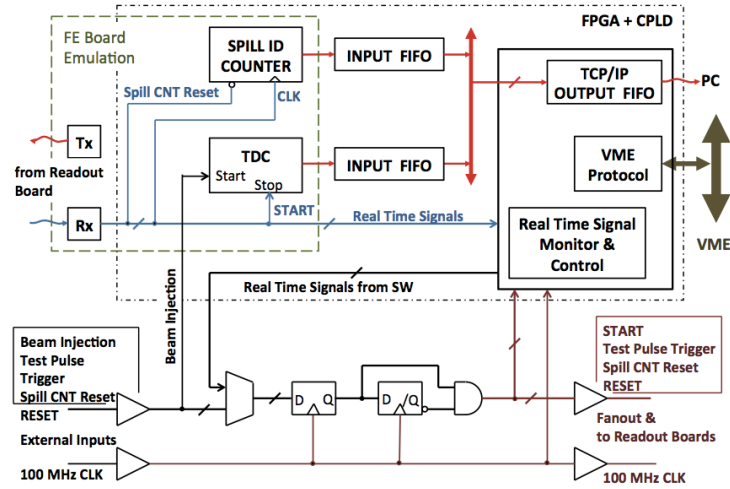
Figure 8.10: *Block diagram of the timing control system*

8.5   Timing control board

The timing control board (Fig. 8.10) receives real time signals such as external system clock (100 MHz), beam injection, test pulse trigger, spill counter reset, reset signals. Those signals are synchronized with the system clock, and then distributed to the readout boards. The START signal is generated from the beam injection signal at this stage. The timing is adjusted by using the same cable length. All readout boards, as well as frontend boards, are operated in synchronous to the system clock.

For system test and monitoring, real-time control signals can also be issued, monitored, and controlled from VME interface.

A copy of real time signals from readout board is received at the front end board emulation section of the timing control board. The front end board emulation section measures time between start and beam injection in the TDC block. The TDC data with the spill ID information are sent to the PC farm. This data and detector data from readout boards form the complete set of the event data.

8.6   PC farm and storage

The scale of the online PC farm and storage are determined from estimated data size and data-transfer speed as described below.

A hit in the silicon strip sensor contains information of sensor address (3 bits), strip address (9 bits), time stamp (13 bits), leading/trailing edge (1 bit), which add up to 4 byte/hit. The data size of a hit become 8 byte when the leading and trailing edge hits are separately recorded.

Typical number of hits in the tracker was estimated in the Monte-Calro simulation which was discussed in chapter 7. There are in total 2.2 M hits/spill for whole silicon vanes. There are $384 \times 6 = 2304$ strips for one frontend modules. Total number of strip is 442k strips. Number of hit per strip is $2.2M$ hit/$442k$ strip $= 5.0$ hits/strip/spill.

Data size from the frontend boards would be 8 kbyte $\times$ 5.0 hits/spill $\times$ 25 spill/s $= 2.3$ MB/s (92 kB/spill). One backend readout board receives data from 8 frontend boards. Data size from the readout board is 2.2 MB/s $\times$ 8 frontend board $= 18$ MB/s (740kB/spill). There are 48 vanes each in the upper and bottom halves of the detector system, respectively. Each vane requires two frontend boards to readout both sides of strips. Therefore, it requires 192 frontend boards and 24 readout boards. The total data size of whole detector system which goes to the PC farm would be 18 MB/s $\times$ 24 readout board $= 440$ MB/s (18 MB/spill).

The data transfer from the readout board to the PC farm utilizes the Gigabit Ethernet technologies (GbE) bridged by network switch(s). If number of PCs in the PC farm is 10, average data transfer rate from the readout boards to a PC is 44 MB/s. The throughput of GbE network switch should be high enough to transfer all data.

Many network switches with GbE (or even 10GbE) compatibility are commercially available in the market. For example, a switch with 48 Ethernet I/O ports could accommodate all outputs from readout boards (24 ports) and inputs to PCs(10 ports).

A PC in the PC farm receives a complete set of data fragments from readout boards in a spill. In a PC, a complete spill event is build from data fragments before the data is written in the disk. At this stage, it is possible to compress the data size to 5 byte/hit by reformatting data in terms of absolute strip address (1 (upper/bottom) + 1 (p-side/n-side) + 11 (strip) + 6 (vane) = 18 bit), time stamp (13 bit), and pulse width (7 bit). In this case, the total data size would be 5 bytes/hit $\times$ 2.2 M hit/spill $\times$ 25 spill/s $= 280$ MB/s (11 MB/spill). The data write rate per PC is 28 MB/s when there are 10 PCs in the PC farm. Data-write speed of PC to the hard disk, which is about 100 MB/s, won't be a bottle-neck of the data acquisition.

Total size of raw data over the proposed run period (10^7 s) would be 280 MB/s $\times$ 10^7 s $= 2.8$ PB. Storage hard-disk system with such a scale is commercially available in the market.

Data size and data-transfer speed at each stage are summarized in Table 8.2.

8.7   High voltage and low voltage distribution

A schematic diagram of high voltage (HV) distribution for sensors and low voltage (LV) distribution for front end electronics are given in Fig. 8.11.

There are 48 vanes and 576 silicon sensors in the system. Individual HV/LV power supplies to each sensor are not a realistic solution due to geometrical constraints to accommodate all of connectors as well as financial constraints. A common HV supply with capability of individual current monitoring

Quantity	Value
Hit data size	8 byte/hit
Number of hits per frontend	11.5k hits/spill
Data size from frontend board	2.3MB/s (92kB/spill)
Data size from readout board	18MB/s (740kB/spill)
Total data size	440MB/s (18MB/spill)
Total data size(w/ reduction)	280MB/s (11MB/spill)
Disk write speed of PC	100MB/s (4MB/spill)
Number of PC	10
Data storage space	2.8 PB

Table 8.2: *Summary of data size and data transfer speed*

and ON/OFF is a better solution.

A care must be taken on the voltage level between the readout strip and sensor. It is known that voltage tolerance of the coupling capacitor between the readout strip and sensor is less than 20 V, while the typical bias voltage is 120 V. The low voltage power supply (LVPS) needs to be operated with a common floating ground which is set at bias voltage of the sensor to keep the voltage level between the readout strip and sensor less than its tolerance voltage. This prevents us from turning individual sensors OFF when the LV of the frontend board is turned ON.

Foreseen power consumption of frontend electronics is about 1000 A at 2.5 V. In such high current, there are issues of voltage drop in cables and stray magnetic field. A DC/DC converters are one of solutions to suppress those issues. The LV power line runs at voltage level of 36 V near to the detector. The DC/DC converter converts the voltage from 36 V to 2.5 V near the detector. A issue of operation of such DC/DC converter in magnetic field and possible pollution to magnetic field needs to be investigated.

The fanout of HV lines with current monitor with ON/OFF switch as well as fanout of LV lines followed by DC/DC converters are installed in the HV/LV distributor box. This box is controlled and monitored by a FPGA via an external serial link. The conceptual circuit diagram of the HV and LV distributor box is shown in Fig. 8.12.

8.8   Frequency standard and clock distributions

The clock system determines the precision of the time stamp in the $g-2$ measurement. The precision of time stamp ΔT relative to the $g-2$ precession period T_{g-2} should be $\frac{\Delta T}{T_{g-2}} << \frac{\Delta \omega}{\omega} = 0.1$ ppm. Thus, $\Delta T << 0.1$ ppm $\times$ 2 μs $= 0.2$ ps. The time stamp must be stable within required precision ($\Delta T << 0.2$ ps) over a cycle of the measurement $T_M = 41 \mu s$. Therefore, required stability of the clock frequency should be $\frac{\Delta f}{f} = \frac{\Delta T}{T_M} << 0.2$ ps/41 μs $= 5 \times 10^{-9}$.
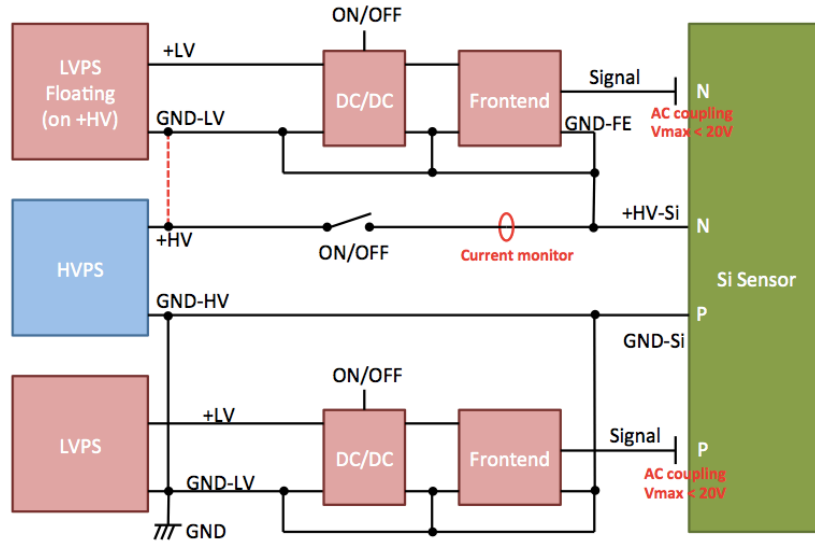
Figure 8.11: Block diagram of the HV and LV distributions

The overview of the clock distribution system is given in Fig. 8.13. The clock system is sourced by the Rubidium frequency standard with the periodic corrections based on the GPS frequency reference and the frequency standard in National Metrology Institute of Japan (NMIJ frequency standard). The NMIJ frequency standard is defined from Hydrogen masers in NMIJ. The NMIJ provides service to broadcast differences between the NMIJ frequency standard and the times from GPS satellites in the Ethernet. The Rb frequency standard module provided by NMIJ [3] has a GPS receiver and an Ethernet I/O port where difference from the national frequency standard can be received. A long-term stability of the frequency is ensured by feedback from GPS frequency reference and NMIJ frequency standards. Specifications for the frequency stability are better than 3×10^{-11}/s, 3×10^{-12}/hour, and 1×10^{-13}/day (allan deviation). There is no need to stop the local frequency standard for calibration as it is periodically calibrated remotely.

The same frequency standard is used in the NMR field monitoring system. In this way, systematic uncertainties of the clock system are canceled in $\frac{\omega_a}{\omega_p}$.
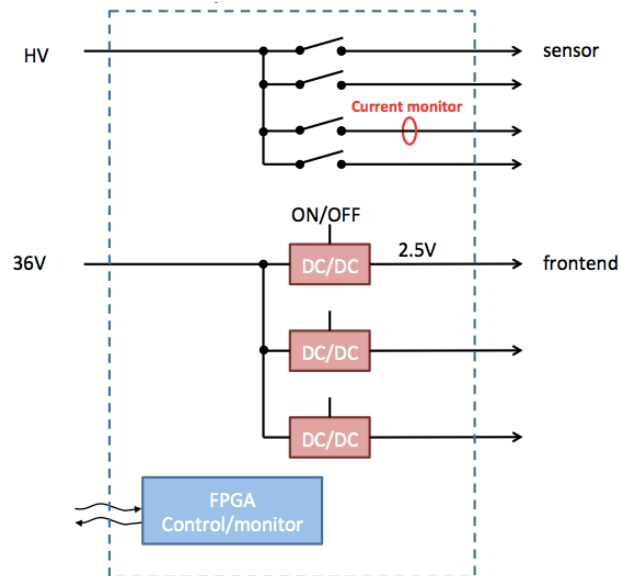
Figure 8.12: *HV and LV distributor box*
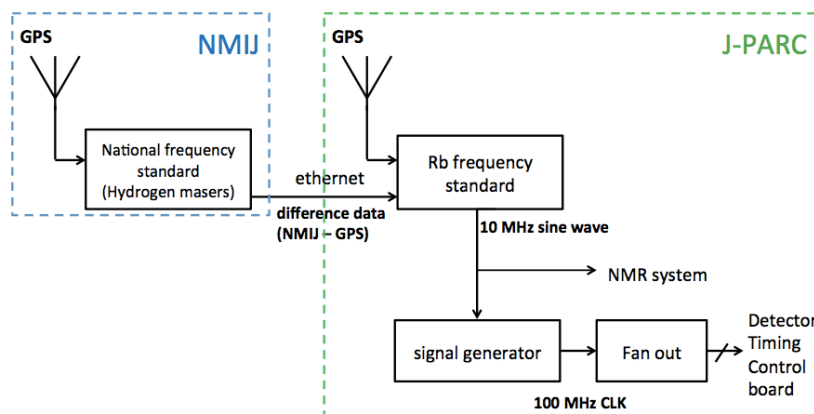
Figure 8.13: *Block diagram of the frequency standard and clock distribution*

8.9 Mechanical structure

The layout of the silicon detector in the storage magnet is shown in Fig. 8.14. The detector is installed in the central region of the storage magnet. The detector system is supported with a support frame which is connected to the upper pole tip of the magnet yoke.

A tungsten tube with a diameter of 96 mm is placed in the most inner part of the detector region. The silicon vane modules are attached to the tungsten tube. Vertical support structures for the silicon vane modules are placed at the end caps. These support structures are made of material with high thermal conductivity so that it can also serve as a heat sink for cooling.

The optical fiber (TX/RX), HV/LV power cables, and cooling lines are externally provided to the detector system. All cables are routed though a hole in the upper pole tip of the magnet yoke. Half of these cables go to bottom side of the detector region though the central hole in the silicon detector. The fiber patch panels and HV/LV distributor boxes are placed in the top and bottom of detector region as shown in Fig. 8.14.

Bundled optical fibers are dis-bundled at the fiber patch panel, and then connected to each frontend board. The HV power cables are sub-divided into each sensor, and the LV cables are sub-divided into each frontend boards after lowering voltage at DC/DC converters in the HV/LV distributor boxes.

The detector region is in atmospheric pressure. The boundary between detector region and muon injection/storage regions is separated by a vacuum wall. The positrons from muon decay should penetrate the vacuum wall. It is desired that the thickness of the wall near the muon storage region (about 200 mm in height) is thinner than $3 \times 10^{-3} X_0$ which is a radiation length of a silicon vane in order not to spoil the vertexing resolution.

A cooling system removes heat generated by 2.5 kW power dissipation at ASICs, DC/DC converters, and other components.
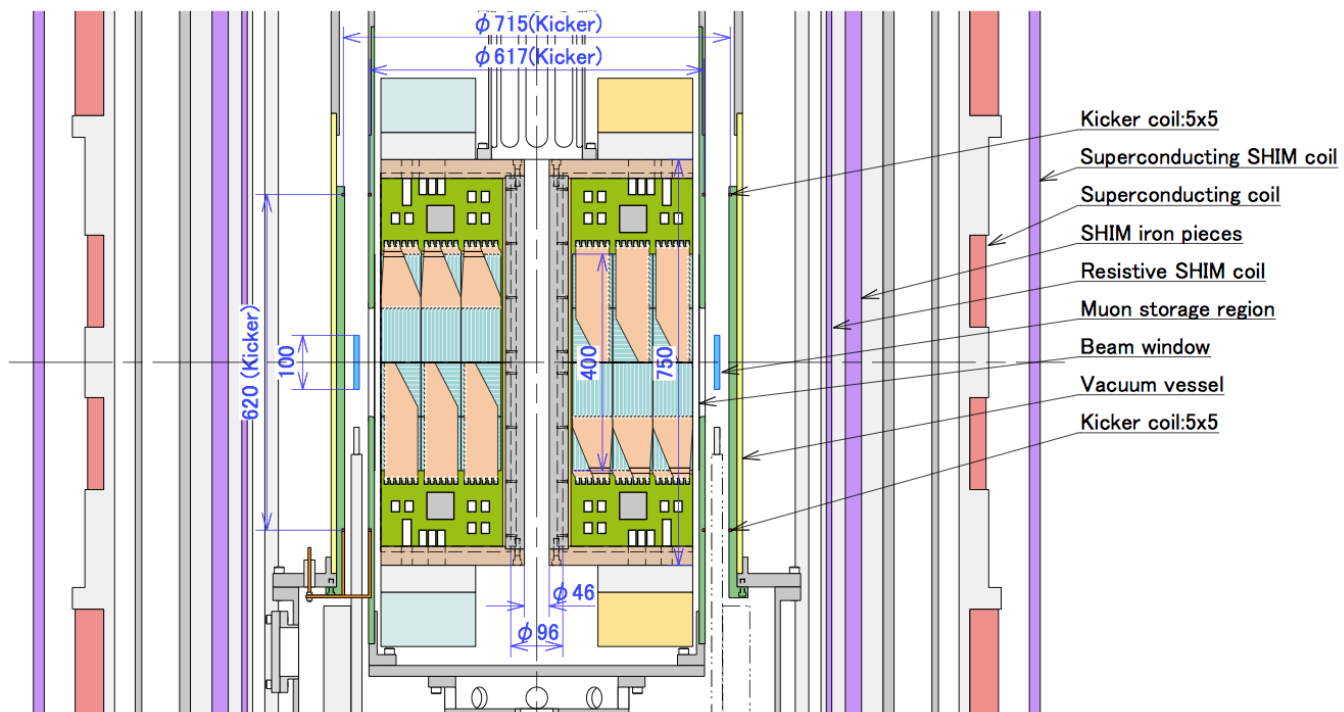
Figure 8.14: *Layout of the silicon detector in the storage magnet*

References for Chapter 8

[1] openIt : Open Source Consortium of Instrumentation http://openit.kek.jp

[2] reference to SiTCP

[3] Frequency standard GCET-SA (National Metrology Institute of Japan)

Muon Storage Magnet
- Field Control and Monitoring -

Contents

9.1 Magnet System

9.1.1 Introduction

The muon storage ring for $g - 2$/EDM experiment will be a precession field 3 Tesla solenoid with cylindrical iron poles and return yoke. The solenoid is being designed now in collaboration with a Japanese private company.

Design constraints of magnetic field described in the chapter 5 are summarized as follows;

- Storage region
  - Axial field (B_z) : 3T
  - Uniformity : < 1 ppm locally
  - Region : 33.3 $\pm$ 1.5 cm in radius, $\pm$ 5 cm in height
- Injection region
  - $B_r \times B_z > 0$
  - Radial field (B_r) has to change smoothly along the beam orbit
  - Region : from the end of the beam injection line to the beam storage region.
- Weak focus field
  - In the storage region, $B_r = -n \dfrac{B_{0z}}{R} z$,
    (B_{0z} : field strength in z direction at the center of the storage region)

where, coordinate system is the same as Fig. 6.4.

9.1.2 Main coil design study

The muon storage ring for this experiment will be a precession field 3 Tesla solenoid with cylindrical iron poles and return yoke. The solenoid is being designed now in collaboration with a private company to a specification of less than 1 ppm variation of the field locally within the storage region.

Figure 9.1 introduce the magnet configuration planed for the storage ring. This conceptual design adopts the iron yoke is used to return the magnetic flux. Thanks to using iron yoke, it becomes easy to achieve good field homogeneity in large volume with simple structure.

Practical design is in progress collaborating with a Japanese private company. Optimization processes of main coil design are as follows;

1. Calculate the magnetic field produced by the coil and iron yoke.
2. Calculate the error field from the target field.
3. Modify the shape of coils and iron yoke.
4. Repeat step 2 and 3 until the error field is converged.

Muon g-2/EDM Experiment, Conceptual Design Report, Revised, December 12, 2011, 11:41 A.M.
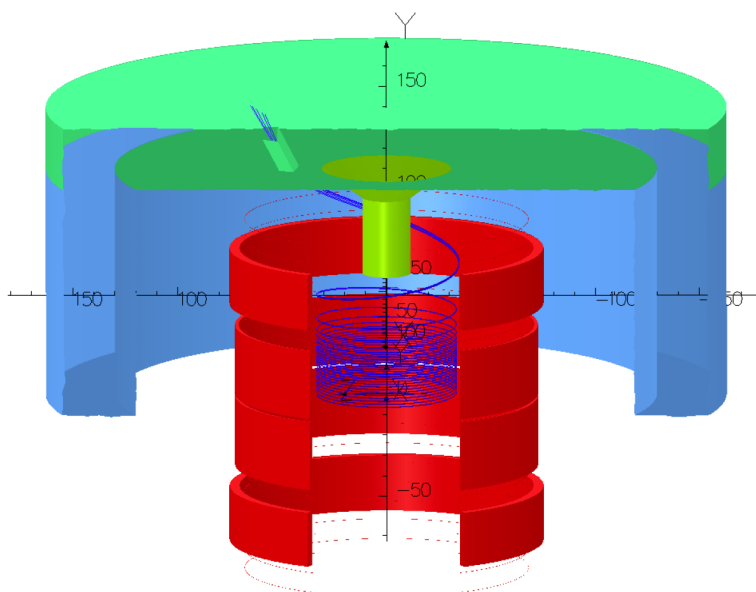
Figure 9.1: *Schematic view of the superconducting solenoid: solenoid coils, one-fourth iron pole tip and return yoke.*

5. After the convergence, the beam track is calculated to check smooth beam injection.

6. Go back to step 2 to improve the beam track.

The steps from 1 to 4 are mainly carried out by the private company, and the beam tracking is calculated by KEK staff.

Four design types have been studied as summarized in Table 9.1. In the Type1 and Type2, the focussing field was not considered, therefore, the uniform field region and number of coils was larger than the Type3 and Type 4. From the view point of simplicity of manufacture and the inner space for the detector, we are mainly studying the Type 4 model as the first candidate at present.

In the above optimization process, magnetic design of weak focusing field is included. It means that the weak focusing field is generated by the iron yoke and the main coils. However, in the next step design, coils only generating weak focusing coil will be designed independently so that the field strength of weak focusing field could be controlled.

9.1.3 Field tuning scheme

In reality, it is impossible to obtain the ideal field distribution due to many reasons, e.g., coils mis-alignment, magnetic materials inside the magnet, mechanical vibration and so on, as shown in the section 9.1.4. In order to achieve high homogeneity of magnetic field below 1 ppm, the error field correction scheme must be established before magnet fabrication as much as possible.

Table 9.1: *Types of Magnet Design*

	Type1	Type2	Type3	Type4
No. of Coils	6	6	4	4
Coil Inner Diameter (mm)	1600	1400	1400	1400
Coil Length (mm)	1889	1532	1428	1441
Yoke Outer Diameter (mm)	3950	3800	3260	3560
Yoke Height (mm)	3600	3050	2800	2900
Yoke Weight (ton)	200	-	<94	114.4
Peak Field on Conductor (T)	5.68	5.52	5.20	5.39
Energy (MJ)	23.4	17.4	12.5	17.2
Target Field				
Uniform Field Height (mm)	±150	±150	±50	±50
Focus Field	No	No	Yes	Yes

It is said in general that a magnet right after fabrication would have a error field of several hundred ppm due to the imperfection of magnet structure, even if a fabrication tolerance is minimized as much as possible. In addition, there would be many error sources that will be described later.

In the present plan, error fields are corrected with the following three step which is the same as commercial MRI and NMR magnet systems.

1. Rough tuning by using iron pieces;
   to put iron pieces inside the magnet bore to compensate the field distribution.

2. Fine tuning by using superconducting shim coils;
   to correct residual error fields by superconducting shim coils.

3. Final fine tuning by using normal conducting shim coils;
   to correct residual error fields after above two steps by normal conducting shim coils.

Tuning by iron pieces

About field tuning by iron pieces, it is generally said that the error field more than 1000 ppm could be corrected to several ppm. As an example, a iron ring is assumed to be placed in the magnet bore as shown in Fig. 9.2. The iron ring has a rectangular cross section of 10 × 20 mm and inner radius of 1030 mm. When the iron ring is placed at the same axial position of upper coil as shown in Fig. 9.2, the magnetic field at the center of the storage position changes by 346 ppm. Furthermore, by arranging the locations of iron pieces, any error field distribution could be corrected [1] - [3].
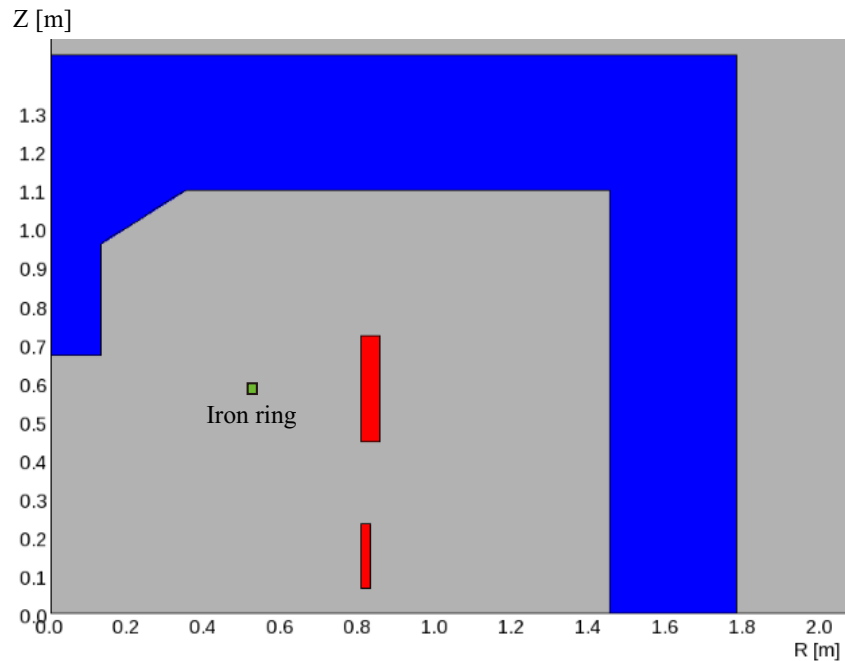
Figure 9.2: *Two dimensional model for calculating effect of iron ring.*

Shim coils design

Small residual error field after tuning by iron pieces is corrected by superconducting and normal conducting shim coils. To achieve high homogeneity, many shim coils are needed to compensate the various mode of error field distribution [4, 5].

To design shim coil pattern, the surface current potential and singular value decomposition (SVD) techniques [6] are employed.

In this technique, the current potential distribution on shim coil winding surface is calculated for correcting the error field, and then, the winding pattern is derived from the current flow line calculated from the current potential distribution. Singular value decomposition (SVD) technique is used for calculating the current potentials correcting the error fields. Using this technique, the current potential can be described by convolutions of eigen distributions. Figure 9.3 shows an example of current flow pattern of each eigen mode decomposed by SVD. Horizontal and vertical axes represent angular position and axial position, respectively. The lines in the figure represent contour lines of current potential, corresponding to the coil winding patterns, and hatched area represents that current direction is opposite to non-hatched area. Current potential patterns of every eigen mode are orthogonal each other, therefore, the magnetic fields generated by the coil winding patterns in the figure are independent. Based on the results of current potential calculation with SVD, the practical winding pattern will be developed.

This design method is also employed to the superconducting magnet for the muonium HFS experiment,

and basic R&D work is done in the collaboration with the HFS experiment.
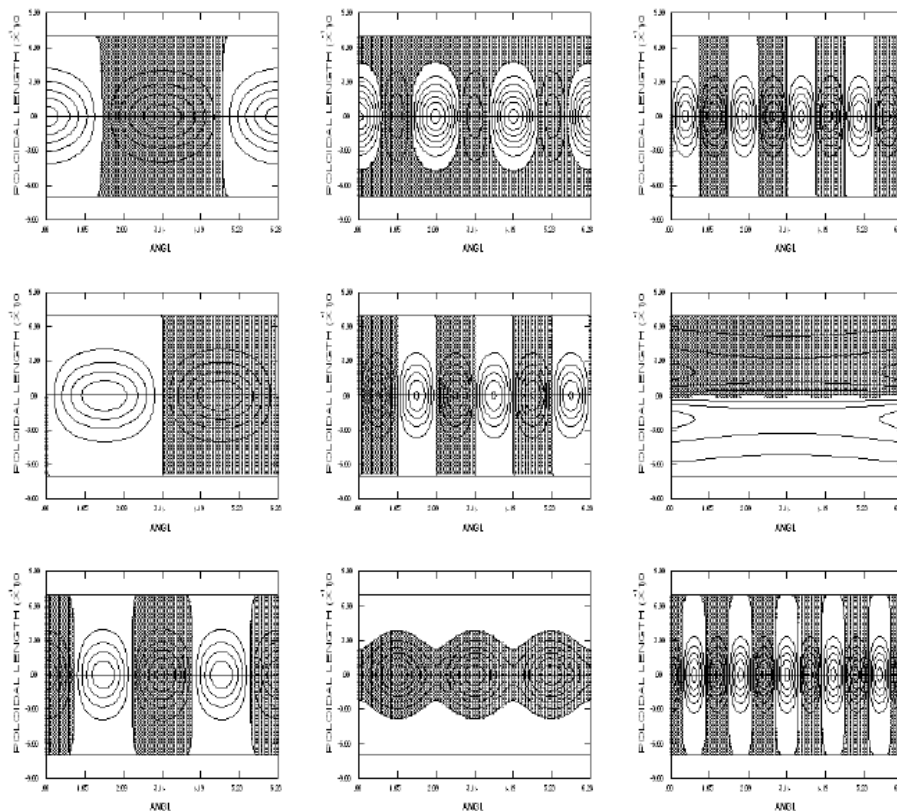
Figure 9.3: *Current potential pattern for the $g - 2$/EDM experiment for the design of shim coils.*

9.1.4 Error field source

In order to estimate the required amount of iron pieces and to decide the power of shim coils, possible error sources are studied to evaluate magnitudes of field errors.

Two types of error sources are considered. One is static, and another is dynamic sources. The possible error sources are summarized as follows.

- Static source
    - Coil misalignment and deformation
    - Magnetic materials
        * Actual iron yoke structure, vacuum chamber, detector, etc.
- Dynamic source
    - Thermal expansion of iron yoke
    - Characteristics of superconductor
        * Magnetization, Strand coupling current and Persistent current operation

 − Mechanical vibration
   ∗ Cryocooler, Seismic ground vibration

In general, error field caused by the static sources would be very large, but amplitude doesn't change with time. Therefore, these could be corrected by iron pieces.

On the other hand, error field due to the dynamic sources fluctuate with time, although it's small compared with the static errors. Only shim coils can correct the dynamic error fields.

In the following section, the present status of the error estimation study is described.

Coil misalignment and deformation seem to be the largest static error source. In order to achieve field quality of 10^{-7}, these construction errors must be the order of 10^{-6} m that is far beyond the achievable construction precision, which is the order of 10^{-3} m for the 1 m big magnet. This indicates that achievable field quality with the main coil is the order 10^{-4} T range.

Coil misalignment About coil misalignment, there are two types of misalignment, that is, misalignment between coils and between coils and yoke. Figure 9.4 shows an example of the calculated field change at the end of storage region due to the coil misalignment for yoke. This calculation was carried out in the Type1 coil model in table 9.1, therefore, the end of storage region was at $x = 0.333$ m and $z = \pm0.1$ m. Figure 9.4(a) and (b) show the results when the coils move in z and x direction, respectively. The linear correlation between the coil misalignment and the field errors are found in these figures. From these results, the relationships between the field error and the coil misalignment can be summarized as shown in table 9.2. Considering the reasonable construction precision of 10^{-3} m, the maximum errors due to this misalignment are about 3 ppm in B_z and 5 ppm in B_r.

Table 9.2: *Summary of correlation between coil misalignment and error field*

	Misalignment in z direction	Misalignment in x direction
B_z	30 ppm/mm	11 ppm/mm
B_r	53 ppm/mm	2 ppm/mm

Coil deformation The largest deformation of the coils in the magnet are occurred during the following three stages; coil winding, cooling the magnet and energizing the magnet. The superconducting strand must be wound around the coil bobbin with enough tension, otherwise a strand moves easily by the electromagnetic force during coil charging, and the superconducting magnet might quench. In order to avoid such a strand slip, a magnet is generally wound at more than several tens MPa winding tension. This causes that the coil bobbin is pressed inward by the compressive stress.

The shrinkage of coils during cooling is the biggest deformation. For example, stainless steel can shrink by about 0.3 % when it cools to 4.2 K. If the coil bobbin is made by a stainless steel and cooled by liquid helium, the coil size would change by about 4 mm. Fortunately, this size reduction
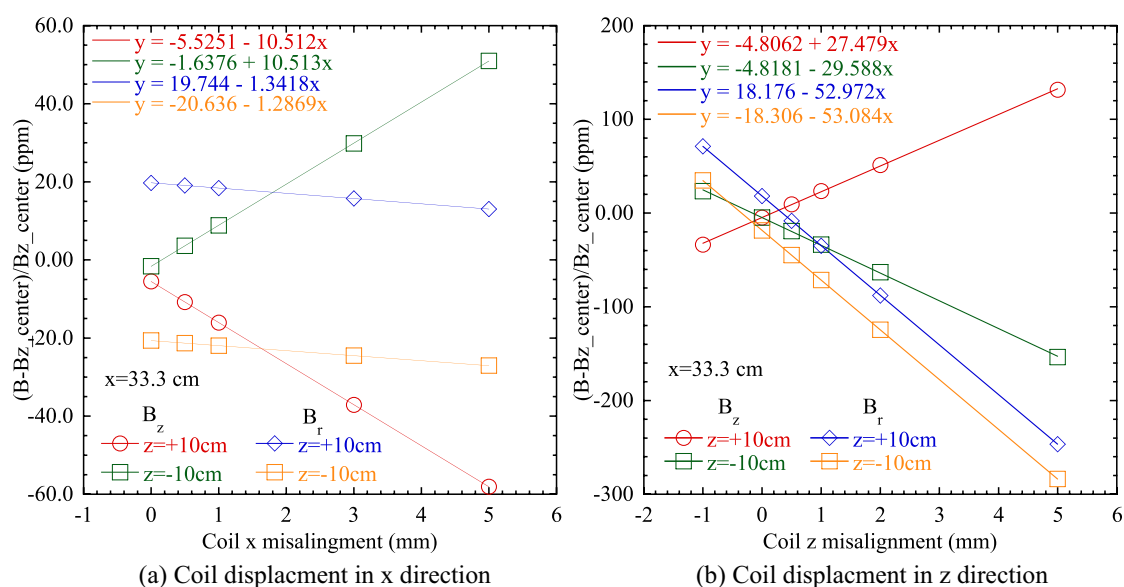
Figure 9.4: *Error field at x= 0.333 m, z = ±0.1 m as a function of coil displacement; (a) displacement in z direction, (b) displacement in x direction.*

by thermal contraction is isotropic, and the variation could be expected. By including this variation into the bobbin size at room temperature in advance, the error field can be minimized.

During the magnet excitation, a hoop stress is applied to coils by electromagnetic force. The coil deformation by the winding tension can be decreased by this hoop stress,

Finally, the bobbin size and the winding tension must be carefully designed so that the residual deformation after the above three stages will be less than 10^{-4} m which is the achievable construction precision.

Magnetic Materials

Three issues have been studied; magnetic materials inside the magnet bore, the effect of actual yoke structure, and non-uniformity of yoke permeability.

Magnetic materials inside magnet bore   Inside the magnet bore, many devices like the positron detector are placed as described in the section9.1.6. Basically, ferromagnetic materials are not allowed inside the magnet bore, but whatever materials have magnetization more or less. Therefore, these effect has to be examined beforehand.

As a first step, the field distortion due to various materials and the circuit components used in the detector is measured using the 1.6 T magnet. The material block or the circuit component is placed at the center of the 1.6 T magnet, and the magnetic field is measured by NMR probe as a function

of distance from the object surface see Fig. 9.5. The preliminary results are shown in Fig. 9.6. Figure 9.6(a) and (b) show the measured data of different metallic materials and electric circuit parts for the detector.
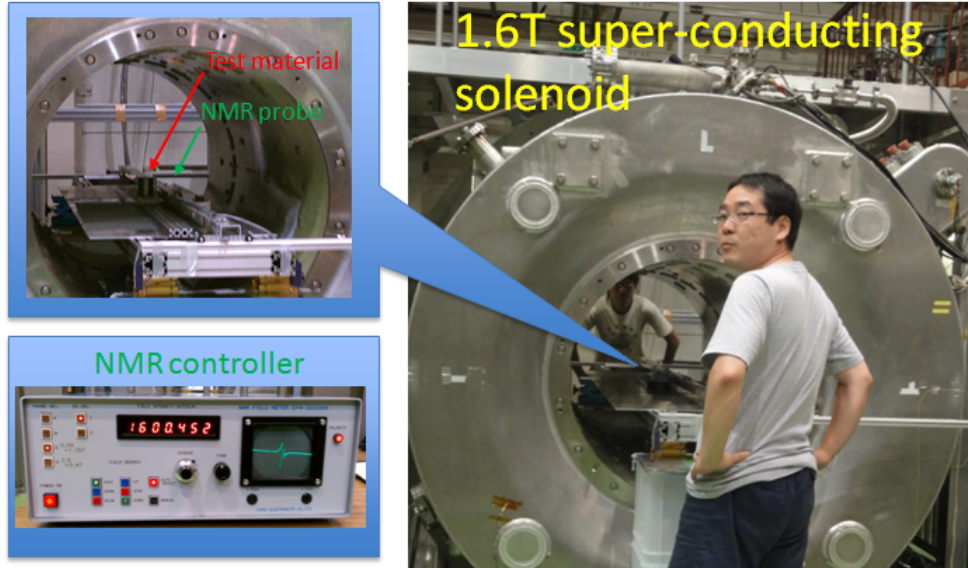
Figure 9.5: *Experimental setup of the measurement of the magnetic field change with different materials.*

(a) Metallic materials

(b) Circuit components
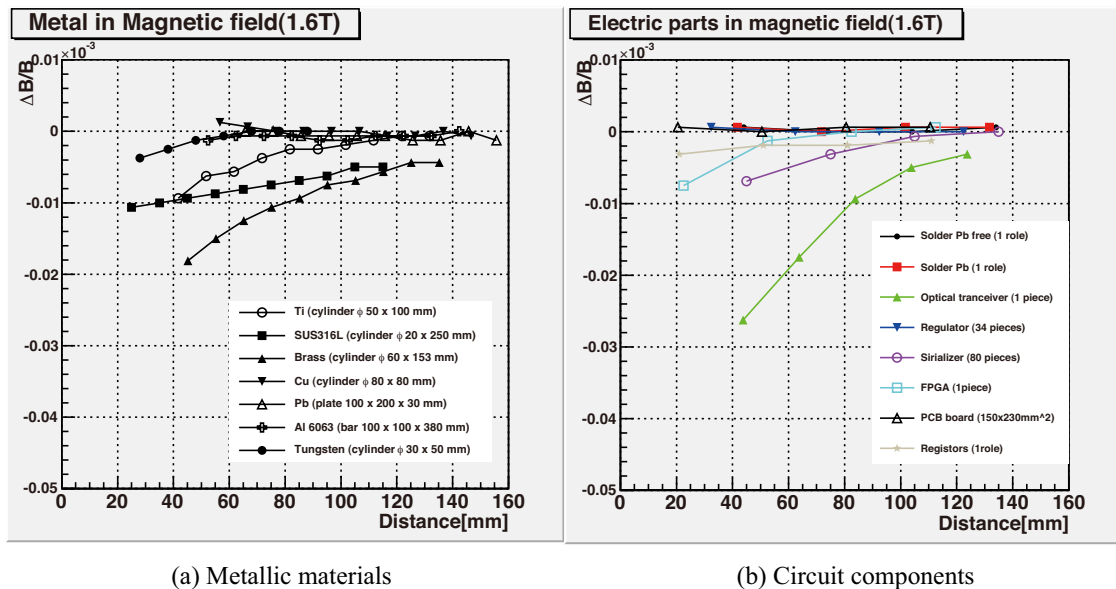
Figure 9.6: *Measured field change with different materials as a function of distance from surface.*

The most important material in the metallic material is stainless steel (SUS), because it is used in the largest quantities for the structural material of the system, e. g., the coil bobbin, the vacuum and helium vessels. In terms of the detector parts, the large magnetization is measured in the op-

tical transducer. Although this transducer will be located far from the storage region, a lot of this component are required for the detector.

Unfortunately, the measured sample sizes are different each other in Fig. 9.6. And also the detail structures of the detector and magnet system have not been designed yet. In order to evaluate these effect quantitatively, more detail study considering the position is in progress. If the effect of the materials inside the bore on the error field is larger than the capability of the field correction due to iron pieces, re-optimization of the main coil structure considering this components will be required.

Effect of yoke tunnel   In the actual iron yoke, many tunnels are required for beam pipe, signal lines, vacuum pipe and so on. The shortage of iron in these tunnels affects the field distribution. For example, about the beam tunnel, Figure 9.7 shows the axial and radial field distribution as a function of z position, at $x = 0.333$ m and $y = 0$ m. Black and red lines represent the results with and without the beam tunnel. There is a clear difference of about 10 gauss. The easy way to correct such error fields is to put irons around the exit of tunnels. Qualitative analysis of this correction scheme is ongoing.
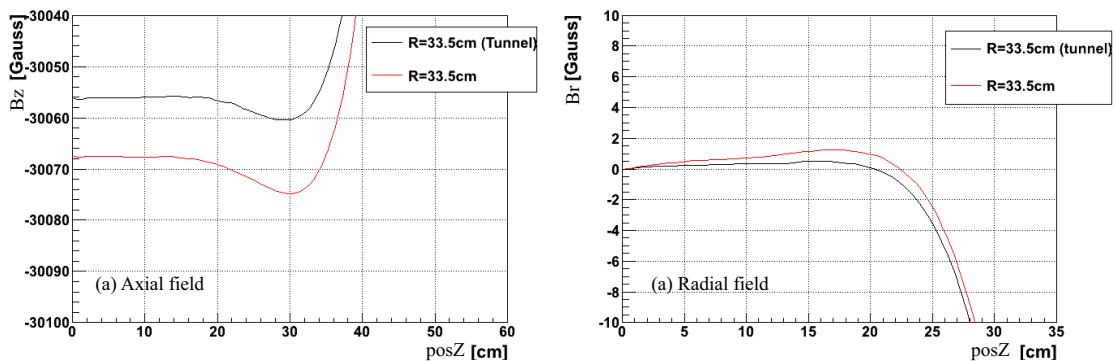
Figure 9.7: *Effect of beam tunnel on field distribution; (a) axial field, (b) radial field.*

Non-uniformity of yoke permeability   The non-uniformity of yoke permeability is also problem. Because the size of iron yoke is very large, iron yoke is expected to consist of many blocks of iron in practice. This might cause that the permeabilities of the blocks are different each other. This effect was roughly estimated with the simple model as shown in Fig. 9.8. In this model, the permeability of one pole tip is changed by $+10$ %, and calculate the field change in the storage region. Figure9.9 shows the field difference from the results with uniform permeability. The center field of the storage region is normalized by 3 T. The deviation in the figure is only about 13 ppm. In addition, the permeability is generally expected more uniform than this assumption. This indicates that the effect of non-uniformity of permeability is sufficiently small to be corrected by iron pieces.
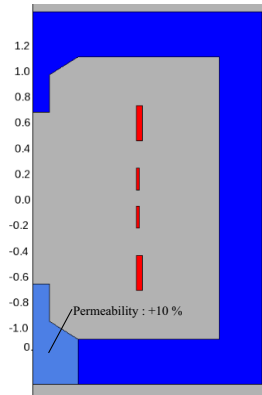
Figure 9.8: *Model for calculation.*
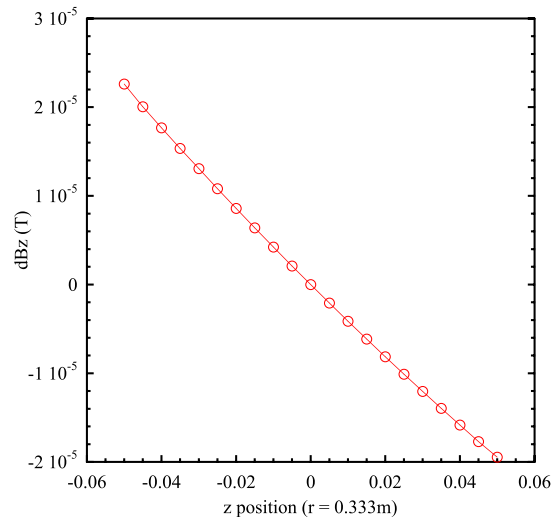
Figure 9.9: *Calculated field change due to non-uniform permeability.*

Thermal expansion of iron yoke

Thermal expansion of iron yoke is one of the dynamic error source of error field. The thermal contraction ratio of iron is about 10^{-5} /K. In order to achieve 10^{-6} m accuracy, the temperature of iron yoke must be controlled by the order of $\pm$ 0.1 K. However, a magnetic flux in the superconducting magnet with persistent current operation must be preserved in principle, therefore, it is expected that field strength does not change so much.

Figure 9.10 shows the calculated field distribution in the storage region along z position. The vertical axis represents the axial field strength at $r = 0.333$ m, each symbol represents the results when the yoke size is changed by +0.1 %, +0.05 %, 0 %(no size change), -0.05 % and -0.1 %. Because these results are calculated using the model before completing the optimization, the field uniformity is not satisfied with the specification. The important point is that the field distributions are the same each

other. The average values of these distributions are shown in Fig. 9.11. The average value changes linearly with the thermal expansion ratio, that is, the temperature change. The ratio is calculated to be 0.094 ppm/K, indicating that the temperature control of ± 1 K is sufficient for the required specification, and it seems manageable.
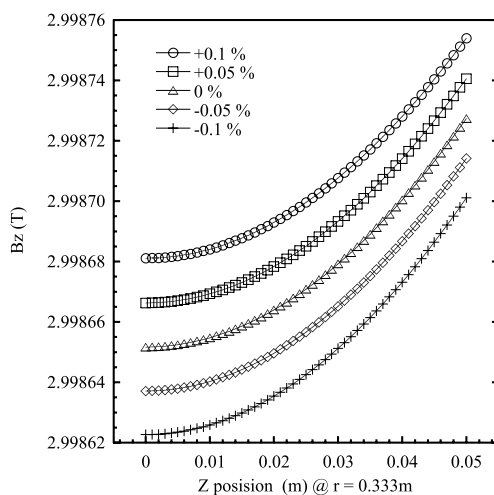
Figure 9.10: *Calculated field distribution with different yoke sizes.*
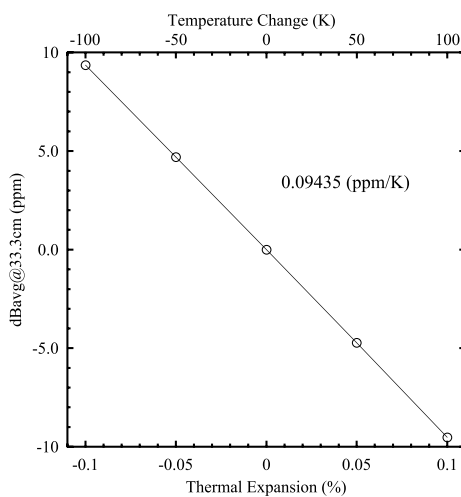
Figure 9.11: *Average field change as a function of expansion ratio of iron yoke.*

Characteristics of superconductor

Characteristic of superconductor is also possible dynamic error source; magnetization, strand coupling current, and persistent current operation.

Magnetization The magnetization of superconductor is an inherent property of type II superconductor. The average magnetization of the superconducting wire can be expressed as

$$M = \frac{4}{3\pi}\mu_0 J_c ak, \tag{9.1}$$

where M is the magnetization, μ_0 is the permeability of the vacuum, J_c is the current critical current density, which is the function of the local magnetic field and temperature, a is the diameter of superconducting filaments, and k is the volumetric ratio of superconducting filaments in the wire. In general J_c can be as large as the order 10^9 A/m^2, a is an order of 10^{-5} m, and k is about the order of 0.1. The magnetization can be estimated as an order 10^{-4} T. The influence to the beam area may be further reduced and can be corrected by corrector coils if the error is stable. The issue is that the magnetization can be changed due to the flux creep effect. The flux creep is the movement of the pinned flux vortex in the superconductor that generally introduced by statistical thermal excitation of the vortex. The effect decreases the magnetization by a logarithmic function. A sufficient idle time after magnet excitation may reduce the influences, however the idle time can be too long to achieve 10^{-7} stability with a reasonable experiment efficiency. Another way to reduce influence is to reduce temperature after magnet excitation. The procedure, however, must be done after all the field optimization is made. The magnet excitation and field optimization procedure should be well studied to achieve 10^{-7} field accuracy and stability.

Strand coupling current The strand coupling current is the coupling current between the superconducting filaments. The influences are generally very small and the time constants are in the range of 10-100 ms. The reasonable idle time after magnet excitation should avoid the problem.

Persistent current operation Time constants of persistent current operation are generally very large, 0.01 - 0.001 ppm/hour, and should not be a problem. There are some coupling with above three effects, however after a reasonable idle time after magnet excitation all the effects should be stable such that operation current change become stable. Note that this time constant is strongly related to the joint resistance of superconducting cable. Connection work between superconducting strands should be carefully performed in the practical fabrication.

Mechanical vibration

Vibration generates dynamic displacement and it can lead to effort field. Therefore, vibration transfer to a magnet should be suppressed as much as possible. The main vibration sources are ground vibration and vibration from a cryocooler.

Seismic ground vibration The magnet for the $g-2$ experiment requires very high field uniformity, and mechanical vibrations excited by the seismic motion might cause the field error changing with time. It is very important to know the characteristics of the ground motion to reduce and control the

mechanical vibrations, therefore, the seismic ground vibration has been measured at Materials and Life science Facility, MLF, in J-PARC, where the new $g-2$ experiment is planed indeed.

A typical power spectrum density (PSD) at MLF is shown in Fig. 9.12. The colored lines represent the data at different time on Sep. 8, 2010. In general, two characteristic peaks are found in PSD data measured on the Kanto plain, that is, the crustal resonance of sedimentary ground in the Kanto plain around 2 - 8 Hz and ocean swell around 0.2 - 0.8 Hz. In terms of the crustal resonance, the peak in the measured data is not clear because the seismic vibration is entirely large at MLF. On the other hand, the peak due to the ocean swell appears very clear around 0.4 - 0.6 Hz, because the J-PARC is located very close to the Pacific Ocean. In addition, the amplitude of the vibration is strongly related to the wave height. Figure 9.13 shows the variation of integral displacement from 0.1 Hz to 100 Hz with time. The wave height in Hitachi-Naka port is also plotted. It shows clear correlation between the displacement and wave height, and the displacement increase by an order of magnitude at maximum.
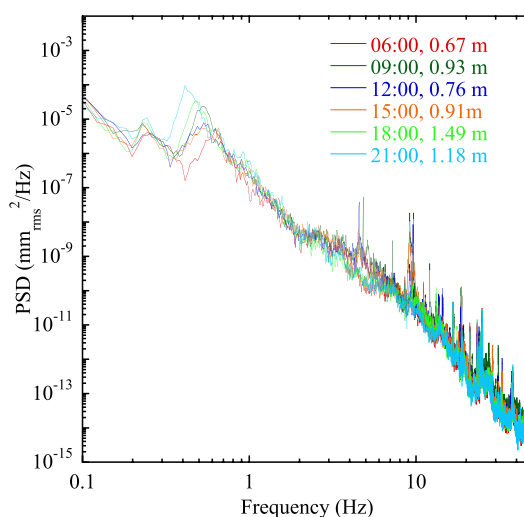
Figure 9.12: *Typical power spectrum densities at MLF in J-PARC.*

Using the measured PSD data, the spectrum analysis of the iron yoke was carried out with ANSYS. The size of iron yoke of Type1 model in Table 9.1 was assumed in this simulation. As a result, yoke displacements are calculated to be 38 μm in z direction at the top of iron yoke at maximum. From the error field due to coil misalignment as shown in 9.2, the error field due to the yoke vibration is expected to be the order of 1 ppm. It is comparable to the required specification, and indicates to require the vibration dumper to isolate the seismic ground vibration from the magnet system. The isolation scheme including the construction method of experimental hall will be studied.

The analysis of coil structure can not be made because the detail structure is not decided yet. After finishing the design, the spectrum analysis of the coil will be made.
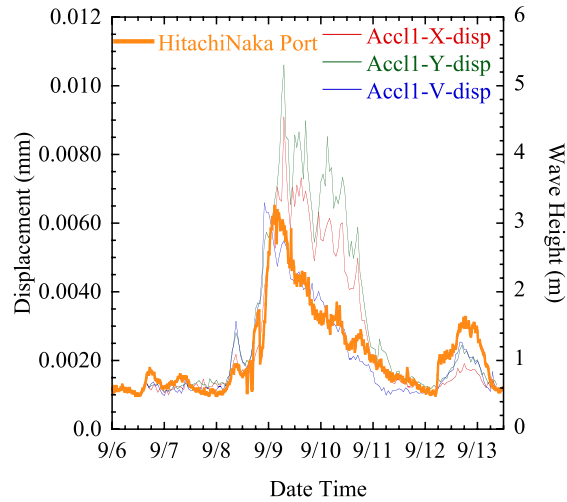
Figure 9.13: *Variation of integral displacement from 0.1 Hz to 100 Hz with time.*

Cryocooler vibration   The cryocooler vibration can be more dominant than seismic ground vibration [7], because the vibration source, the cryocooler head, is placed very close to the magnet. Therefore, development of a low vibration cryostat is essential.

In order to design a cryostat with low vibration, we should consider how the vibration from a cryocooler is transferred to a magnet. Then, it is necessary to establish how to evaluate vibration transfer experimentally and analytically. Based on this consideration, effective damping method can be proposed.

As a first step, we have started vibration measurement using a model cryostat. The objective of this preliminary experiment is to evaluate vibration transfer from a cryocooler to a He vessel.

Figure 9.14 shows a structure of our model cryostat. A GM cryocooler with 1.5 W at 4 K is equipped at the top of the cryostat. The cryostat was designed as the cryocooler can be replaced to other one such as a pulse-tube cryocooler. The GM cryocooler is connected to the vacuum vessel with a flexible bellows in order to suppress direct vibration transfer. The He vessel is hung from the top flange of the vacuum vessel. He re-condenser is connected to the 2nd cold stage of the cryocooler with flexible heat link. This is also necessary for both high thermal conductivity and less vibration transfer. The vacuum vessel and cryocooler are supported by the frame independently and all of these components are put on a stone surface plate. The vacuum and He vessels have several optical windows to observe vibration transfer using a laser displacement sensor.

Vibration measurement was performed with laser displacement sensors, accelerometers and seismometers. From the FFT analysis for the raw time-series-data, power spectrum density (PSD) as a function of frequency can be calculated. This reveals dominant vibration frequency in the system.

As one of the examples, the PSD at the re-condenser measured with a laser displacement sensor is shown in Fig. 9.15. The peaks were observed at 1 Hz and its harmonic frequencies with turning on
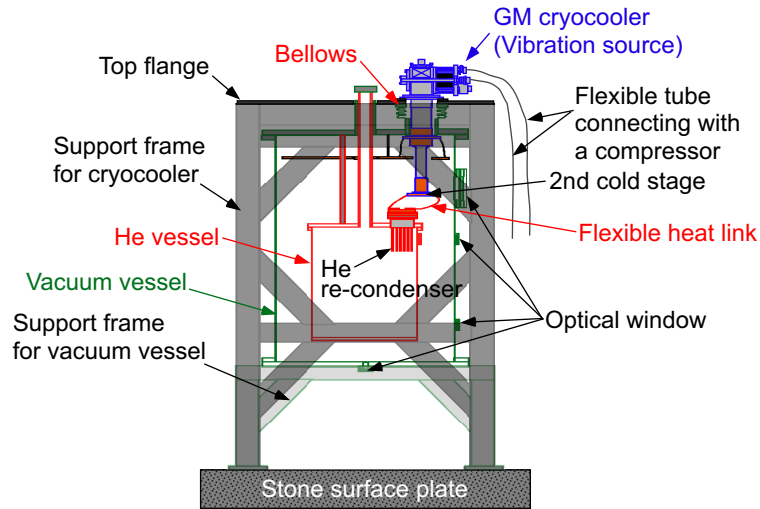
Figure 9.14: *Structure of the model cryostat for vibration measurement.*

the GM cryocooler. This clearly indicates that vibration of the cryocooler can be transferred to the He re-condenser. We also combined vibration measurements with accelerometers and seismometers and the PSD at the different positions were compared. As a result, we confirmed that vibration from the cryocooler was transferred to the He vessel through the support frame and stone surface plate. This indicates that the vibration transfer through the support structure should be also important as well as direct transfer.
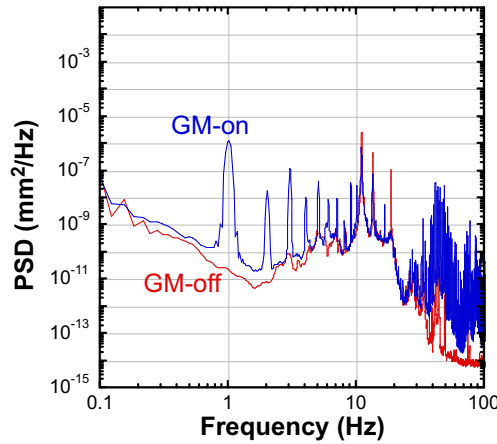
Figure 9.15: *Power spectrum density (PSD) as a function of frequency at He re-condenser with GM-off and on.*

Based on these preliminary results, we will consider how to reduce the vibration transfer. One of the solutions is using a damping alloy. It has been reported that a special kind of Mn alloy has very high damping factor with other merits of high strength, high workability and nonmagnetic. One of the advantages of this material compared with other damping material such as rubber is that this can

reduce the vibration in a wide range of frequencies from 10^{-2} Hz to MHz. We can expect reduction in vibration amplitude with 1 Hz by inserting a plate of this alloy between the support structure and stone surface plate. From the report of the development of low vibration pulse-tube cryocooler system [8], it is known that the rigid support of the flexible tube between compressor and cold head is important. That support structure will be modified in the next test.

In addition, we will perform structural analysis numerically. This will be effective to estimate resonance frequency in the system. Combining with these experimental and analytical estimation, a cryostat for $g-2$ magnet will be designed from the view point of low vibration.

9.1.5   Quench Protection

The stored energy of the magnet is very large as shown in Table 9.1, therefore, the quench protection scheme must be studied in detail to avoid a burnout of the magnet. From the view point of coil protection, there are two important parameters, coil peak temperature and coil resistive voltage. Peak temperature in coils during a quench has to be checked in order to avoid burnout of coils, and also peak resistive voltage should be confirmed to be sufficiently small. Numerical calculations are carried out to find the best protection scheme for the magnet system. As an example of the quench protection study, the simulation results of the magnet with 6 coils structure are shown below.

Figure 9.16 shows the electrical circuit for the quench protection study in the case of persistent current operation mode. All the coils including the shield coils and the persistent current switch (PCS) are connected in series. From the magnetic force view point, the coils placed on the symmetrical position are connected in the same circuit. The diodes having the forward voltage of 5 V are connected in parallel with each section as shown in Fig. 9.16. These enhance the current decay in the coil and reduce the maximum temperature of the coil.
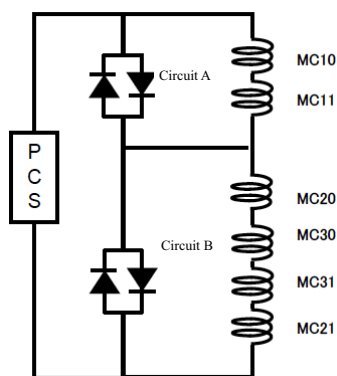
Figure 9.16: *Electrical circuit for the study of quench protection during the persistent current operation.*

The coil and strand parameters for the quench simulation are summarized in table 9.3 and table 9.4.

Table 9.3: *Coil Parameters for Quench Study*

	Unit	Value
Cross section		Rectangular
Size with Insulation	(mm)	2.05 × 1.60
Size w/o Insulation	(mm)	1.95 × 1.5
Corner R	(mm)	0.3
Cu/Sc Ratio		4
Insulation Thickness	(mm)	0.05
No. of Filaments		336
Filament Diameter	(mm)	46.5
Iop	(A)	417
Peak Field	(T)	5.5
Base Temperature	(K)	4.2
Ic at the Peak Field	(A)	1364.8
Tc at Iop	(K)	6.95

Table 9.4: *Strand Parameters for Quench Study*

	Unit	Value
Cross section		Rectangular
Size with Insulation	(mm)	2.05 × 1.60
Size w/o Insulation	(mm)	1.95 × 1.5
Corner R	(mm)	0.3
Cu/Sc Ratio		2 or 4
Insulation Thickness	(mm)	0.05
No. of Filaments		336
Filament Diameter	(mm)	46.5
Filament twist pitch (m)	0.1	
Iop	(A)	417
Peak Field	(T)	5.5
Base Temperature	(K)	4.2
Ic at the Peak Field	(A)	1364.8
Tc at Iop	(K)	6.95

Iop : Operation Current

Ic : Critical Current

Tc : Critical Temperature

In this simulation, the adiabatic conditions are assumed for the coils. The quench back due to AC loss in the superconductor between coils are considered. The AC loss in other components, like iron yoke and thermal shield etc., are not included.

Figure 9.17: *Quench simulation results*

Figure 9.17 shows the simulation results during the quench of the MC10 coil. In Fig. 9.17(a), the current in the Circuit A decreases with the time constant of about 8s, because this circuit includes the quenched coil. On the other hand, the current in the Circuit B increases slightly first due to the mu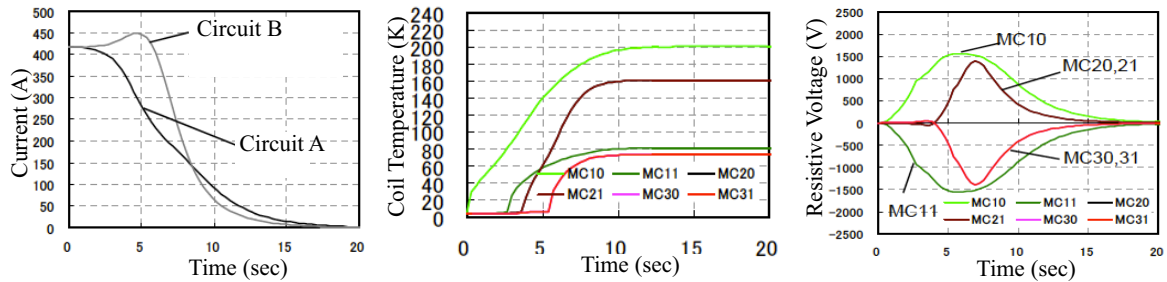tual inductance coupling, and then, the current decreases to zero, because the coils in the Circuit B quench due to the AC loss caused by the field changing.

The peak temperature of the quenched coil MC11 is about 200 K in Fig. 9.17(b), which is sufficiently low compared with room temperature. In addition, the peak resistive voltage in the coil is less than 1.6 kV in Fig. 9.17(c), which is a manageable value. These results indicate that the magnet can be protected from a burnout without any additional active protection scheme.

Next, the influence of thermal conductivity of epoxy resin was examined. The coil conductor is impregnated with epoxy resins in order to avoid quenches caused by the conductor slip, and the thermal conductivity of the epoxy resin might affect the quench propagation in coils. Three types of epoxy resins were examined; typical epoxy resin used in the magnet development in the Japanese private company, Epitoke 828 and Apiezon N grease. Figure 9.18 shows the thermal conductivity data used in the calculation.

Figure 9.19 shows the calculated results of the quench behavior. As a results, the quench behaviors are not different so much each other, indicating that the heat conduction through epoxy resin is not dominant on the quench behavior of this magnet.

The influence of twist pitch of superconducting filaments was also examined. AC loss is strongly related to the filament twist pitch, in general, the larger twist pitch, the larger AC loss in the coil. Figure 9.20 shows the calculated results with the filament pitches of 0.05 m and 0.2 m. In these figures, the peak temperature and coil resistive voltage increase with the decrease of the twist pitch. When the AC loss is small due to the small twist pitch, it takes longer time to the coils besides the first quench coil. In other words, it becomes longer to consume the stored energy only in the first quench coil, therefore, the temperature and voltage become high.

In order to check the validity of these results, the measurement of the ac loss will be carried out in the HFS magnet, and the results will be compared with the calculated results.

(A) Typcal epoxy resin   (B) Epitoke 828 and Apiezon N
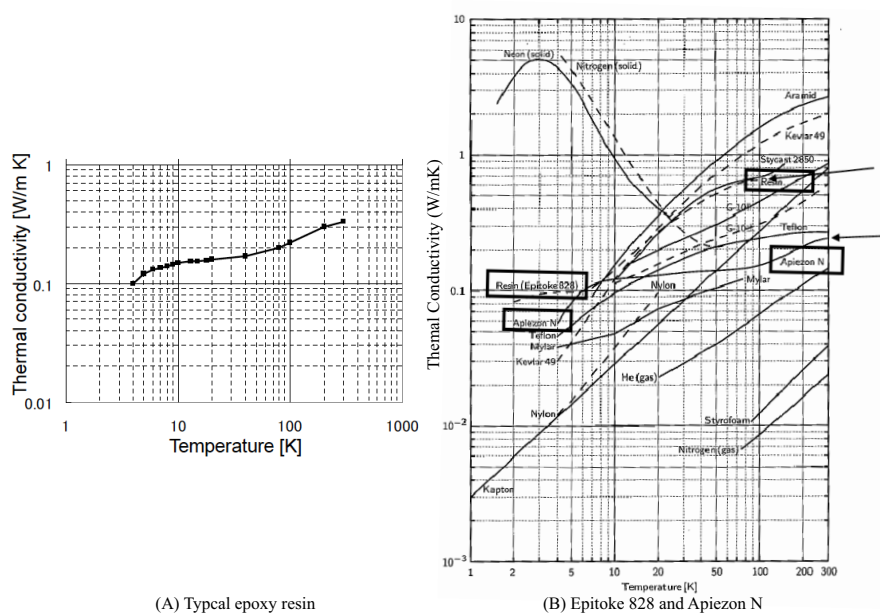
Figure 9.18: *Thermal conductivity data used in the quench simulation.*

9.1.6 System design

Mechanical design

Figure 9.21 shows the latest mechanical design made by the Japanese private company.

Figure 9.22 shows the latest arrangement of devices inside the magnet bore. Various devices have to be placed inside the magnet, especially, around the storage region; the positron detectors, the kicker magnet, the vacuum chamber for muon beam, the NMR probe for the field monitoring, and so on. Considering interference between devices as well as assembling procedures, the discussion of the detail design is under way.

Cryogenic design

A conceptual design proposal of the storage magnet cryogenic system is shown in Fig. 9.23. The requirements to the cryogenics from the view point of good field quality of the solenoid are 1) sub-micron mechanical stability, 2) good temperature controllability and stability of superconducting coil. There are also additional requirements to the room temperature system to avoid mechanical vibration to the magnet system. Since the superconducting solenoid will be made from the wire and operated with a relatively low current, the system may be cooled with several cryo-coolers. The cooling of the coil, however, should be made by liquid helium to ensure the good temperature stability. The temperature control can be made with a pressure control of the helium vessel. The precise pressure control system should be implemented. The cryo-coolers are used for re-condensation of helium.
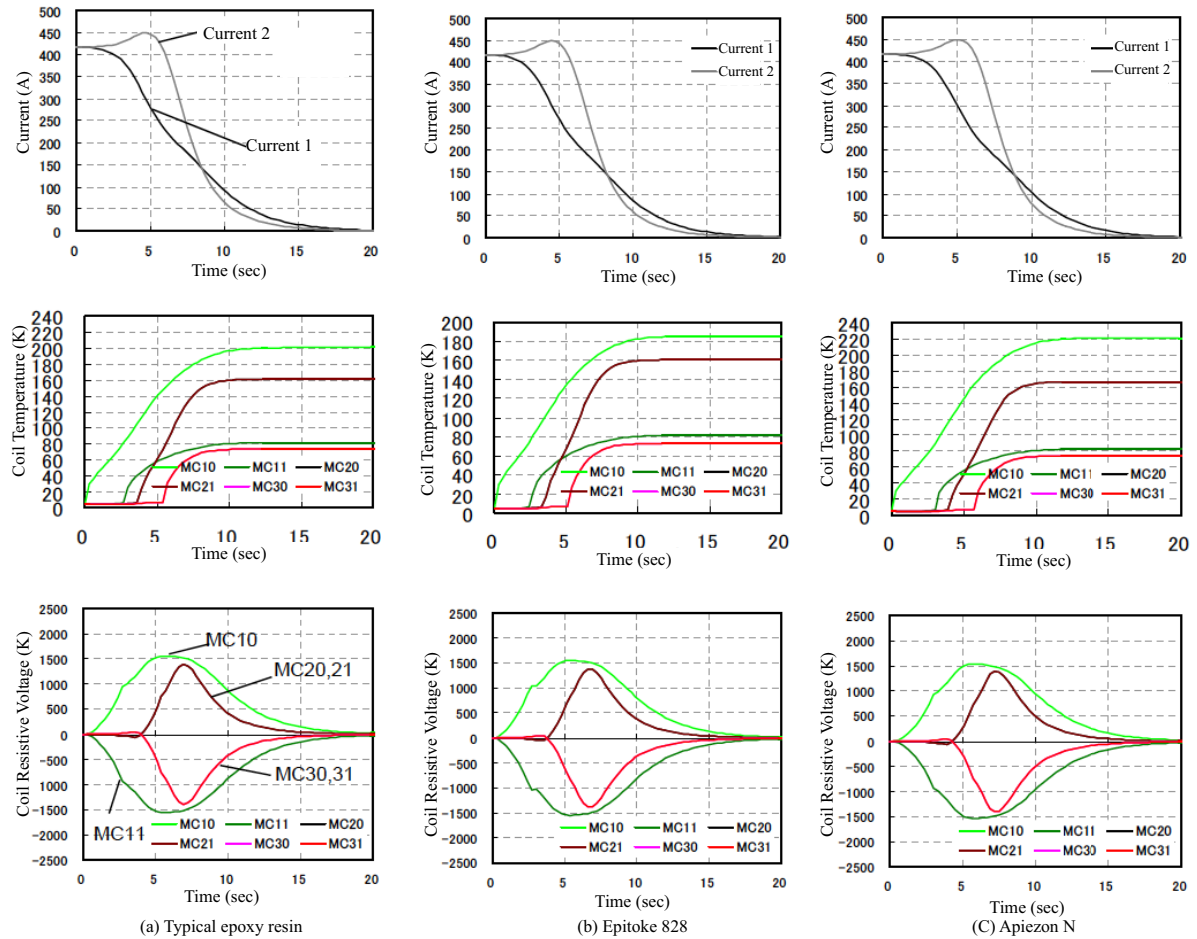
Figure 9.19: *Quench simulation results with different epoxy resins.*

Number of corrector coils as well as their operation current may affect to the cryogenics heat load. They should be optimized such that the system can be achieved with cryo-coolers. Since the vibration of the system may cause the devastating effect to the field quality, vibration dumpers should be carefully implemented to achieve vibration level below 0.1 micron for the solenoid system as described in the previous section.

9.2 Field monitoring system

There are many methods of measuring magnetic field: hall probe, flux measurements with pick up coils, nuclear magnetic resonance (NMR), and so on. The optimal choice depends on the nature of the field to be measured; AC or DC field, gradient or absolute field, etc. In this experiment, a superconducting solenoid having a high uniformity of the central field is adopted for the muon storage magnet. From the field measurement view point, the measurement region around the solenoid could
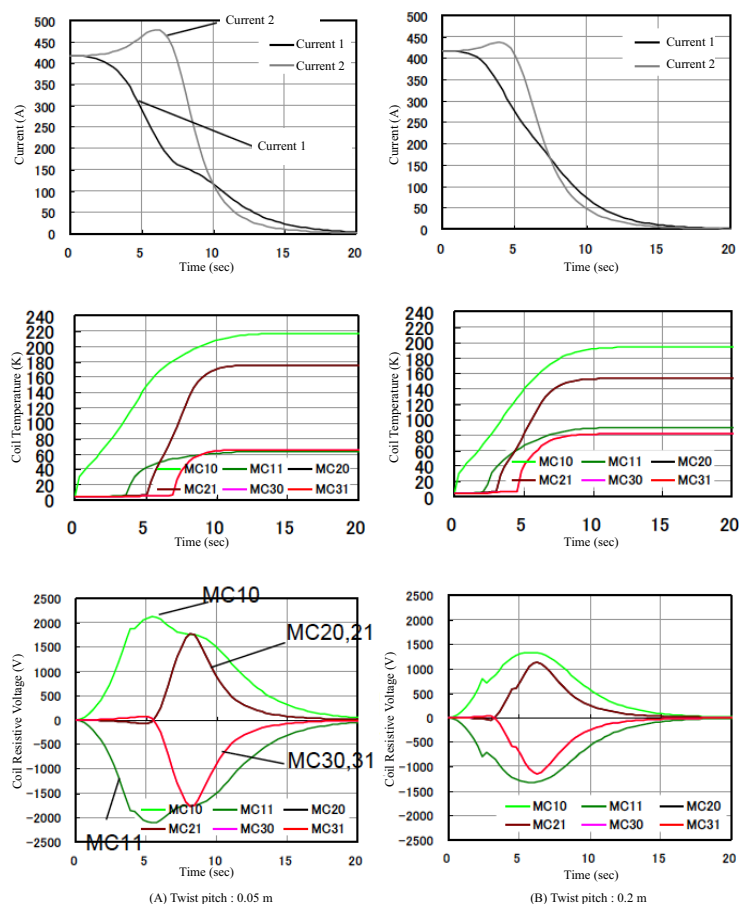
Figure 9.20: *Quench simulation results with the twist pitch of 0.05 m and 0.2 m.*

be divided into three regions, that is, the beam injection region, the beam storage region and the weak focus field. Table 9.5 summarizes the characteristics of each region, required accuracy and first candidate of field measurement suitable for each region.

Table 9.5: *Field monitoring methods for each region*

	Storage region	Injection region	Weak focus field region
Field strength	3 T	1.5 - 3 T	several gauss
Required accuracy	0.1 ppm	1×10^{-4}	0.1 gauss
Required data	Only axial field (basically)	Vector data	Radial field
First candidate method	NMR probe	hall probe	hall probe
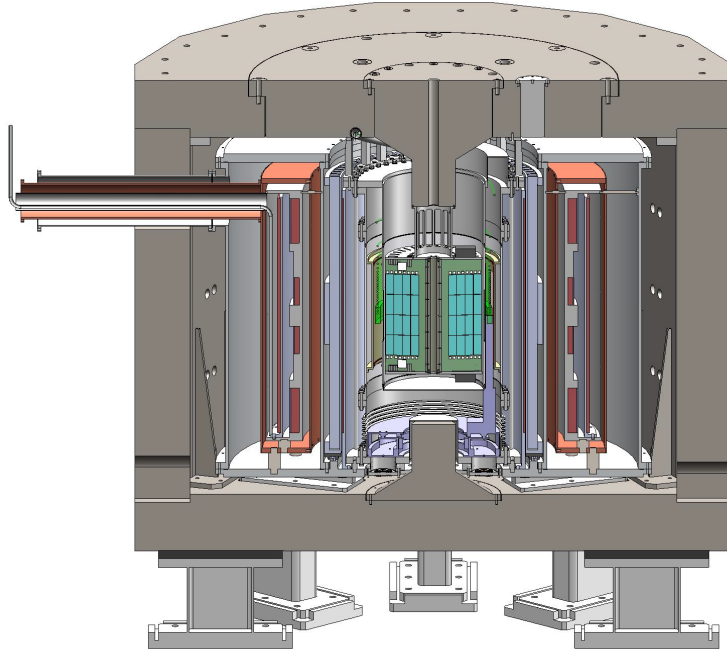
Figure 9.21: *Overview of mechanical design of superconducting magnet system for the $g - 2$ experiment.*
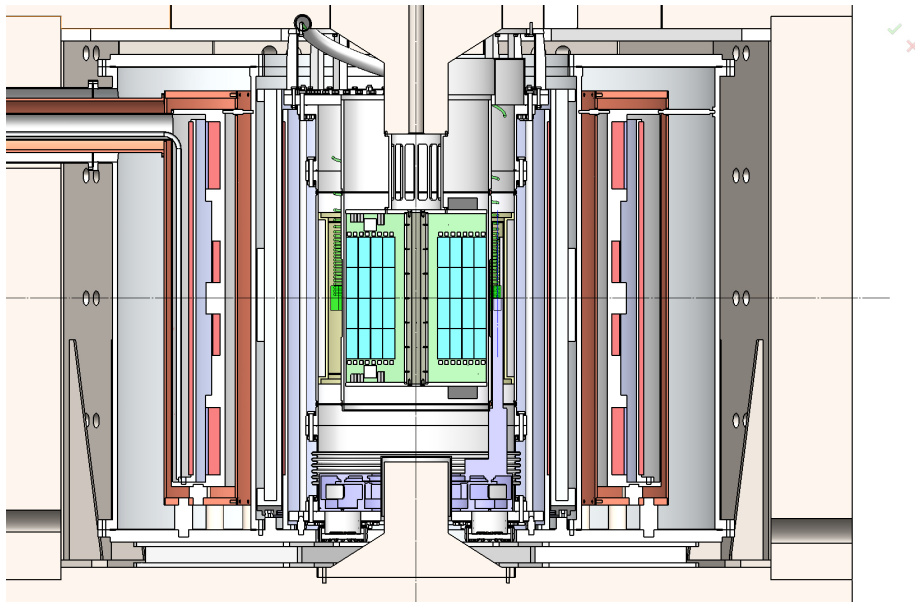
Figure 9.22: *Arrangement plan inside magnet bore.*
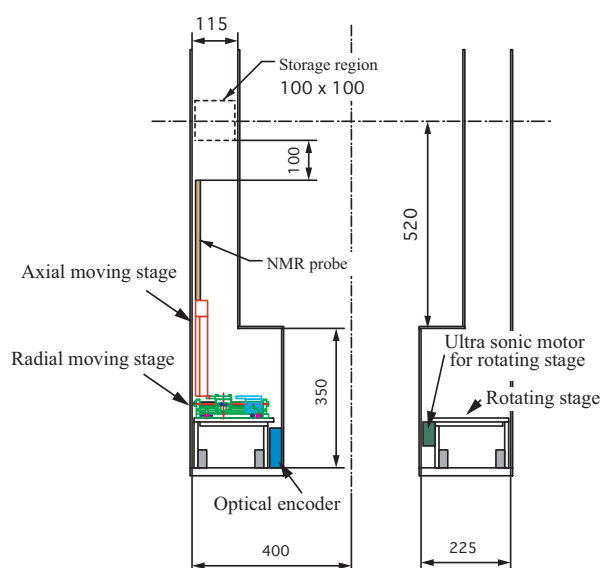
Figure 9.23: *Conceptual design of cryogenic system of storage magnet*

9.2.1 Storage region

From the beam optics study, the beam storage region should be cylindrical shape with an inner diameter of about 280 mm, a outer diameter of 380 mm and a height of 400 mm (no interference with the kicker coils), and the region must have high field homogeneity at a ppm level locally, and be measured along the muon storage orbit (integrated) to below 0.1 ppm, with a central field of 3 T. The NMR method is the only solution for measuring with this precession.

**Measurement strategy with NMR system**

It is not easy to measure this magnetic field at a sub-ppm level, since there are no magnets with such a high homogeneity at 3 T which can be used to fine-tune the NMR system. So, the adjustment of the NMR system at a sub-ppm level of accuracy is planned to progress in parallel with the development of the superconducting solenoid for muon storage. This strategy has two steps of development of the NMR measurement system. In the first step, a commercial NMR system with an accuracy of 1 ppm will be purchased for a rough evaluation of the solenoid field at the initial R&D phase. Based on the measurement results, the solenoid field would be regulated to reach a field homogeneity of 1 ppm in the beam storage region. In the second step, an NMR system which can reach a sub-ppm level precision will be purchased, and would be fine-tuned using the solenoid in collaboration with the company making the NMR system.

Positioning system

In both steps, a probe positioning system made of nonmagnetic materials should be developed, which can control the probe position in the solenoid in the cylindrical coordinate system. The precision of 1 mm should be sufficient for the position control, since the size of the probe would be 5 mm in diameter. That precision could be easily achievable with commercial devices, however, materials composing the positioning system should be carefully selected. It should be placed near the solenoid so that a limited space around the solenoid could be made effective use, and the accuracy of the position control could be easily improved. Figure 9.24 shows the conceptual design of the positioning system. This system consists of three stages, rotating stage, radial moving stage and axial moving stage. These are mainly made by a ceramic material, and driven by ultra sonic motors, which can work in the strong magnetic field. More detail design work is in progress.
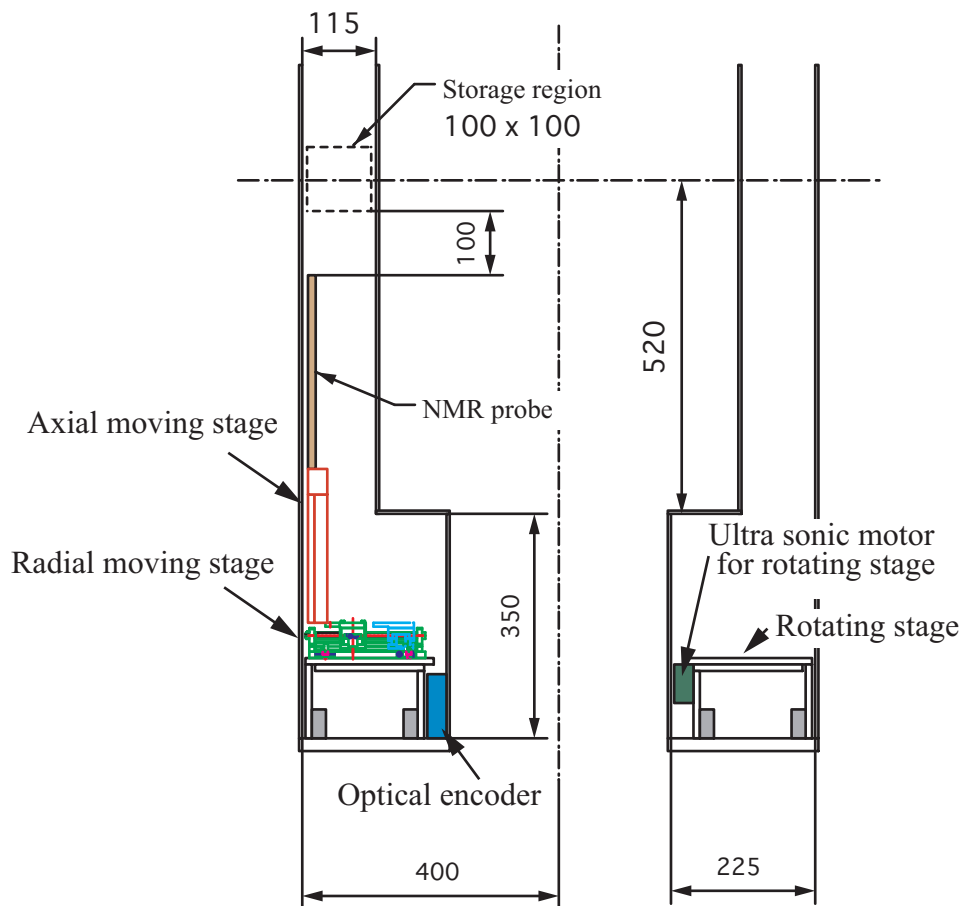

Figure 9.24: *Conceptual design of positioning system.*

NMR system

In the present system, continuous wave type NMR (CW-NMR) system is used. Typical block diagram of CW-NMR is shown in Fig. 9.25. In a CW-NMR, there are some points to improve an accuracy and resolution. The most important point is the stability and accuracy of RF signal of RF generator. Therefore, in our system, the reference frequency generator with GPS is planned to used for stabilizing the RF signal. This generator has an accuracy of 1×10^{-12} which is secured by GPS clock frequency. This accuracy is sufficiently small compared to the required field uniformity of 1 ppm. Other improvements in our system is the increase of the purity of NMR sample. Usually, NMR sample is water, and the pulse width of resonant absorption signal, in other words the resolution, can be reduced with the increase of water purity.
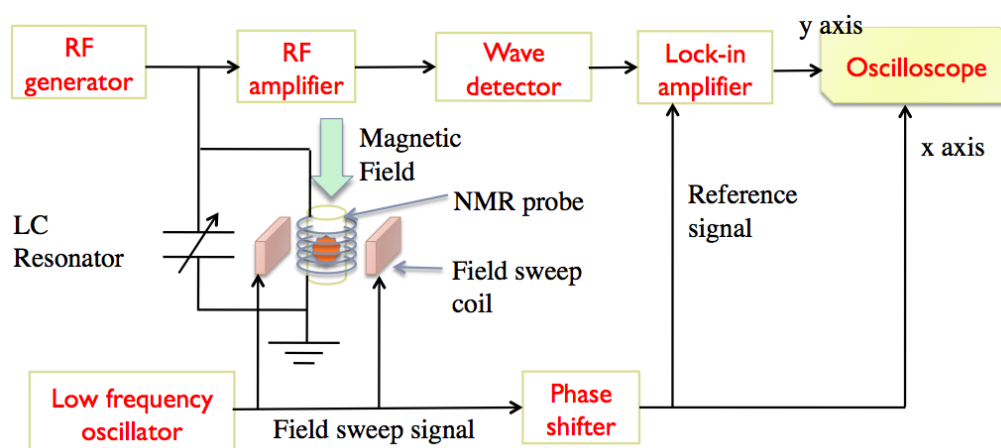
Figure 9.25: *Typical diagram of continuous wave type NMR system.*

Prototype test In the first step of the development of the NMR measurement system, a field distribution measurement in a 3 T solenoid is planned using an NMR system with 1 ppm accuracy. The objectives of the measurement are to fine-tune the NMR system and to build the prototype of positioning system.

Arrangements to use a 3 T solenoid are successfully progressing with the National Institute of Radiological Sciences (NIRS) at Chiba city. The solenoid is designed for MRI medical applications, and placed horizontally, which is different from the solenoid for the $g-2$ experiment, which will be placed vertically. However, this MRI magnet will be useful to check whether the components of the positioning system work in a high magnetic field and provide a high accuracy field measurement. Figure 9.26 shows the overview and the photo of the field measurement system for the horizontal solenoid.

Using the commercial NMR probe and the prototype stage, the field measurement was carried out in the 3 T MRI magnet at NIRS. In this test, it is confirmed that the developed positioning stage can move smoothly even in high magnetic field of 3 T. Figure 9.27 shows the example of measured field
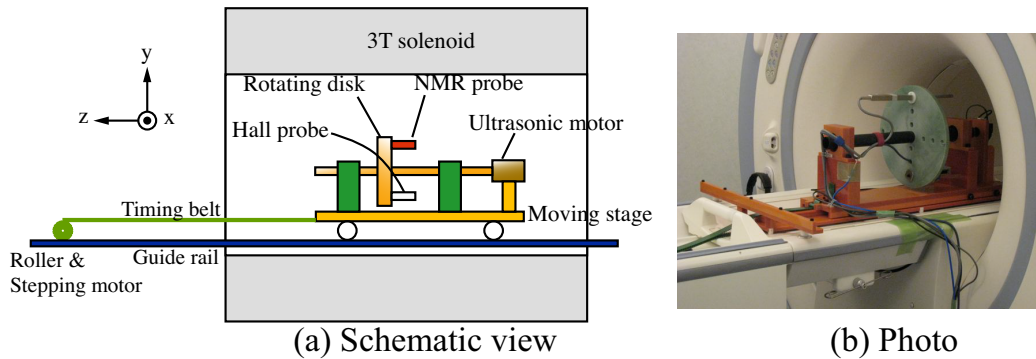
Figure 9.26: *Schematic view and photo of prototype field measurement system.*

distribution at the magnet center. The rotating axis does not coincide with the magnet central axis at $(x, y) = (0, 0)$, therefore, the measured field distribution was not symmetric.
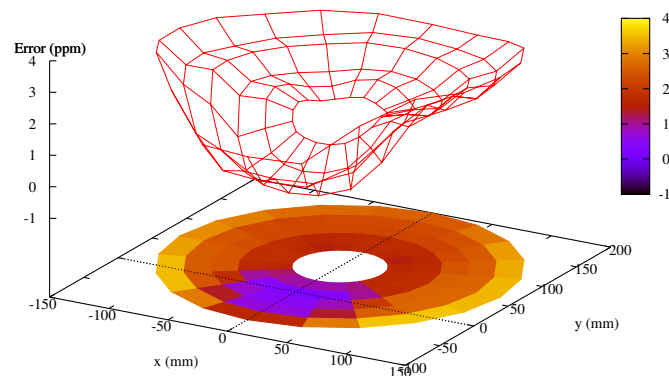
Figure 9.27: *Example of measured field distribution at the magnet center. Vertical axis represent the field difference from the magnet center.*

As for the stability, Figure 9.28 shows the results of stability measurement. Figure (a) shows the error frequency distribution from the frequency of input RF signal. The standard deviation (σ) is 1.4×10^{-4} ppm, indicating that the RF signal is highly stabilized by the reference frequency generator with GPS. However, in the figure (b), the output value distribution from the mean value of the NMR system is not so stabilized, and σ is 0.025 ppm. There are some possible reason for this, the electrical noise from the signal modulation circuit and pre amps in the NMR system, the measurement error of voltmeter and so on. However, the reason is not specified. In the next test at NIRS, the new NMR

system with lower electrical noise than the previous system will be tested.

(a) RF input signal   (b) Output signal of NMR system
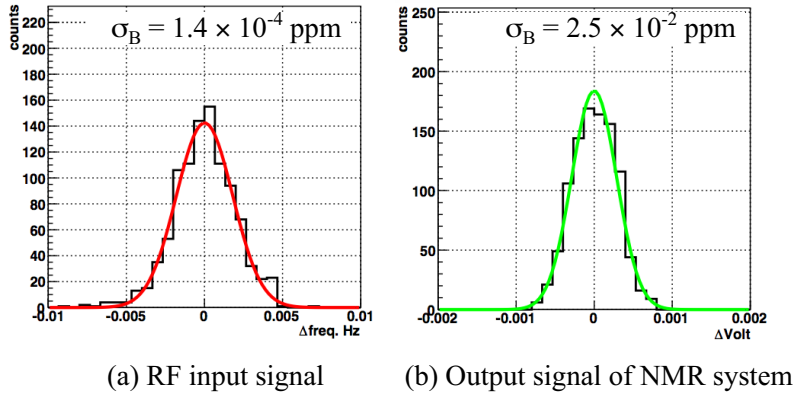
Figure 9.28: *Stability of frequency of RF input signal and output voltage of NMR system.*

9.2.2 Injection region

The beam injection region is the region from the end of the injection beam line to the beam storage region around the solenoid center, and it includes a stray field region outside the solenoid. The muon beam passes through the beam injection region only one time, therefore,the tolerance of the magnetic field error is much larger than that in the beam storage region. It is enough to measure the magnetic field in the beam injection region with an accuracy of 1×10^{-4}. And also, the direction of measured field has to be understood, because the flux line curves especially around the stray field region. Only hall probe method can satisfy both requirements.

Three axes hall probe is convenient to measure a magnetic field vector, and it's planed to be used for the measurement in the injection region. The present issue to use the hall probe is a misalignment of hall sensors in the probe. As shown in Fig. 9.29, three hall sensors are implemented in one probe, and these are slightly tilted with respect to x, y and z axes because of the structural tolerance.
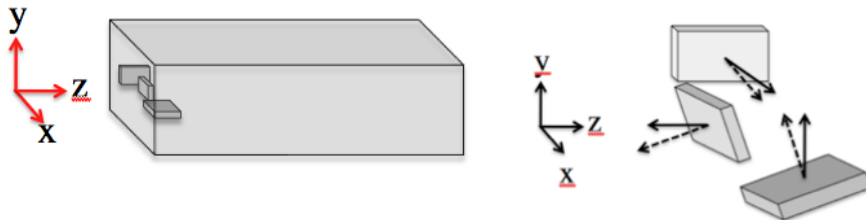
Figure 9.29: *Schematic view of hall sensors in three axes probe.*

For example, the sensors in our commercial probe have the tilt angles of 0.4 - 0.7 degree, although

these directions are not identified yet. Apparent field due to this misalignment disturb the precise field measurement with three axes hall probe, therefore, these tile angles and directions have to be measured and compensated. Three axes Helmholtz coils are being prepared for the tilt measurement. These coils have a field uniformity of 1×10^{-4} in 10 mm DSV (diameter spherical volume). For the

Figure 9.30: *Three axes Helmholtz coils.*

precise correction of the tilt angles the axes of the Helmholtz coils are also compensated precisely by a different method from hall sensors. So, five axes moving stage with pickup coil as shown in Fig. 9.31 is being developed in parallel with the Helmholtz coils. This stage enable us to control the pickup coil position in x, y, z, θ and ϕ direction with an accuracy of 0.01 mm and 0.02°. The reason for using the pickup coil is that measurement direction is obtained directly from its geometry. By using the five axis stage with the pickup coil, the axes of Helmholtz coil can be compensated with an accuracy of 0.02°. Both devices, Helmholtz coils and five axes stage, will be ready in 2011, and the misalignments
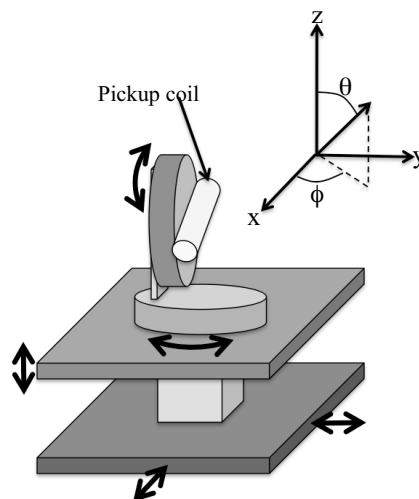
Figure 9.31: *Conceptual design of five axes moving stage.*

of the hall sensors in the probe will be measured in 2012.

9.2.3 Weak focus field

Weak focus field is a radial field in the storage region as discussed in the previous section, and the field strength is smaller than several gauss. In addition, strong field of 3 T is also applied in axial direction simultaneously.

At present, there are tow ideas to measure the weak focus field. First one is to use hall probes assembled around the storage region. This is the simplest way to measure the field. However, as mentioned in the previous section of mechanical design, many devices have to be placed around the storage region, therefore, the arrangement of hall probes are limited to some extent. In addition, it is difficult to measure magnetic field of several gauss precisely by hall probes, if the strong field is superimposed onto the weak focus field. Therefore, the main magnetic field have to be off during the measurement of weak focus field.

Another idea is to use NMR probe prepared for the measurement of the storage region. In the space without current source, the following equation is given from the Maxwell's equation.

$$\frac{dB_r}{dz} = \frac{dB_z}{dr}. \tag{9.2}$$

It means, if the axial field distribution as a function of radius could be measured precisely, the radial field by this equation can be calculated.

Actually, both ideas can be implemented at the same time, and further studies are in progress for both cases.

References for Chapter 9

[1] F. Romeo and D. I. Hoult, "Magnet Field Profiling: Analysis and Correcting Coil Design," *Mag. Resonance in Med.* Vol. 1, No. 1, pp. 44-65, 1984.

[2] D. I. Hoult and D. Lee, "Shimming a Superconducting Nuclear-Magnetic-Resonance Imaging Magnet with Steel," *Rev. Sci. Instrum.* Vol. 56, No. 1, pp. 131-135, 1985.

[3] J. Vetter, G. Ries and T. Reichert, "A 4-Tesla Superconducting Whole-Body Magnet for MR Imaging and Spectroscopy," *IEEE Trans. on Magn.* Vol. 24, No. 2, pp. 1285-1287, 1988.

[4] M. D. Sauzade and S. K. Kan, gHigh Resolution Nuclear Magnetic Resonance Spectroscopy in High Magnetic Fields,h *Adv. in Electronics and Electron Physics* Vol. 34. pp. 1 - 93, 1973.

[5] A. Belov, V. Bushuev *et al.*, "Passive Shimming of the Superconducting Magnet for MRI," *IEEE Trans. on Appl. Supercond.* Vol. 5, No. 2, pp. 679-681, 1995.

[6] M. Abe, T. Nakayama, S. Okamura and K. Matsuoka, "A new technique to optimize the coil winding path for the arbitrarily distributed magnetc field and application a helical confinement system," *Phys. Plasmas.* Vol. 10, No. 4, pp. 1022-1033, 2003.

[7] T. Tomaru, T. Suzuki, T. Haruyama, T. Shintomi, A. Yamamoto, T. Koyama and R. Li, "Vibration analysis of cryocoolers," *Cryogenics* Vol. 44, pp. 309-317, 2004.

[8] Y. Ikushima, R. Li, T. Tomaru, N. Sato, T. Suzuki, T. Haruyama, T. Shintomi and A. Yamamoto, "Ultra-low-vibration pulse-tube cryocooler system - cooling capacity and vibration," *Cryogenics* Vol. 48, pp. 406-412, 2008.

[9] ANSYS®Academic Research, ANSYS, Inc

CHAPTER 10

Measurement of ω_a - Analysis strategy

Contents

10.1   Extraction of ω_a from positron time spectrum

The anomalous muon spin precession at frequency ω_a leads to a modulation in the number of positrons above the minimum energy threshold E_{lab}^{th} which was defined in Section 7.1.1. In the ideal case, the positron time spectrum can be expressed as:

$$N(t) = N_0(t)\mathrm{e}^{-t/\gamma\tau}\left[1 - A\cos(\omega_a t + \phi)\right], \qquad (10.1)$$

where $\gamma\tau = 6.615$ μs $2\pi/\omega_a = 2.111$ μs, $A = 0.46$ for $E_{lab}^{th} = 200$ MeV. In general, the scaling factor $N_0(t)$ depends on time. For example, early-to-late efficiency changes in the positron tracking could introduce such a dependence. Such early-to-late effect could be suppressed by taking a ratio of several positron samples with different initial phases in the anomalous spin precession. (1) data randomly divided by four subsets and give offsets of half of the $g - 2$ precession period as was done in the E821, (2) data taken with alternative muon spin orientation at injection (forward/backward), and (3) data divided by subsets of positrons decaying left-hand-side and right-hand-side of the muon momentum. The ratio has a form of

$$r^{ab}(t) = \frac{N^a(t) - N^b(t)}{N^a(t) + N^b(t)} = A\cos(\omega_a t + \phi), \qquad (10.2)$$

where indexes a, b are labels of subsamples with a different offset for (1), orientations of muon polarization $(+, -)$ for (2), and direction of decay (left, right) for (3). The anomalous spin precession ω_a is extracted by fitting to these ratio distributions.

The extraction of ω_a relies on χ^2 minimization. The readout electronics stores the positron decay during the period of 41 μs with the 5 ns time stamp. This reads to 8200 time bins in the positron time spectrum. The reduce chi-squared, χ^2/dof (dof = degrees of freedom), will be used to judge the goodness of fit as was done in BNL E821 [1]. The acceptable fit should provide $\chi^2/\mathrm{dof} = 1$ with a variance of $\sqrt{2/dof}$ which is a property of the χ^2 distribution. For 8000 degrees of freedom, variance of the χ^2/dof is 0.016.

10.2   Blinding policy and mechanism

A blind analysis [2] is required in the measurement of the anomalous precession frequency ω_a to avoid human bias in the analysis.

In the E821, each analysis of ω_a contain an individual frequency offset which is defined by analysis personnel. The individual offsets are replaced to a common offset when each analysis demonstrated a high level of internal consistency, such as a reduced χ^2 equal to unity within the expected statistical spread, no pronounced structures in the fit residuals, both in time and frequency domains, the fit results must be independent of any specific subset of data.

The KTeV experiment inserted a unknown random offset in the fitting program to extract ϵ/ϵ' [3]. The random offset was made by a pseudo random number generator. Analysis personnel could see the data histograms etc. to evaluate data quality, optimize the selection cuts, and Monte Carlo simulation.

In this case, even analysis personnel don't know the result until the random offset is removed in the fitting program.

We employ similar blinding techniques discussed above in the measurement of ω_a.

References for Chapter 10

[1] G.W. Bennett *et al.* Muon G-2 Collaboration, Phys. Rev. **D73** (2006) 072003.

[2] J.K. Klein and A. Roodman Annu. Rev. Nucl. Part. Sci. 55, 141 (2005)

[3] A. Alavi-Harati et al. [KTeV Collaboration], Phys. Rev. Lett. 83, 22 (1999).

Measurement of $g - 2$ and EDM − Conversion

Contents

11.1   Measurement of $g-2$ and EDM - Conversion

11.1.1   Extraction of $g-2$ and EDM

We will describe basic idea to extract $g-2$ and EDM from the measured values based on Eq. 11.1 Their error will be also propagated as usual.

$$
\begin{aligned}
\vec{\omega}_{tot} &= \vec{\omega}_a + \vec{\omega}_\eta \\
\vec{\omega}_a &= \frac{-e}{m}\left[a\vec{B} - \left(a - \frac{1}{\gamma^2 - 1}\right)\frac{\vec{\beta}\times\vec{E}}{c}\right] \\
\vec{\omega}_\eta &= \frac{e}{m}\left[\frac{\eta}{2}\left(\vec{\beta}\times\vec{B} + \frac{\vec{E}}{c}\right)\right]
\end{aligned}
\tag{11.1}
$$

The muon spin rotates around the direction of the $\vec{\omega}_{tot}$ with frequency of $\omega_{tot} \equiv |\vec{\omega}_{tot}|$. ω_{tot} is calculated to be

$$
\omega_{tot} = \left(\frac{e}{m}aB\right)\sqrt{1+\delta}
\tag{11.2}
$$

$$
\begin{aligned}
\delta &= G^2\frac{|\vec{\beta}\times\vec{E}|^2}{c^2 B^2} + 2G\frac{\vec{B}\cdot(\vec{\beta}\times\vec{E})}{cB^2} \\
&\quad -2\left(\frac{\eta}{2a}\right)\left(\frac{\vec{B}\cdot\vec{E}}{cB^2} + G\frac{(\vec{\beta}\times\vec{B})\cdot(\vec{\beta}\times\vec{E})}{cB^2}\right) \\
&\quad +\left(\frac{\eta}{2a}\right)^2\left(\frac{|\vec{\beta}\times\vec{B}|^2}{B^2} + \frac{E^2}{c^2 B^2} + \frac{\vec{E}\cdot(\vec{\beta}\times\vec{B})}{cB^2}\right)
\end{aligned}
\tag{11.3}
$$

$$
G \equiv -\left(1 - \frac{1}{a(\gamma^2 - 1)}\right),
$$

where $B = |\vec{B}|$ and $E = |\vec{E}|$.

Extraction of $a = \frac{g-2}{2}$

Based on Eq. 11.2, the leading component of ω_{tot} is eaB/m and remaining terms, δ, can be regarded as perturbation. Therefore, the measurement of ω_{tot} is sensitive to obtain $a = (g-2)/2$. We evaluate the size of δ with its upper limit.

$$
\begin{aligned}
\delta &< G^2\beta^2 R_{EB}^2 + 2G\beta R_{EB} \\
&\quad +2\left(\frac{\eta}{2a}\right)\left(R_{EB} + G\beta^2 R_{EB}\right) \\
&\quad +\left(\frac{\eta}{2a}\right)^2\left(\beta^2 + R_{BE}^2 + \beta R_{EB}\right) \\
R_{EB} &\equiv \frac{E}{cB}
\end{aligned}
$$

To obtain Eq. 11.4, we utilized the relation of $\vec{a}\cdot\vec{b} < |\vec{a}||\vec{b}|$ and $\vec{a}\times\vec{b} < |\vec{a}||\vec{b}|$. Based on the condition of $\eta/a \ll 1$ and $GR_{EB} \ll 1$, the leading contribution to ω_{tot} is

$$
\sqrt{1+\delta} < \sqrt{1+\delta_{max}} \sim 1 + G\beta R_{EB} + \frac{1}{2}\left(\frac{\eta}{2a}\right)^2\beta^2.
\tag{11.4}
$$

Quantitative evaluation can be performed by using following numbers.

$$B = 3.0 \text{ T}, \quad \beta = 0.94 \sim 1, \quad \gamma = 3.0, \quad a = 1.1659 \times 10^{-3},$$

$$G \sim 111$$

Size of the second term of Eq. 11.4 depends on the residual electric field $\vec{E}$. Referring to the original shape of the term in Eq. 11.3, it is proportional to $\vec{B} \cdot (\vec{\beta} \times \vec{E}) = \vec{E} \cdot (\vec{B} \times \vec{\beta})$. Since the major component of $\vec{B}$ and $\vec{\beta}$ is perpendicular to each other, vector of their cross product is roughly parallel to r-direction. Therefore, the size of this term is determined by the size of r-component of $\vec{E}$. To keep the contribution smaller than statistical uncertainty of 0.1 ppm, i.e.,

$$G\beta R_{EB} = G\beta \frac{E}{cB} \ll 0.1 \text{ ppm}, \tag{11.5}$$

the electric field must be $E \ll 8.6$ mV/cm. The experimental apparatus is designed to meet the requirement.

The third term of Eq. 11.4 depends on the size of EDM, η. For example, when we use current experimental precision limit of $|\vec{d_\mu}| \sim 10^{-19} e$ cm as the EDM size for the evaluation, it can be converted to $\eta \sim 2.2 \times 10^{-6}$ and the contribution is about 0.38 ppm.[1] Expected precision of EDM obtained in this experiment is better than $|\vec{d_\mu}| \sim 10^{-21} e$ cm . In this case, the second term of Eq. 11.4 is smaller than $\sim 3.8 \times 10^{-11}$, which is negligible compared to the statistical uncertainty.

Extraction of EDM (η)

EDM appears tilt of $\vec{\omega}_{tot}$ from $\vec{\omega}_a$. Such effect can be detected by measuring up-down asymmetry of the decay positron. The size of asymmetry is proportional to the z-component of the spin, which is described as

$$\frac{\omega_\eta}{\omega_{tot}} = \frac{\eta}{2a} \left[\frac{\frac{|\vec{\beta} \times \vec{B}|^2}{B^2} + \frac{E^2}{c^2 B^2} + 2\frac{(\vec{\beta} \times \vec{B}) \cdot \vec{E}}{cB^2}}{1 + \delta} \right]^{-\frac{1}{2}}, \tag{11.6}$$

where $\omega_\eta \equiv |\vec{\omega}_\eta|$. Because EDM is expected to be small and relative uncertainty of the measurement is estimated to be $> 10^{-2}$, only leading contribution is important.

$$\frac{\omega_\eta}{\omega_{tot}} \sim \frac{\eta}{2a} \frac{|\vec{\beta} \times \vec{B}|}{B} \sim \frac{\eta\beta}{2a}. \tag{11.7}$$

To obtain the right hand side, we employed the fact that the direction of $\vec{\beta}$ and $\vec{B}$ is almost orthogonal and the deviation from that is negligible.

Actual amplitude of measured asymmetry also depends on the kinematical acceptance of the detector. If we apply the same event selection as the measurement of a, up-down asymmetry include the factor $\mathcal{A} = 0.46$ (same number as proposal). In addition, the factor from the geometrical coverage must be

---

[1] η is defined by the relation of $\vec{d_\mu} = \eta \frac{\mu_B^\mu}{c} \vec{s}$, where $\mu_B^\mu \equiv \frac{e}{2m_\mu}$ and $\vec{s}$ is spin vector with its size of $|\vec{s}| = \frac{1}{2}\hbar$ for muons.

taken into account. Here we performed the evaluation in case that all events in up or down region is accumulated. Finally, the amplitude of the asymmetry is

$$\mathcal{A}_{UD} = \mathcal{A}\frac{\int_0^\pi \sin\phi\, d\phi}{\int_0^\pi d\phi}\frac{\omega_\eta}{\omega_{tot}} \sim 0.46\frac{\eta\beta}{\pi a}. \tag{11.8}$$

Because kinematical acceptance of the measurement, the time dependence of the asymmetry is not simple sine function but modulated as follows.

$$\mathcal{A}_{UD}(t) = \mathcal{A}_{UD}\frac{\sin(\omega_{tot}t)}{1 + \frac{2}{\pi}\mathcal{A}\cos(\omega_{tot}t)} \tag{11.9}$$

The uncertainties of β, a and $\mathcal{A}$ is estimated to be small compared to the statistical uncertainty of $\sim 10^{-21}e$ cm.

Uncertainty of EDM from initial spin direction

When the muon spin at the injection is tilted from the longitudinal direction, the muon spin in the storage ring rotates around ω_{tot} keeping the initial tilt. We evaluate the extraction of EDM in such condition. In this section, we assume that magnetic field is parallel to vertical, electric field is negligible and the beam runs along ideal orbital trajectory. In this condition, ω_{tot} has following components.

$$\omega_z = -\frac{e}{m}aB, \quad \omega_r = -\frac{e}{m}\frac{\eta}{2}\beta B, \quad \omega_\phi = 0 \tag{11.10}$$

Figure 11.1 shows condition when muon spin is tilted from the ideal direction by angle of θ. z-component of the spin direction, which is related to the amplitude of up-down asymmetry to extract EDM, can be calculated to be

$$\begin{aligned} s_z(t) &= -\cos\phi\sin\theta - \sin\phi\cos\theta\sin(\omega_{tot}t) \\ &= -\frac{\omega_z}{\omega_{tot}}\sin\theta - \frac{\omega_r}{\omega_{tot}}\cos\theta\sin(\omega_{tot}t) \\ &\sim \sin\theta + \frac{\eta\beta}{2a}\cos\theta\sin(\omega_{tot}t). \end{aligned} \tag{11.11}$$

Comparing the second term and Eq. 11.7, the amplitude of the up-down asymmetry is diluted by $\cos\theta$. However, it is not expected to be significant because the contribution is square of θ when θ is small. The first term indicates that finite θ causes constant term of $\sin\theta$ in s_z and it causes offset in terms of the up-down asymmetry. Statistically, the offset does not affect the sensitivity of the amplitude of the asymmetry.

General discussion about perturbation of EDM signal

The motion of spin at the muon rest frame is described by following time-differential equation with given frequency vector ω.

$$\frac{d\vec{s}}{dt} = -\vec{s} \times \vec{\omega} \tag{11.12}$$

Muon g-2/EDM Experiment, Conceptual Design Report, Revised, December 12, 2011, 11:41 A.M.
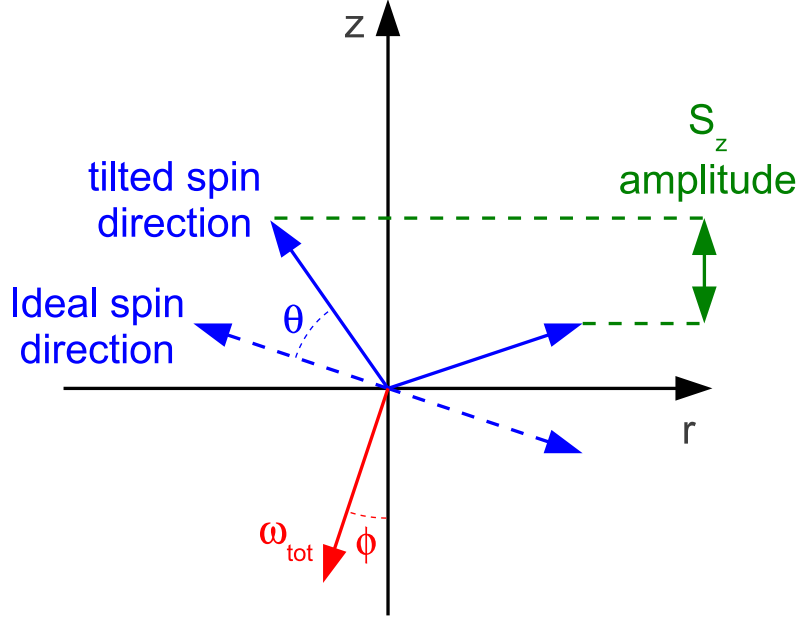
Figure 11.1: *Explanatory drawing of the condition with spin tilted.*

The solution is

$$
\begin{aligned}
s_x &= \frac{\omega_z \omega_x}{\omega \omega_r} s_n \cos(\omega t + \varphi) - \frac{\omega_y}{\omega_r} s_n \sin(\omega t + \varphi) + \frac{\omega_x}{\omega} s_p \\
s_y &= \frac{\omega_z \omega_y}{\omega \omega_r} s_n \cos(\omega t + \varphi) + \frac{\omega_x}{\omega_r} s_n \sin(\omega t + \varphi) + \frac{\omega_y}{\omega} s_p \\
s_z &= -\frac{\omega_r}{\omega} s_n \cos(\omega t + \varphi) + \frac{\omega_z}{\omega} s_p,
\end{aligned}
\tag{11.13}
$$

where $\omega \equiv |\vec{\omega}|$ and $\omega_r \equiv \sqrt{\omega_x^2 + \omega_y^2}$. s_p and s_n is components of the spin vector which is parallel and normal to ω, respectively, and they fulfill $s \equiv |\vec{s}| = \sqrt{s_p^2 + s_n^2}$. φ is arbitrary phase at $t = 0$ and is determined by the initial boundary condition.

As mentioned in Section 11.1.1, the EDM signal appears as up-down asymmetry whose amplitude is proportional to s_z. Based on Eq. 11.13, s_z consists of oscillating term and constant term. The amplitude of the oscillation depends on the EDM size, η, and the constant term behave as the dilution factor. To evaluate the size of s_p and s_n, we consider small perturbations for as follows.

$$
\begin{aligned}
\vec{\omega} &= (\delta\omega_x, \delta\omega_y, \omega_z + \delta\omega_z), \qquad \delta\omega_x \sim \delta\omega_y \sim \delta\omega_z \ll \omega \\
\vec{s}(t=0) &= (s + \delta s_x, \delta s_y, \delta s_z), \qquad \delta s_x \sim \delta s_y \sim \delta s_z \ll s.
\end{aligned}
$$

We set spin vector to x-direction with small perturbation at initial condition. s_p and s_n are obtained to be

$$
s_p = \frac{\vec{\omega} \cdot \vec{s}}{\omega} = s \left(\frac{\delta\omega_x}{\omega} + \frac{\omega_z}{\omega} \frac{\delta s_z}{s} + \frac{\delta\vec{s}}{\omega} \cdot \frac{\delta\vec{s}}{s} \right) \sim s \left(\frac{\delta\omega_x}{\omega} + \frac{\omega_z}{\omega} \frac{\delta s_z}{s} \right)
$$

$$s_n = \sqrt{s^2 - s_p^2} \sim s \left[1 - \frac{1}{2} \left(\frac{\delta\omega_x}{\omega} + \frac{\omega_z}{\omega} \frac{\delta s_z}{s} \right)^2 \right] \tag{11.14}$$

Therefore, deviation of δs_z and $\delta\omega_x$ contribute to s_p and s_n. For the term of δs_z, we already discussed in previous section. $\delta\omega_x$ is equivalent to projection of $\vec{\omega_{tot}}$ in Eq. 11.1 to the direction of muon momentum.

$$\frac{\omega_x}{\omega_{tot}} = \frac{1}{\sqrt{1+\delta}} \left[-\frac{B_x}{B} - G\frac{\beta_y E_z - \beta_z E_y}{cB} + \frac{\eta}{2}\frac{\beta_y B_z - \beta_z B_y}{B} + \frac{\eta}{2}\frac{E_x}{cB} \right] \tag{11.15}$$

If we assume $\beta_y \sim \beta_z \ll \beta \sim 1$ and require Eq. 11.5, size of the second, the third and the fourth term are $\ll 10^{-7}$, $\ll 10^{-6}$ and $< 10^{-15}$, and they are negligible. Therefore, s_p and s_n introduced by δ_x can be approximated to be

$$s_p \sim -s\frac{B_x}{B}, \qquad s_n \sim s\left(1 - \frac{B_x^2}{2B^2}\right). \tag{11.16}$$

The term s_p introduces the offset in time dependence of the asymmetry. However, it does not affect the sensitivity of extracting asymmetry. Though s_n dilutes the amplitude of the asymmetry, the order of the effect is the square of B_x/B. Even if $B_x < 30$ Gauss, which is sufficiently conservative estimation, the dilution factor is 10^{-6}.

11.1.2 λ value from J-PARC MuHFS experiment

From Eq. 11.2, a can be solved as follows.

$$a = \frac{R}{\lambda\sqrt{1+\delta} - R}, \qquad R \equiv \frac{\omega_{tot}}{\omega_p}, \qquad \lambda \equiv \frac{\mu_\mu}{\mu_p}, \tag{11.17}$$

where $\omega_p = \frac{g_p eB}{2M_p}$ is Larmor frequency of a proton at given magnetic field of B, $\mu_p = \frac{g_p e\hbar}{4M_p}$ and $\mu_\mu = \frac{g_\mu e\hbar}{4m}$. λ in Eq. 11.17 is obtained by other independent experiment. Currently new experiment, namely MuHFS, to measure λ is planned at J-PARC. In this section, we discuss the correlation of ω_p and λ when we share detector to measure magnetic filed of both experiments. The Larmor frequency at MuHFS experiment, ω_p^{HFS}, appears to extract λ as follows.

$$\lambda \equiv \frac{\mu_\mu}{\mu_p} = \frac{1}{2} \left[\frac{-(\Delta\omega^{HFS})^2 + \omega_p^{HFS} r_e' \Delta + \Delta^2}{\omega_p^{HFS}(\omega_p^{HFS} r_e' + \Delta)} \right] \left[1 - \frac{\alpha^2}{3} + \frac{\alpha^2}{2}\frac{m_e}{m_\mu} \right]^{-1}, \tag{11.18}$$

where $\Delta\omega^{HFS}$ (hyper file splitting frequency) and Δ are obtained by the measurements. α is fine structure constant. m_e and m_μ is the mass of electron and muon, respectively. r_e' is defined as

$$r_e' \equiv \frac{g_J \mu_B^e}{\mu_p} = \frac{g_e \mu_B^e}{\mu_p} \left(1 - \frac{\alpha^2}{3} + \frac{\alpha^2}{2}\frac{m_e}{m_\mu} + \frac{\alpha^3}{4\pi} \right) \sim 1.3 \times 10^3 \tag{11.19}$$

We concentrate on the correlation between ω_p and ω_p^{HFS} in the remaining part of this section. a and the error of a due to the error of λ and ω_p can be written as follows.

$$a = \frac{\omega_{tot}}{\lambda\omega_p - \omega_{tot}}, \qquad \Delta a = \frac{\omega_{tot}}{(\lambda\omega_p - \omega_{tot})^2}\Delta(\lambda\omega_p), \tag{11.20}$$

where we ignored the contribution of δ in Eq. 11.2. Considering the correlation , we define uncertainties of ω_p and ω_p^{HFS} as follows.

$$\Delta\omega_p = \Delta_u\omega_p \oplus \Delta_c\omega_p, \qquad \Delta\omega_p^{HFS} = \Delta_u\omega_p^{HFS} \oplus \Delta_c\omega_p^{HFS}, \qquad (11.21)$$

where $\oplus$ means quadratic sum and subscripts of u and c indicate uncorrelated and (positive) correlated term, respectively. The uncertainty of $\lambda\omega_p$ is calculated to be

$$
\begin{aligned}
\frac{\Delta(\lambda\omega_p)}{\lambda\omega_p} &= \left[\left(\frac{\Delta\omega_p}{\omega_p}\right)^2 + \left(\frac{\omega_p^{HFS}}{\lambda}\frac{\partial\lambda}{\partial\omega_p^{HFS}}\right)^2 \left(\frac{\Delta\omega_p^{HFS}}{\omega_p^{HFS}}\right)^2 \right.\\
&\quad \left. +2\left(\frac{\omega_p^{HFS}}{\lambda}\frac{\partial\lambda}{\partial\omega_p^{HFS}}\right)\left(\frac{\Delta_c\omega_p}{\omega_p}\right)\left(\frac{\Delta_c\omega_p^{HFS}}{\omega_p^{HFS}}\right) \right]^{-\frac{1}{2}}\\
&= \left[\left(\frac{\Delta_u\omega_p}{\omega_p}\right)^2 + \left(\frac{\omega_p^{HFS}}{\lambda}\frac{\partial\lambda}{\partial\omega_p^{HFS}}\right)^2 \left(\frac{\Delta_u\omega_p^{HFS}}{\omega_p^{HFS}}\right)^2 \right.\\
&\quad \left. +\left(\frac{\Delta_c\omega_p}{\omega_p} + \left(\frac{\omega_p^{HFS}}{\lambda}\frac{\partial\lambda}{\partial\omega_p^{HFS}}\right)\left(\frac{\Delta_c\omega_p^{HFS}}{\omega_p^{HFS}}\right)\right)^2 \right]^{-\frac{1}{2}}. \qquad (11.22)
\end{aligned}
$$

Using Eq. 11.18, the differential of λ becomes

$$
\begin{aligned}
\frac{\omega_p^{HFS}}{\lambda}\frac{\partial\lambda}{\partial\omega_p^{HFS}} &= -\left(1 - \frac{\Delta}{\omega_p^{HFS}r_e' + \Delta}\right.\\
&\quad \left. -\frac{(\Delta\omega^{HFS})^2 - \Delta^2}{\omega_p^{HFS}r_e'\Delta - ((\Delta\omega^{HFS})^2 - \Delta^2)}\right)\\
&\sim -(1 - 0.007 - 0.44) \sim -0.55. \qquad (11.23)
\end{aligned}
$$

We calculated the numerical value based on the MuHFS magnetic field of 1.7 T. Related numbers in this condition are followings.

$$
\begin{aligned}
\omega_p^{HFS} &= 2\pi \times 7.238 \times 10^7\\
\Delta\omega^{HFS} &= 4.463 \times 10^9\\
\Delta &= 2.566 \times 10^9 - 1.898 \times 10^9 = 0.668 \times 10^9
\end{aligned}
$$

Therefore, following Eq. 11.22, the correlation of ω_p and ω_p^{HFS} suppress the uncertainty of a.

11.1.3   Uncertainty from non-uniformity of $\vec{B}$, $\vec{E}$ and $\vec{\beta}$

For now, we discussed the uncertainty of $g − 2$ or EDM based on the uniform field or velocity. Non-uniform field or velocity would contribute to the uncertainty of measurements. Such effect modulate the time dependence of measured asymmetry and it's possible to affect frequency of $|\omega_{tot}|$. It is useful to perform frequency analysis to evaluate such effect.

Final form of the analysis should include the measured value of the magnetic field, sampled by the muons stored in the ring. Since we should be able to obtain the decay vertex distributions, which

provide a good beam trajectory monitor, we should be able to integrate the field with a very good accuracy basing on the measurements without relying on the simulation results.

We have been developing the spin tracking software, which integrates the measured map of the field over the muon beam trajectories. Normal Runge-Kutta approach would not be sufficient in its speed, since the software should track order $1 \times 10^{13} \mu^+$'s in a reasnable time scale ($<$ week). More precise and fast approaches are being developed basing on the Perturbative Taylor Expansion (PTE) technique. We should be able to report more in details when it comes to an appropriate stage.

Schedule and Cost

Contents

12.1 Schedule

A technical schedule of the experiment is shown in Fig. 12.1. Here, we evaluated technically-feasible aspect of the project schedule, assuming sufficient budget and manpower are allocated in time without significant delay.

H-line

The specifications for the beam line has been determined. The design of the beam line is advanced based on the simulation studies. The radiation dose at the surface-muon production target has been measured, and evaluated future does. The front-end magnets, HS1 and HB1, and other front-end devices are under mechanical design work, and under fabrication to install during the summer shutdown in FY2012. The downstream beam line components are planned to be installed in FY2013. The optimization of the final beam line elements before the muonium production target and radiation shielding has been in progress and planned to be completed in FY2012.

Muon source, laser and initial acceleration

The experiments at TRIUMF and RAL studied the muonium production targets. The optimization of the configuration to maximize the number of muoniums in the laser area with an extraction scheme is underway. A demonstration is planned at J-PARC MUSE in FY2012. The design and demonstration of the holding magnetic field with a extraction scheme are planned in FY2012.

The Lyman-α laser at RIKEN-RAL is upgraded with enhanced stability and maximum power. The linearity of the ionization efficiency with power is studied at RIKEN-RAL in FY2011-2012. The experiments at RIKEN-RAL also measures the muonium distribution by scanning the laser position to confirm the muonium production model which was developed based on the TRIUMF data as well as previous publications. The 100 μJ Lyman-α laser is under development at RIKEN. Development of the laser system will be completed and tested at RIKEN in FY2012. The laser system will be installed at U-line where ionization of muonium is to be demonstrated in late FY2012.

Linac

The conceptual design of the muon linac has been developed with realistic simulations. The mechanical design of the I-H linac will be completed in FY2011. The spare RFQ for the J-PARC proton linac was identified as a RFQ for the muon linac. A prototype test of muon acceleration with the RFQ and low-beta part of I-H linac is planned at U-line in FY2012. Acceleration of muon with proposed configuration of accelerators will be demonstrated.

The fabrication of cavities and couplers for I-H linacs, RF system is planned in FY2012-2013. We plan to complete assembly, and start commissioning by the end of FY2013.

Muon g-2/EDM Experiment, Conceptual Design Report, Revised, December 12, 2011, 11:41 A.M.

Storage magnet

Requirements for the spiral injection and the weak-focusing field have been identified. The conceptual design of the magnetic field in compatible with the spiral injection and the weak-focusing has been developed. The designs of the main coils, shim coils, yoke, and cryostat are under development with realistic magnet models, to be completed in FY2012. Evaluation of error fields, and field tuning scheme has been developed.

A magnet for the Mu-HFS experiment shares many common features in the magnet design, except that the Mu-HFS magnet is smaller and lower magnetic field (1.7 T) than the $g-2$ magnet.

The prototype of the field monitoring system with NMR and hall probes has been developed and tested with the 3 T MRI magnet at NIRS. The field monitoring system with improved design will be produced in FY2012. The performance of the field monitoring system will be demonstrated with the magnet for the Mu-HFS experiment in FY2012-2013.

Construction and assembly of the storage magnet will start FY2013. Installation and commissioning will be completed in FY2015.

Kicker

The specifications for the kicker system has been identified. A conceptual design of the electromagnetic and mechanical model has been developed. The eddy currents in the peripheral structures made of conductors are being evaluated. These studies will be integrated in the designs of the storage magnet, positron detector, and field monitoring system.

A prototype of the kicker coils and power supply system has built at KEK. It will be evaluated towards FY2012. The design of the real-life model has started. The evaluation and assembly will be completed by the end of FY2013. The integration with the beam transport and assembly is planned in FY2014-2015.

Detector

Requirements on the positron detector has been identified. A full Monte-Calro simulation model was built. Studies on track reconstruction for a single positron track has completed. Extension to the multi-track events will be completed by early FY2012. Optimum design on the strip configuration will be determined in FY2012.

Evaluation of silicon-strip sensor is in progress. It will be completed by the end of FY2011. Beam tests are planned in FY2012 and FY2013 at J-PARC or elsewhere.

A design and evaluation of the silicon-strip sensor with the optimum strip patterns is planned in FY2012. Mass production of the silicon sensor will start from FY2013 and completed in FY2014.

Design of front-end readout chips for the ASD and TDC parts has been completed. A prototype will be evaluated in FY2012. A combined ASIC with ASD plus TDC will be designed and evaluated in FY2013. The front-end and readout boards will be designed and tested in FY2012-2013.

The mechanical design will be finalized by the end of FY2012. Assembly of detector components will start from the middle of FY2014, finish by the end of FY2015. Overall commissioning starts from FY2016.
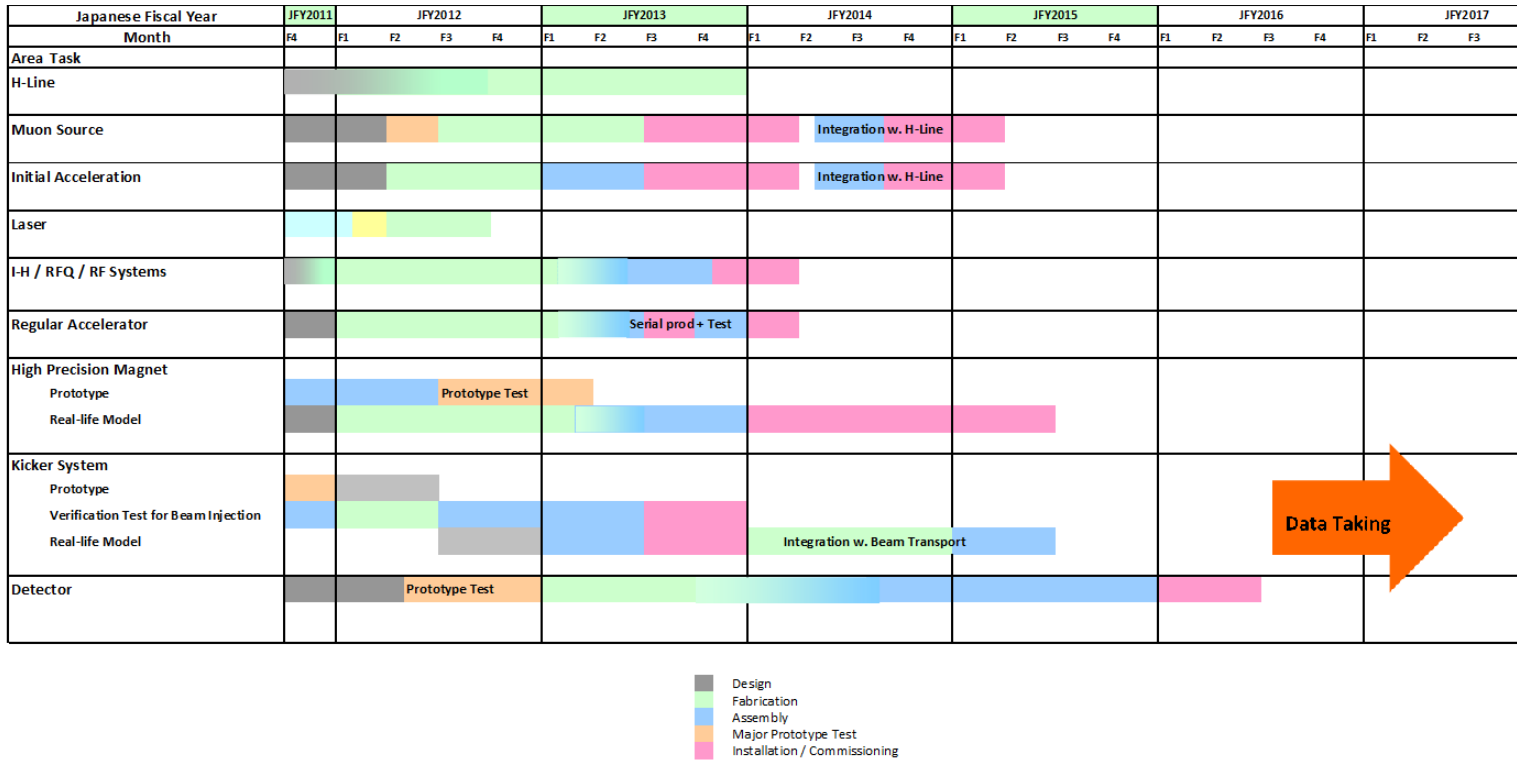
Figure 12.1: *Technical schedule. See text for assumptions made.*

12.2 Cost

A cost estimate is given in Table 12.1. This is still preliminary without engineering designs, but we will give the basis for each number.

- **Surface muon transport**
  The surface muons produced at the production target will be transported to the experimental hall for muonium production. The first capture solenoid should be made radiation resistive. Therefore, the cost estimate is based on the current conceptual design which requires 960 m of minerally insulated coil (MIC).

- **Laser Ionization of Muonium**
  The laser for this experiment is being prepared at RIKEN. While the parts-by-parts cost changes time to time, the ocverall cost seems to be stable.

- **Muon LINAC**
  There is a major change in the baseline design of the Muon Linac. The change may produce a significant cost saving over to the previous design. However, we think it would be too early to reflect that saving into the cost estimate at this point. The estimate should be updated after the accleration test with the first prototype IH and RFQ from J-PARC LINAC.

- **Ultra-precision magnet and monitor**
  A major cost driver for the magnet would be person-power to achieve the required precision. Since the magnet is the heart of the experiment, we will work out the details with the in-house experts. Consequently, the cost would be minimized. Especially we have been constructing the prototype magnet. We should be able to have a clearer idea on the cost once the prototype is completed.

- **Detector**
  We currently assume silicon detectors for the tracking detector for muon decays.

Table 12.1: *Preliminary estimate of the cost of this experiment.*

Item	Cost (Oku-yen)
Surface Muon Transport	Facility will cover
Ultra-Cold Muon Source	
High-power Laser System	3.0
Initial Acceleration System	0.5
Muon LINAC	15
Ultra-precision Magnet	
Solenoid	10
Field Monitor	1
Detector System	
Silicon Tracker	2.5
Readout Electronics	0.5
TOTAL	33 + Facility